Springer Series in Materials Science

Volume 174

For further volumes:
http://www.springer.com/series/856

The Springer Series in Materials Science covers the complete spectrum of materials physics, including fundamental principles, physical properties, materials theory and design. Recognizing the increasing importance of materials science in future device technologies, the book titles in this series reflect the state-of-the-art in understanding and controlling the structure and properties of all important classes of materials.

Kartik N. Shinde · S. J. Dhoble
H. C. Swart · Kyeongsoon Park

Phosphate Phosphors for Solid-State Lighting

Springer

Kartik N. Shinde
Department of Physics
N.S. Science and Arts College
Bhadrawati
India

H. C. Swart
Department of Physics
University of the Free State
Bloemfontein
South Africa

S. J. Dhoble
Department of Physics
R.T.M. Nagpur University
Nagpur
India

Kyeongsoon Park
Faculty of Nanotechnology
and Advanced Materials Engineering
Sejong University
Seoul
Republic of South Korea

ISSN 0933-033X
ISBN 978-3-642-34311-7 ISBN 978-3-642-34312-4 (eBook)
DOI 10.1007/978-3-642-34312-4
Springer Heidelberg New York Dordrecht London

Library of Congress Control Number: 2012952582

© Springer-Verlag Berlin Heidelberg 2012
This work is subject to copyright. All rights are reserved by the Publisher, whether the whole or part of the material is concerned, specifically the rights of translation, reprinting, reuse of illustrations, recitation, broadcasting, reproduction on microfilms or in any other physical way, and transmission or information storage and retrieval, electronic adaptation, computer software, or by similar or dissimilar methodology now known or hereafter developed. Exempted from this legal reservation are brief excerpts in connection with reviews or scholarly analysis or material supplied specifically for the purpose of being entered and executed on a computer system, for exclusive use by the purchaser of the work. Duplication of this publication or parts thereof is permitted only under the provisions of the Copyright Law of the Publisher's location, in its current version, and permission for use must always be obtained from Springer. Permissions for use may be obtained through RightsLink at the Copyright Clearance Center. Violations are liable to prosecution under the respective Copyright Law.
The use of general descriptive names, registered names, trademarks, service marks, etc. in this publication does not imply, even in the absence of a specific statement, that such names are exempt from the relevant protective laws and regulations and therefore free for general use.
While the advice and information in this book are believed to be true and accurate at the date of publication, neither the authors nor the editors nor the publisher can accept any legal responsibility for any errors or omissions that may be made. The publisher makes no warranty, express or implied, with respect to the material contained herein.

Printed on acid-free paper

Springer is part of Springer Science+Business Media (www.springer.com)

Preface

The theme of luminescence and phosphors has assumed ever more significance in the overall scheme of scientific progress. This book is aimed at providing a sound introduction to the phosphate phosphor for undergraduate and postgraduate students. I hope that it will also be of value to teachers of these courses. The reader will find a fairly comprehensive bibliography for further investigation.

The luminescent materials known as phosphors convert energy into electromagnetic radiation, usually in the visible energy range. Phosphors are solid luminescent materials that emit photons when excited by an external energy source. Luminescence continues to play a major technological role for mankind. Solid-state luminescence is now set to significantly displace gas discharge luminescence in many areas, in much the same way as gas discharges have already displaced tungsten filament incandescence. Almost all modern phosphors are synthesized by solid-state reactions at high temperatures. Updated versions of these techniques are presented in this book along with other techniques such as sol–gel and combustion that have been developed over the past few decades. In the domain of lighting devices, from the first lamp made by Edison to the compact fluorescent lamp used everywhere today, progress and improvement are obvious. However, there is a need to continue research in this field because excitation sources have changed and it is known that a good phosphor for electronic or ultraviolet excitation is not necessarily a good choice for excitation in vacuum ultraviolet (VUV). Till date, in order to produce light with a fluorescent lamp it was necessary to put mercury inside the lamp to generate ultraviolet photons at $\lambda = 254$ nm. These would subsequently excite the phosphor-coated inner surface of the lamp. However, in the near future, it will be mandatory to replace/reduce the use of mercury in lighting devices, because mercury is very harmful for the environment.

The past few decades have seen spectacular developments in research on luminescence. There has been phenomenal growth in the subject and significant progress has been made. Rare earth ion-activated phosphors have numerous applications in the display, lighting, and medical industries. In recent years, the luminescent properties of phosphate materials have been widely investigated for their many advantages, such as excellent thermal and chemical stability, and the development of optical devices based on rare earth (RE) ion-doped materials has proven to be one of the most interesting fields of research. In this context, phosphates are investigated because of their low cost, their high stability for use in lamp applications, and their important crystallographic possibilities with regard to the accommodation of luminescent ions.

Phosphate structures are generally rigid, resistant to chemical attack, and (when anhydrous) insoluble and thermally stable. This leads to some applications as nuclear waste immobilization hosts or negative thermal expansion materials. Phosphate anions do not absorb significantly in the UV-visible region and so solid phosphates can also find use as optical materials such as glasses, phosphors, nonlinear media, and lasers. Solid phosphates constitute many minerals, notably apatites, which are also found in living organisms as rigid components such as bones and teeth.

Considerable improvement in the field of luminescent materials has been made by the introduction of rare earth ions as activators. These ions possess unique optical behavior when doped into materials and have paved the way for the development of optical amplifiers and phosphors. The optical value of these ions results from the electronic transitions occurring within the partially filled 4f energy shell of the lanthanide series. Rare earth-activated alkaline phosphate-based compounds are of interest due to their unusual stability and useful luminescent properties. They are used for different applications such as phosphors for lamps, color TV screens, long lasting devices, laser hosts, scintillators, and pigments.

The energy transfer phenomenon has been studied extensively in inorganic phosphors, crystals, solutions, and glasses. Hence, in order to contribute to such knowledge, an attempt has been made in this book to consider efficient phosphors based on rare earth-activated phosphates, to study their luminescence properties, and to explore potential new materials and applications. These phosphors are synthesized using low-cost and time-saving synthesis methods, such as wet chemical synthesis and combustion synthesis. One of the objectives of the book is to better understand the mechanism of energy transfer and photoluminescence behavior of some phosphate phosphors. Efforts have been made to identify new phosphate phosphors which could be used for solid state lighting and whose efficiency is either of the same order or better than that of commercial phosphors.

Phosphates are among the most important class of inorganic compounds. As its title indicates, this book is devoted specifically to phosphate phosphors. Each chapter consists of a short general introduction to a specific class, followed by some examples from the literature and by my own work. Solid-state lighting using light-emitting diodes (LED) and phosphor material to generate white light is the current research focus in the lighting industry. Solid-state lighting technology has several advantages over conventional fluorescent lamps, such as reduced power consumption, compactness, efficient light output, and longer lifetime. Solid- state lighting will have its impact in reducing global electricity consumption. White light-emitting diodes can save about 70 % in energy terms and do not require any harmful ingredients, in contrast to conventional light sources, such as incandescence light bulbs and luminescent tubes. White LEDs thus have a great potential to replace the latter and are considered to represent the next generation of solid-state lighting devices. Research on tricolor phosphors suitable for near-ultraviolet/ultraviolet excitation has attracted considerable attention because of their important applications in solid-state lighting. Simple syntheses from easily available starting materials of known phosphate phosphors used as lamp phosphors were also investigated. Possible future developments are pointed out. Studies of mixed cation phosphates are also described. Many mixed anion phosphates are known to chemists and geologists. However, no luminescence measurements are available on these halophosphate and orthophosphate materials.

I have provided the exact formulas for calculations and conditions required to make all of the phosphors known at the time of writing. Each formula is the result of many hours of experimentation to optimize the final phosphor composition. I have retained much of the material presented in the book because I believe one should know what the history of any given subject entails. The last part is organized in some cases with the structure of an academic paper, that is, with an experimental part and a results and discussion section. I think this is a good choice since not only "general" data are presented, but specific procedures to prepare the described compounds, adding to the "fundamental" knowledge are also presented. Hence, the present book is both a review of a specific theme and a preparative manual. I have enjoyed preparing this book and hope that you find reading it both profitable and enlightening.

Contents

Chapter 1
Introduction

1.1 A Short History of Lighting [1]

The history of the light bulb can certainly be traced back to Messrs Swan and Edison, but it is equally certain that they would not have made their respective leaps without the benefit of Michael Faraday's research on electricity. His discoveries of the electric motor and the dynamo in the 1830s allowed for the continuous supply of electricity to make usable light a viable option. Although gas lighting predominated, and indeed continued until after the end of the Second World War, the first appearance of electric lighting was around 1880 and followed the development of the incandescent lamp by Edison and Swan (Fig. 1.1). These were very crude devices, as were the materials available to them. This resulted in efficacies of a very low level (less than 5 lm/W) at a correspondingly high cost.

In the beginning, this form of lighting was restricted to the very well-off and to some commercial and retail establishments. However, in the 1920s, the lamp was improved by using a tungsten filament and filling the bulb void with gas, which increased the life of the filament by reducing tungsten evaporation. Research at the turn of the century was ongoing in the area of gas-filled lamps, as it was anticipated that the next generation of lamps would need improvements with regard to efficacy and longevity, but the restricting factor here was the lack of a suitable current-limiting device. Work continued for many years in this field and the first commercial installation of low pressure sodium lamps was installed at Purley Way, Croydon, in 1932. Lamp efficacy was subsequently increased to some 50 lm/W. In the same year, the high pressure mercury lamp saw its introduction as street lighting in Wembley, Middlesex, with efficacies around 36 lm/W. It is interesting to note that Philips had its headquarters in Croydon and the GEC (as it was then known) had its offices in Wembley [1].

Although these advances were pushing forward the frontiers of technical development, color rendering was at a very poor level. The next development took place in the United States when the low-pressure mercury lamp (commonly known as the fluorescent tube) was launched. This produced useful quantities of light with

K. N. Shinde et al., *Phosphate Phosphors for Solid-State Lighting*,
Springer Series in Materials Science 174, DOI: 10.1007/978-3-642-34312-4_1,

efficacies around 30 lm/W. A great leap forward was made in 1942 with the discovery of the halophosphate phosphors, bringing greater stability in light output and further increasing lumen output to around 55 lm/W. It is interesting to note that in the United States they have until recently remained steadfast in their use of the 38-mm diameter lamp, while Europe changed with much greater enthusiasm. It is likely that our much higher energy costs played a major role in this. To this day, it is still the norm to see the older technologies in use in the majority of States.

In 1973, the first of the fluorescent triphosphor lamps were developed (Fig. 1.1). This produced an increase of 50 % in lumen output with the added advantages of extra life and the birth of the technology that was to result in the compact fluorescent lamp. It was the development of this range of lamps which heralded the possibility of making major reductions in a huge variety of installations. Savings of the order of 50 % were easily achieved and lighting design was given a new light source, significantly smaller than anything that had been previously available. Commerce and industry fell over themselves to use this lamp, but the British public was not interested in such an ugly new light source. Indeed, it must be said that they were not cost effective for domestic use, as many manufacturers priced them at a level that was never going to encourage significant use. This, together with the fact that there were virtually no acceptable domestic fittings, could easily have spelt the end as far as the public were concerned. It took several campaigns from groups such as the Energy Saving Trust to stimulate the slightest glimmer of interest, and it was only when some of the big D.I.Y. operations started doing serious deals with the manufacturers that they started moving with the public.

Compact fluorescent lamps range over many shapes and sizes, from 5 to 58 W, and some would say that the enormous choice may have led to confusion. There are three main features to choose from, over, and above those required to select a standard fluorescent lamp: (i) Physical size of lamp required to fit the luminaire. (ii) Deciding whether to use standard wire-wound or electronic ballast. (iii) Deciding whether or not to retrofit a version that has the control gear incorporated within it.

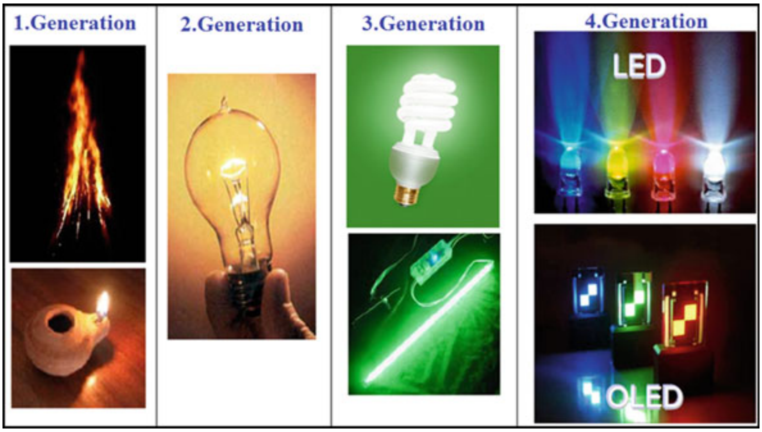

Fig. 1.1 Generations of lighting

We are already experiencing a general downward trend in the pricing of this range of lamps, and there is a strong possibility that they will follow a similar trend to standard fluorescent lamps. The importance of the advent of electronic ballast for use with fluorescent and compact fluorescent lamps should not be underestimated. There were several advantages in increasing the frequency of modulation through the lamps: (i) Fluorescent lamps lost their "flicker", and this brought with it huge labor savings since the incidence of headaches and other debilitating symptoms caused by the 50 Hz flicker in some of the longer fluorescent lamps disappeared, thereby reducing absenteeism from work. Indeed, this form of flicker was also instrumental in bringing about many cases of epilepsy. There is even an instance of a local authority doing a deal with its facility managers in which fluorescent tubes replaced in planned maintenance are being recycled in local schools, a practice that can in no way be condoned. (ii) The energy used to operate these lamps was cut by reducing ballast losses from 15 % down to about 2 %. It was also possible to manufacture lower wattage lamps, offering further energy reductions. (iii) Virtually all noise was eliminated from the control gear [2].

Tungsten halogen lamps entered the market place about 1960, although the possibility of using chlorine had first been developed back in the 1880s, and iodine in 1933. This type of lighting was initially used mainly for floodlighting, and although the first lamps were 1,000 W, lower powered versions soon followed and are widely used around the world today.

The 1960s saw the introduction of the metal halide lamp, which was developed independently in both Europe and the USA with a different composition of elements. In both cases, starting voltages in excess of 1,400 V were required, and large and heavy associated control gear had to be either incorporated in the luminaire or installed within a maximum distance of 2 m from the lamp [3]. The benefits of this lamp constituted a further leap forward, but various control restrictions were associated with it. In the early days when the lamp became commercially available there were many variations in lamp color, even with lamps from the same batch. Indeed, there were many disappointments with this lamp, and it was not until 1994 that it could be used without fear, thanks to the incorporation of an electronic ballast. In fact, during the first 30 years of its history, reliability had always been a serious bone of contention. The main or controlling feature of this lamp is current, and it was the inability to totally control the current that caused the wild fluctuations in color rendering.

Linked with this problem was that of short lamp life. It was generally but incorrectly believed by many lighting designers that this lamp had a life of around 6,000 h, but certainly in the early days many lamps seemed to be failing in the first 3,000 h. This was due to slight changes in the operating voltage/current which gave the white lamp a greenish tinge that predicted imminent failure. It may be that many of these so-called failures were in fact the result of unstable voltage/current. Although up to 3 years ago the nominal voltage in the UK was 240 V $+10\,\%$ $-6\,\%$, it was a working reality that supply voltage was sometimes in excess of the maximum.

The ceramic metal halide was first introduced by Philips in 1994 and was one route by which consistency of color was returned. By 1999, both GE and Osram had working alternatives and an increase in length of life to 9,000 h was being claimed.

However, it seems that there is insufficient evidence for this to be considered certain yet. Dimming has only recently been achieved with the metal halide lamp and with it an increase in life to in excess of 10,000 h, a consistency of color, and a significant reduction of startup times, which can be in excess of 6 min [4].

In 1965, the high-pressure sodium lamp was released, bringing with it a jump in efficacy to some 90 lm/W and color rendering that allowed the lamp more uses. The much warmer color than metal halide or mercury made it a winner with external lighting designers. In 1986, the sodium lamp took a step forward with the introduction of white sodium lamps, generically known as white SON. This was a very much smaller version, allowing greater flexibility that brought it considerable popularity with designers in the retail sector.

In 1966, the first dichroic extra low voltage lamps were released. These lamps mainly operated at 12 V and gave luminaire manufacturers several decades in which to design delivery systems that became “de rigeur”. It has to be said that they opened up the next generation of lighting, but unfortunately over the years became one of the most misused lamps of this generation. People not only lit alcoves and specific features with them, but it became the fashion to use them to light entire areas, and even entire groups of shops. Here are two examples: (i) Woolworth’s decided to develop a range of superstores. A well-known designer was brought in and, in his enthusiasm, illuminated the entire shed with low-voltage M50 dichroic lamps. The Sunday Times newspaper, which had just launched a color section, did a full article on it. There were over 3,000 lamps in the installation. It looked the very epitome of all that was chic, but 3 months later over 2,000 of the lamps had failed. The shed was closed down and fluorescent battens were hung throughout the store. (ii) Another well-known group of over 260 shops relied totally on low-voltage lighting as its only source of illumination. After the initial refits, air conditioning had to be installed just to keep the shops at a comfortable working level. The level of maintenance needed was high and so was the overall cost.

Low-voltage lighting probably offers the lighting designer his most useful tool due to the precision of control this range of lamps allows. The introduction of the electronic transformer made it possible to incorporate several new features: (i) The virtual elimination of noise or hum, particularly when lamps are dimmed. (ii) The often added soft start option meant that lamp filaments were not subjected to previous pressure levels and this resulted in a significantly longer life. (iii) Sizes of electronic transformers were further reduced, allowing even greater flexibility. (iv) Electronic transformers emit less heat.

Coming now to the present day, we have the induction lamp. Early reports are very good. Its exceptional life (some 60,000 h) ensure that it will always be useful for areas of difficult or dangerous access. It has an output of some 65 lm/W, and works internally at relatively low temperatures of about 250 °C. These lamps all work at high frequency, in excess of MHz. There is the added advantage of no apparent stroboscopic effects. Its control gear is electronic, and if there is a drawback to this lamp, it may lie within the control box. This is not a low-price alternative, but superiority of performance will certainly justify this type of lamp in some situations.

It seemed at one time that fiber optics would overtake SELV systems in popularity. Although they were most effective systems, they were let down by their inability to match the M50 dichroic lamp which had taken on the mantle of industrial standard. This system works on the principle of a metal halide lamp within a “light box” and a fiber optic cable transmitting the light to a dichroic emitter. It is still not possible to achieve greater brightness than one would hope to get from a wide beam 35 W dichroic lamp, but it has the huge advantage of being safe, as there is no passage of electricity, only light, and this makes for a superb underwater fitting at any depth. The losses in the cable are insignificant and theoretically allow cables to be run for great distances with no apparent diminution of light output. And it can even go around corners. The only daunting feature is the very high price of the cable.

An interesting system of dimming was much used in the past. It exploits a spinning disk with sections cut out. The light from the metal halide lamp passes through this on its way to the cable, and speeding up or slowing down the speed of revolution can achieve different levels of dimming. Nowadays, there are more sophisticated systems of electronic dimming, but they are more expensive, even if they are more effective. Several of the clearing banks have used fiber optics at their banking tills, with the added advantage of negligible heat transfer, hence less air conditioning required and yet more financial savings.

It may be that the light-emitting diode (LED) will eventually take on the universal mantle (Fig. 1.1). This lamp was first used in traffic signals in 1995. We are all now familiar with them as information signs on the UK motorway network. With energy savings of around 60 % and an extremely long life, there is once again the added advantage of minimal heating. The light bulb has come a long way since 1880, but development of new lamps will arrive in quicker succession. They will become safer, more energy efficient, and more adaptable than those in use today. New sources will undoubtedly be utilized and control systems will be honed to greater degrees. In 20 years time, there is no doubt that our “new” technologies will appear “old hat” [1].

A dozen years into the twenty-first century, most artificial light in modern homes comes from a nineteenth century technology—the incandescent lamp. Considered for generations as the symbol of a bright idea, incandescent bulbs occupied about 80 % of screw-in light fixtures in the United States in 2009. Compact fluorescents entered the picture in the 1980s. They use electronic ballasts that eliminate flicker and deliver 50–70 lm/W. That energy efficiency, along with declining prices and lifetimes several times longer than incandescents, has earned them places in many homes. Yet, they still comprise a relatively small share of the home-lighting market. And even fewer homes are using solid-state technology based on light-emitting diodes (LEDs), which are potentially even more efficient and longer lived than fluorescents. With LED lighting now an available option, energy agencies around the world are encouraging people to, well, flip the switch on older technologies.

So why are we having such a hard time changing the lights? The answer is that energy efficiency is not all that matters in illumination. Issues of brightness, color, and even human psychology also come into play. Many people prefer the old-fashioned glow of a hot filament. And while compact fluorescents fit the familiar screw-in sockets, they have their own set of problems. In addition to containing a small amount of mercury, they are fragile and cannot be dimmed, and they have bulky ballasts that do not fit into some light fixtures. New solid-state bulbs largely avoid those problems, but the technology is young and the bulbs are costly. Neither fluorescents nor LEDs can match the warm black-body emission of the century-old incandescent tungsten filament. And many people feel the new lights are too harsh, and that they look ugly in some fixtures, especially those for small-base candelabra bulbs.

It is also important to remember that all new technologies take time to reach their own particular "tipping point". In fact, the incandescent bulb itself did not gain instant acceptance, as described above. The bulbs developed independently by Thomas Edison and Joseph Swan in 1879 used fragile carbon filaments, which emitted a mere 3.5 lm/W in 1900, after two decades of refinement. When the tungsten filament was patented in 1904, only a few percent of American homes had electricity. But progress was under way. In 1908, George H. Jones wrote in the *Transactions of the Illuminating Engineering Society*: "The many recent improvements in electrical appliances, the introduction of high efficiency lamps, and the great reduction in the cost of electricity are combining to put the 'House Electrical' within the reach of thousands ..." 5 years later, General Electric introduced a coiled tungsten filament emitting 12 lm/W; similar bulbs are still in use, emitting 10–17 lm/W. The fraction of wired United States homes did not reach 70 % until 1930, half a century after the invention of the incandescent bulb.

Businesses were faster to wire up and embrace the next big thing in lighting—the linear fluorescent lamp, invented by General Electric in the 1930s. By 1943, a 40-W fluorescent could produce 52 lm/W by exciting phosphors with the bright ultraviolet emission of a mercury discharge. That high efficiency made fluorescents a hit in industry, stores, office buildings, and schools, and by 1951 they were generating more light in the United States than incandescent bulbs. But home use was limited by their harsh white color, their tendency to flicker, and their need for special light fixtures and power-converting ballasts.

1.1.1 The New Great White Hope

How can we make illumination both attractive and efficient? That is the challenge facing the new great white hope of energy-efficient lighting—solid-state lighting. Although young, the technology is moving fast, and one can generally find solid-state bulbs in any large hardware store or online.

LEDs emit light when carriers recombine in a suitable semiconductor; at visible wavelengths, their normal bandwidth is about 25 nm. In 1962, Nick Holonyak Jr. made the first efficient visible LED, emitting in the red, from gallium arsenide-phosphide. Other colors followed, and most were used in displays and indicator lights. Shuji Nakamura's successful 1993 fabrication of bright blue LEDs from indium-gallium nitride at the Nichia Corporation in Japan opened the door to solid-state lighting. Combining red, green, and blue LEDs can produce white light, and adjusting the ratios of the three gives a wide range of colors. However, the need for three emitters increases costs and complexity, and green LEDs are less efficient than red or blue emitters. RGB LEDs are now used mainly as backlights for high-end displays and monitors, where their wide gamut of colors offsets limitations such as the uneven aging of different-color LEDs.

Virtually all other LED illumination uses blue LEDs, both to provide blue light and to illuminate phosphors that generate longer wavelengths. Typically, a 460-nm LED pumps a cerium-doped yttrium–aluminum garnet phosphor, which fluoresces from 500 to 700 nm, with peak output at 550 nm in the yellow. This approach cuts costs and gives high efficiency, although the resulting light is stronger in the blue than in the red, making it look harsh. Newer and more expensive lamps add other phosphors to boost red emission and a few include red LEDs.

Solid-state lighting started out small in a specialized niche—flashlights, which do not require high color fidelity but do need efficient use of battery power. White LEDs fit the bill nicely, and they now dominate the flashlight market. They also found similar niches in headlamps for hikers and headlights for bicycles. With small LED flashlights selling for a couple of dollars—including AAA batteries—or being handed out as trade-show freebies, you might expect sales to be modest. But the market-research firm Strategies Unlimited says $927 million in LED flashlights were sold in 2008—more than one-third of all LED lighting sales that year.

The tiny size and low power requirements of white LED lamps have created other market niches. In fact, such flashes are almost impossible to create without them because the flash modules must be very small to fit in phones. White LEDs are also crucial for solar-powered lawn lights, which collect enough solar energy during the day to power LED lamps for hours at night. Solid-state emitters promise a long lifetime, with accelerated aging tests predicting that the LEDs can operate for 25,000–50,000 h before their output drops to 70 %. This is a huge improvement over the 1,000-h life of standard incandescent bulbs, and better than the 6,000–15,000 h of compact fluorescents, which may not last that long outdoors. Long lifetime alone can command a premium price for LEDs in outdoor architectural lighting fixtures, where workers need a cherry picker to replace bulbs.

1.1.2 Advantages and Drawbacks of Directional Lighting

Unlike hot filaments and fluorescent tubes, which radiate in all directions, LED emission is inherently directional, usually from the top of the chip. This makes LEDs a better fit for directional applications, including street lights, floodlights, and car headlights as well as flashlights. The degree of directionality depends on the design of the lamp and fixture. "You can get very sophisticated optics to give sophisticated patterns from directional LEDs," says Brian Terao of Osram Opto Semiconductors. The company's thin GaN chips direct 97 % of their light energy through the top of the semiconductor, and they are packaged to spread that light in an oval, or in circular beams spreading across 80, 120, or 150°. "Street lights are a perfect example of the advantage of directionality," says Terao. Omnidirectional sources radiate light everywhere, wasting energy and producing light pollution. “LEDs allow you to direct light where it’s wanted,” illuminating a roadway or parking lot without sending light upward or to the side. He recommends using fixtures designed for LEDs to get the true benefits of this technology, because such designs can better distribute light to where it is needed. Some such fixtures focus LEDs up into a downward-facing reflector, while others focus them down through lenses onto the road.

State, local, and federal agencies and the US Department of Energy (DoE) established the Municipal Solid-State Street Lighting Consortium to promote the new lamps. The California Department of Transportation is replacing high-pressure sodium lights, which last a couple of years, with solid-state fixtures, lasting up to a decade, on bridges statewide. The effect is striking from above, says Hausken. Flying into San Francisco airport, he saw the deck of the San Mateo bridge illuminated, yet he could not see the solid-state lamps directly because all their light went downward.

But what works in the municipal setting is not necessarily what works at home. Replacing the bulbs already occupying some 4.7 billion Edison screw-in light fixtures in residences is a key goal for energy conservation, but a difficult one to implement. “The first underlying issue is the cost” of LED lamps, says Narendran. However, he adds, “most of the incandescent replacements are not truly replacements.” This is because the replacement lamps do not spread the light omnidirectionally in the same way as do the filament bulbs to which most consumers are accustomed. This is a problem because of the directional nature of the LED lamps sold as replacements. Even in the few solid-state products that have the rounded profile of a standard incandescent bulb, only the upper half radiates light across 180°. “If your sockets are facing downward, you’re in good shape,” says Terao. But put the same LED bulb into a table lamp with a shade, he says, “and you’ll probably see most of the light going upwards. If it’s a table lamp, you’re not going to want light on the ceiling.”

In contrast, directional LED bulbs fit naturally into “downlights” that are recessed into ceilings, a popular modern design that focuses light onto work areas such as a kitchen counter or desk. But the drive circuits, placed between the screw base and the LED emitters, must be designed to cope with the heat they generate. Although many LED bulbs are designed for downlighting, others warn that they are “not for use in totally enclosed recessed fixtures.”

1.1.3 The Tricky Problem of Color

Color is a tough problem in developing new illumination systems. Our visual systems evolved to recognize objects by their color under varying conditions of natural light, and our visual response can be quite complex.

The sun is a black-body emitter with an effective temperature of 5,780 K, and our eyes evolved to be most sensitive near the peak of the black-body curve in the green. The spectrum of sunlight reaching the ground varies considerably during the day, depending on solar elevation and atmospheric conditions. When the Sun is due overhead, light reaching the ground has an effective temperature of 5,500–6,000 K.

When it is near the horizon, Rayleigh scattering depletes blue light, shifting the color temperature to about 5,000 K. The scattered blue light gives the sky that is away from the Sun—or the diffuse light on an overcast day—a color temperature higher than that of the Sun. Our eyes adapt automatically, so we do not notice the changes in color during the day.

Tungsten-filament bulbs are also black-body emitters, but their temperatures are typically 2,700 K so their emission is much redder. (In illumination, reddish light is called "warm", although its color temperature is cooler than that of the Sun; "cooler" light comes from hotter emitters.) However, we still perceive that light as white because our color response varies with light intensity, and the redder incandescent light looks better at the dimmer levels of interior lighting than direct sunlight would look at the same brightness.

Normally, we view objects by reflected light, so we see a convolution of the spectrum emitted by the light source and that reflected by the object. Our visual systems can accommodate for the differences in black-body spectra, but fluorescent and LED bulbs are not black-body emitters, introducing an effect called color rendering. The emission spectra of fluorescent and LED bulbs depend on the choice of wavelength-converting phosphors. Designers of early fluorescent lamps picked phosphors to match the blue-rich light of the solar spectrum, with a color temperature of 5,000–6,000 K, for use in brightly lit factories and offices. Today's cool white fluorescents have color temperatures around 4,100 K, but at the low intensity usually used in homes that seems harsh to the eye and causes color-rendering problems. Early solid-state lamps used phosphors optimized for high efficiency, which emitted bluish light with high color temperatures. That was fine for flashlights, but residential users want a redder blend. Thus, as LEDs have improved, more red phosphors have been added to the mix.

Osram now offers four different phosphor systems, ranging from a bluish one for flashlights to a reddish one with a color temperature of 2,700 K. By adding a separate red LED to the phosphor and blue LED, Osram's "Brilliant Mix" bulb renders colors very well, with a CRI of about 90. In August, Philips won the DoE's L-Prize challenge with bulbs that exceeded a CRI of 90, and that also consumed less than 10 W while generating 900 lm, roughly equivalent to a 60-W incandescent. The eye can be quite sensitive in side-by-side color comparisons that do not require one to look directly at the bulbs. Looking at reflections of a Philips 2,700 K Ambient LED bulb and a 3,000 K Ecosmart bulb on a glass flat, the orange tinge of the Philips bulb is striking compared to the stark white Ecosmart bulb. Color quality has improved markedly since the first solid-state lamps came on the market. "Some of the early ones were very dim and very blue," says Geoffrey Landis, a physicist at the NASA Glenn Research Center in Ohio, who has bought 40 of them for his home in the past 3 years. He finds new bulbs with 2,700 K color temperature "pretty much indistinguishable from incandescent bulbs."

1.1.4 Cost, Quality, and Lifetime

Price is one of the biggest obstacles to getting LEDs beyond flashlights and into the home. Normal retail prices are \$30–\$40, and even people in the business hesitate to pay that much. Another problem is teaching people what to look for. In May 2011, the DoE warned that confusing labels can make buying solid-state lamps "a risky endeavor". New "lighting facts" boxes specify brightness, energy use, and color temperature, but most consumers are accustomed to buying incandescent bulbs by their wattage, and that equivalent may be exaggerated. Often the difference is small; my 429-lm bulb is designated as being equivalent to a 40-W incandescent, which typically emits 460 lm. But the difference can also be significant, particularly for brighter LEDs, which are scarce. The MaxximaStyle BR40 is advertised on many Websites as a "100-W equivalent", but its 920 lm output falls far short of the nominal 1,750 lm from a 100-W incandescent. The DoE also warned that lifetime claims may be exaggerated, reporting that more than half of the bulbs it tested were not likely to meet projected lives of 12,000–50,000 h. LEDs can last that long, but the drive electronics or plastics used in the bulb could fail earlier, Terao says. The long-term testing needed to verify lifetime claims can also delay the introduction of new products.

The emission of phosphors exposed to the high temperatures and intense light in an LED bulb can degrade, shifting their color, says Charles Hunt of the University of California at Davis. In November, he warned the Nineteenth Color and Imaging Conference that phosphor emission could drop by half after 5,000 h of operation, making the light harshly blue. However, phosphors and bulb technology are improving. A DoE spokeswoman said that the Philips bulbs that won the L-Prize have shown a color shift of less than 1 % after 12,000 h of testing. Meeting the L-Prize goals for 900-lm bulbs was an important milestone. Philips plans to introduce them commercially early this year. The DoE reports that bulb cost per lumen has fallen 25 % annually since 2005. Light production reached 200 lm/W in laboratory bulbs by the end of 2010, but commercial products lagged, with cool white bulbs yielding only 132 lm/W, and warm white only 62 lm/W. The DoE expects to reach 250 lm/W for bare bulbs, and 200 lm/W for bulbs in light fixtures.

In the longer term, the DoE is looking to organic LEDs (OLEDs) for the next generation of lighting. OLEDs will not be as bright or tolerate the high temperatures of today's inorganic LEDs, but they could be the basis for inexpensive light panels emitting diffused light from an area on the wall or ceiling, rather than intense light from a bulb. Small laboratory OLEDs have reached an efficacy of 68 lm/W. By the end of the decade, the DoE hopes they will match the efficacy of inorganic LEDs and scale them to 200 cm^2.

At the end of the day, the toughest problem may be esthetics. People do not want light fixtures that look ugly, or that make their furnishings appear unattractive. It will likely take some time and some further development before our society truly begins to see LEDs in a new light. Since fire was first harnessed, artificial lighting has gradually broadened the horizons of human civilization. Each new advance in lighting technology, from fat-burning lamps to candles to gas lamps to the incandescent lamp, has extended our daily work and leisure further past the boundaries of sunlit times and places. The incandescent lamp did this so dramatically after its invention in the 1870s that the light bulb became the very symbol of a "good idea" (see Fig. 1.2).

Luminescence continues to play a major technological role for mankind. Solid-state luminescence is now set to significantly displace gas discharge luminescence in many areas, in much the same way as gas discharges have already displaced tungsten filament incandescence. One can say this with confidence owing to the high conversion efficiencies now demonstrated for inorganic and organic light-emitting diodes. Technologically important forms of luminescence may be split up into several categories. Although there are a variety of ways of exciting luminescence, all forms of luminescence are generated by means of accelerating charges.

The portion of the electromagnetic spectrum visible to the human eye is in the wavelength range 400–700 nm. The evolution of the relatively narrow sensitivity range of the human eye is complex, but is intimately related to the solar spectrum, the absorbing behavior of the terrestrial atmosphere, and the reflecting properties of materials. Green is the dominant color in nature and, not surprisingly, it is the wavelength at which the human eye is most sensitive.

The word 'phosphor' comes from the Greek language and means 'light bearer', to describe light-emitting or luminescent materials; barium sulfide is one of the earlier known naturally occurring phosphors [5]. A phosphor is luminescent, that is, it emits energy from an excited electron as light. The excitation of the electron is caused by absorption of energy from an external source such as another electron, a photon, or an electric field. An excited electron occupies a quantum state whose energy is above the minimum energy ground state. Luminescence is defined as the emission of light by bodies which is in excess of that attributable to black-body radiation. It persists considerably longer than the periods of electromagnetic radiations in the visible range after the excitation stops.

The different aspects of luminescence and the complex processes involved in the origin of light emission offer interesting challenges for researchers in this field.

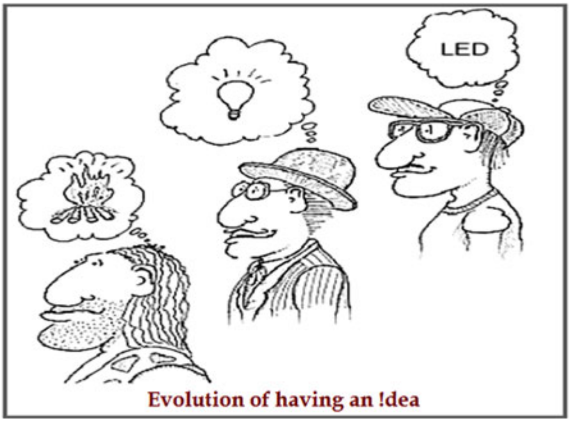

Fig. 1.2 Evolution of having an idea

It may be considered as one field of research but leading to many and varied areas of application, which range from radiation monitoring for health and safety to phosphors for lamps and display purposes, and X-ray imaging and other methods of medical diagnosis.

Luminescence is an old field of scientific research. In 1652, Zechi made an important contribution to the understanding of photoluminescence, the luminescence which persists after the excitation agency is removed. He observed that the color of the phosphorescence light in a material was independent of the color of the exciting light, and also clearly distinguished the phenomenon from scattering. About 200 years later, Stoke identified fluorescence, the luminescence that occurs during excitation. He showed that the incident and emitted light differed in color and enunciated his well-known Stoke's law regarding the increase in wavelength which accompanies photoluminescence. In 1867, E. Bequerel distinguished two types of phosphorescence or afterglow, which were attributed respectively to monomolecular and bimolecular decay mechanisms.

The last few decades have seen spectacular changes in research on luminescence. There has been a phenomenal growth in the subject, and significant progress has been made in the field of luminescence research. Rare earth ion-activated phosphors have numerous applications in the display, lighting, and medical industries [6–9]. Phosphor-converted white light-emitting diodes (LEDs), with characteristics of high efficiency, long lifetime, and energy saving, have attracted much attention [10–16]. In recent years, the luminescent properties of phosphate materials have been widely investigated as a result of certain advantages, such as excellent thermal and chemical stability [17, 18], and development of optical devices based on rare earth (RE) ion-doped materials is one of the most interesting fields of research. Multicomponent glasses, which typically consist of network formers and modifiers, provide a wide range of excellent properties and new applications. Moreover, the technological applications of RE luminescence encompass not only fluorescent tubes and color televisions, but also optical amplifiers and, perhaps very soon, OLEDs [19].

In order to obtain a warm white light, the new technologies are based on the combination of a blue diode with two red and green phosphors (R, G) [20] or the combination of a ultraviolet diode with three phosphors emitting the primary colors (RGB) [21]. But while blue and green luminescence are beginning to be well established [22], red emission is still not fully optimized because of the low quantum yield of the current red phosphors [23]. In this context, phosphates are investigated because of their low cost, their high stability for use in lamp applications, and their important crystallographic possibilities for accommodating luminescent ions [24]. More precisely, trivalent europium can be easily introduced into those matrices by substitution of alkaline, alkaline earth, or rare earth elements giving rise to suitable red emission [25].

Recent research is characterized by strong interactions among other branches of solid-state physics and between different areas of luminescence research using inorganic and organic materials. Both experimental and theoretical approaches have been explored.

1.2 Classification of Luminescence

Luminescence is traditionally classified as fluorescence and phosphorescence. Historically, luminescence characterized by temperature-independent decay was called fluorescence, while that exhibiting temperature-dependent decay was called phosphorescence. However, according to modern conventions, fluorescence refers to emission of relatively short persistence (10^{-6}–10^{-12} s), whereas phosphorescence persists considerably longer (sometimes even for seconds). The line of demarcation is rather arbitrary. In short, fluorescence is the emission of visible light by a material under the stimulus of visible or invisible radiation of shorter wavelength. If the fluorescent glow persists for an appreciable time after the stimulating rays have been cut off, this afterglow is termed phosphorescence. Sometimes, the phosphorescence may differ in color from the original fluorescence.

A further classification of the phenomenon is made on the basis of the source of excitation. A variety of luminescence phenomena are observed in natural or man-made materials. The nomenclature given to these is invariably related to the exciting agent which produces the luminescence. The following description summarizes the main types of luminescence emission phenomena.

1.2.1 Photoluminescence

All solids, including semiconductors, have so-called energy gaps for the conducting electrons. In order to understand the concept of a *gap* in energy, first consider that some of the electrons in a solid are not firmly attached to the atoms, as they are for single atoms, but can hop from one atom to another. These loosely attached electrons are bound in the solid by differing amounts and thus have quite different energies. Electrons with energies above a certain value are referred to as *conduction* electrons, while electrons with energies below a certain value are referred to as *valence* electrons. This is shown in Fig. 1.3, where they are labeled as conduction and valence *bands*. The word 'band' is used because the electrons have a multiplicity of energies in either band. Furthermore, there is an energy *gap* between the conduction and valence electron states. Under normal conditions, electrons are forbidden to have energies between the valence and conduction bands. If a light particle (photon) has energy greater than the band gap energy, then it can be absorbed and thereby it raises an electron from the valence band up to the conduction band, across the forbidden energy gap (see Fig. 1.3). In this process of photoexcitation, the electron generally has excess energy which it loses before coming to rest at the lowest energy in the conduction band. At this point, the electron eventually falls back down to the valence band. As it falls down, the energy it loses is converted back into a luminescent photon which is emitted from the material. Thus, the energy of the emitted photon is a direct measure of the band gap energy E_g. The process of photon excitation followed by photon emission is called *photoluminescence*.

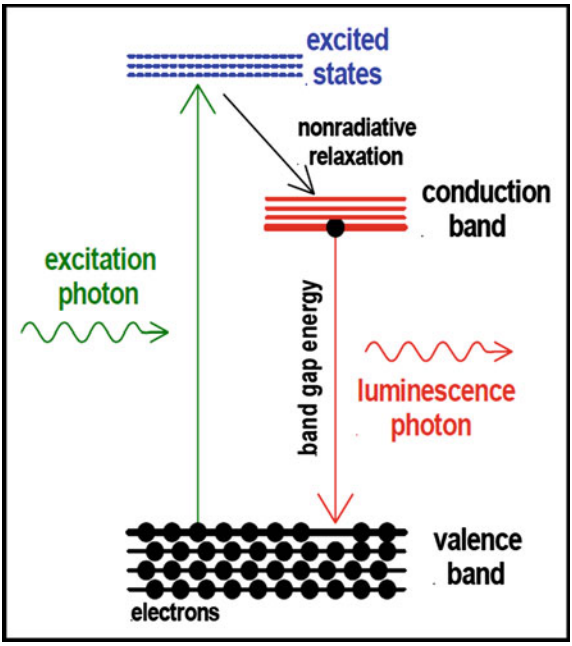

Fig. 1.3 Photoluminescence process

This is the emission produced by excitation by photons. The fluorescent lamp used in household and general lighting is the principal example of this. Photoluminescence should not be confused with reflection, refraction, or scattering of light, which cause most of the colors in daylight or bright artificial lighting. Photoluminescence is distinguished in that the light is absorbed for a significant time, and generally produces light of a frequency that is lower than, but otherwise independent of, the frequency of the absorbed light. For example, 254 nm ultraviolet radiation from the mercury vapor discharge is absorbed by one of the activator impurities in the phosphor coated on the inner side of the glass tube. Some of this energy is transferred by resonance to a second impurity. By adjusting the relative concentrations of these activator impurities, one can produce the desired modification in the color of the light. There are a wide variety of organic and inorganic phosphors, used in consumer items such as road and traffic signals, displays, laundry whiteners, etc., in addition to a host of others used in industrial and scientific applications. Laser technology is based on a kind of photoluminescence in which emission is coherent.

1.2.2 Cathodoluminescence

Cathodoluminescence (CL) is an optical and electrical phenomenon whereby a beam of electrons is generated by an electron gun and then impacts on a luminescent material such as a phosphor, causing the material to emit visible light. The most common example is the screen of a television using a cathode-ray tube (CRT). In CRTs, zinc and cadmium sulfide phosphors are used. CL is the emission of photons of characteristic wavelengths from a material that is under high-energy electron bombardment. The electron beam is typically produced in an electron microprobe or scanning electron microscope, or in a CL microscopy attachment to a petrographic microscope. The nature of CL in a material is a complex function of composition, lattice structure, and superimposed strain or damage to the structure of the material. Different minerals exhibit fluorescent or phosphorescent kinetic behavior which can have an effect on the quality of CL images, depending on the manner in which the image is obtained.

1.2.3 Radioluminescence

Radioluminescence is the phenomenon by which light is produced in a material by bombardment with ionizing radiation such as beta particles. Radioluminescence is used for emergency exit signs or other applications where light must be produced for long times without external energy sources. Radioluminescence is luminescence caused by nuclear radiation. Older glow-in-the-dark clock dials often use paint with a radioactive material (typically a radium compound) and a radioluminescent material. The term may be used to refer to luminescence caused by X-rays, also called photoluminescence.

1.2.4 Electroluminescence

Electroluminescence is luminescence caused by electric current. This should not be mistaken for what occurs in ordinary incandescent electric lights, in which the electricity is used to produce heat, and it is the heat that in turn produces light. Application of electric fields can produce luminescence in many phosphors. There is another type of electroluminescence, known as injection luminescence. In this, electrons are injected from an external supply across a semiconductor *p–n* junction. On applying a DC voltage across the junction, such that the electrons flow to the p-region, luminescence is produced by the electron–hole recombination in that region. Light-emitting diodes (LEDs), which are now commonly used as display devices in many scientific instruments, are based on this principle. Electroluminescence is usually performed on the finished devices (such as LEDs), since a device structure is required to inject current. Conventional electroluminescence evaluation could not provide a fast response for material development since the fabrication of devices is usually time consuming and costly.

1.2.5 Chemiluminescence

Chemiluminescence is the luminescence in which the excitation energy is supplied by chemical reactions. The glow-in-the-dark plastic tubes sold in amusement parks and the oxidation of white phosphorous in air are the best-known examples of chemiluminescence.

Not all chemical molecules are capable of luminescencing. An example of chemiluminescence is lyoluminescence. This is caused during the dissolution of certain compounds which have been previously bombarded by X-rays. A well-known example is the case of X-irradiated NaCl, which emits a flash of light when quickly dissolved in water. Another good example of chemiluminescence is the determination of nitric oxide:

$$\mathrm{NO} + \mathrm{O_3} \rightarrow \mathrm{NO_2^*} + \mathrm{O_2}$$
$$\mathrm{NO_2^*} \rightarrow \mathrm{NO_2} + h\nu \quad (\lambda = 600\text{--}2{,}800\,\mathrm{nm})$$

1.2.6 Bioluminescence

Bioluminescence is luminescence caused by chemical reactions in living things; it is a form of chemiluminescence. Fireflies glow by bioluminescence. Biochemical reactions inside the cells of certain living organisms can produce electronic excited states of the biomolecules. Fire flies, glow worms, some bacteria and fungi, and many sea creatures, both near the surface and at great depths, are striking examples of luminescence in living beings.

1.2.7 Triboluminescence

Triboluminescence (TL) is phosphorescence that is triggered by mechanical action or electroluminescence excited by electricity generated by mechanical action. A large number of inorganic and organic materials subjected to mechanical stress emit light. This has also been called mechanoluminescence by some authors. The spectrum of triboluminescent light is similar to the photoluminescence spectrum of many substances.

1.2.8 Thermoluminescence

Thermoluminescence is phosphorescence triggered by temperatures above a certain point. This should not be confused with incandescence, which occurs at higher temperatures; in thermoluminescence, heat is not the primary source of the energy, only the trigger for the release of energy that originally came from another source.

It may be that all phosphorescence requires a minimum temperature, but many phosphors have a minimum triggering temperature below everyday temperatures and are not normally thought of as thermoluminescent sources.

In contrast to the various types of luminescence phenomena listed above, the prefix ‘thermo’ here does not refer to the form of excitation energy, but rather to the form of stimulation of luminescence, which was excited in a different way. The primary agent for the induction of thermoluminescence (TL) in a material is ionizing radiation (X-rays or γ radiation) or sometimes even ultraviolet rays to which the material is exposed. The light produced by subsequent heating of the material is called TL.

The most broadly investigated and utilized of all thermally stimulated phenomena is the emission of light during the heating of a solid sample that has been previously excited. The initial excitation (typically by irradiation) is the source of energy, whereas the heating serves only as a trigger which helps to release this accumulated energy. The term thermally stimulated luminescence (TSL) is more descriptive, but thermoluminescence is traditionally more often utilized and popularly accepted.

As noted, except for very unusual cases, the occurrence of the TL curve following a given irradiation is a one-off effect. Cooling the sample and reheating it does not normally result in a second TL emission.

1.2.9 Ionoluminescence

Ionoluminescence (IL), also called ion beam induced luminescence (IBIL), is a luminescence phenomenon caused by energetic ions interacting with solid matter. The light emitted under ion irradiation originates from electron transitions followed by recombination processes within the outer electron shells of the sample atoms. The chemical bonding of the atom affects the energy levels of those electron shells. Therefore, the IL method can provide information on the chemical form of elements which cannot be obtained by other ion beam analytical methods. Moreover, it allows the detection of rare earth elements in the host materials with a minimum detection level of a few ppm. In material science, the IL method can be applied to study intrinsic and extrinsic luminescence phenomena and is capable of microcharacterizing both geological and synthetic inorganic materials.

1.3 Phosphors

The luminescent materials known as phosphors convert energy into electromagnetic radiation, usually in the visible energy range. Phosphors are solid luminescent materials that emit photons when excited by an external energy source, such as an electron beam (cathodoluminescence) or ultraviolet light (photoluminescence). Phosphors are composed of an inert host lattice which is transparent to the excitation radiation and an activator, typically a $3d$ or $4f$ electron metal, which is excited under energy bombardment. The process of luminescence occurs by absorption of energy at the activator site, relaxation, and subsequent emission of a photon and a return to the ground state. The efficiency of a phosphor depends on the amount of relaxation that occurs during activation and emission. Relaxation is the process in which energy is lost to the lattice as heat, and it needs to be minimized in order to extract the highest luminous efficiency, defined as the ratio of the energy emitted to the energy absorbed.

Phosphors have a long history beginning more than 100 years ago, but they are becoming more and more widely used and economically valuable. Phosphor technology has come a long way from the early black and white television, on which the BBC made television broadcasts to the public for the first time in 1936, to the new 60-inch plasma display panels. Likewise, in the domain of lighting devices, from the first lamp made by Edison to the compact fluorescent lamp used everywhere now, progress and improvement are obvious. But there is a need to continue research in this field because the excitation sources have changed and it is known that a good phosphor for electronic or ultraviolet excitation is not necessarily a good choice for excitation in vacuum ultraviolet (VUV).

Up until now, in order to produce light with a fluorescent lamp it was necessary to put mercury inside the lamp to generate ultraviolet photons at $\lambda = 254\,\text{nm}$ which could in turn excite the phosphor-coated inner surface of the lamp. However, in a near future it will be mandatory to replace/reduce the use of mercury in any lighting device because mercury is very harmful for the environment. Mercury can be replaced by a mixture of rare gasses (xenon and neon) which emits VUV photons in the range 147–190 nm. This means that the fluorescence properties of phosphors induced by such VUV photons have to be studied and improved if efficacy decreases. In the field of plasma display panels (PDPs), the key factors distinguishing between success and failure are going to be quality and longevity, and both factors depend directly on phosphors: luminous efficiency, color rendering, and longevity are all properties which depend on the nature and quality of the phosphors. Furthermore, color rendering can be further improved by using new luminescent materials allowing better color coordinates, i.e., a more saturated color, especially for the red and green components. Another crucial characteristic of phosphors for PDPs is the fluorescence lifetime: shorter is better in order to produce the highest number of gray levels.

1.3.1 Phosphor Properties

1.3.1.1 Notation

Most phosphors consist of a host composition plus the activator, added in carefully controlled quantities. The activator itself is a substitutional defect and is subject to lattice phonon perturbations. Therefore, it is essential that the charge on the substitutional cation should be equal to that of the host lattice cation. Otherwise, the resulting phosphor is not efficient.

We denote a phosphor by $:\mathrm{M}_a\mathrm{YO}_b:\mathrm{N}_x$, where M is the cation, YO is the anion, and N is the activator. It is understood that the N-ion is in solid solution in the host matrix, and the above formula is actually :$(1 - x)\ \mathrm{M}_a\mathrm{YO}_b \cdot x\ \mathrm{NYO}_b$. Thus for a tin-activated strontium pyrophosphate phosphor, we would write:

$$\mathrm{Sr_2P_2O_7{:}Sn_{0.02}} = \mathrm{0.99Sr_2P_2O_7{:}0.01Sn_2P_2O_7}$$

In this case, the host cation is $\mathrm{Sr^{2+}}$ and the activator cation is $\mathrm{Sn^{2+}}$. Thus, the first part is a shorthand notation for the latter. However, suppose we have the phosphor: $\mathrm{Sr_2P_2O_7{:}Sb^{3+}_{0.02}}$. In this case, the actual formula differs considerably from the shorthand formula. We know that, if a trivalent ion substitutes on a divalent ion, it must do so in conjunction with a substitutional defect, usually a vacancy. Thus, the actual formula is $\mathrm{0.99\ Sr_2P_2O_7{:}0.01(Sb^{3+},\ V^{+})_2\ P_2O_7}$. If we added $\mathrm{Na^+}$ for charge compensation, we would have

$$\mathrm{0.99Sr_2P_2O_7{:}0.01(Sb^{3+}, Na^{+})_2P_2O_7} \text{ or } \mathrm{Sr_2P_2O_7{:}Sb^{3+}{:}Na^{+}}$$

1.3.1.2 Quantum Efficiency

It is known that the proper choice of host and activator is essential to obtain an efficient phosphor. Now, consider the case where 100 photons are incident upon the phosphor. Of these, a few will be reflected, some will be transmitted, and, if the phosphor is an efficient combination of host and activator, most of the photons will be absorbed. But not all the absorbed photons result in an activated center, and once these centers become activated, not all will then emit a photon. Some will be deactivated via relaxation processes. To determine just how efficient a phosphor actually is, the quantum efficiency (quantum efficiency) is measured. This is defined by

$$\mathrm{QE} = \text{photons emitted/photons absorbed.}$$

To obtain specific values, we measure the total energy emitted and the total energy absorbed. It is easier to measure the intensity of photons emitted as a function of wavelength. This gives

$$\mathrm{QE} = (\mathrm{I}\ d\lambda)\ \text{emission}/(\mathrm{I}\ d\lambda)\ \text{absorption.}$$

Generally, phosphors with quantum efficiency values of 80 % or greater are considered to be efficient phosphors.

1.3.2 Applications

There is a worldwide trend in the physical sciences toward applied research, particularly relevant to environmental and energy conservation problems. The substantial advances in understanding luminescent phenomena and the discoveries of unusual luminescent processes, for example up-conversion and quantum splitting, present exceptional opportunities for the applications of luminescence. In some instances, these potential applications depend on improvements in efficiencies and stabilities of inorganic luminescent materials, in other instances, on the problems of adapting the available scientific understanding of luminescent phenomena to established techniques. Luminescent materials find applications ranging from commonplace issues like lighting to very sophisticated ones such as lasers. Some of the applications of luminescence are given in Fig. 1.4.

1.4 Important Applications of Phosphors

1.4.1 Lamp Phosphors

Kuch and Retschinky [26] reported production of light by mercury (Hg) discharge in 1906. Efficient emission was obtained when a compact lamp was developed using tungsten wires sealed in silica [27]. In a tungsten filament lamp, large amounts of energy are wasted as heat. In contrast, in discharge lamps such as Hg vapor lamps, about 60 % of energy is converted to light (7.2 % at 185 nm and 85 % at 254 nm) [28, 33]. However, for lighting purposes, the ultraviolet radiation has to be converted into visible light and hence the need for suitable photoluminescent phosphors.

A lamp phosphor should possess the following characteristics:

(i) High absorption efficiency: Absorption of ultraviolet (185 and 254 nm) light and conversion into visible light is indicated by quantum efficiency. Lamp phosphors have quantum efficiency above 80 %. This property of the lamp is represented by a factor called visual sensitivity, which is defined by

$$q = \int E(\lambda)V(\lambda)\mathrm{d}\lambda / \int E(\lambda)\mathrm{d}\lambda,$$

where E is the energy of the emitted photon and V is the sensitivity of the eye. The lamp output is also often expressed in terms of light emitted per unit energy consumed. Theoretically, the maximum output can be 310 lm/W [29]. Lamp and phosphor performances have been characterized using various other indices [30–33].

(ii) Good color rendition: The object should appear in its natural color. The colors of various objects are compared under the lamp and the black-body radiator illuminations. The color-rendering index (CRI) is taken as 100 % if the color points are the same under illumination with the above two sources. Since a single phosphor does not yield a good CRI, a blend of phosphors has to be used. Apart from the CRI, lamps are often characterized by the correlated color temperature, the temperature of the black-body radiator with the same color points. The human eye has three different receptors for color vision. The observation of a light beam with spectral energy distribution $E(\lambda)$ can be described by tristimulus

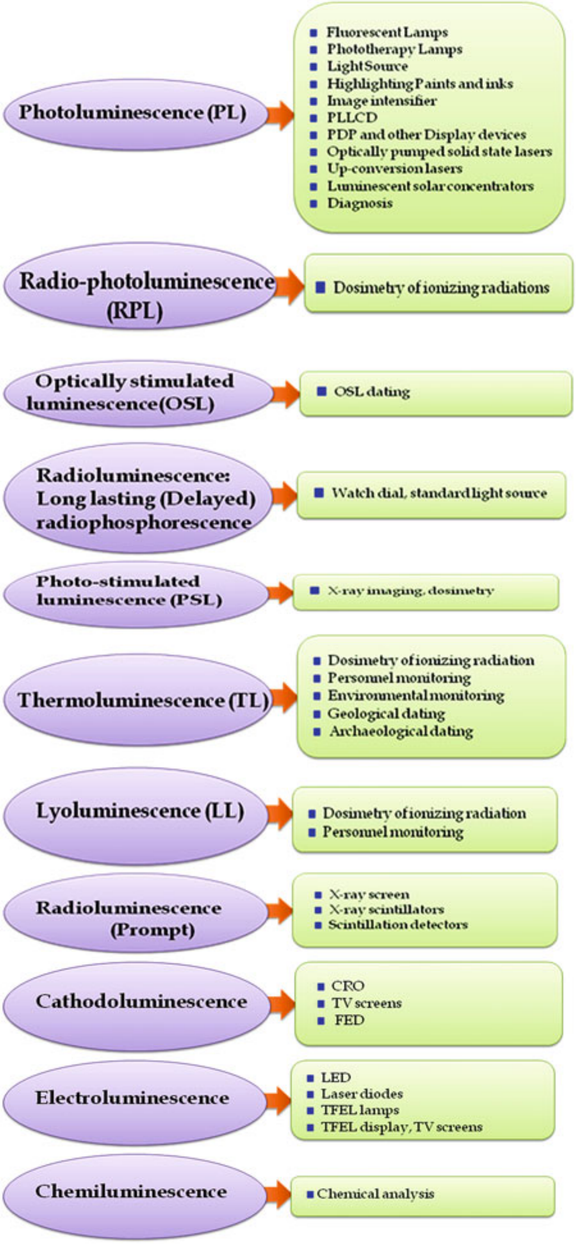

Fig. 1.4 Types of luminescence and their applications

values related to the sensitivities of these three receptors. Color perception depends upon the ratios of the three tristimulus values. Normalized tristimulus values sum to unity. Stating normalized values of any two is thus sufficient. These two values define the color point of the lamp source [34, 35]. Color saturation is important for display applications. In order to display all colors of the visible spectrum by synthesizing them from the three primary colors, the latter have to be as saturated as possible, that is the color coordinates have to be positioned close to the borders of the color triangle.

(iii) High quenching temperature: Not all the energy in discharge is given up as light; an appreciable proportion is lost as heat. Depending on the rate at which the heat can be dissipated, the lamp temperature will be higher than the ambient. Emission from the lamp phosphor should not be susceptible to these changes, and hence the need for a high luminescence quenching temperature.

(iv) Transparency in the visible range, good persistence, and long lifetime: Gas discharges are usually operated on ac. This gives rise to flicker in ultraviolet light. The phosphors, with emission lifetimes of the order of several milliseconds, help to reduce this flicker [36].

(v) Stability against Hg discharge, good maintenance: Phosphors are bombarded by electrons to produce ions in the discharge and VUV radiation [37]. Phosphors are also exposed to chemical attacks or physical adsorption involving Hg, present in the lamp. Many phosphors show useful properties (i–iv above) but degrade under Hg discharge.

(vi) Stability under industrial handling: Phosphors are subjected to various thermal, mechanical, and chemical treatments when they are applied on the inner walls of the lamp. To disperse the phosphor uniformly in a coating solution, various steps such as milling in dry or liquid medium, baking, etc., are necessary. They must retain their properties after undergoing these processes and should have minimum losses.

Not all these qualities can be found in a single phosphor. This is quite understandable, since conditions (i) and (ii) are mutually exclusive. Lamp phosphors must necessarily compromise on some of these conditions. A good account of the history of fluorescent lamps and lamp phosphors can be found in the book by Amick [38]. Various landmarks in this history have been briefly discussed by Pappalardo [39].

1.4.2 Tri-Color Lamps

Research on lamp phosphors saw a spurt in activity with the prediction of tri-color lamps [40]. Haft and Thornton [41] developed a tri-color lamp based on these predictions. Theoretically, it is predicted that a good CRI (close to 100 %) can be obtained if three narrow band emission centers round 450, 540, and 610 nm are combined. Haft and Thornton used Y_2O_3:Eu^{3+} for red, Eu^{2+} doped strontium chloroapatite for blue, and Mn^{2+} doped zinc silicate for green emission.

It is known that the characteristic rare earth emission is in the form of narrow bands. Particularly, Eu^{2+} (blue), Tb (green), and Eu^{3+} (red) emissions are suitable for tri-color lamps. Opstelten et al. [42] reviewed materials for tri-color lamps. A large number of suitable phosphors were described by Verstegen [43].

Special lighting areas such as museums and bay windows of stores demand a very natural appearance of illuminated objects. For this purpose, color 90 or deluxe lamps have been developed. In these lamps, the emission maximum of the blue phosphor is shifted toward longer wavelength and the red and green emitters are replaced by broadband emitters covering the whole spectral range [44]. Color 90 lamps with low color temperature ($T < 3{,}000\,\mathrm{K}$) demand a reduction in the intensity of blue emission lines (405, 435 nm) from the mercury plasma. A fourth phosphor with relatively long wavelength (blue-violet) absorption and emitting at 565 nm (yellow) is employed. For this concept, (Ce, Gd, Tb)MgB_5O_{10}:Mn has been developed as the red band emitter. A green broadband emitter with sufficient efficiency and stability is not yet known. (Ba, Sr, Ca)SiO_4:Eu, which emits between 550 and 580 nm depending on the exact composition, has been developed as an alternative green band emitter.

1.4.3 Phosphors for Special Lamps

Although the most widespread use of lamps is for lighting purposes, there are several other important applications, and phosphors with different characteristics are needed for these.

For blue printing, "black light" lamps emitting in the region 340–380 nm are needed. In the old days, the Hg 365 nm line was used for this purpose. Clapp and Ginther [45] examined a large number of phosphors and found $BaSi_2O_5$:Pb to be suitable for such applications. KCl:Tl also exhibited good emission, but it is hygroscopic. Barium silicate phosphor has been in use for a long time [33, 46]. In general, alkaline earth silicates activated with Pb are good phosphors for black light emission. Eu^{2+} activated alkaline earth sulfates are also efficient ultraviolet emitters (370–385 nm), but the excitation spectrum overlaps only moderately with 254 nm Hg emission. Awazu and Mato [47] developed YPO_4:Ce,Tb, which was more sensitive than barium silicate. Tb efficiently absorbs ultraviolet radiation and transfers to the $^2D_{3/2}$ level of Ce^{3+}. More recently, Ce^{3+} and Eu^{2+} have been increasingly used as activators to yield ultraviolet emission. Ce^{3+} is used in hexa-aluminate hosts, where it has good maintenance characteristics.

Erythemal lamps, often used for sun tanning, emit in the region 290–320 nm, because erythemal activity has a maximum at 297 nm [48].

1.4.4 Phosphors for CRTs

The most common application of CL is in CR tubes. For this application, the phosphor material should have specific characteristics [49, 50]. In oscilloscopes, green emitting phosphors with short or long persistence are desired, depending on the application. CR tubes are also used in various instruments and consumer products. The requirements of these CR tube phosphors vary depending upon the application, e.g., in radars, such as planned position indicators (PPI), the beam scans the screen at the rate of a few rotations/second [51]. The persistence of the phosphor should be such that the intensity remains constant for the period of rotation and then drops to zero. This is not possible so a compromise must be made. In image intensifier tubes [52], some persistence is also desired. In these tubes, light is focused by a lens onto a photocathode, and the electrons thereby emitted are accelerated and made to fall on the viewing screen. Earlier, willemite was used in these tubes. Later, a double layer of ZnS:Ag (blue) and (ZnCd)S:Ag (yellow) was employed. In the flying spot scanner, fast (100 ns) build-up and decay is necessary. Ce-based phosphors can be used for this purpose [53–55]. In beam indexing tubes, a similar phosphor requirement also exists [56]. Ce-activated phosphors for this purpose have been described by Ropp [57].

1.4.5 Flat CRT Displays and Field Emission Displays (FEDs)

A field emission display (FED) is a new type of flat-panel display in which electron emitters, arranged in a grid, are individually controlled by "cold" cathodes to generate colored light. Conventional CRTs work by bombarding phosphors with an electron beam that has been generated and accelerated at high power in a large vacuum container, which does not have portability. Displays with high information content are becoming increasingly prominent and important in today's society. From the development of high-definition television and large area displays to high-resolution computer monitors and laptop computers, the demands on display performance continue to increase. The next generation of flat-panel displays include such devices as field emitter displays (FEDs). These offer substantial advantages over liquid crystal displays (LCDs) in that the viewing angle and response time of the screens are far superior. Furthermore, since FEDs employ phosphors, the span of operating temperatures is greater than for LCDs, and the estimated price and power consumption of FED screens are expected to be better than those of present day LCDs.

There are two ways in which electrons can be produced to stimulate phosphor materials to emit light, depending on the type of cathode used. The CRT is a thermionic cathode device using high accelerating voltages, while the FED uses a cold cathode, in which electrons are produced by tunneling at high fields. In FEDs, an array of micrometer sized conical electron emitters spaced a few micrometers apart replaces the bulky single electron gun found in CRTs. The smaller the arrangement (called a Spindt cathode), the smaller the voltage on the sheet required to extract the electrons. Spindt cathodes emit electrons which are accelerated toward the phosphors by a high voltage on the anode. When they strike the phosphor, light is emitted. The whole thing can be under a centimeter thick and as large as required, and it is much easier to make than an LCD.

Therefore, the operating conditions for FEDs are different and more demanding than for the more ubiquitous CRTs. These displays operate at low voltages, 1–8 kV compared with 20 kV for CRTs, and have higher electron beam current densities. Regardless, both CRTs and FEDs require a thin layer of phosphor (either a thin film or powder) to be deposited upon a glass substrate (the screen). Both physical vapor deposition and chemical vapor deposition methods are used to produce thin-film phosphors. These thin-film phosphors require stringent control of stoichiometry and crystallinity for good efficiency. Thin film deposition methods have been reviewed and summarized in a recent book on electroluminescent displays [58]. Electrophoretic coating produces screens of high packing density, high light transmission, and low noise, with fine particle size phosphors. This technique has been most successfully used in small, high-resolution screens for applications such as helmet-mounted displays [59]. The application to the screen of phosphor powders is dependent upon various interrelated parameters such as particle size distribution, particle shape, and screening method [60].

1.4.6 Light-Emitting Diodes (LEDs) and Diode Lasers

As the name suggests, an LED is a device in which electroluminescence results by motion of charge across a *p–n* junction and the subsequent recombination. LEDs find applications in display devices, and during the 1970s Nixie tubes were replaced by LEDs. Materials for LEDs should have band gaps greater than 1.8 eV for emission in the visible region and they should be amenable to growth in large single crystal form, suitable to batch production, and conducible to doping with both *n*-or *p*-type to form efficient homojunctions, as well as having good injection and luminescence efficiency.

After the invention of maser in 1954 by Townes and his collaborators [61] and the subsequent operation [62, 63] of optical masers and lasers in ruby, semiconductors were suggested for use as laser materials. The theoretical calculations of Bernard and Duraffourg [64] in 1961 set forth the necessary conditions for lasing using quasi-fermi levels. In 1962, Dumke [65] showed that laser action was indeed possible in direct band gap semiconductors and set forth an important criterion for such action. In late 1962, three groups headed by Hall [66], Nathan [67], and Quist [68] announced almost simultaneously that they had achieved lasing in semiconductors. The pulsed radiation of 0.84 μm was obtained from a liquid nitrogen cooled, forward biased GaAs *p–n* junction. Shortly afterwards, Holonyak and Bevacqua [69] announced laser action in a ternary compound $GaAs_{1-x}P_x$ junction at 0.71 μm. In 1970, Hayashi et al. [70] achieved the continuous operation of a junction laser at room temperature by the use of double heterojunctions.

Lasers are of great importance in modern R&D. Efforts are made to obtain lasers emitting in various spectral regions. Using photoluminescence one may obtain laser emission characteristic of the phosphor by utilizing a light source (not necessarily a laser) emitting in a different region. Penzkofer [71] has given an exhaustive list of solid-state laser materials. The optical, structural, and physical properties of solid-state laser materials are given by Reisfeld [72]. Welker introduced GaP semiconductors in 1952 [73]. Wolf et al. [74] reported light emission from a point contact GaP diode. EL was found in many III–IV semiconductors [75].

Besides display applications, LEDs are useful in other optical applications and optoelectronic devices. After the development of ultra pure silica fibers, InP and $In_xGa_{1-x}As_yP_{1-y}$ assumed tremendous importance for long wavelength (1.67 nm) optical emitters and detectors [76–78]. $In_xGa_{1-x}As$ (band gap varying between 0.36 and 1.4 eV) [79, 80] and $GaA_{sx}Sb_{1-x}$ [81] are also useful with optical fiber communication systems. Recently, an In_xAl_{1-x}/As system has also been studied for optical applications [82, 83]. The invention of the blue light-emitting diode based on GaN [84] and use of the MOCVD technique for LED chip production have revolutionized this field. It is possible to vary the emission wavelength of GaN-based blue LEDs between 370 nm (band gap of pure GaN) and 470 nm by increasing the In content in an InGaN device. By varying the In content of the InGaN active layer, the emission spectrum of GaN LEDs has been successfully extended into the green spectral region with still higher efficiencies. As a consequence, it is possible to generate white light by direct conversion from electrical current in LEDs with an efficiency superior to halogen lamps. LEDs emitting at 370 nm, covered with RGB line emitter phosphors (which have efficient absorption at 370 nm), can provide white light with good CRI. The search for stable inorganic rare earth phosphors with high absorption in the UV/blue spectral region is therefore an attractive research task.

Neodymium-doped yttrium orthovanadate Nd^{3+}:YVO_4 is a very powerful [85] solid-state laser material. Nd^{3+} ions in this material present a broad and strong absorption band around 808 nm and a very intense emission in the 1 μm range, and this allows a miniaturization of the devices leading to diode-pumped microchip lasers [86–88]. Extensive research is being devoted to the development of solid-state lasers emitting in the eye-safe spectral range with the possibility of efficient diode-pumped sources. A promising range of applications is foreseen for such devices, including LIDAR, metrology, and medical applications. The microchip concept, where the mirrors are coated directly on the crystal faces, results in very compact sources with high spatial quality beams [89].

1.4.7 Diagnostic Applications

Photoluminescence can be used as a diagnostic tool by making use of the interaction of certain photoluminescent ions with biochemicals signifying the presence of some disease.

1.5 Thermoluminescence (TL)

1.5.1 Fundamental Aspects of Thermoluminescence

When an insulating crystal is exposed to ionizing radiation electrons and holes are produced, some of which get trapped in defects in the crystal lattice of the solid. Subsequently, when the temperature is raised high enough to cause the removal of the electrons or holes from their traps, they wander around until they recombine at centers giving off light. This light emission phenomenon is called thermoluminescence [90]. It can also be explained in another way. The extra energy that the crystal contains as a result of radiation exposure can be released by heating the material. When heat is applied, some of the released energy appears in the form of light, causing the material to emit luminescence. If the crystal is then cooled and reheated, it does not re-emit light, because the energy excess which produced the first emission has now been released from the crystal. This effect is known as thermoluminescence (TL). It appears only while irradiated crystals undergo a progressive temperature increase, and should not be confused with incandescence, which is the light radiated continuously by hot bodies.

Such processes have been used either for radiation dosimetry, i.e., determination of the integrated radiation dose humans have been exposed to, or dating of archeological specimens and geological sediments. When these materials are exposed to radiation, the absorbed energy is ‘trapped’ and held indefinitely. When the materials are heated at a later date in a device known as a TLD reader (the basis for the word ‘thermo’), the trapped energy is released in the form of light (luminescence). The amount of light is then related to the radiation dose and the unknown exposure is estimated.

The phenomenon of thermoluminescence, sometimes called thermally stimulated luminescence, has been known for a long time [91]. The credit for its discovery goes to Robert Boyle, who reported his observations of a strange “glimmering light” to the Royal Society of London on 28 October 1663, in an experiment in which he heated a diamond in the dark [92]. The use of thermoluminescence for radiation measurements was mentioned as early as in 1895 [93]. A number of other famous scientists, such as Henri Becquerel, also carried out work on thermoluminescence. However, E. Wiedemann of Germany was probably the first (1895) to report the use of thermoluminescence from artificially prepared $CaSO_4$:Mn for the detection of radiation due to an electrical discharge. In 1904, Marie Curie noted that the thermoluminescence properties of crystals could be restored on exposure to radium. Lyman [94] used the method for measurements in the far ultraviolet range.

Thermoluminescence entered the world of dosimetry in the early 1950s [95] and is now deeply entrenched as a method for measuring accumulated radiation exposure under widely varying circumstances. More specifically, Randall and Wilkins [96] carried out experimental and theoretical work in 1945, developing a model which allowed quantitative calculations of thermoluminescence kinetics to be carried out. Garlick and Gibson in 1949 provided a sound understanding of some aspects of the thermoluminescence process. The application of TL to dosimetry dates from the 1940s, when the increase in the number of workers exposed to radiation led to efforts to seek new types of dosimeter. Work on this topic gathered momentum with the report of Daniels et al. [97], based on extensive work on the feasibility of using thermoluminescence in dosimetry and other related applications. The topic became a subject of widespread interest when they demonstrated its usefulness in radiation dosimetry in 1953. Thereafter, Daniels [98] and Cameron et al. [99, 100] developed LiF-based phosphors for the measurement of X, γ, and β-rays and thermal neutrons. In the late 1960s and 1970s, a lot of work was done in this field all over the world, and it was made commercially available [101]. Also TL was subsequently applied to archeological dating in the early 1960s [102, 103] and to geological dating at the beginning of the 1980s [104]. Interest in TL has continued to increase, not only in dosimetric applications but also as a tool in solid-state physics, archeology, and the earth sciences. Sunta [105], Lindel [106], and Lucas [95] have given a more historical perspective.

1.5.2 Thermoluminescence Dosimetry (TLD) Phosphors

During thermoluminescence, part of the energy absorbed by insulating materials is emitted during the heating as light in the form of a “glow curve” which may present several peaks. The positions, shapes, and intensities of the glow peaks are related to the various parameters of the trapping states responsible for the thermoluminescence. The most important parameters are the trap depth (E), which is the thermal energy required to liberate the trapped electrons or holes, and the frequency factor (s) [33]. Measuring the dose of radiation emitted by a radioactive source is referred to as dosimetry.

There are several dosimetry methods, but those based on thermoluminescence detectors have many advantages in sensitivity, range, simplicity of reading, ruggedness, small size, and potentially low cost. This has attracted the attention of many investigators. Some of the relative merits of TLD phosphors are sensitivity, useful range, linearity, energy dependence, fading of signal, neutron and γ response, sensitivity to daylight, etc. A good TL dosimetry phosphor should have a high sensitivity (i.e., a high value of α) and low zero dose output, particularly for use in personnel dosimetry, where rather low doses need to be measured. It is also important that the glow curve peaks to be used for personnel dosimetry purposes should be stable against fading at normal ambient temperatures, i.e., ~20–30°C. For environmental monitoring, stability at temperatures up to ~50 °C may be necessary. On the other hand, the glow peaks should not occur at such high temperatures that interference from black-body radiation becomes important. Ideally, the dose absorbed by a phosphor to be used in personnel dosimetry should correspond approximately to that absorbed by human tissue in the same radiation field over a wide range of photon energies. This implies that the effective atomic number of the phosphor should be close to that of tissue (about 7.4). Phosphors containing significant quantities of high Z elements over-respond to low energy photons compared to tissue, because of the very high Z-dependence of the photoelectric absorption coefficient, which dominates the γ-ray attenuation coefficients at low energies. Large numbers of organic and inorganic solids exhibit thermoluminescence, but only a small number of them possess the characteristics necessary for use in dosimetry.

Required characteristics of TLD phosphors are:

- A simple and reproducible glow curve structure (ideally a single glow peak around 200 °C) that will not change for a wide range of exposures.
- High γ-ray sensitivity.
- Negligible fading of TL signal on storage for a few months at room temperature.
- No fading upon postirradiation storage of the sample under normal conditions of temperature, humidity, light, etc.
- Emission spectrum falling into the range of commonly available detectors around 4,500 Å.
- Linear response (dose vs. TL), i.e., correlation between exposure and thermoluminescence intensity.
- Complete absence of pyroluminescence, spurious thermoluminescence.
- Easy method of preparation, which will lead to batch homogeneity.
- Practically infinite shelf life.
- Properties such as toughness and nontoxicity, etc., which will facilitate handling.
- Reusability after readout.
- Simple annealing procedure for reuse (insensitive to thermal history).
- Chemical stability and inertness to extreme climatic variations.
- Effective Z close to that of tissue, which also leads to energy independence.
- Insensitivity to exposure conditions such as humidity, temperature, atmosphere, etc.
- Insensitivity to daylight.
- Completely selective or completely non-selective response to various types of radiation.

In fact, not a single solid possesses all the characteristics desired for a thermoluminescence dosimetry phosphor. Not a single material has been found which exhibits all these characteristics. However, compromising on some factor or other, several materials have been used as thermoluminescence dosimetry phosphors (TLDs).

Commercially used thermoluminescent materials

Thermoluminescent properties of materials enable them to be used in dosimeters, which measure doses of radiation. Since characteristics of materials differ, different materials with different thermoluminescent properties are preferred for different purposes. LiF and CaF_2 are the most common thermoluminescence materials, followed by sulfates [107]. Some of the key thermoluminescent materials used in dosimeters are given in Table 1.1.

The first thermoluminescent material used in dosimeters is TLD-100. The most popular form is the hot pressed chip, and many commercial manufacturers of TLD dosimeter badges use chips of this size as the central element of their badge design [108]. Since they are not suitable for automating routine handling procedures, powders are rarely used in personnel dosimetry. It is also possible to design LiF-based dosimeters sensitive to neutrons by enriching them in the ^{6}Li isotope [107]. However, LiF-based dosimeters do not have a simple glow curve. LiF:Ti, Mg, for instance, has a glow curve that consists of at least seven peaks, and this makes it harder to implement the material. The number of curves makes it more difficult to heat dosimeters. The heating process should include preheating for the depletion of shallow traps and additional high-temperature annealing for the depletion of deep traps [107]. The simplest curves belong to CaF_2:Mn and Al_2O_3:C. Both of these materials are extremely sensitive to radiation, and yet they have a simple TL curve.

CaF_2:Mn dosimeters may be obtained as single crystals, extruded rods, and hot pressed chips [108]. They come in the same sizes as LiF dosimeters. There is a single maximum in the glow curve and it is observed around 313 °C at a heating rate of $10\,°\mathrm{C}\cdot\mathrm{s}^{-1.}$ Further studies have shown that the glow curve actually consists of several closely spaced peaks which seem to be on the glow curve. However, this does not affect the commercial use of these dosimeters.

Calcium fluoride doped with Dy is available as single crystals, polycrystalline chips, or powders [108]. The procedure for this material does not differ from CaF_2:Mn. The commercial name for CaF_2:Dy is TLD-200. CaF_2:Dy does not have a single peak. Instead, there are at least four peaks in the glow curve and these curves are known as I–IV. They occur around 160, 185, 245, and 290 °C. Peaks also appear at higher temperatures, between 350 and 400 °C.

Table 1.1 Characteristics of thermoluminescent materials used in commercial dosimeters [107]

Thermoluminescent material	Dosimeter type
LiF:Mg, Ti	TLD-100
LiF:Mg, Cu, P	TLD-100H
LiF:Mg, Ti	TLD-600
LiF:Mg, Cu, P	TLD-100H
CaF_2:Dy	TLD-200
CaF_2:Mn	TLD-400
$CaSO_4$:Dy	TLD-900

1.6 Phosphates

Phosphates are compounds that contain oxyanions of phosphorus (V), ranging from the simple orthophosphate group to condensed chain, ring, and network anions. Oxyanions of phosphorus in lower oxidation states such as phosphite (HPO_3^{2-}) are also known. A very large number of solid phosphates have been prepared or found as minerals. Their diversity results from variations in the phosphate species, the large number of cations to which they may be coordinated, and the presence of other anions or molecules, notably H_2O. Their chemistry is similar to that of solid silicates and borates. Much attention is focussed on phosphates of metallic elements and other small cations (H^+, NH^{4+}), although a variety of phosphate salts of large organic or inorganic coordination complex cations are also known. Background information on the chemistry of phosphates and related phosphorus species can be found in the texts by Corbridge [109] and Kanazawa [110].

Phosphate structures are generally rigid, resistant to chemical attack, and (when anhydrous) insoluble and thermally stable. This leads to some applications as nuclear waste immobilization hosts or negative thermal expansion materials. Many solid phosphate hosts permit diffusion of extra-framework species leading to potential uses as ion exchangers and conductors, and as microporous catalysts. Phosphate anions do not absorb significantly in the UV-Vis region, so solid phosphates can also find use as optical materials such as glasses, phosphors, nonlinear media, and lasers. Solid phosphates constitute many minerals, notably apatites, which are also found in living organisms as rigid components such as bones and teeth. Amorphous phosphorite deposits are important sources of phosphate fertilizers.

Phosphate Anions

Solid phosphates are conveniently classified according to the anions they contain.

1.6.1 Orthophosphates [111]

The orthophosphate group, PO_4^{3-}, (often shortened to 'phosphate') is the most ubiquitous oxyanion of phosphorus. In solid orthophosphates, all four oxygen atoms are usually coordinated to cations, resulting in a strongly bonded three-dimensional framework, although layered or chain structures sometimes occur. Figure 1.5 shows the covalent bonding in the tetrahedral PO_4^{3-} anion may be described as the average of four resonance hybrids such as Fig. 1.5a, giving the average structure Fig. 1.5b with tetrahedral (Td) symmetry. These two views of the bonding illustrate important features of phosphate chemistry. Figure 1.5a shows that up to three covalent (P)O–X bonds may be formed with high valence elements X, notably PV in condensed phosphates, whereas Fig. 1.5b shows that all four oxygen atoms are equally involved in predominantly ionic bonding in metal orthophosphates. In ionic phosphates, terminal P=O and P–O bonds within the same tetrahedral group are equivalent and are strengthened by P:3dπ–O:2pπ overlap. The orthophosphate group usually displays

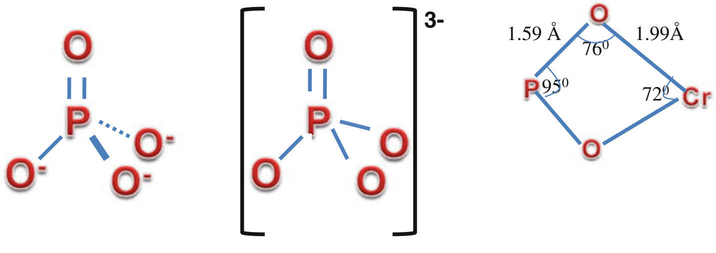

(a) (b) (c)

Fig. 1.5 Three different bonding in orthophosphate

a near-regular tetrahedral geometry. Analysis of geometric data from 85 reliably determined crystal structures gives a mean P–O bond length of 1.536 Å with distances lying in the range 1.50–1.58 Å, and tetrahedral angles between 97 and 115°. Distorted geometries can occur when the orthophosphate group acts as a bidentate ligand, resulting in a strained four-membered ring. Figure 1.5c shows the geometry of the ring formed by phosphate tetrahedra and CrO_6 octahedra sharing a common edge in a-$CrPO_4$, as determined by low-temperature neutron diffraction. The acid orthophosphate anions, (mono)hydrogenphosphate HPO_4^{2-} and dihydrogenphosphate H_2PO_4, also have extensive solid-state chemistries. Protonation lowers the bonding symmetry, since the P–O(H) bonds have single bond character and the non-protonated oxygens are consequently bonded more strongly to phosphorus. Analysis of 21 acid orthophosphate structures gives P–O(H) distances in the range 1.56–1.62 Å, whereas the average P–Ot bond distance (Ot = terminal oxygen) of 1.52 Å is slightly shorter than that in orthophosphates. The nonprotonated oxygen atoms are readily coordinated to cations, whereas the protonated sites are often uncoordinated, but are hydrogen bonded to nearby P–OH groups or other suitable species. This tends to result in more open structures with lower dimensionalities for acid orthophosphates than for orthophosphates.

Orthophosphates occur in diverse forms. Structural variety results from the large number of cations that form stable orthophosphates and the incorporation of additional molecules, notably water, or anions. Virtually every metallic element forms an orthophosphate, sometimes in a variety of oxidation states, e.g., from V^{II} to V^{V} in $NaV^{II}V_2^{III}(PO_4)_3$, $V^{III}PO_4$, $V^{IV}O(H_2PO_4)_2$, and $V^{V}OPO_4$. The former compound is one of many mixed valence orthophosphates. A very large number of mixed cation orthophosphates are also known; a complex example is $Mg_{21}Ca_4Na_4(PO_4)_{18}$. Hydrated phosphates are common and variation of the water content may be possible; $VO(HPO_4){\cdot}nH_2O$ structures have been characterized for $n = 1/2, 1, 2$ (two forms), 3, and 4. Orthophosphates containing additional anions include $Ca_2(PO_4)F$, $Fe_2(PO_4)O$, $Ca_{10}(PO_4)_6S$,$LiMn(PO_4)(OH)$, $Zr_2(WO_4)(PO_4)_2$, $Ca_5(PO_4)_2(SiO_4)$, $Pb_3Mn(PO_4)_2(SO_4)$, and $Na_3Ca(SiO_3)PO_4$ (containing an infinite catenasilicate chain). Solid solutions involving substitutions of the cations or the orthophosphate group (e.g., for orthoarsenate, vanadate, and silicate groups) further extend the range of possible phases.

1.6.2 Diphosphates [111]

The diphosphate anion $P_2O_7^{4-}$ (also known as pyrophosphate) is the simplest polyphosphate anion and is found in many solids. Variations in composition and structure are similar to those described above for the orthophosphates. The bonding and consequent geometry of the Ob–PO_3 (Ob = bridging oxygen) group is very similar to that of the (H)O–PO_3 group. P–Ob distances are in the range 1.58–1.64 Å, whereas the reported mean P–Ot distance for 17 diphosphates is 1.512 Å. P–O–P angles lie in the range 120–160°. Unusually large values are a result of disorder of the bridging oxygen atom, notably in the 'linear', centrosymmetric diphosphate groups (4) present in thortveitite-type transition metal diphosphate structures, $M_2P_2O_7$. Disorder is evidenced by anomalous P–Ob distances and Ob–P–Ot angles, and a large amplitude of thermal vibration for the bridging oxygen. Careful refinement of $Mn_2P_2O_7$ using single crystal X-ray and powder neutron diffraction data shows that the bridging oxygens lie 0.2 Å on either side of the inversion center, giving a P–O–P angle of 166°, in better agreement with well-ordered diphosphate groups. In general, apparently linear P–O–P linkages in condensed phosphates arise from such disorder and do not reflect a stable geometry. All three acid diphosphate anions have been found in the solid state, e.g., $Mn(HP_2O_7)$, $Na_2(H_2P_2O_7){\cdot}6H_2O$, and $Cs(H_3P_2O_7){\cdot}H_2O$. However, trihydrogendiphosphate salts are rare due to the low pKa of the doubly protonated phosphate group (H_3PO_4 has $pK1 = 2.1$). The bridging oxygen is of very low basicity and does not coordinate even to highly charged cations. This is a universal feature in the chemistry of condensed phosphates.

1.6.3 Polyphosphates [111]

Linking phosphate tetrahedra into chains through two vertices results in polyphosphate anions, $PnO3n + 1^{(n+2)-}$, also known as oligophosphates. Finite chains containing up to six tetrahedra have been found in the solid state. They become less common with increasing n. A large number of anhydrous and hydrated triphosphates have been characterized, including structures containing the mono- and dihydrogentriphosphate anions. Only the terminal phosphate groups are protonated, as bridging $-OP(O_2H)O^-$ groups have low pKa values. The layered triphosphates $MH_2P_3O_{10} \cdot 2H_2O$ (M = Al, Cr, Mn, Fe) are intercalation hosts. Tetraphosphates are less common than triphosphates and the best defined examples are crystalline, anhydrous materials. An acid tetraphosphate, $(NH_4)_4H_2P_4O_{13}$, has been reported. Pentaphosphate anions have been structurally characterized in $Mg_2Na_3P_5O_{16}$, $CsM_2P_5O_{16}$ (M = V, Fe), and the mixed phosphate $Rb_2Ta_2H(PO_4)_2(P_5O_{16})$. One hexaphosphate,

$Ca_4P_6O_{19}$, has been reported [111], but the structure has not been determined. There is evidence for longer polyphosphate anions up to at least $P_8O_{25}^{10-}$ in solution, but no well-defined solid derivatives have yet been prepared. A number of solid structures containing two polyphosphate anions have been reported [111]. All have complex stoichiometries involving at least two cationic species. Examples are $K_2Ni_4(PO_4)_2P_2O_7$, $CsTa_2(PO_4)_2P_3O_{10}$, $NH_4Cd_6(P_2O_7)_2P_3O_{10}$, and $CaNb_2O(P_2O_7)P_4O_{13}$. $KA_{l2}(H_2P_3O_{10})P_4O_{12}$ contains the dihydrogentriphosphate and cyclotetraphosphate anions.

1.6.4 Cyclophosphates [111]

Previously known as cyclopolyphosphates, these rings may contain up to 12 tetrahedra, but those with three, four, and six units are most common. The cyclotri- and cyclotetraphosphate rings adopt puckered geometries typical of saturated six- and eight-atom rings. The predominance of even-membered cyclophosphates reflects their ability to pack efficiently in the solid state, rather than any inherent stability over odd-membered ones. This is often reflected by a high internal symmetry in the crystalline state; an analysis of 30 reliably determined cyclohexaphosphate structures shows that eighteen have inversion symmetry and a further seven have threefold ($D3d$) internal symmetry. Both hydrated and anhydrous cyclophosphates have been prepared, but no acid anions have been found in these solids, due to the low basicity of two-connected phosphate groups [111]. A common structural feature, especially with large rings, is the formation of layers of cyclophosphate groups. This enables a large range of hydration numbers to be observed, as cations can be coordinated between two layers in anhydrous salts, or by cyclophosphate groups on one side and water molecules on the other in some hydrated compounds. Fully hydrated cations can also lie between the layers and further noncoordinated water molecules may occupy the intra-annular and interlamellar spaces. Examples of highly hydrated cyclohexaphosphates are $Nd_2P_6O_{18}\cdot 12H_2O$ and $Cu_3P_6O_{18}\cdot 14H_2O$.

1.6.5 Catenaphosphates [111]

The infinite chain catenaphosphate anion $(PO^{3-})^{\cdot}$ represents the infinite limit of the poly- and cyclophosphate series. Catenaphosphates are formed at high temperatures and so all reported structures are anhydrous, e.g., $Al(PO_3)_3$, $UO_2H(PO_3)_3$, and $Cs_2Co(PO_3)_4$. P–Ot and P–Ob distances are ~1.48 and ~1.60 Å, respectively, similar to values for two-connected phosphate tetrahedra in other anions. The cations lie between parallel, infinite polyphosphate chains, resulting in strongly bonded three-dimensional structures. Thermal decomposition of hydrogenphosphates has resulted in the acid catenaphosphates $Na_2H(PO_3)_3$, $BiH(PO_3)_4$, and $UO_2H(PO_3)_3$. In $BiH(PO_3)_4$, one of the terminal oxygens on every fourth phosphate tetrahedron is protonated; this is the only nonbridging oxygen not to coordinate to Bi^{3+}. As cyclophosphates and the catenaphosphate anion (together termed metaphosphates) share the basic composition (PO^{3-}) n, crystal structure analysis is often the only way to determine which species is present, although IR spectroscopy may be useful. Different isomers of the same metaphosphate composition are often found. Six crystal forms (A–F) of $M(PO_3)_3$ (M = Al, Cr, Mn, Fe, Ga) have been identified, three of which have been structurally characterized and found to contain cyclotetraphosphate (form A), cyclohexaphosphate (B), and catenaphosphate (C) anions. However, structures containing two metaphosphate anions are very rare. An example is $Pb_2Cs_3(P_4O_{12})(PO_3)_3$, in which both cyclotetraphosphate and catenaphosphate groups are present.

1.6.6 Ultraphosphates [111]

Possible ultraphosphate anions containing x two-connected and y three-connected tetrahedra have stoichiometry $P_{x+y}O_{3x+5y/2}{}^{x-}$. All observed anions have $y = 2$, and so may be written $PnO3n + 1^{(n+2)-}$, where $n = 4, 5, 6$, and 8. Solid ultraphosphates are anhydrous, as the P–O–P bridges between three-connected phosphate tetrahedra are susceptible to hydrolysis. The potential of lanthanide ultraphosphates MP_5O_{14} as laser materials has driven the exploration of ultraphosphate chemistry. The list of characterized ultraphosphates is: MP_4O_{11} (M = Mg, Ca, Mn, Co, Ni, Cu,Zn), MP_5O_{14} (M = Lanthanide, Y, Bi), $NiHP_5O_{14}$, $M_2P_6O_{17}$ (M = Ca, Cd, Sr), $(UO_2)_2P_6O_{17}$, $(TaO_2)_4P_6O_{17}$, and $Na_3MP_8O_{23}$ (M = Al, V, Cr, Fe, Ga). The structures of these anions vary from discrete anions to infinite ribbons, sheets, and three-dimensional frameworks. The MP_4O_{11} structures contain infinite layers of fused eight- and twelve-membered rings, but the MP_5O_{11} structures vary with the cation radius and fall into three principal types. Types I ($M = La - Ho$, Bi) and III ($M = Dy - Lu$, Y) both contain infinite ribbons (5), while in type II materials ($M = Tb - Lu$, Y), a complex three-dimensional phosphate framework is formed. A unique polymorph of CeP_5O_{11} contains infinite sheet anions. Sheets of fused 14-membered rings are found in $M_2P_6O_{17}$ compounds, whereas $UO_2P_6O_{17}$ contains an infinite three-dimensional anionic network. The $Na_3MP_8O_{23}$ structure contains the unique cage phosphate anion $P_8O_{23}^{6-}$ (6), which has a threefold symmetry axis. This is the only molecular ultraphosphate anion known to have been characterized. Phosphorus pentoxide may be regarded as a neutral ultraphosphate containing only three-connected phosphate tetrahedra. Two extended forms of P_2O_5 are known, one containing infinite sheets, and the other a three-dimensional framework. The third form, molecular P_4O_{10} (7), consists of four tetrahedra each joined through three vertices, and is the most highly condensed phosphate species.

1.6.7 Substituted Anions [111]

Condensing phosphate tetrahedra with other XO_4^{n-} groups results in P-substituted anions such as the polyphosphate derivatives $Na_3PS_2O_{10}$, $Na_4P_2S_2O_{13}$, $Na_3PCr_3O_{13} \cdot 3H_2O$, and $Li_3PCr_4O_{16}$. The phosphate groups are found in the bridging positions of these chains. Infinitely extended tetrahedral anions are formed by condensing phosphate and other tetrahedral groups. Electronegative nonmetals can substitute for oxygen in phosphate anions. Many fluoro- and difluoro-orthophosphates are known, e.g., $CaPO_3F \cdot 2H_2O$, $Cu(PO_2F_2)_2$, and sodium salts of all the thio-orthophosphate anions ${PO_{4-n}S_n}^{3-}$ $(n = 1 - 4)$ have been crystallized. Condensed thiophosphates have also been reported, e.g., $Cs_3P_3O_6S_3$ and $Na_4P_4O_8S_4 \cdot 6H_2O$, and analogous cycloimidophosphate anions are found in $K_3P_3O_6(NH)_3$ and $Cs_4P_4O_8(NH)_4 \cdot 6H_2O$. In the cyclothiophosphates, one terminal sulfur atom is present on each phosphate unit. However, the NH groups occupy the bridging positions in the cycloimidophosphate rings. Many monovalent and divalent cation salts of the ${P_3O_6(NH)_3}^{3-}$ anion have been prepared [111]. $AgPO_2(NH_2)_2$ is a rare example of a diamidophosphate, the nitrogen analog of a dihydrogenphosphate.

1.7 Origin, Objective, and Scope

Considerable improvement in the field of luminescent materials has been made by the introduction of rare earth ions as activators. Rare earth ions possess unique optical behavior when doped into materials and have paved the way for the development of optical amplifiers and phosphors. The optical value of these ions results from the electronic transitions occurring within the partially filled 4*f* energy shell of the lanthanide series.

Rare earth activated alkaline phosphate based compounds are of interest due to their unusual stability and useful luminescent properties. They are used for different applications such as phosphors for lamps, color TV screens, long-lasting devices, laser hosts, scintillators, and pigments. The energy transfer phenomenon has been studied extensively in inorganic phosphors, crystals, solutions, and glasses. Hence, in order to contribute to such knowledge, an attempt has been made in the present work to produce efficient phosphors based on rare earth activated phosphates to study their luminescence properties and explore potential new materials and applications.

These phosphors are synthesized using low cost and time saving synthesis methods, i.e., wet chemical synthesis and combustion synthesis. One of the objectives of this book is to better understand the mechanisms of energy transfer and the photoluminescence behavior of these compounds. Efforts are made toward finding new phosphate phosphors which could be used for the lamp industry.

Simple syntheses of known phosphate phosphors which are used as lamp phosphors, using easily available starting materials, have also been investigated.

The studies have been completed as far as possible within the available time. Possible future developments are pointed out. Studies of mixed cation phosphates are described. Many mixed anion phosphates are known to chemists and geologists.

References

1. Source: http://www.docstoc.com/docs/27529069/A-History-of-Lamp-Technology
2. I.F. Davies, E.T. Glenny, Light sources over 50 years. Light. J. **39**(2) (1974), http://www.raylight.co.uk/resources/documents/lamphistory.doc
3. J. Gordon Cook, *Michael Faraday: Lives to Remember Series* (Adam & Charles Black, London, 1963)
4. CIBSE Code for Interior Lighting (1994, updated 1997)
5. S. Shionoya, W.M. Yen, *Phosphor Handbook* (CRC Press, New York, 1998), p. 608
6. F. Xiao, Y.N. Xue, Y.Y. Ma, Q.Y. Zhang, Phys. B: Condens. Matter **405**, 891 (2010)
7. X.M. Zhang, H.-J. Seo, Phys. B: Condens. Matter **405**, 2436 (2010)
8. X.M. Zhang, H.J. Seo, J. Alloys Compd. **503**, L14 (2010)
9. X.M. Zhang, W.L. Li, L. Shi, X.B. Qiao, H.J. Seo, Appl. Phys. B: Lasers Opt. **99**, 279 (2010)
10. T.W. Kuo, W.R. Liu, T.M. Chen, Opt. Express **18**, 1888 (2010)
11. Y. Lan, L. Yi, L. Zhou, Z. Tong, F. Gong, R. Wang, Phys. B: Condens. Matter **405**, 3489 (2010)
12. K.Y. Jung, Y.C. Kang, Phys. B: Condens. Matter **405**, 1615 (2010)
13. Y. Chen, F. Cao, Y. Tian, L. Xiao, L. Li, Phys. B: Condens. Matter **405**, 435 (2010)
14. K. Shioi, N. Hirosaki, R.-J. Xie, T. Takeda, Y.Q. Li, J. Alloys Compd. **504**, 579 (2010)
15. A. Xie, X. Yuan, F. Wang, Y. Shi, J. Li, L. Liu, Z. Mu, J. Alloys Compd. **501**, 124 (2010)
16. H.Y. Jiao, Y.H. Wang, Appl. Phys. B: Lasers Opt. **98**, 423 (2010)
17. Ch. Basavapoornima, L. Jyothi, V. Venkatramu, P. Babu, C.K. Jayasankara, Th. Tröster, W. Sievers, G. Wortmann, J. Alloys Compd. **509**, 1172–1177 (2011)
18. I.M. Nagpure, K.N. Shinde, S.J. Dhoble, A. Kumar, J. Alloys Compd. **481**, 632 (2009)
19. Y.S. Tang, S.F. Hu, C.C. Lin, N.C. Bagkar, R.S. Liu, Appl. Phys. Lett. **90**, 151108 (2007)
20. S.K. Singh, A.K. Singh, D. Kumar, O. Prakash, S.B. Rai, Appl. Phys. B Lasers Opt. **98**, 173 (2010)
21. P.C. De Sousa, O.A. Serra, J. Lumin. **129**, 1664 (2009)
22. C.C. Lin, Y.S. Tang, S.F. Hu, R.S. Liu, J. Lumin. **129**, 1682 (2009)
23. P. Thiyagarajan, M. Kottaisamy, K. Sethupathi, M.S.R. Rao, Displays **30**, 202 (2009)
24. Y.L. Huang, C.F. Jiang, Y.G. Cao, L. Shi, H.J. Seo, Mater. Res. Bull. **44**, 793 (2009)
25. R.A. Benhamou, A. Bessiere, G. Wallez, B. Viana, M. Elaatmani, M. Daoud, A. Zegzouti, J. Solid State Chem. **182**, 2319 (2009)
26. K. Kuch, T. Retschinsky, Ann. Physik **20**, 563 (1906)
27. B. Jonas, Philips Tech. Rev. **3**, 119 (1938)
28. W. Elenbaas, Philips Tech. Rev. **18**, 167 (1957)
29. D.B.M. Klaassen, D.M. de Leeuw, T. Welker, J. Lumin. **37**, 21 (1987)
30. W. Harrison, Light Light. **44**, 148 (1951)
31. T. Welker, J. Lumin. **48–49**, 49 (1991)
32. A. Brill, W. Hoekstra, Philip. Res. Rep. **16**, 356 (1961)
33. W. Elenbaas, *Fluorescent Lamps and Lighting* (Philips Technical Library, Eindhoven, 1959)
34. B.M.J. Smets, in *Advances in Non-Radiative Processes in Solids*, ed. by B. Di Bartolo (Plenum Press, New York, 1990)
35. B. Di Bartolo, *Advances in Nonradiative Process in Solids* (Plenum Press, New York, 1991), p. 353
36. C. Zwiker, *Fluorescence Lighting* (Philips Technical Library, Eindhoven, 1952)
37. F.M. Ryan, J. Lumin. **24–25**, 827 (1981)

38. C. Amick, *Fluorescence Lighting Manual* (McGraw Hill, New York, 1960)
39. R.G. Pappalardo, in *Spectroscopy of Solid State Laser Materials*, ed. by B. Di Bartolo (Plenum Press, New York, 1982)
40. M. Koedam, J.J. Opstelten, Light. Res. Techol. **3**, 205 (1971)
41. H.H. Haft, W.A. Thornton, JIES **2**, 29 (1972)
42. J.J. Opstelten, D. Radielovic, W.L. Wanmaker, J. Electrochem. Soc. **120**, 1400 (1973)
43. J.M.P.J. Verstegen, J. Electrochem. Soc. **121**, 1623 (1974)
44. T. Justel, H. Nikol, C. Ronda, Angew. Chem. Int. Ed. **37**, 3084 (1998)
45. R.H. Clapp, J. Ginther, J. Opt. Soc. Am. **37**, 358 (1948)
46. J.W. Gilliland, M.S. Hall, Electrochem. Technol. **4**, 378 (1966)
47. K. Awazu, K. Mato, J. Electrochem. Soc. **116**, 282 (1969)
48. H. Piazena, H. Meffert, Radiat. Prot. Dosim. **91**, 185 (2000)
49. H.A. Leverenz, F. Seitz, J. Appl. Phys. **10**, 479 (1939)
50. H.A. Leverenz, RCA Rev. **5**, 131 (1940)
51. H.A. Leverenz, RCA Rev. **7**, 199 (1946)
52. M.N. Kassey, N.I. Harrison: RCA report, P1, T, 710
53. A. Brill, H. Klasen, Philips Res. Rep. **7**, 421 (1952)
54. G. Blasse, A. Brill, Appl. Phys. Lett. **11**, 53 (1967)
55. A.H. Gomes de Mesquta, A. Brill, Mater. Res. Bull. **4**, 643 (1969)
56. A. Brill, G. Blasse, A.H. Gomes de Mesquta, J.A. de Poorter, Philips Tech. Rev. **32**, 125 (1971)
57. R.C. Ropp, J. Electrochem. Soc. **115**, 531 (1968)
58. Y.A. Ono, *Electroluminescent Displays* (World Scientific, Singapore, 1995)
59. Y.K. Sasaki, J.B. Talbot, Adv. Mater. **11**, 91 (1999)
60. L. Ozawa, *Cathodoluminescence, Theory and Applications* (VCH, Weinheim, 1990)
61. J.P. Gordon, H.J. Zeiger, C.H. Townes, Phys. Rev. **95**, 282 (1954)
62. A.L. Schawlow, C.H. Townes, Phys. Rev. **112**, 1940 (1958)
63. T.H. Maiman, Nature (London) **187**, 493 (1960)
64. M.G.A. Berard, G. Duraffourg, Phys. Status Solidi **1**, 699 (1961)
65. W.P. Dumke, Phys. Rev. **127**, 1559 (1962)
66. R.N. Hall, G.E. Genner, J.D. Kingsley, T.J. Soltys, R.O. Carslon, Phys. Rev. Lett. **9**, 366 (1962)
67. M.I. Nathan, W.P. Dumke, G. Burns, F.J. Dill Jr, G.J. Lasher, Appl. Phys. Lett. **1**, 62 (1962)
68. T.M. Quist, R.H. Rediker, R.J. Keyes, W.E. Krag, B. Lax, A.L. McWhorter, H.J. Zeigler, Appl. Phys. Lett. **1**, 91 (1962)
69. N. Holonyak Jr., S.F. Bevacqua, Appl. Phys. Lett. **1**, 82 (1962)
70. I. Hayashi, M.B. Panish, P.W. Foy, S. Sumski, Appl. Phys. Lett. **17**, 109 (1970)
71. A. Penzkofer, Prog. Quantum Electron. **12**, 291 (1998)
72. R. Reisfeld, in *Spectroscopy of Solid State Laser Materials*, ed. by B. Di Bartolo (Plenum Press, New York, 1987), p. 343
73. H.J. Welker, IEEE Trans. Electron Devices **23**, 664 (1976)
74. G.A. Wolf, R.A. Herbert, J.P. Border, Phys. Rev. **100**, 1144 (1955)
75. R. Braunstein, Phys. Rev. **99**, 1892 (1955)
76. T. Li, IEEE JSAC **1**, 356 (1983)
77. J.C. DeWinter, M.A. Pollack, A.K. Srivastava, J.L. Zyskinn, J. Electron. Mater. **14**, 729 (1985)
78. J.M. Olson, S.R. Kurtz, A.E. Kibbler, in *Proceedings of the IEEE Photovoltaic Specialists Conference*, vol. 777 (1988)
79. G.C. Osbourn, Phys. Rev. B **27**, 5126 (1983)
80. G.E. Burlman, T.E. Zipperian, L.R. Dawson, J. Electron. Mater. **19**, 221 (1986)
81. M.J. Chang, Y.T. Chang, H. Ren, P. Harper, R.M. Cohen, G.B. Stringfellow, J. Electron. Mater. **15**, 79 (1986)
82. W.P. Hong, J. Singh, P. Bhattacharya, IEEE Trans. Electron Dev. **7**, 480 (1986)
83. A.S. Brown, J.A. Henije, M.J. Delaney, Appl. Phys. Lett. **52**, 1142 (1988)
84. S. Nakamura, G. Fasol, *The Blue Laser Diode* (Springer, Berlin, 1997)

85. S. Nakamura, MRS Bull. **22**, 29 (1997)
86. D.G. Matthews, J.R. Boon, R.S. Conroy, B.D. Sinclair, J. Mod. Opt. **43**, 1079 (1996)
87. B.H.T. Chai, G. Loutts, J. Lefaucheur, X.X. Zhang, P. Hong, M. Bass, I.A. Shesherbakov, A.I. Zagumennyi, OSA Proc. Adv. Solid-State Lasers **20**, 41 (1994)
88. G. Feugnet, C. Bussac, C. Larat, M. Schwarz, J.P. Pocholle, Opt. Lett. **20**, 157 (1995)
89. G.L. Bourdet, G. Lescroart, R. Muller, Opt. Commun. **150**, 141 (1998)
90. J. Azorin, Nucl. Tracks II **3**, 159 (1986)
91. R.K. Bull, Nucl. Tracks Radiat. Meas. II **1/2**, 105 (1986)
92. A.S. Pradhan, Radiat. Prot. Dosim. **1**(3), 153 (1981)
93. E. Wiedemann, G.C. Schmidt, Ann. Phys. Chem. Neue Folge **54**, 604 (1895)
94. T. Lyman, The transparency of air between dosimetry 1100 and 1300 Å. Phys. Rev. **48**, 149 (1935)
95. A.C. Lucas, Radiat. Prot. Dosim. **47**, 451 (1993)
96. J.T. Randall, M.H.F. Wilkins, Phosphorescence and electron traps. Proc. R. Soc. Lond. A **184**, 366 (1945)
97. F. Daniels, Final Report, USAEC Res. Cont. AT (11-1) 27 (1951)
98. F. Daniels, C.A. Boyd, D.F. Saunders, Science **117**, 343 (1953)
99. J.R. Cameron., D. Zimerman, G. Kenney, R. Bush, R. Bland, R. Grant, Science **134**, 333 (1961)
100. J.R. Cameron, N. Suntharalingam, G.N. Kenney, *Thermoluminescence Dosimetry* (University Wisconsin Press, Madison, 1968)
101. Harshaw, US patent, 1059518, filed 1964, published (1967)
102. M.J. Aitken, M.S. Tite, J. Reid, Nature **202**, 1032 (1964)
103. V. Mejdahl, Archaeometry **11**, 99 (1969)
104. A.G. Wintle, D.J. Huntley, Can. J. Earth Sci. **17**, 348 (1980)
105. C.M. Sunta, Radiat. Prot. Dosim. **8**, 25 (1984)
106. B. Lindel, Radiat. Prot. Dosim. **68**, 83 (1996)
107. V. Kortov, Radiat. Meas. **42**, 576–581 (2007)
108. S. McKeever, M. Moscovitch, P. Townsend, *Thermoluminescence Dosimetry Materials: Properties and Uses* (Nuclear Technology Publishing, Ashford, 1995)
109. D.E.C. Corbridge, *The Structural Chemistry of Phosphorus* (Elsevier, Amsterdam, 1974)
110. T. Kanazawa, *Inorganic Phosphate Materials, Materials Science Monographs*, vol. 52 (Elsevier, Amsterdam, 1989)
111. J.P. Attfield, *Phosphates: Solid State Chemistry, Encyclopedia of Inorganic Chemistry*, 2nd edn. (2006), pp. 1–52

Chapter 2
Basic Mechanisms of Photoluminescence

The phenomena which involve absorption of energy and subsequent emission of light are classified generically under the term luminescence. Phosphors are luminescent materials that emit light when excited by radiation, and are usually microcrystalline powders or thin-films designed to provide visible color emission. After decades of research and development, thousands of phosphors have been prepared and some of them are widely used in many areas. Excitation by absorbance of a photon leads to a major class of technically important luminescent species which fluoresce or phosphoresce. In general, fluorescence is "fast" (ns time scale) while phosphorescence is "slow" (longer time scale, up to hours or even days). For convenience, the topic of photoluminescence (PL) will be broadly divided into that based on relatively large-scale inorganic materials, mainly exhibiting phosphorescence, and that of smaller dye molecules and small-particle inorganic ("nanomaterials"), which can either fluoresce or phosphoresce. Their applications differ. For many of the derived technical applications, it is irrelevant whether the luminescence is fluorescence or phosphorescence. Either way the current range of applications is extensive, and in one case has been recognized by the award of a Nobel Prize, in 2008.

2.1 Excitation and Emission Spectra

Figure 2.1 shows a typical spectrum of the excitation and emission of a fluorochrome. These spectra are generated by an instrument called a *spectrofluorimeter*, which comprised two spectrometers: an illuminating spectrometer and an analyzing spectrometer. First, the dye sample is strongly illuminated by a color of light that is found to cause some fluorescence. A spectrum of the fluorescent emission is obtained by scanning with the analyzing spectrometer using this fixed illumination color. The analyzer is then fixed at the brightest emission color, and a spectrum of the excitation is obtained by scanning with the illuminating spectrometer and measuring the variation in emission intensity at this fixed wavelength. For the purpose of designing filters, these spectra are normalized to a scale of relative intensity.

K. N. Shinde et al., *Phosphate Phosphors for Solid-State Lighting*,
Springer Series in Materials Science 174, DOI: 10.1007/978-3-642-34312-4_2,

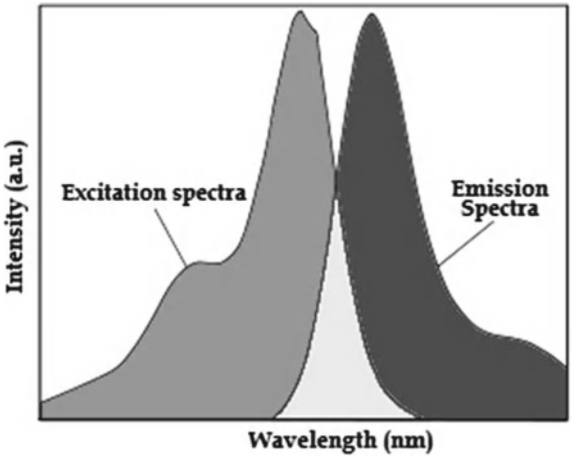

Fig. 2.1 Generic excitation and emission spectra for a fluorescent dye

These color spectra are described quantitatively by wavelength of light. The most common wavelength unit for describing fluorescence spectra is the *nanometer* (nm). The colors of the visible spectrum can be broken up into the approximate wavelength values [1]:

Violet and indigo	400–450 nm
Blue and aqua	450–500 nm
Green	500–570 nm
Yellow and orange	570–610 nm
Red	610 *to approximately* 750 nm

On the short-wavelength end of the visible spectrum is the near-ultraviolet (near-UV) band from 320 to 400 nm, and on the long-wavelength end is the near-infrared (*near-IR*) band from 750 to approximately 2,500 nm. The broad band of light from 320 to 2,500 nm marks the limits of transparency of crown glass and window glass, and this is the band most often used in fluorescence microscopy. Some applications, especially in organic chemistry, utilize excitation light in the mid-ultraviolet band (190–320 nm), but special UV-transparent illumination optics must be used. There are several general characteristics of fluorescence spectra that pertain to fluorescence microscopy and filter design. First, although some substances have very broad spectra of excitation and emission, most fluorochromes have well-defined bands of excitation and emission. The spectra of Fig. 2.1 are a typical example. The difference in wavelength between the peaks of these bands is referred to as the *Stokes shift* [1].

In practical applications, phosphors are often excited by cathode rays, X-rays, or UV emission of a gas discharge, which correspond to applications in displays, medical imaging and lighting, respectively, such as cathode-ray-tube (CRT) color TV, X-ray fluorescent screens, and fluorescent lamps. Energy transfer mechanism from one dopant (sensitizer) to another (luminescent center) is sometimes used to enhance the sensitivity of a phosphor. Earlier, several researchers have tried to sensitize this phosphor by co-doping with different rare earth metals. Energy transfer between pairs of rare earth ions at dilution level below the self quenching limits has been known to take place generally through multipolar interaction like dipole–dipole interactions or dipole–quadrupole interactions [2–4]. The use of energy transfer or metal enhancement effects has been applied in assays and in sensing with molecular fluorophores for sometime. These effects are also observed in nanoparticles and such approaches might lead to even more robust and flexible analytical methods for nanoscale inorganic phosphors. When absorption of UV or even visible light leads to emission, one speaks of optical excitation of luminescence. This process takes place in, e.g., fluorescent lamps and phosphor-converted LEDs, in which phosphors are used to at least partly change the wavelength of the radiation emitted by the LEDs. Optical absorption can take place on the already discussed impurities (optical centers), being either the activator ions or the sensitizer ions. Sensitizer ions are used when the optical absorption of the activator ions is too weak (e.g., because the optical transition is forbidden) to be useful in practical devices. In such a case, energy transfer from the sensitizer ions to the activator ions has to take place. The optical absorption leading to emission can also take place by the host lattice itself (band absorption). In this case one speaks of host lattice sensitization. Energy transfer from host lattice states to the activator ions (in some cases also involving sensitizers) has to take place.

The absorption of energy, which is used to excite the luminescence, takes place by either the host lattice or by intentionally doped impurities. In most cases, the emission takes place on the impurity ions, which, when they also generate the desired emission, are called activator ions. When the activator ions show too weak an absorption, a second kind of impurities can be added (sensitizers), which absorb the energy and subsequently transfer the energy to the activators. This process involves transport of energy through the luminescent materials. Quite frequently, the emission color can be adjusted by choosing the proper impurity ion, without changing the host lattice in which the impurity ions are incorporated. On the other hand, quite a few activator ions show emission spectra with emission at spectral positions which are hardly influenced by their chemical environment. This is especially true for many of the rare-earth ions. Generally, luminescence of phosphors involves two processes: excitation and emission. Many types of energy can excite the phosphors. Excitation by means of energetic electrons is cathodoluminescence (CL). PL occurs when excited by photon (often ultra-violet), electroluminescence (EL) is excited by an electric voltage, chemiluminescence is excited by the energy of a chemical reaction, and so on. The process of emission is a release of energy in the form of photon. The basic luminescence mechanisms in luminescent centers are illustrated in Fig. 2.2. In the host lattice with activator, the activator is directly excited by incoming energy; the electron on it absorbs energy and is raised to an excited state. The excited state returns to the ground state by emission of radiation [5].

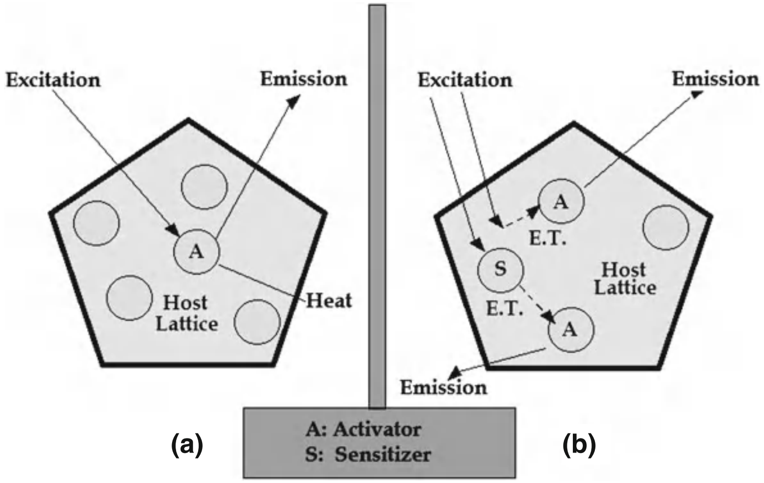

Fig. 2.2 Schematic diagram showing (**a**) direct excitation of the activator and (**b**) indirect excitation followed by energy transfer from the sensitizer or host to the activator [2]

2.1.1 Radiative Transition

There are several possibilities of returning to the ground state. The observed emission from a luminescent center is a process of returning to the ground state radiatively. The luminescence quantum efficiency is defined as the number of photons emitted divided by the number of photons absorbed, and in most cases is equal to the ratio of the measured lifetime to the radiative lifetime of a given level. The processes competing with luminescence are radiative transfer to another ion and nonradiative transfers such as multiphonon relaxation and energy transfer between different ions or ions of a similar nature. The last transfer is also named cross-relaxation. Figure 2.3 shows the configurational coordinate diagram in a broad band emission. Assumption is made on an offset between the parabolas of the ground state and the excited state. Upon excitation, the electron is excited in a broad optical band and brought in a high vibrational level of the excited state. The center thereafter relaxes to the lowest vibrational level of the excited state and give up the excess energy to the surroundings. This relaxation usually occurs nonradiatively. From the lowest vibrational level of the excited state, the electron returns to the ground state by means of photon emission. Therefore, the difference in energy between the maximum of the excitation band and that of the emission band is found. This difference is called the Stokes shift [6]. The radiative transfer consists of absorption of the emitted light from a donor molecule or ion by the acceptor species. In order to that such transfer takes place, the emission of the donor has to coincide with the absorption of the acceptor. The radiative transfer can be increased considerably by designing a proper geometry.

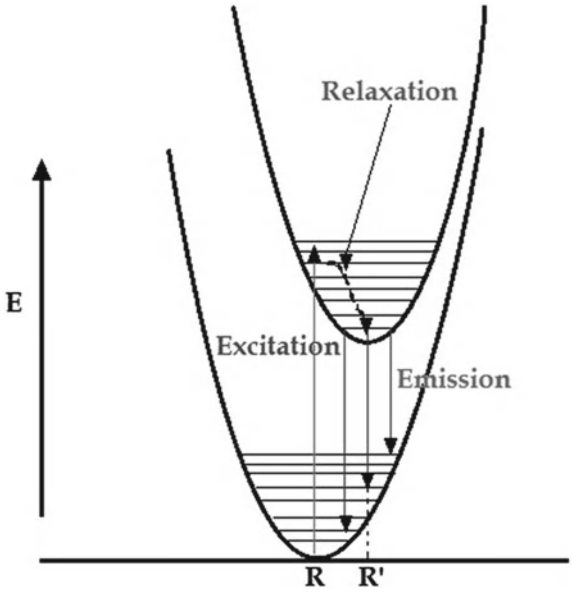

Fig. 2.3 Configurational coordinate diagram in a luminescent center

2.1.2 Nonradiative Transition

The energy absorbed by the luminescent materials which is not emitted as radiation is dissipated to the crystal lattice. It is crucial to suppress those radiationless processes which compete with the radiation process. In order to understand the physical processes of nonradiative transitions in an isolated luminescent center, the configurational coordinate diagrams are presented in Fig. 2.4. In Fig. 2.4a, there is a Stokes shift between the ground state and the excited state. The relaxed-excited-state may reach the crossing of the parabolas if the temperature is high enough. Via the crossing, it is possible for electrons to return to the ground state in a nonradiative manner. The energy is given up as heat to the lattice during the process [7]. In Fig. 2.4b, the parabolas of ground state and excited state are parallel. If the energy difference is equal to or less than four to five times the higher vibrational frequency of the surrounding, it can simultaneously excite a few high-energy vibrations, and therefore is lost for the radiation of phonons. This is called multiphonon emission. In a three-parabola diagram as shown in Fig. 2.4c, both radiative and nonradiative processes are possible. The parallel parabolas (solid lines) from the same configuration are crossed by a third parabola originated from a different configuration. The transition from the ground state to the lower excited state (solid line) is optically forbidden, but it is allowed to transit to the upper excited state (dash line). Excitation to the transition allowed parabola then relaxes to the relaxed excited state of the second excited parabola. Thereafter, emission occurs from it.

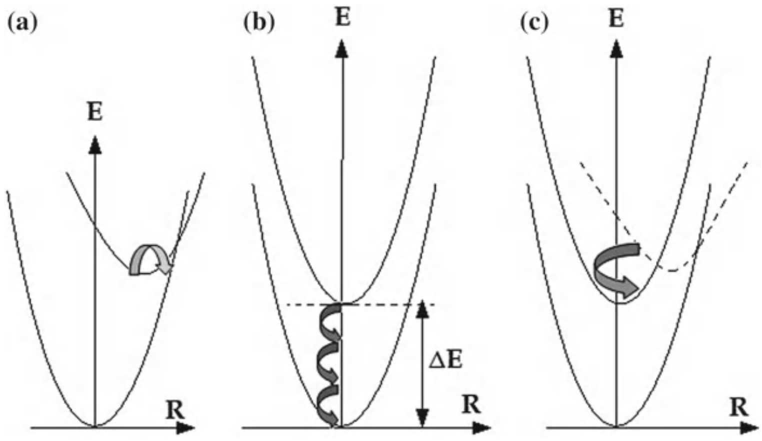

Fig. 2.4 Configurational coordinate diagram representing nonradiative transitions

The nonradiative processes competing with luminescence are energy loss to the local vibrations of surrounding atoms (called phonons in solids) and to electronic states of atoms in the vicinity, such as *energy transfer*, which may be resonant (including as a special case energy migration between identical systems, which may ultimately emit radiation) or phonon assisted [the excess energy being dissipated as heat, or, to a much smaller extent, the thermal reservoir supplying low-energy phonons ($kT = 210\,\mathrm{cm}^{-1}$ at 300 K) to a slightly higher level of an adjacent system]. Special cases of energy transfer are cross-relaxation, where the original system loses the energy ($E_2 - E_1$) by obtaining the lower state E_1 (which may also be the ground state E_0) and another system acquires the energy by going to a higher state. Cross-relaxation may take place between the same lanthanide (being a major mechanism for quenching at higher concentration in a given material) or between two differing elements which happen to have two pairs of energy levels separated by the same amount [7].

2.1.3 Multiphonon Relaxation [8]

Today, multiphonon relaxation in lanthanide ions is a well-understood process, contrary to other transition metal ions, which still require additional understanding. Excited electronic levels of rare earths in solids decay nonradiatively by exciting lattice vibrations (phonons). When the energy gap between the excited level and the next lower electronic level is larger than the phonon energy, several lattice phonons are emitted in order to bridge the energy gap. It was recognized that the most energetic vibrations are responsible for the nonradiative decay since such a process can conserve energy in the lowest order. The most energetic vibrations are the stretching vibrations of the glass network polyhedra; it was shown that these distinct vibrations are active in the multiphonon process, rather than the less energetic vibrations of the bond between the *R* and its surrounding ligands. It was demonstrated that these less energetic vibrations may participate in cases when the energy gap is not bridged totally by the high-energy vibrations. The experimental results reveal that the logarithm of the multiphonon decay rate decreases linearly with the energy gap, and hence with the number of phonons bridging the gap, when the number of phonons is larger than two [8].

2.1.4 Cross-Relaxations [8]

A special case of energy transfer is cross-relaxation, where the original system loses the energy $(E_3 - E_2)$ by obtaining the lower state E_2 (which may also be the ground state E_1) and another system acquires the energy by going to a higher state E_2'. Cross-relaxation may take place between the same lanthanide (being a major mechanism for quenching at higher concentration in a given material) or between two differing elements, which happen to have two pairs of energy levels separated by the same amount. The cross-relaxation between a pair of *R* ions is graphically presented in Fig. 2.5. The two energy gaps may be equal or can be matched by one or two phonons. Cross-relaxation has been measured in a variety of ions and it is a dominating factor in nonradiative relaxations at high concentration. The nonradiative relaxation rates can be obtained by analysis of the decay curves of *R* fluorescence using the formula of the general form where the population number of state i, N_i, is proportional to the intensity of emitted light, I_i:

$$\frac{\mathrm{d}N_i(t)}{\mathrm{d}t} = -\left(\gamma_\mathrm{R} + X_i + \sum_{i \neq j} W_{ij}\right) N_i(t) + \sum_{i \neq j} W_{ij} N_i(t)$$

$\mathrm{d}N/(t)/\mathrm{d}t$ is the decrease of intensity after pulse excitation, γ_R is the reciprocal of the lifetime of the excited state in the absence of a cross-relaxation process. $\sum W_{ij}$ is the probability for cross-relaxation, W_{ji} is the probability of the inversed process, and W_{ij} is the rate of cross-relaxation. Theoretically, the cross-relaxation rate for a dipole–dipole transfer can be obtained from the formula [9].

$$\begin{aligned} P_{SA}{}^{(\mathrm{DD})} = {} & \frac{1}{(2J_s+1)\,(2J_A+1)} \frac{2}{3} \left(\frac{2\pi}{h}\right) \left(\frac{e^2}{R^3}\right)^2 \left[\sum\nolimits_t \Omega is\ \langle J_s || \cup^{(t)} || \, J_s' \rangle^2\right] \\ & \times \left[\sum\nolimits_t \Omega iA\ \langle J_A || \cup^{(t)} || \, J_A' \rangle^2\right]_{\bar{s}} \end{aligned}$$

Here Ωt are the Judd–Ofelt intensity parameters, $\langle J || \cup^{(t)} || J' \rangle$ is the matrix element of the transition between the ground and excited state of the sensitizer and activator, respectively. The calculation of these matrix elements in the intermediate-coupling

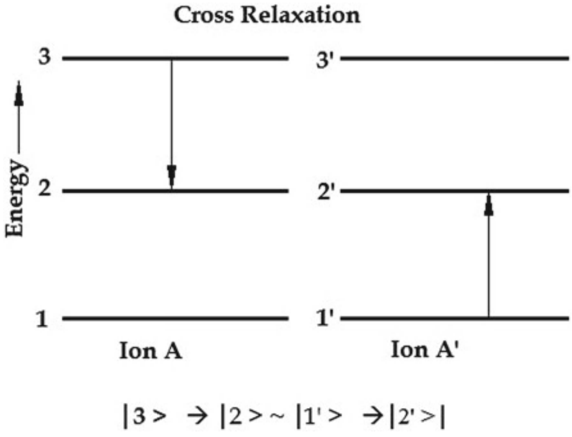

Fig. 2.5 Scheme for cross-relaxation between two ions of the same, or of different nature [8]

scheme is now a well-known procedure and may be found in [9]. *S* is the overlap integral and *R* is the interionic distance.

2.1.5 Up-Conversion [8]

Up-conversion in its most general sense is the phenomenon whereby one or more photons of lower energy are absorbed by a material, and re-emitted as a higher energy photon. Materials able to cause this effect are known as up-converters. A main attraction is that they can be tuned to respond to near IR energy near 980 nm from commonly available and cheap diode lasers, and emit a range of photon energies at visible wavelengths. A major type of up-converter is based on rare earth-(RE)-doped salts of various metals, usually fluorides, in solid crystal or glass matrices. Up-conversion in such materials can occur by several different mechanisms whose full description goes beyond the scope of this book [10]. They rely on the multitude of accessible excited states within the different RE cations. Besides the RE materials there are others which bring about an up-conversion effect on photoirradiation, and which will be the subject of more detailed description later. They are introduced now for convenience. They in turn follow different mechanisms for up-conversion. Figure 2.6 summarizes diagrammatically some of the absorption–emission processes which lead to up-conversion. The vertical arrows represent absorption or emission of a photon, while the curved arrows represent energy transfer between species (usually ions).

- Mechanism (a) is the most common in RE systems. Here, two photoexcited RE ions (same species or different) each transfers its energy to a third ion which emits from the higher energy state. Ytterbium as Yb^{3+} is commonly used as a primary absorber of input photoradiation, and this transfers energy to emitter ions,

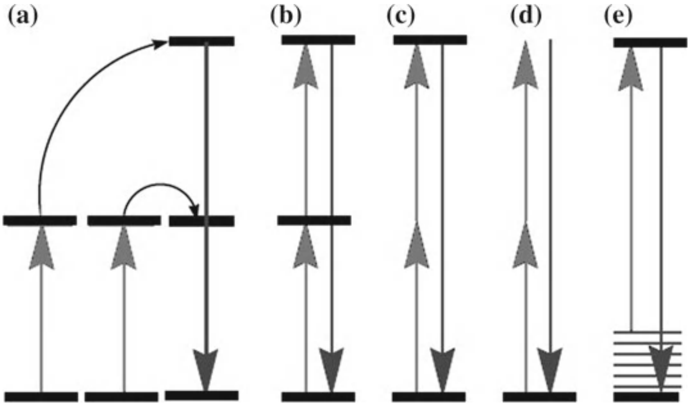

Fig. 2.6 Simplified representations of some up conversion processes

commonly Er^{3+} and Tm^{3+}. The efficiency of this energy transfer up-conversion (ETU) is surprisingly high and, of the five mechanisms shown in Fig. 2.6, this is the most efficient. Three-photon ETU is also well-known.

- In (b), initial absorption leads to an intermediate excited state, which lives long enough to allow ready absorption of a second photon to give a higher excited state, hence its name of 2-step absorption. Emission from this clearly gives a higher energy, up-converted, and photon. This process is about two orders of magnitude less efficient than (a). Mechanisms related to (a) and (b) can involve subsequent absorption steps to reach yet higher excited states, prior to luminescence. Furthermore, there are not only several other distinct processes for RE up-conversion, but there are also combination processes, some including conventional down-conversion steps, so it must be accepted that an overview presented here for RE up-converters is very limited [1].
- Mechanism (c) is two-photon absorption, this time without a real intermediate excited state. This implies simultaneous absorption of two photons, which inevitably has a lower probability and the mechanism is thus much less efficient. However, by means of intense laser irradiation, two (or even multi) photon absorption (2PA, 3PA, etc.) has become well characterized for some organic dyes and specially modified derivatives. CaF_2 doped with Eu^{2+} is a 2PA example from RE chemistry. However, up-conversion from this material is about 10^{10} times less efficient than for an ETU material such as YF_3 doped with Er^{3+} and Yb^{3+}.
- Second harmonic generation (SHG) (d), under nonlinear optics (although mechanisms (a)–(c) are also nonlinear in character). Here, the interaction of two photons in the SHG material does not proceed by way of any excited energy state. The efficiency of up-conversion for the traditional SHG material KDP (potassium dihydrogen phosphate) is about eight orders of magnitude less efficient than that for ETU (a).

- Finally, the mechanism of up-conversion represented by (e) is sometimes called hot-band absorption. An electron in a vibrationally excited level of the ground state of a species is preferentially excited. Emission then proceeds back to a lower vibrational level within the ground state, and up-conversion by only a few units of thermal energy is observed.

2.2 Features of Rare Earth (RE) Ions with Respect to Luminescence

In display application of luminescence mostly inorganic solids doped with rare earth impurities are used. It is necessary to understand the mechanism of these display materials. Basically, there are four important parameters, viz. excitation type and spectrum, relaxation to emitting state and the decay time, and emission intensity and emission spectrum. RE spectra were observed extremely sharp (line-spectra). The above-mentioned four factors vary from one-host materials to another.

The characteristic properties of the RE ions are attributable to the presence in the ion of a deep-lying 4*f* shell, which is not entirely filled. The electrons of this shell are screened by those in the outer shells (except for La^{3+} and Lu^{3+}), and as a result they give rise to number of discrete energy levels. Since the presence of crystal lattice scarcely affects the position of these levels, there is a resemblance between the energy level diagram of a free ion and that of the incorporated ion. In case of the latter, usually the terms are shifted to lower wave numbers. Some empirical laws have been formulated regarding the magnitude of this effect [11–14].

In spite of the resemblance of the energy levels of free RE ions and the RE ions in solids, there is an important difference in the emission properties. In solids, the emission of RE ions is observed at different spectral position than the absorption. The difference between the absorption and emission wavelength is described as 'Stokes Shift'. The shift for the transition within 4*f* shell results from the fact that the absorption and emission takes place between different levels. Usually, absorption corresponds to the transition from ground state to higher excited states. Electron in the higher excited state then loses energy to lattice till the states lying just below the previous excited states are available. When the difference between the adjacent states is large, then the energy corresponding to this transition cannot be transferred to lattice and it is given out in the form of emission. The emission thus corresponds to the transition from the intermediate state to the ground state.

RE ions are usually trivalent. Ions corresponding to configurations $4f^0(La^{3+})$, $4f^7(Gd^{3+})$ and $4f^{14}(Lu^{3+})$ are stable. The RE element next to these three tends to exchange electron and acquire this stable configuration. For understanding the luminescent properties of rare earth ions, it is necessary to know their key energy levels. The energy level may be divided into three categories, those corresponding to $4f^n$ configuration, $4f^{n-1}5d$ configuration, and those corresponding to charge transfer involving the neighboring ions.

2.2.1 *Discrete f–f Transition*

Except for Ce^{3+} and Yb^{3+}, number of discrete 4*f* energy levels is large. For Gd^{3+}, there are as many as 327 levels of 4*f* configuration. These levels further increase in number due to crystal field splitting. Most often the levels relevant to photoluminescence that can be excited by UV light and other levels are ignored.

The transitions within 4*f* shells are strictly forbidden, because the parity does not change. The forbidden transitions are observed due to the fact that the interaction of RE ion with crystal field or with the lattice vibrations can mix state of different parities into 4*f* states.

Coupling of 4*f* electrons with transient dipoles induced in the ligands by the radiation field leads to an amplification of the even parity multipolar transition amplitudes for transitions within 4*f* shell. These transitions are called as induced electric dipole transition. Quite often, the transition corresponding to selection rules $(\Delta S = 0, L \leq \pm 2$ and $J \leq \pm 2)$ shows large variations in oscillator strengths depending upon the surround environment. These have been termed as the *hypersensitive transitions*. Table 2.1 lists the various hypersensitive transitions for different RE^{3+} ions.

The transitions that are not allowed as electric dipole may take place as magnetic dipole. The magnetic dipole transitions obey the selection rules $\Delta L = 0$, $\Delta S = 0$, $\Delta I = 0$ and$\Delta J = 1(0 \rightarrow O$ excluded). Spin orbit coupling weakens the selection rule on ΔL and ΔS.

Interaction of RE ions with lattice vibrations also can mix the state of different parities into 4*f* states. Vibronic transitions of RE ions are due to coupling of $4f^n$ state with the vibrational mode of the lattice.

Table 2.1 Hypersensitive transitions of rare earths

Rare earth	Excited state	Ground state
Ce	–	–
Pr	$^3H_5, {}^3F_2$	$^3H_4$
Nd	$^4G_{5/2}, {}^2G_{7/2}, {}^4G_{7/2}$	$^4I_{9/2}$
Pm	$^5G_{12}, {}^5G_3$	$^5I_4$
Sm	$^4H_{7/2}, {}^6F_{1/2}, {}^6F_{3/2}$	$^6H_{5/2}$
Eu	$^7F_2$	$^7F_1, {}^7F_0$
Gd	–	–
Tb	$^7F_5$	$^7F_6$
Dy	$^6F_{11/2}, {}^6H_{13/2}, {}^6H_{11/2}$	$^6H_{15/2}$
Ho	$^5G_6, {}^3H_6$	$^5I_8$
Er	$^2H_{11/2}, {}^4G_{11/2}$	$^4I_{15/2}$
Tm	$^3F_4, {}^3H_4, {}^3H_5$	$^3H_6$
Yb	–	–

2.2.2 Broad Energy Bands

In addition to the discrete 4*f* levels there are other levels present. These are usually in the form of broad bands and play vital role in excitation. For Ce^{3+} and Eu^{2+}, these are vital for emission as well.

The bands referred to fall into two groups. In the first group, one of the 4*f* electrons is raised to the higher 5*d* levels. Transitions from configuration $4f^n$ to $4f^{n-1}$ are allowed. The second group of bands corresponds to the promotion of an electron from one of the surrounding ions to 4*f* orbit of the central ion. This is referred to as the charge transfer state and written as $4f^n 2p^{-1}$.

2.2.3 f–d Transition

$4f^{n-1}5d$ levels may be understood as formed by the electron in the 5*d* orbital interacting with $4f^{n-1}$ core. As a consequence of this strong crystal field effect on the 5*d* electron, $4f^{n-1}5d$ configurations of RE ions in solids are very different from those of free ions. $4f^n \rightarrow 4f^{n-1}5d$ absorption of most of the RE^{3+} and RE^{2+} ions exhibit two features. First, they consist of strong bands corresponding to the components of 5*d* orbital split in the crystal field. Consequently, their spectra are similar when ions are embedded in same type of host. Second, the structures of 5*d* bands can be fitted to energy differences in the ground multiplets of the $4f^{n-1}$ configurations.

For most of the trivalent RE ions, transitions from configuration $4f^n$ to $4f^{n-1}5d$ correspond to wavenumbers exceeding 50,000 cm^{-1}, and thus not accessible to UV excitation. In case of Ce and Tb, they are usually accessible to UV excitation the position of these bands shifts to higher wavenumbers as one moves along the RE series from Ce to Gd. For Tb, the position is suddenly lowered and again the increasing trend is observed up to Yb^{3+}. Table 2.2 compares the characteristics of *f–f* and *f–d* transitions.

Table 2.2 Comparison of *f–f* and *f–d* transition of rare earths

	f–f	*f–d*
Electric dipole oscillator strength	10^{-6}	10^{-1}–10^{-2}
Ion lattice coupling	Weak	Strong
Emission wavelength	200–500 nm	150–1,000 nm
Line width	10 cm^{-1}	>1,000 cm^{-1}
Life time	10^{-2}–10^{-5} s	10^{-8}–10^{-6} s

2.2.4 CT Bands

CT bands will depend on the ligand. It has been observed that the energy will decrease with the electronegativity of the ligand ion. Tetravalent ions often show absorption in the visible region of the spectrum, which corresponds to the CT state. In case of Eu^{3+}, the CT band provides strong excitation. No other RE ion is as much investigated for the CT bands as Eu^{3+}.

2.3 Excitation by Energy Transfer

Apart from the *f–d* allowed transitions and the CT bands, strong excitation can often be achieved by the energy transfer. A RE ion or other species may absorb the energy and transfer to another RE ion which may lose the energy radiatively. When the energy transfer results in the increase in RE emission it is termed as the sensitization. The RE ion from which the emission results is called as the activator and the one which absorbs energy as the sensitizer.

An unwanted feature of the energy transfer is the reduction in emission. Indeed, there are many more examples of energy transfers resulting into reduction of the desired emission than the one in which sensitization has been achieved. The concentration quenching of RE emission most often takes place through the energy transfer. One may expect that the RE luminescence will increase with increase in the concentration of luminescent ions. In practice, this is valid only up to certain limiting concentration above which a RE ion in excited state loses energy to a nearby ion in the ground state. The excitation energy, thus hops from one ion to the other and ultimately it may reach a killer site (e.g., an impurity ion which absorbs the energy and dissipates it nonradiatively). The concentration quenching may take place through cross-relaxation also. In this process, the excitation ion comes to a less excited state. When the transition from this less excited state to the ground state is nonradiative, luminescence is completely quenched. Otherwise one observes emission at the longer wavelengths taking place at the cost of the short wavelength emission.

Since the interaction with lattice will be temperature dependent, it is quite understandable that the position, splitting, and lifetimes of various levels can be temperature dependent. It is quite common to find that at lower temperatures the host lattice offers conditions conductive for luminescence while at high temperatures, the nonradiative processes become dominant. This has been termed as thermal quenching. For many applications it assumes prime importance. It determines the operating temperature of the device based on the luminescent materials. In some cases (e.g. Y_2O_3:Eu), increase in luminescence efficiency at which high temperatures has been observed. This occurs due to the thermal quenching of the processes which compete with the desired emission.

2.4 Rare Earths Energy Levels and Transitions

There are 14 rare earth elements and they lie between lanthanum (^{57}La) and hafnium (^{72}Hf). Their atomic configurations consist of partially filled 4*f* shells. It is important to note that ions with either filled 4*f* levels such as Lu^{3+} or ions that have no 4*f* electrons such as La^{3+}, will have no electronic energy levels to induce excitation in/or near the visible region. The azimuthal quantum number (l) of 4*f* orbitals is 3, which gives $2l + 1 = 7$ orbital state (7 orbital orientation) and allows 14 electrons to stay. In the nonexcited state, these electrons will be distributed in such a way that they will have the maximum combined spin angular momentum (S). According to Hund's rule, the spin angular momentum S is added to the orbital angular momentum L to give the total angular momentum J. For the lowest ground state, $J = L - S$, when the number of 4*f* electrons is less or equal to 7, and $J = L + S$, when the number of 4*f* electrons is larger than 7.

2.4.1 Electronic Transitions

An electronic state is indicated by notation $^{2S+1}L_J$, where L represents the letters S, P, D, F, G, H, I, K, L, M, N… corresponding to the resultant orbital quantum number of 4*f* electrons $L = 0, 1, 2, 3, 4, 5, 6, 7, 8\ldots$, respectively [15]. An electronic state is actually expressed as an intermediate coupling state and can be described as a mixed state of several $^{2S+1}L_J$ states and a spin–orbit interaction. This mixing due to spin–orbit is actually small for the levels near the ground states, and it is larger for the states that are neighbors with the same J numbers. The effect of the mixing is very large in the optical transition probabilities, although it is relatively small on the energy levels. Rare earth ions (doubly or triply charged) can be present in ionic solids. For the case of the triply charged, all 5*d* and 6*s* orbitals are empty and the 4*f* is partially occupied. The optically active 4*f* electrons are shielded from the crystalline electric field by the outer 5*s* and 5*p* shells. The resulting effect is that the neighboring ligands have very little affection on the 4*f* electrons. The energy levels of the 4*f* electrons are very similar to the free ion levels characterized by the L, S, and J values with allowance made for some term mixing [15] and this is because of the weak interaction with the lattice environment. The spectral lines (either of emission or absorption) are sharp and the energy positions are not (usually) crystalline host dependent.

For the case of divalent rare earth ions, the energy separation between the $4f^n$ and $4f^{n-1}5d$ configurations will be large and the transitions between these two may be observed by normal spectroscopy. These transitions are dipole-allowed and are about 10^6 times stronger than the very frequently observed $4f \rightarrow 4f$ transitions in trivalent (rare-earth) ions. The emission and excitation spectra of the divalent europium ion are mainly composed of two types of electronic transitions: a strong $4f \rightarrow 5d$ transition with a high energy and a weak $4f \rightarrow 4f$ transition at low energies. The gross feature of the spectra of this type of rare earth ions is considered to arise from the T_{2g} and E_g components of the 5*d* electron in the cubic crystalline field. The strongest lines were actually assigned to pure electronic transitions from $4f^n$ to $4f^{n-1}5d$ which was assumed to be caused by the interaction between the $4f^{n-1}$ core and the 5*d* electron, the $4f^{n-1}5d$ level being spaced with the energy gaps in the $4f^{n-1}$ ground multiplets [16].

Optical absorption of 4*f* electrons transitions is strongly forbidden by the parity selection rule [17]. However, this rule can be relaxed. When an ion occupies a crystalline site there are uneven components of the crystal field. These components mix a small amount of opposite parity wavefunctions into the 4*f* wavefunctions, and this causes intra-configurational 4*f* transitions to gain some intensity.

The allowed optical inter-configurational transitions for rare earth ions are divided into two types: $4f^n \rightarrow 4f^{n+1}\mathrm{L}^{-1}$, $\mathrm{L} =$ ligand (charge-transfer transitions) and $4f^n \rightarrow 4f^{n-1}5d$ transitions. And both are allowed and have broad absorption band. The first type of charge transfer is found in rare earth elements that like to be reduced and is commonly observed in tetravalent rare earth ions. The second (5*d* transition) on the other hand is found for the ones which like to be oxidized and is commonly observed in divalent rare earth ions.

2.4.2 Stark Splitting

As mentioned above, 4*f* electrons of rare earth are shielded from crystal environment by 5*s* and 5*p* shells. However, in a crystal field, the *J* degeneracy of spin–orbit state $^{2S+1}L_J$ can be shifted and split. This is called Stark splitting. In other words, this effect is the splitting of the spectral line into several components in the presence of an electric field. This effect is the analogous to the Zeeman effect in a magnetic field, but in this case the splitting is not symmetric. This splitting only occurs when the ion is polarized by the electric field resulting in a dipole moment. This dipole moment only depends upon magnitude (M_J), not direction, so the energy levels will be split into $J + 1$ or $J + 1/2$ levels.

This splitting is usually much less than the separation of the spin–orbit levels. Because of this, the main features of the energy levels diagrams remain almost unchanged for the rare earth ions in different host materials. On the other hand, the crystal-field splitting will vary for different host, and it will show the different symmetries and strengths of the crystal fields.

2.4.3 Multiphonon Process

Most 4*f* emitting levels are separated from the next lower level in a distance of at least $2 \times 10^3\ \mathrm{cm}^{-1}$. Excited states of this kind release their energy via either of two competitive ways: light emission or by phonon emission. The rate of phonon emission is dependent on the number of phonons emitted at the same time to bridge the energy gap. The probability of multiple phonon transitions is given by the relation:

$$w \infty \exp^{-kE} / h\nu_{\max}$$

where w is the phonon transition rate, E is the energy gap closest to the lower level and $h\nu_{\max}$ is the maximum energy of phonons (coupled to the emitting states). When E increases the phonon emission rate decreases rapidly; therefore, the competitive light emission process (radiative) becomes the dominant one. On the contrary, if the phonon energy is large or E is small, the phonon transition probability can be very high, and the radiative transition of the upper excited level can be seriously quenched.

2.4.4 Crystal Field Splitting

Wavefunctions of 5*d* of rare earth such as Eu^{2+} and 3*d* electrons of transition ions such as Mn^{2+} are quite extended. They will strongly interact with ligand ions in crystals. As a result, the resultant orbital states of *d* electrons will be split. The splitting is usually much larger than the splitting by *L–S* coupling. Crystal-field splitting depends on several factors:

(1) number of electrons in the *d* orbitals
(2) oxidation state of the crystal (a high oxidation state will lead to a high-energy splitting)
(3) the arrangement of the ligands around the crystal
(4) the nature of the ligands

The most common type of complex is the octahedral. In this case, six ligands form an octahedral field around the metal ion and the ligands point directly into the *d*-orbitals and cause high-energy splitting. The second most common type of complex is the tetrahedral, for this case four ligands form a tetrahedral field around the metal ion, for this case the electrons are not oriented directly against the orbitals; therefore, the energy splitting level is lower than the previous case. The physics of this phenomenon is the following: as we know the transition metals have ions with partially filled orbitals (five of them) and they are degenerate. When a ligand approaches the metal ion, the electrons from the ligand are at different distances to the *d*-orbitals, and the electrons in the *d*-orbitals and the ones in the ligand have an acting repulsive force, because the *d*-orbitals are repulsed unequally by the ligand, and obviously the *d*-orbitals will split into energy.

In some cases, there are more than one *d*-electron and in these cases we observe a strong crystal field. These electrons affect each other electrostatically through a potential of the form:

$$\frac{\sum e^2 r}{r}$$

2.5 Energy Transfer

The process in which the excitation of a certain ion migrates to another ion is called energy transfer. It is very important to understand this effect in order to develop efficient luminescent materials. The luminescent materials had several types of energy transfer [18]:

i. ***Resonant energy transfer between ions of same energy level***—for this case, the excitation energy of a certain ion migrates to another one of the same species that is in the ground state. This type of transfer is also divided into three categories: First, multipolar interaction, and this is both transitions are of electric dipole character; the second is the exchange interaction, and this is when the donor and the acceptor are both located so close that their electronic wave functions overlap and the transfer is due to a quantum mechanical interaction; and lastly, the phonon-assisted energy transfer, which occurs when there is a difference E between the transition energies of the donor and the acceptor, and is compensated by either a phonon emission or absorption.
ii. ***Spectral diffusion***—in this case, the excited ion can give its energy to other ions that are at different sites and/or lattice environment, due to the fact that the doping ions stay at a slightly different lattice environment. This will translate to a shift in the emission spectrum to longer wavelengths and an increment on the width of the emission peak.
iii. ***Energy donation***—in this case, the energy transfer can occur between different ions, one of them is called a donor and the other an acceptor. An ion at an excited higher energy level can transfer most of its energy to other ions. The other ions stay at a lower energy levels and release the differential energy in the form of phonons.
iv. ***Sensitizer's transfer***—a donor that usually has a strong absorption of external radiation and transfers it very efficiently to an acceptor is called a sensitizer; the caused emission is greatly enhanced. This process is also known as sensitization of the luminescence.
v. ***Quenching centers transfer***—in this case, the acceptor kills the emission of the active center or the donating ions, and these ions neither emit at the required wavelength nor emit at all. Mostly, the phosphors that exhibit this type of luminescence are activated by sensitizers or co-activators (i.e. Mn^{2+}).

It is important to determine the optimum concentration of dopant to be used, in order to obtain efficient luminescence with a minimum energy loss. For display application, the purity of color is the most important issue. For many ions emissions can be from different upper excited states. The way to keep this emission from the upper states from occurring, and to purify the luminescence is to quench the emission via cross relaxation [19]. In this process, the excited ions from the upper states prefer to release part of their energy to the neighboring ions at the ground state, and then move to the lowest metastable state. Then these ions will return to the ground state and release the remaining energy at the desire wavelength. In order to be able to do this, the doping concentration should be sufficiently high, but it is important to note that in a heavily doped system the average distance between the ions becomes smaller, and therefore the excited ions can move around in the host causing resonant energy transfer. Such transfer gives more chance to send the excitation to a quenching center, which will release the energy through a nonradiative process. This phenomenon is called concentration quenching, as we briefly described earlier. A compromise concentration should then be determined and this will give an efficient sensitization (efficient upper-state quenching) and a maximization of the number of activators to participate in the luminescence process. However, the concentration should not lead to any concentration quenching. These centers also can produce an undesired afterglow [20]. The sensitization is used to enhance the energy excitation efficiency.

In rare earth phosphors, when UV or VUV radiations populate optically a 5*d*-state, radiative and/or nonradiative channels are available for energy relaxation in the solid state. Energy transfer to the emitting 4*f*-level occurs through lattice phonon relaxation and intra-system energy crossing when the energies match. The efficiency of the latter process depends upon the magnitude of the square overlap integrals between absorption and emission. Following the well-known configuration coordinate model, coordinate displacement between the equilibrium positions of the ground and 5*d* excited states, called the Franck–Condon shift, can be adjusted in phosphor design by choosing suitable host anionic groupings in order to fix the emission frequency or to increase the phosphor efficiency. It is worthwhile considering that the variation of the energy of the lowest 4*f*–5*d* level versus the number of *f*-electrons in the shell follows the variation of 3+/4+ redox potential along the lanthanide series. It is related to the ability of the trivalent rare earth ion to lose one electron, and consequently to the stabilization energy of the 4+ state. In large band gap materials, the energy levels of the impurity center are sparsely distributed between the valence and conduction bands. This is especially true for trivalent rare earth ions

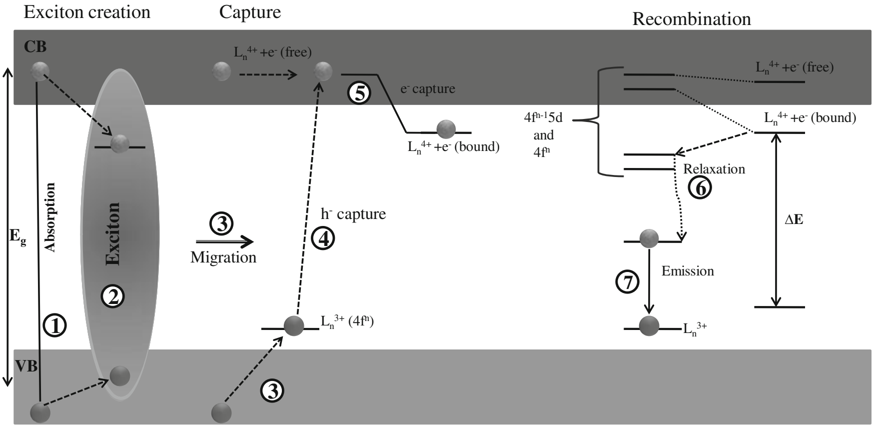

Fig. 2.7 Energy scheme of exciton and free charge carriers recombination on rare earth impurity involving the autoionization states

with discrete quasi-atomic states displayed within the large forbidden band gap of insulators (Fig. 2.7). In the combined host + rare earth impurity system, the VUV absorption can promote one electron from the ground state of the rare earth ion to excited 5*d*-states that overlap energetically the conduction band of the host. In the case of a strong coupling between these 5*d*-states and the continuum of the solid, the electron can be completely delocalized in the conduction band and the autoionization process of the rare earth ion occurs, giving rise to the $(\mathrm{Ln}^{3+} + h^{+}) + e^{-}$ (free) state. The capture of the free-electron interpreted in the frame of the model of the exciton trapped on the impurity center as $(\mathrm{Ln}^{3+} + h^{+}) + e^{-}$ (bounded) state, results in energy emission that corresponds to the excess of the exciton recombination energy. Part of this energy can be transferred to the 4*f* emitting level through; for example, dipole–dipole interaction in the case of allowed transitions or higher order multipole interactions for the quasi-forbidden ones.

The propensity of the rare earth ion to give up one electron should be regarded as its hole acceptor capability. It means that these ions embedded in a solid will develop a more or less intense short range potential for hole attraction depending upon the stabilization energy of the 4+ state. This is the case for Ce^{3+} and Tb^{3+} with one more *f*-electron than respectively the empty and half shell.

References

1. J. Reichman, *Handbook of Optical Filters for Fluorescence Microscopy* (Chroma Technology, Brattleboro, 2010)
2. C. Ronda, *Luminescence From Theory to Applications* (Wiley-VCH, New York, 2008)
3. I. Parreu, J.J. Carvajal, X. Solans, F. Díaz, M. Aguiló, Chem. Mater. **18**, 221 (2006)
4. I. Parreu, R. Solé, J. Gavaldá, J. Massons, F. Díaz, M. Aguiló, Chem. Mater. **15**, 5059 (2003)
5. P. Bamfield, M.G. Hutchings, *Chromic Phenomena Technological Applications of Colour Chemistry*, 2nd edn. (The Royal Society of Chemistry, Cambridge, 2010)
6. R.S. Meltzer, S.P. Feofilov, J. Lumin. **102**, 151 (2003)
7. G. Blasse, B.C. Grabmaier, *Luminescent Materials*, vol. 34 (Springer, Berlin, 1994), p. 35
8. K.A. Gschneidner Jr., L. Eyring, *Handbook on the Physics and Chemistry of Rare Earths* (Elsevier Science, Amsterdam, 1987)
9. R. Reisfeld, Struct. Bond. **30**, 65 (1976)
10. L. Strekowski (ed.), *Heterocyclic Polymethine Dyes*, Topics in Heterocyclic Chemistry (Springer, Berlin, 2008), p. 14
11. J.S. Kim, E.S. Oh, J.C. Choi, M. Lee, J.H. Bahng, H.L. Park, T.W. Kim, Int. J. Inorg. Mater. **3**, 183 (2001)
12. M.-G. Ko, J.-C. Park, D.-K. Kim, S.-H. Byeon, J. Lumin. **104**, 215 (2003)
13. M. Leskela, L. Niinisto, Mater. Chem. Phys. **31**, 7 (1992)
14. Sony's OLED display (2005), p. 1
15. B. Henderson, G.F. Imbusch, *Optical Spectroscopy of Inorganic Solids* (Oxford University Press, Oxford, 1989), p. 645
16. O.J. Rubio. J. Phys. Chem. Solids. **52**(1), 101 (1991)
17. G. Blasse, B.C. Brabmaimer, *Luminescence Materials* (Springle, New York, 1994), p. 108
18. P. Goldberg, *Luminescence of Inorganic Solids* (Academy Press, New York, 1966), p. 765
19. E. Nakazawa, S. Shionoya, J. Phys. Soc. Jpn. **28**, 1260 (1970)
20. D. Jia, W. Jia, D.R. Evans, W.M. Dennos, H. Liu, J. Zhu, W.M. Yen, J. App. Phys. **88**(6), 3402 (2000)

Chapter 3
Synthesis of Phosphate Phosphors

Phosphors exhibit a number of interesting size and surface dependent optical properties, which have stimulated an exponential development of material science and technology in the past era because the luminance properties, as well as morphological and structural characteristics, strongly depend on phosphors synthesis conditions. There is no rigid definition of what constitutes a suitable synthesis. The major criterion by which syntheses are judged is the potential value to the scientific community. An ideal synthesis is one that presents a new or revised experimental procedure applicable to a variety of related compounds, at least one of which is critically important in current research. However, syntheses of individual compounds that are of interest or importance are also acceptable. Syntheses of compounds that are readily available commercially at reasonable prices are not acceptable.

3.1 Sample Preparation Methods and Calculations

Looking at the chemical formula of most of the inorganic phosphors one may feel that the synthesis of the luminescent materials should be straightforward as the host materials are well-known [1]. However, in practice, the synthesis of the phosphors with desired characteristics can be quite tricky. The difficulties arise as one has to consider several aspects such as the incorporation of the activators at the desired sites, elimination of the unwanted impurities, specific grain size, and morphology suitable for the application, cost of production, batch homogeneity, and reproducibility, and so on. Many methods of preparation are listed in Table 3.1. All these methods are not used in the present study. Hence, methods which were used for the materials synthesized and described in this book are summarized in this chapter with full details later at the experimental synthesis part added at the beginning of each phosphor material reported later in this book.

K. N. Shinde et al., *Phosphate Phosphors for Solid-State Lighting*,
Springer Series in Materials Science 174, DOI: 10.1007/978-3-642-34312-4_3,

Table 3.1 A list of various methods for preparing the samples

Sr. No.	Technique	Method
1	Wet chemical	Co-precipitation, recrystallization
2	Solid state	Melting
		Solid-state diffusion
3	Novel synthesis	Molten salt
		Solvothermal method
		Sol–gel
		Hydrolytic sol–gel
		Nonhydrolytic sol–gel
		Pechini and citrate gel methods
		Polymer pyrolysis
		Spray pyrolysis and sonochemical
		Cryochemical synthesis (including freeze drying)
		Solid-state metathesis

3.2 Wet Chemical Method

Wet chemical synthesis is one of the simplest syntheses techniques currently available (also called the one-step synthesis) [2, 3]. Hence, the molecular motions and the chemical reactions may proceed very swiftly in the liquid state. Reactions of the type acid + base → salt often yield precipitate of the desired compound. Wet chemical synthesis is an ideal technique used for producing fine, chemically homogeneous, and pure, single-phase powders in the synthesized condition. This procedure is attractive because of its capacity to yield products at low temperatures in the range of only 80–120 °C. For preparing the nanocrystalline mixed phosphate phosphors by the wet chemical method and the constituents with stoichiometric ratios are dissolved in double-distilled deionized water (DDW), and then allowed to evaporate till the mixture becomes anhydrous. The evaporation was done at 80 °C for 8 h. The dried samples were then slowly cooled at room temperature. The resultant polycrystalline mass was crushed to fine particle in a crucible (See Fig. 3.1). The powder was used in the rest of the study. The one-step wet chemical synthesis is very simple, safe, energy saving, less time consuming, and can be easily exploited to prepare phosphors with enhanced optical properties. This synthesis technique has been extensively applied to the preparation of various materials. In the wet chemical methods the rare-earth dopant activators are uniformly distributed, but calcinations are required to get the fine crystalline structured powder phosphors. The wet chemical techniques are not suitable for the synthesis of complex oxide phosphors. For preparing the phosphate phosphors, the wet chemical method is used extensively. Constituent chlorides with stoichiometric ratios are dissolved in DDW in a glass beaker (Borosil) and are evaporated till the mixture becomes anhydrous. Use of chlorides as starting materials helps preventing the hydrolysis. The constituents may have vast differing melting points, and loss of one or more constituents during crystal growth is inevitable.

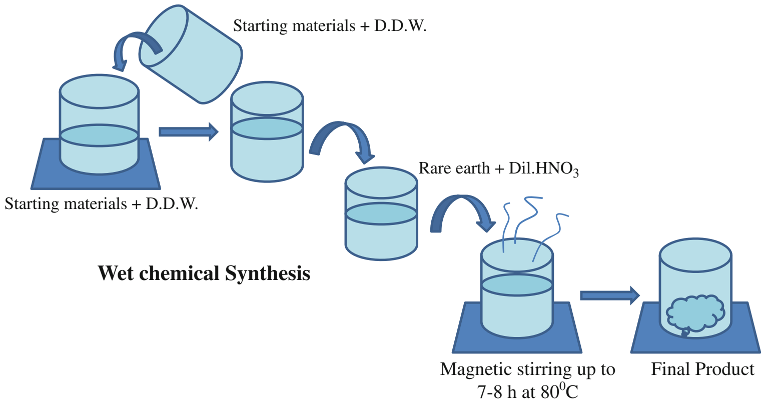

Fig. 3.1 Steps involving in wet chemical synthesis

Example: Calculation stoichiometric composition of $Li_2Sr_2Al_2PO_4F_9$:Eu_1 mol%

Quantity of **Host** in mol = **1-** Quantity of **Dopant** in mol => 1 − 0.01=0.99

Quantity of Reactants = M.W. × Mols in Reaction

Quantity of LiCl $= 42.40 \times 2 => 84.8$
Quantity of $SrCl_2.6H_2O$ $= 266.62 \times 2 \times 0.99 => 527.90$
Quantity of $Al(NO_3)_3.9H_2O$ $= 375.13 \times 2 => 750.26$
Quantity of $NH_4H_2PO_4$ $= 115.03$
Quantity of NH_4F $= 37.04 \times 9 => 333.36$
Quantity of Eu_2O_3 $= 351.90 \times 0.01 => 3.519$

But in practice the reactants are not taken in such big quantities. Therefore, a smaller amount in the same proportion (as calculation above) is taken. Thus,

If $\mathbf{SrCl_2}$ is **3 g** then, $$\frac{527.90}{3} = 175.96 \text{ (Dividing Factor)}$$

All quantities are divided by this factor.

Therefore, $LiCl = 84.8/175.96 = \mathbf{0.4819\,g}$
$Al(NO_3)_3 = 750.26/175.96 = \mathbf{4.2638\,g}$
$NH_4H_2PO_4 = 115.03/175.96 = \mathbf{0.6537\,g}$
$NH_4F = 333.36/175.96 = \mathbf{1.8945\,g}$
$Eu_2O_3 = 3.519/175.96 = \mathbf{0.019\,g}$

The nanocrystalline complex fluorides halophosphate phosphors are prepared by the wet chemical method. For example, the $Li_2Sr_2Al_2PO_4F_9$ phosphors were prepared by the wet chemical method. LiCl, $SrCl_2.6H_2O$, $Al(NO_3)_3.9H_2O$, NH_4H_2

PO_4, and NH_4F of AR grade were taken in a stoichiometric ratio and dissolved separately in DDW, resulting in a solution of $Li_2Sr_2Al_2PO_4F_9$. In the present investigation, materials were prepared according to the chemical formula $Li_2Sr_{2-x}Al_2PO_4F_9$: Eu_x.Eu_2O_3 soluble in dil. HNO_3 was then added to the solution to obtain $Li_2Sr_2Al_2PO_4F_9$:Eu^{2+}. In this formula, x-value indicates the concentration of impurity in mol%. The solution of reagents was mixed together to obtain a homogeneous solution. The molar ratio of Eu (RE) ion was changed in relation to the $Li_2Sr_2Al_2PO_4F_9$ phosphor. The compositions of the reagents were calculated using the total oxidizing and reducing valences of the components, which served as the numerical coefficients, so that the equivalent ratio is unity. It is confirmed that no undissolved constituents were left behind and all the chemicals had completely dissolved in water. The compounds $Li_2Sr_2Al_2PO_4F_9$:Eu^{2+} in their powder form were obtained by evaporating at 120 °C for 8 h. The dried samples were then slowly cooled to room temperature. The resultant nanocrystalline powder was crushed to fine particles in a crucible. The powder was used in the rest of the study. This method has advantage using a simple experimental procedure and chemicals that are easily available, nontoxic, and easily handled at ambient conditions of humidity and pressure. Same method of synthesis was used for preparation of Eu, Dy, and Ce-activated $Li_2Sr_2Al_2PO_4F_9$, $Na_2Sr_2Al_2PO_4F_9$, $Li_2Sr_2Al_2PO_4Cl_9$, and $Na_2Sr_2Al_2PO_4Cl_9$ phosphors.

3.3 Solid-State Diffusion

In solid-state diffusion (SSD), the constituents are made to react through the diffusion process. The temperature is maintained just enough to have adequate diffusion to complete the reaction on time without melting the constituents. Reaction time and the temperature bear a reciprocal relation. It may not always be possible to lower the latter sufficiently, e.g., several phosphates cannot be formed even by the SSD at the temperatures below 1,000 °C.

The lamps and LEDs are coated with phosphor by using a rearrangement of phosphor powder particles. A lamp phosphor is, therefore, needed as a powder. Conventional synthesis of lamp phosphors requires temperature greater than 1,000 °C. Thus, corresponding metal oxides/carbonates are grounded well and heated $>$ 1,000 °C (See Fig. 3.2). The mechanism of solid-state reactions is diffusion control, and hence repeated grinding and repeated heating are required. A controlled atmosphere is necessary to master the valence of the activator and the stoichiometry of the host lattice. Therefore, doping of the activator in the oxide host has been delicate. There are some drawbacks of this conventional method ,i.e, formation of the final product is inhomogeneous, formation of large particles (in micrometer range) with low surface area, and hence mechanical particle size reduction is required, which introduces impurity and defects and presence of defects, which are harmful to luminescence.

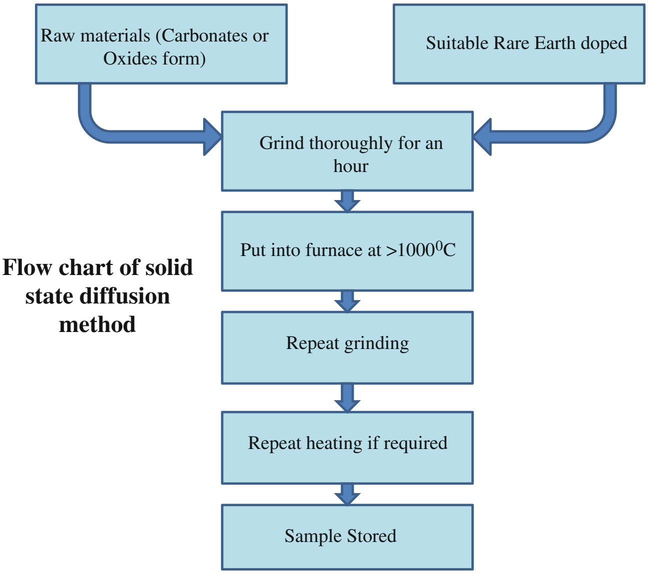

Fig. 3.2 Flow chart of SSD method

Example: Synthesis of $Na_2Zn_5(PO_4)_4$:Eu Using Solid-State Diffusion

For this stoichiometric composition, the metal carbonate and ammonium dihydrogen phosphate were calculated using the total oxidizing and reducing valences of the components.

The proposed chemical reaction of Na_2Zn_5 $(PO_4)_4$: Eu phosphor is:

$$\begin{aligned} &\mathbf{10\,ZnO + 2\,Na_2CO_3 + 8\,NH_4H_2PO_4} \\ &\quad \mathbf{\rightarrow 2\,Na_2Zn_5(PO_4)_4 + 12\,H_2O + 2\,CO_2 + 6\,NH_4 + N_2} \end{aligned}$$

The Eu doped $Na_2Zn_5(PO_4)_4$ phosphate-based phosphor was synthesized by SSD. The analytical grade pure materials ZnO, Na_2CO_3 and $NH_4H_2PO_4$ were used as starting materials. These materials were weighed in the proper molar ratio then Eu_2O_3 was introduced as a dopant, mixed, and ground homogeneously in an agate mortar. The mixture was heated to 1,000 °C in a silica crucible and kept at this temperature for 2 h, in order to allow ammonia, water, and nitrogen oxide to evaporate. The mixture was crushed once again and the powder was heated at 800 °C for 24 h, thereby obtaining the white phosphor powders.

3.3.1 *Novel Synthesis*

During the recent years, several methods have been used for simplifying the phosphor synthesis. These may broadly be called as ‘Novel Synthesis’. The novel syntheses not only provide simpler methods for phosphor preparation but also often provide the control over particle size and morphology. Some of the novel syntheses have been listed in Table 3.1. In this study, the combustion synthesis has been used quite frequently, and hence it is described in detail in the following section.

3.4 Combustion Synthesis

Combustion method is yet another chemical route method which does not require further calcinations and repeated heating. This method was accidentally discovered in 1988 in Prof. Patil's lab, India. It is an exothermic reaction and occurs with the evolution of heat and light. Such a high temperature leads to the formation and crystallization of phosphor materials. For any combustion, fuel and oxidizer are required. When the mixture of fuel and oxidizer is ignited, combustion takes place. For the combustion synthesis of oxides, metal nitrates are used as oxidizer, and fuels employed are hydrazine-based compounds or urea or glycine (see Fig. 3.3). Stoichiometric compositions of metal nitrates and fuels are calculated based on propellant chemistry (Table 3.2). Thus, maximum heat generated in combustion synthesis [4]. There are some advantages to this method i.e., the generation of high reaction temperature which can volatilize low boiling point impurities, and therefore results in higher purity products, the simple exothermic nature of the self-propagating high temperature and the short exothermic reaction time result in low operating and processing costs,and the larger amount of gas evolved during combustion results in a porous product in which the agglomerates formed are so weak that they can be easily crushed and ground into a fine powder.

In most of the novel methods, lower reaction temperatures are achieved by obtaining the reactants in a fine form. An ingenious way of lowering the operating temperature is to use the heat generated in exothermic chemical reaction itself for the synthesis. These may be broadly called as self heat generating synthesis (SHGS). The most obvious advantage of the method is that the heat is not supplied 'without' but 'within' (except for that needed to initiate the reaction), which eliminates the use of refractory muffles, insulators, and crucible materials.

One of the earliest discovered SHGS was self-heat propagating synthesis. In this process, the reactants are thoroughly mixed and pressed to form a bar. One end of the bar is heated to high temperature using some sort of flame. Once the exothermic reaction starts, it propagates across the length of the bar. Temperatures as high as 7,000 °C have been obtained in such reactions to produce nitride and carbide materials (Table 3.2).

Later, volumetric SHGS termed as combustion synthesis was introduced. Exothermic reactions between metal nitrates and fuels such as urea are exploited in the combustion synthesis. Nitrate to fuel ratio can be adjusted to vary the temperature generated. Highest temperatures are attained when this ratio is such that the oxidizing and reducing valences of the oxidizers and fuel are balanced.

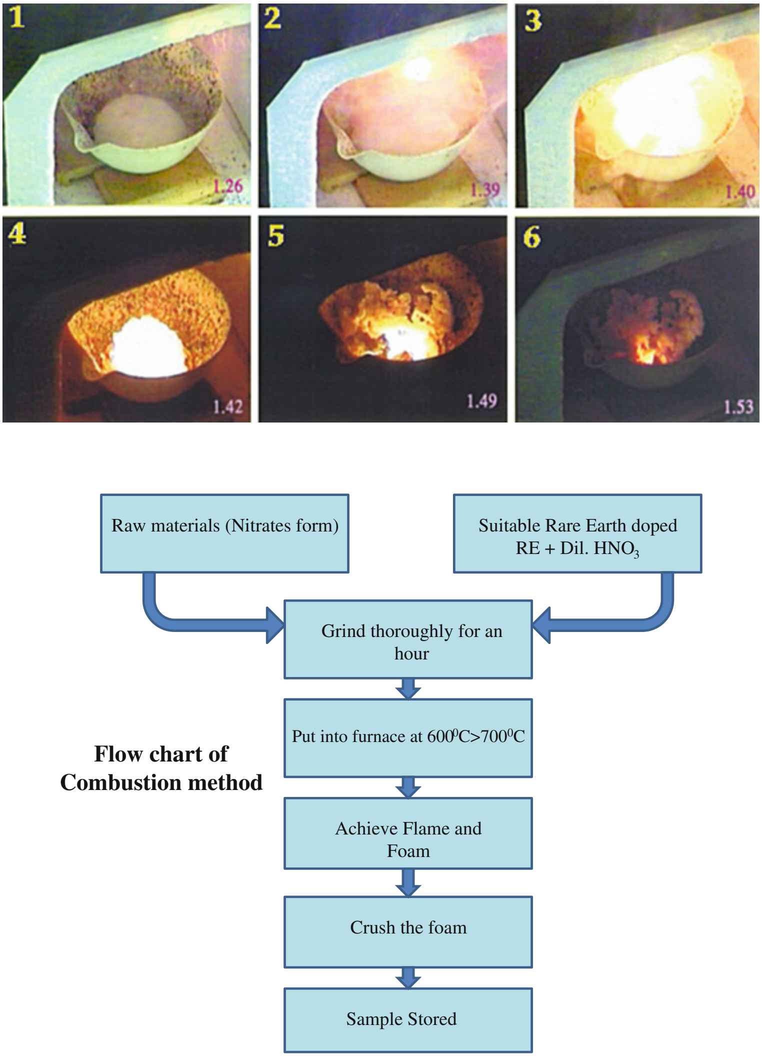

Fig. 3.3 Real images during combustion synthesis and Flow chart of combustion method

In the reaction between metal nitrates and urea-

For monovalent metal-

Oxidizer $M(NO_3)$ $\quad M(1) + O3(-6) = -5$

Fuel Urea NH_2CONH_2 $\quad H(4 \times 1) + C(4) + (O^{-2}) = 6$

Hence, mol ratio of MNO_3:urea is 5:6, so that the oxidizing and reducing valences are balanced. For divalent and trivalent nitrates the corresponding ratios will be 10:6 and 15:6, respectively.

Table 3.2 Fuels used in combustion synthesis

Fuel	Formula	Valences
Urea	NH_2CONH_2	6
Tetraformal trisazine (TFTA)	$C_4H_{16}N_6O_2$	28
Carbohydrazide (CH)	CH_6N_4O	8
Glycine	$C_2H_5NO_2$	7
Malonodihydrazide (MDH)	$C_3H_8N_4O_2$	16
3methyl pyrazole-5 one (3MP5O)	$C_4H_6N_2O$	20
Dofirmyl hydrazine	$C_2H_4N_2O_2$	8

Example: Synthesis of $M_5(PO_4)_3F$:Eu (where M=Ca/Ba/Sr) Using Combustion Synthesis

For this, stoichiometric composition of the metal nitrates (oxidizers) and urea (fuel) was calculated using the total oxidizing and reducing valences of the components which serve as the numerical coefficients, so that the equivalence ratio is unity and the heat liberated during combustion is maximum.

First, we had calculated the amount of urea (fuel) required for this composition,

The valences are taken as, Sr = +2, P = +5, Eu = +3.
Amount of urea required for $Sr_5(PO_4)_3F:Eu_{0.5}$ can be calculated as under below
$Sr(NO_3)_2$ is the divalent oxidizer
$NH_4H_2(PO_4)$ is the pentavalent oxidizer
NH_4F is the monovalent oxidizer
Eu_2O_3 is the trivalent oxidizer
Oxidizing Valence of $Eu_2O_3 = 15/6$

Oxidizing Valence of $Sr(NO_3)_2 = 5 \times 10/6$
Oxidizing Valence of $NH_4H_2(PO_4) = 3 \times 25/6$
Oxidizing Valence of $NH_4F = 5/6$

Amount of net valence Urea required as

$$= 15/6 + 5 \times 10/6 + 3 \times 25/6 + 5/6 = 145/6 = 24.1666$$

Eu_2O_3 (99.90 %, Sigma chem.) was dissolved individually in dil. HNO_3 (5m % s.d. fine chem.) and evaporated until dry, so as to convert them into respective nitrates. The proposed chemical reaction is-

$$\begin{aligned} &15\,Sr(NO_3)_2 + 9\,NH_4H_2PO_4 + 24.16\,NH_2CONH_2 + 3\,NH_4F \\ &\quad \rightarrow 3\,Sr_5(PO_4)_3F + 40\,N_2 + 19\,CO_2 + 71\,H_2O \end{aligned}$$

The starting AR grade materials (99.99 % purity) taken were strontium nitrate ($Sr(NO_3)_2$), di-ammonium hydrogen phosphate ($NH_4H_2PO_4$), ammonium fluoride (NH_4F), and europium oxide (Eu_2O_3). Urea (NH_2CONH_2) was used as fuel for combustion. The materials were prepared according to the chemical formula $Sr_{(5-x)}(PO_4)_3F{:}Eu_x$. The mixture of reagents was crushed together to obtain a homogeneous powder. Eu^{3+} ion was introduced in the form of $Eu(NO_3)_3$ solution by dissolving Eu_2O_3 in HNO_3 solution. The compositions of the metal nitrates (oxidizers) and urea (fuel) were calculated using the total oxidizing and reducing valences of the components, which served as numerical coefficients, so that the equivalent ratio is unity and the maximum heat is liberated during combustion. After stirring for about 15 min, precursor solution was transferred to a furnace preheated to 500–600 °C and the porous products were obtained. Large amounts of escaping gases dissipate heat and prevent the material from sintering, and thus provide conditions for formation of crystalline phase. The molar ratio of europium rare-earth ion was changed in relation to $Ba_5(PO_4)_3F$, $Sr_5(PO_4)_3F$ and $Ca_5(PO_4)_3F$ phosphor.

All the above-mentioned chemicals were weighed on digital (METLLAR Toledo made) balance. First of all Eu_2O_3 is converted into $Eu(NO_3)_3$ by mixing Eu_2O_3 into 2 ml of dil. HNO_3. Then weighed quantities of each nitrate and urea were mixed together and crushed in mortar for 1h to form a thick paste. The resulting paste is transferred to a China crucible ($3''$ J brand) and introduced into a vertical cylindrical muffle furnace (35 cm height and 20 cm diameter) maintained at $500 \pm 10\,°C$, Fig. 3.3. The mixture underwent dehydration and then decomposition with liberation of NH_3 and NO_2. The process being highly exothermic continued and the liberated gases swollen the mixture into large volume. Large exothermicity resulted into a flame changing the mixture into gaseous phase. Flame temperature as high as 1,400–1,600 °C converted the vapour phase oxides into mixed aluminates. The flame persisted for $\approx$30 s. The crucible was then taken out of the furnace and the foamy product was crushed into a fine powder. The flow chart of the process is shown in Fig. 3.3.

3.5 Sol–Gel Synthesis

The sol–gel process involves the evolution of inorganic networks through the formation of a colloidal suspension (**sol**) and gelation of the sol to form a network in a continuous liquid phase (**gel**). The precursors for synthesizing these colloids consist usually a metal or metalloid element surrounded by various reactive ligands. The starting material is processed to form a dispersible oxide and forms a sol in contact with water or dilute acid. Removal of the liquid from the sol yields the gel, and the sol–gel transition controls the particle size and shape. Calcination of the gel produces the oxide. Sol–gel processing refers to the hydrolysis and condensation of alkoxide-based precursors such as Si(OEt) 4 (tetraethyl orthosilicate or TEOS). The reactions involved in the sol–gel chemistry are based on the hydrolysis and condensation of metal alkoxides M(OR)**z** can be described as follows:

$$MOR + H_2O \rightarrow MOH + ROH \text{ (hydrolysis)}$$

$$MOH + ROM \rightarrow M\text{-}O\text{-}M + ROH \text{ (condensation)}$$

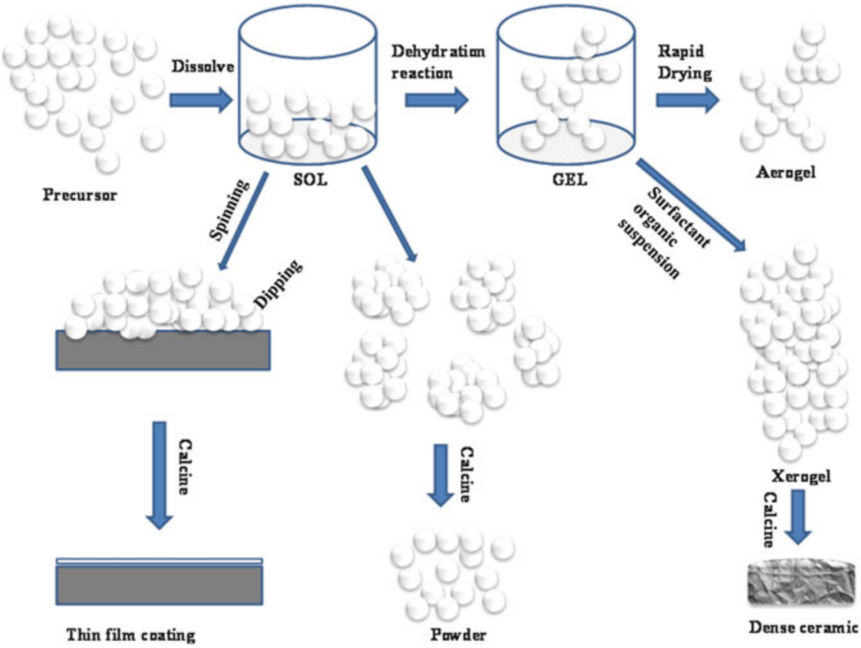

Fig. 3.4 Steps involve in sol–gel method

Sol–gel method of synthesizing nanomaterials is very popular among chemists and is widely employed to prepare oxide materials. The sol–gel process can be characterized by a series of distinct steps (see Fig. 3.4).

1. Formation of different stable solutions of the alkoxide or solvated metal precursor.
2. Gelation resulting from the formation of an oxide- or alcohol-bridged network (the gel) by a polycondensation reaction that results in a dramatic increase in the viscocity of the solution.
3. Aging of the gel (Syneresis), during which the polycondensation reactions continue until the gel transforms into a solid mass, accompanied by contraction of the gel network and expulsion of solvent from gel pores. Ostwald ripening (also referred to as coarsening, is the phenomenon by which smaller particles are consumed by larger particles during the growth process) and phase transformations may occur concurrently with syneresis. The aging process of gels can exceed 7 days and is critical in the prevention of cracks in gels that have been cast.
4. Drying of the gel, when water and other volatile liquids are removed from the gel network. This process is complicated due to fundamental changes in the structure of the gel. The drying process itself has been broken into four distinct steps: (i) the constant rate period, (ii) the critical point, (iii) the falling rate

period, and (iv) the second falling rate period. If isolated by thermal evaporation, the resulting monolith is termed a *xerogel*. If the solvent (such as water) is extracted under supercritical or near supercritical conditions, the product is an *aerogel*.

5. Dehydration, during which surface-bound M–OH groups are removed, there by stabilizing the gel against rehydration. This is normally achieved by calcining the monolith at temperatures up to 800 °C.
6. Densification and decomposition of the gels at high temperatures ($T > 800\,^{\circ}C$). The pores of the gel network are collapsed, and remaining organic species are volatilized. The typical steps that are involved in sol–gel processing are shown in the schematic diagram below (Fig. 3.4).

The interest in this synthesis method arises due to the possibility of synthesizing nonmetallic inorganic materials like glasses, glass ceramics, or ceramic materials at very low temperatures compared to the high temperature process required by melting glass or firing ceramics. The major difficulties to overcome in developing a successful bottom-up approach are controlling the growth of the particles, and then stopping the newly formed particles from agglomerating. Other technical issues are ensuring that the reactions are complete, so that no unwanted reactant is left on the product and completely remove any growth aids that might have been used in the process. Also production rates of nanopowders are very low by this process. The main advantage is that monosized-nano particles may be obtained by any bottom up approach.

The sol–gel method exhibits several advantages over classical processing, stemming primarily from the fact that the initial system begins as a liquid mixture,and subsequently forms a SiO_2 network upon standing [5–7]. This means that the high purity and homogeneity can be achieved and the processing can be done at room temperature. The sol–gel synthesis was used for the synthesis of silicates [8, 9] using the tetraethoxysilane (TEOS) as the source of silica and the metal nitrates/oxides. This sol–gel process is widely used for oxide materials which are by far the mostly used materials in phosphor technology. Nowadays, there is a tremendous effort to understand and control materials on a nanometric scale. Research directed toward luminescent materials and in particular phosphors does not escape to this tendency. The goal is to control phosphor structure and morphology at a nanoscopic level to tailor its macroscopic properties such as emission spectrum or luminous efficiency. Another objective is to master the shape of the final material either from a granulometric point of view or in the view of producing thin films. In effect, the macroscopic properties of phosphors, luminous efficiency for instance, are strongly dependant on the morphology of the material. The sol–gel synthesis of inorganic materials gives a procedure to obtain good quality optical materials. Due to these advantages, such as low temperature processing, easy shaping, higher sample homogeneity and purity, etc., different matrices are now investigated as potential matrices for rare-earth luminescence.

The metal alkoxide, TEOS, $Si(OC_2H_5)$ was dissolved in an ethanol (C_2H_5OH) to obtain a homogeneous reaction mixture. To this the stoichiometric amount (100 wt%) of DDW (H_2O) was added to hydrolyze the alkoxy functionalities present in the reaction mixture. The alcohol is not simply a solvent; it can participate in esterification or alcoholysis reaction. As water is produced as the by-product of the condensation reaction, Si to H_2O ratio of 1:4 is sufficient for complete hydrolysis and condensation. The ethanol to TEOS ratio is 1:3. Few drops of 0.01 M HCl, work as a catalyst. This solution was stirred with the magnetic stirrer continuously for 2 h (Sol A).

The metal alkoxide first undergoes hydrolysis reaction in which the alkoxide group (OR) is replaced with hydroxyl groups (OH). The silanol (SiOH) then undergoes self-condensation to produce polymeric silica (Si–O–Si) plus the corresponding alcohol or water as indicated in the following reaction [10].

$$\mathrm{Si(OR)_4 + H_2O = (HO)Si(OR)_3 + ROH}$$
$$\mathrm{(OH)Si(OR)_3 + H_2O = (HO)_2Si(OR)_2 + ROH}$$
$$\mathrm{(OH)_2Si(OR)_2 + H_2O = (HO)_3Si(OR) + ROH}$$

Alcohol condensation (Alcoxolation):

$$\underline{\equiv}\,\mathrm{Si{-}OR + HO{-}Si}\,\underline{\equiv} \quad = \quad \underline{\equiv}\,\mathrm{Si{-}O{-}Si}\,\underline{\equiv} + \mathrm{ROH}$$

Water condensation Oxolation:

$$\underline{\equiv}\,\mathrm{Si{-}OH + HO{-}Si}\,\underline{\equiv} \quad = \quad \underline{\equiv}\,\mathrm{Si{-}O{-}Si}\,\underline{\equiv} + \mathrm{HOH}$$

The stoichiometric amount of metal nitrates/oxides was dissolved in 3M nitric acid (HNO_3), and subsequently mixed with ethanol (C_2H_5OH) to form a transparent mixture (Sol B). The two solutions were then slowly mixed under constant stirring. After rigorous stirring the ammonia water (NH_4OH) was added. The gel was dried, heated for 2 h at 200, 300, 500, 700, and 1000 °C. The resultant products were white and crystalline. The flow chart of the steps for sol–gel synthesis is shown in the Fig. 3.5.

Traditionally, phosphor films are generally deposited by using the sputtering technique, and only in recent decades the sol–gel method has been considered as a low cost alternative approach for the preparation of novel nanostructured materials including luminescent powders and films. The sol–gel process refers broadly to the room temperature solution routes for preparing oxide materials. The solutions of precursors are reacted to form the irreversible gels that dry and shrink to rigid oxide glasses and powders. The sol–gel route presents a lot of advantages: low-temperature synthesis, possible formation of powders with uniform grain morphology, and achievement of homogeneous multicomponent films. An advantage in using the nanocrystalline phosphors is that nonradiative transition could significantly be controlled with a decrease in the crystal grain size.

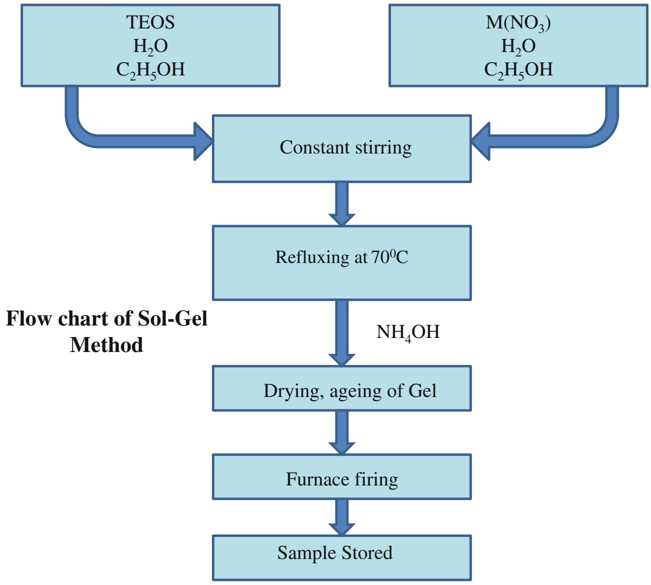

Fig. 3.5 Flow chart of sol–gel method

3.6 Microwave Assisted Synthesis

It was known that the sintering treatment is an important factor for controlling size and crystalline. Microwave-assisted sintering is a novel synthesis method in the rapidly developed research field. It has been reported that microwave-assisted sintering consumes less energy and reduces the activation energy, thus lowering the sintering temperatures of the phosphors, as compared with conventional sintering treatments. Even some phosphors prepared by microwave-assisted sintering have been reported in recent years [11–14]. In a microwave synthesis, sources are heated over the whole sample quickly and uniformly, because microwave energy is immediately absorbed by the sample (Fig. 3.6). Therefore, microwave heating techniques have a significant advantage of reduction in manufacturing costs, i.e, energy saving and shorter processing time. In addition, it is possible to heat a particular component in the mixtures. There are several advantages in microwave heating compared with conventional heating techniques, in view of potentials for (1) energy saving and shorter processing time, (2) improved product uniformity and yields, (3) improved or unique microstructures and properties, and (4) synthesis of new materials.

Firing is a necessary step for solid-state phosphor synthesis since activation energy must be supplied for the activators to go into the crystal structure of the host material. By solid-state reaction, conventional synthesis of phosphors takes many hours even

Fig. 3.6 Microwave oven for synthesis of phosphor

in the presence of a flux. Microwave processing is a relatively new technique and characterized by substantially accelerated reaction kinetics in the material systems if properly chosen. Using microwave processing, various phosphors have been synthesized. The high efficiency phosphors developed for field emission displays, plasma displays, and white light emitting diodes (LED) tend to be degraded by the operating environment and/or the devices' manufacturing conditions. The temperature of the sample was monitored with an optical pyrometer. The temperature was controlled by adjusting the input power. During the microwave processing, the sample was rotating horizontally about the axis. The samples were microwave heated up and held at the designed temperatures for typically 10–20 min. The microwave-synthesized products were characterized for particle size, brightness, phase composition, morphology, luminescence emission, and color coordinates. Optimization of the parameters is required to achieve desired properties [15].

3.7 Effect of Temperature

3.7.1 Some Definitions Concerning Temperature

(a) **Calcination** is a thermal treatment process in the presence of air applied to ores and other solid materials to bring about a thermal decomposition, phase transition, or removal of a volatile fraction. The calcination process normally takes place at temperatures below the melting point of the product materials.

(b) **Sintering** is a method used to create objects from powders. It is based on atomic diffusion. Diffusion occurs in any material above absolute zero, but it occurs much faster at higher temperatures. In most sintering processes, the powdered material is held in a mold, and then heated to a temperature below the melting point. The atoms in the powder particles diffuse across the boundaries of the particles, fusing the particles together and creating one solid piece. Because the sintering temperature does not have to reach the melting point of the material, sintering is often chosen as the shaping process for materials with extremely high melting points such as tungsten.

(c) **Annealing** is a heat treatment wherein a material is altered, causing changes in its properties such as hardness and ductility. It is a process that produces conditions by heating to above the critical temperature, maintaining a suitable temperature, and then cooling.

(d) **Quenching** is the rapid cooling of a workpiece to obtain certain material properties. It prevents low-temperature processes, such as phase transformations, from occurring by only providing a narrow window of time in which the reaction is both thermodynamically favorable and kinetically accessible. For instance, it can reduce crystallinity and thereby increase toughness of materials.

Sintering is conventionally used for developed ceramic substance and has also found uses in such fields as powder metallurgy and synthesis of rare-earth doped luminescence phosphors [16]. The source of power for solid-state processes is the change in free or chemical potential energy between the neck and the surface of the particle. This energy creates a transfer of material through the fastest means possible; if transfer were to take place from the particle volume or the grain boundary between particles, then there would be particle reduction and pore destruction. The pore elimination occurs faster for a trial with many pores of uniform size and higher porosity where the boundary diffusion distance is smaller. Control of temperature is very significant for sintering the process, since grain-boundary diffusion and volume diffusion rely heavily upon temperature, the size and distribution of particles of the material, the materials composition, and often the sintering environment to be controlled. Through diffusion and other mass transport mechanisms, materials from the particles are carried to the necks (Fig. 3.7), allowing them to grow as the particle bonding enters the *intermediate stage*. The intermediate stage of bonding is characterized by the pores beginning to round. As the mass transport continues, the pores will become even more rounded and some will appear to be isolated away from the grain boundaries of the particles. This is referred to as the *final stage* of bonding [16].

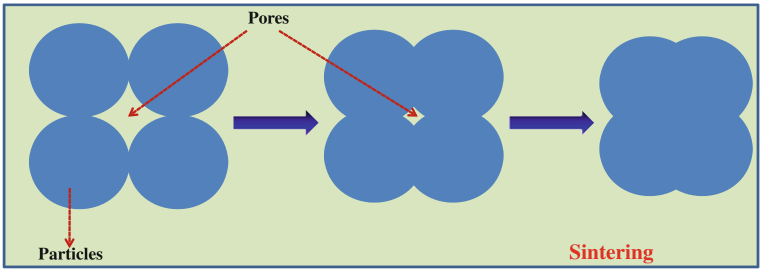

Fig. 3.7 Steps involving in sintering process

The last step of the sintering process is to cool the bonded compact to a temperature at which it can be handled. This cooling is performed in an atmosphere that is no longer required to chemically react with the compact. The atmosphere in this stage of the process aids in the transport of the heat away from the compact and minimizes the reoxidation of the compact during cooling. Luminescence phosphors owe their practical importance to their property of absorbing incident energy and converting it into visible radiations. This phenomenon, known as luminescence, is driven by electronic processes in the material due to the presence of trapping levels created by the presence of impurity atoms or lattice defects. *Solid-state diffusion* (SSD) reaction is the most popular method used in the synthesis of commercial luminescence phosphors as it is easily reproducible and amenable to large-scale production. The products obtained yield high luminescence efficiency. However, SSD has some disadvantages, such as (1) process complexity and energy consuming (firing at high temperature, repetitive heat treatment, milling, and sieving), (2) inhomogeneous mixing and contamination by impurities, and (3) product with irregularly shaped and aggregated particles unsuitable for screen brightness and high resolution. Deagglomeration of sintered phosphor chunks is quite cumbersome involving crushing, milling, sieving, and so on. As a result, many attempts have been carried out to find alternative methods for the preparation of phosphors. Superior display performance requires improvement in phosphors particle characteristics such as grain morphology and particle size on the luminescent intensity, efficiency, and resolution. Powders with optimal properties are obtained by different methods such as *chemical precipitation, the sol–gel, solution combustion, plasma chemical, hydrothermal, spray pyrolysis, microwave*, and so on. However, in most cases, high temperature sintering of samples prepared by these methods was often found to be essential as it increased their luminescence efficiencies due to improved crystallization and optimal incorporation of dopants in the host crystals.

References

1. J.P. Fackler, Jr., *Inorganic Syntheses*, vol. 21 (Wiley, Hoboken, 1982)
2. F. Wang, X. Fan, D. Pi, M. Wang, Solid State Commun. **133**, 775 (2005)
3. C. Pandey, J.K. Bhasin, S.M. Dhopte, P.L. Muthal, S.V. Moharil, Mater. Chem. Phys. **115**, 804 (2009)
4. S. Ekambaram, K.C. Patil, M. Maaza, J. Alloy. Compd. **393**, 81 (2005)
5. J.C. Brinker, G.W. Scherer, *Sol-Gel Science, The Physics and Chemistry of Sol-Gel Processing* (Academic press, New York, 1990)
6. L.L. Hench, J.K. West, Chem. Rev. **90**, 33 (1990)
7. J. Livage, C. Sanchez, J. Non-Cryst. Solids **145**, 11 (1990)
8. M. Stiebler, J. Reichardt, R. Hirrle, S. Kemmler-Sack, Phys. Status Solidi A **119**, 317 (1990)
9. J. Lin, D.U. Sanger, M. Mennig, K. Barner, Mater. Sci. Eng. B **64**, 73 (1999)
10. D.E. Rodrigues, B.G. Risch, G.L. Wilkes, Chem. Mater. **9**, 2709 (1997)
11. L. Zhang, X. Zhou, H. Zeng, H. Zeng, X. Dong, Mater. Lett. **62**, 2539 (2008)
12. E. Sirres, D.D. Rego, J. Mater. Process. Tech. **48**, 619 (1995)

13. K. Uematsu, K. Toda, M. Sato, J. Alloy. Compd. **389**, 209 (2005)
14. R.Y. Yang, H.Y. Chen, C.M. Hsiung, S.J. Chang, Ceram. Int. **37**, 749 (2011)
15. K.Y. Jung, H.W. Lee, Y.C. Kang, S.B. Park, Y.S. Yang, Chem. Mater.**17**(10), 2729 (2005)
16. A. Lakshmanan, in *The Role of Sintering in the Synthesis of Luminescence Phosphors*, ed. by A. Lakshmanan. Sintering of Ceramics—New Emerging Techniques (InTech, 2012)

Chapter 4
Methods of Measurements (Instrumentation)

Measurement is an integral part of interaction among humanity and the physical world. It provides us a dependable and reproducible path of quantifying the world in which we live. Instrumentation is done for the sake of obtaining the required information pertaining to the completion of a process. The correlation of physical and chemical properties with structural characteristics, productions, and preparation conditions are of crucial importance for the development of new products and the optimization of existing products. Comprehensive knowledge of the material properties of a product under production or application conditions is therefore critical for its success. Thus so far, we have focused on the relationship between the structure of a material and its properties/applications. However, we have not yet focused on how one is able to determine the structure and composition of materials. That is, when a material is fabricated in the lab, how are we able to assess whether our method was successful? Depending on the nature of the material being investigated, suitable techniques may be utilized to assess its structure and properties. Whereas, some techniques are qualitative, such as providing an image of a surface, others yield quantitative information such as the relative concentrations of atoms that comprise the material.

In order for a solid to be well characterized, one needs to know about:

- the crystal structure, as given by the unit cell, its dimensions, and the fractional coordinates of the atoms present in the cell;
- the crystal defect that are present, their nature, numbers, and distribution;
- the impurities that are present and whether they are distributed at random or are concentrated into small regions;
- for polycrystalline solids–powders or ceramics—the number, size, shape, and distribution of the crystalline particles; and
- optical and thermal characteristics of the synthesized materials.

No single technique is capable of providing a complete characterization of a solid. Rather, a variety of techniques are used in combination. There are three main categories of physical technique which may be used to characterize solids: diffraction,

K. N. Shinde et al., *Phosphate Phosphors for Solid-State Lighting*,
Springer Series in Materials Science 174, DOI: 10.1007/978-3-642-34312-4_4,

microscopic, and spectroscopic techniques. In addition, other techniques such as thermal analysis and physical property measurements give valuable information in certain cases.

4.1 X-Ray Diffractometer (XRD)

X-ray diffraction (XRD) is an efficient analytical non-destructive technique used to investigate structural properties of crystalline materials. It is also used in applications such as phase identification, determination of grain size, composition of solid solution, lattice constants, and degree of crystallinity in a mixture of amorphous and crystalline substances. A diffraction pattern is produced when a material is irradiated with a collimated beam of x-rays. The x-ray spectra generated by this technique provide a structural fingerprint of the material (unknown). The relative peak height is generally proportional to the number of grains in a preferred orientation and peak positions are reproducible. The intensity of the diffracted x-rays is measured as a function of diffraction angle 2θ and the specimen orientation.

X-ray diffraction is considered as the most versatile, non-destructive analytical tool for identifying the constituents of a multiphase mixture qualitatively and quantitatively and also to determine the amorphous content of the sample. XRD pattern contains information not only about the phase composition of crystalline sample but also contains information about crystalline size, crystallinity, solid solution, stress, and texture [1]. Qualitative identification is carried out by comparing the x-ray diffraction pattern known as a diffractogram, of the unknown sample with the internationally recognized JCPDS data base which contains the reference patterns for more than 75,000 phases. XRD is mainly used in industrial X-ray laboratories for the following purposes:

- Characterization of the components of the materials processed/produced;
- Identification of the physical state of the components;
- Quantitative estimation of each component present in the materials; and
- Determination of the spatial distribution of the components.

Every crystalline material gives its unique X-ray diffraction pattern. The study of diffraction patterns from unknown phases offers a powerful method of qualitative identification. Qualitative analysis of even a complex sample involves only the proper identification and matching of the diffraction peaks with the data. To understand the diffraction mechanism, diffraction theories were developed under a few simplifying assumptions which often rely on the nature of the crystal. The assumptions are:

- The velocity of the x-ray beam traveling through the crystal is the velocity of light. The interaction between the incident and diffracted beams is neglected.
- The multiple scattering effects are excluded. This means that the scattered waves are not subjected to re-scattering at other lattice points.
- Absorption plays no role in the diffraction.

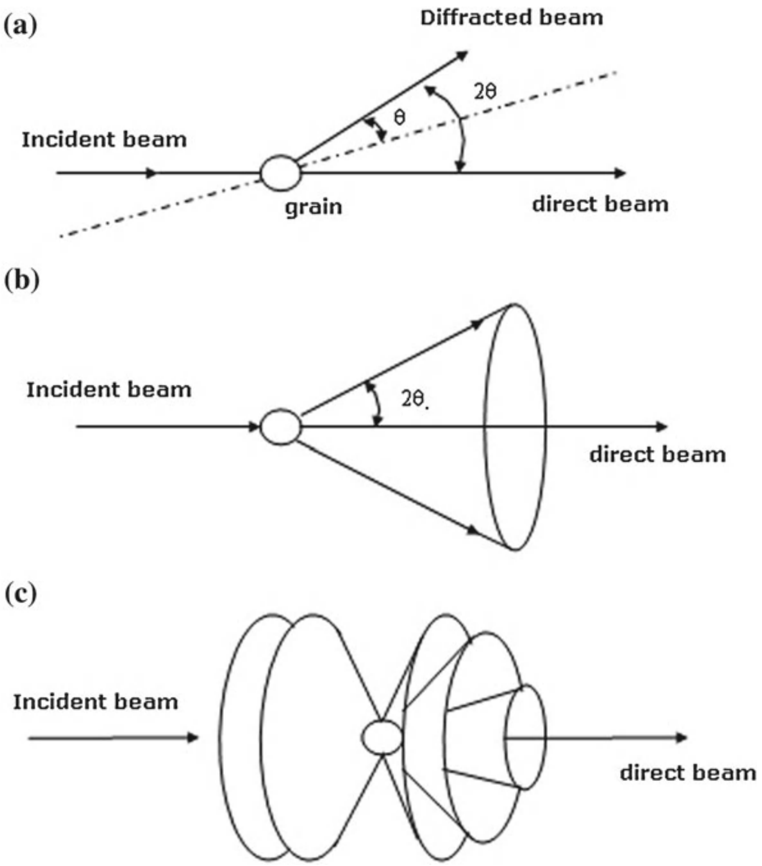

Fig. 4.1 Diffraction of X-rays by (**a**) a lattice layer of a single grain (**b**) identical lattice layers from many grains (**c**) different lattice layers by many grains [6]

This theory is therefore valid for diffraction in small crystals. When the diffraction occurs in large and perfect crystals multiple scattering results. In other words, the crystal lattice is so regular over a large volume that the reflected wave of a reflection must be further reflected back into the direction of the incident wave [2–5].

Principle

The X-ray diffraction method was deviced by Debye and Scherrer and independently by Hall in America [5]. The basic requirement is that material to be studied should be crystalline in nature. This technique has the merit that a small amount of material can be analyzed.

An ideal powder sample contains thousands of small randomly oriented crystal and hence many planes are expected to be in proper position to permit diffraction as per the Bragg's law,

$$2d \sin\theta = n\lambda$$

Fig. 4.2 Photo of the X-ray diffractometer [1]

Figure 4.1a shows a single grain of the sample, which has a lattice layer, perpendicular to the plane of the paper and inclined at an appropriate diffraction angle θ to the incident beam. Hence, the diffracted beam is inclined to the lattice by the same angle θ and to the direct beam by an angle 2θ. In the powder sample there may be many such grains having the lattice layers inclined at an angle θ to the incident beam corresponding to these lattice layers, the diffracted beam will be inclined to the direct beam by an angle 2θ. Thus, there will be a cone of diffracted beams with an apex at the specimen and the axis along the incident beam direction and the semi-vertical angle 2θ as shown in Fig. 4.1b. The other lattice layers simultaneously with different interplanar spacing will give rise to various diffraction cones as shown in Fig. 4.1c. The production of useful powder diffraction depends upon the selection of characteristic Cu, K_α radiation best suited for the application [6, 7].

The instrument that was used to take the X-ray diffraction patterns for the various samples discussed in this book to confirm their phases and crystallinity is shown in Fig. 4.2. This XRD is equipped with a generator PW 1830 and PW 3710 mPd control controlling unit employing CuK_α/FeK_α radiation. This unit contains a highly stabilized X-ray generator to enable accurate intensity measurements [1].

4.2 FTIR Spectrometer

Infrared (IR) spectroscopy is one of the most common spectroscopic techniques used by organic and inorganic chemists. Simply, it is the absorption measurement of different IR frequencies by a sample positioned in the path of an IR beam. The main goal of IR spectroscopic analysis is to determine the chemical functional groups in the sample. Different functional groups absorb characteristic frequencies of IR radiation. Using various sampling accessories, IR spectrometers can accept a wide range of sample types, such as gases, liquids, and solids. Thus, IR spectroscopy is an important and popular tool for structural elucidation and compound identification. The infrared region of the electromagnetic spectrum extends from the red end of the visible spectrum to the microwave region. The region includes radiation at wavelengths (λ) between 0.7 and 500 μm or, in wavenumbers (ν), between 14,000 and 20 cm^{-1}. Wave numbers are directly proportional to frequency, as well as the energy of the IR absorption [8]. In the contrast, wavelengths are inversely proportional to frequencies and their associated energy. FTIR analysis of the sample was carried out on Shimadzu FTIR instrument model 8101A (Fig. 4.3) at the Department of Pharmacy, R. T. M. Nagpur University, Nagpur. The pellets used for reading spectra were prepared by mixing 1–2 mg of the sample with a pinch of KBr. The spectrum in the range of 400–4,600 cm^{-1} was recorded at room temperature.

This spectroscopy is one of the most common spectroscopic techniques used by organic as well as inorganic chemists. The main goal of IR spectroscopic analysis is to determine the chemical functional groups in the sample. The application of infrared spectroscopy as a quantitative tool varies widely from one laboratory to another. However, the use of high-resolution grating instruments materially increases the scope and reliability of quantitative infrared work. The applications are as follows:

- Identification of types of organic and inorganic compounds;
- Determination of functional groups in organic materials;

Fig. 4.3 Photo of the Shimadzu model FTIR 8101A spectrometer

- Quantitative determination of compounds in mixtures;
- Determination of molecular conformation (structural isomers) and stereochemistry (geometrical isomers);
- Determination of molecular orientation (polymers and solutions); and
- Identification of compounds by matching spectrum of unknown compound with reference spectrum (fingerprinting).

4.3 Spectrofluorophotometer (Shimadzu RF-5301 PC)

The present PL work was carried out using the set-up for the spectrofluorophotometer (Shimadzu RF-5301 PC) at the Department of Physics, Kamla Nehru Mahavidyalaya, Nagpur (India) and Nanotechnology laboratory, Shivaji Science College, Nagpur (India).

The spectrofluorophotometer irradiates a sample with excitation light and measures the fluorescence emitted from the irradiated sample to perform a qualitative or quantitative analysis. A typical configuration of the spectrofluorophotometer is schematically described below (Fig. 4.4) taking the RF-5301PC instrument as an example [9].

The excitation monochromator (1) isolates a band of a particular wavelength from the light to the Xenon lamp to obtain excitation light. Since, brighter excitation light contributes to higher sensitivity of the spectrofluorophotometer, the excitation monochromator incorporates a diffraction grating with a larger aperture to collect the largest possible amount of light. The cell holder (2) is filled with the phosphor sample. The emission monochromator (3) selectively receives fluorescence emitted from the sample and its photomultiplier tube measures the intensity of the fluorescence. This monochromator has a diffraction grating whose size is same as that of the excitation monochromator to collect the greatest possible amount of light.

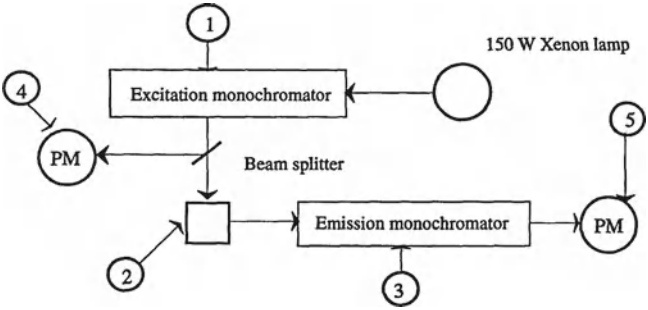

Fig. 4.4 Constitution of RF-5301 PC. (*1*) Excitation monochromator. (*2*) Cell holder. (*3*) Emission monochromator. (*4*) Monitor side photomultiplier tube. (*5*) Fluorescence side photomultiplier tube

The photomultiplier tube (4) is for monitoring. Generally, the xenon lamps used on spectrofluorophotometers are characterized by very high emission intensity and an uninterrupted radiation spectrum. However, their tendency to unstable light emission will result in greater signal noise if no countermeasure is incorporated. In addition, the non-uniformity in the radiation spectrum of the Xenon lamp and in the spectral sensitivity characteristics of the photomultiplier tube (these criteria are generally called instrument functions) causes distortion in the spectrum. To overcome these factors, the photomultiplier tube (4) monitors a portion of excitation light and feeds the resultant signal back to the photomultiplier tube (5) for fluorescence scanning. (This scheme is called the light-source compensation system).

4.3.1 Optical System of Spectrofluorophotometer

The optical system and instrument of the RP-5301PC are illustrated in Figs. 4.5 and 4.6, respectively. A 150 W xenon lamp (1) serves as the light source. The lamp housing contains generated ozone in it and decomposes the ozone by means of the heat produced by the lamp. The bright spot on the Xenon lamp is magnified and converged by the ellipsoidal mirror (2) and then further converged on the inlet slit of

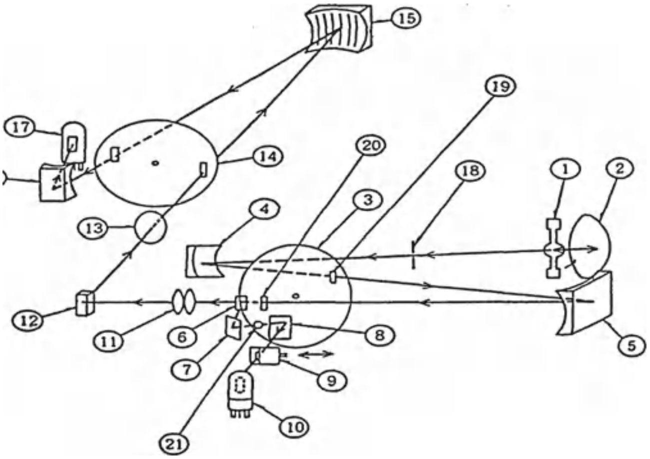

Fig. 4.5 Optical system of RF-5301PC. (*1*) Xenon lamp, 150 W. (*2*) Ellipsoidal mirror, SiO2-coated. (*3*) Slit Assy., excitation side. (*4*) Concave mirror. (*5*) Concave grating (for excitation). (*6*) Beam splitter quartz plate. (*7*) Teflon reflector plate 1. (*8*) Teflon reflector plate 2 ®-. (*9*) Optical attenuator. (*10*) Photomultiplier for monitoring, R212-14. (*11*) Condenser lens (dual-lens). (*12*) Cell. (*13*) Condenser lens. (*14*) Slit Assy., emission side. (*15*) Concave grating (for emission). (*16*) Concave mirror. (*17*) Photomultiplier for photometry, R3788-02. (*18*) Focal point. (*19*) Inlet slit. (*20*) Outlet slit. (*21*) Aperture for light quantity balancing

Fig. 4.6 Photo of the RF-5301 PC Spectrofluorophotometer

the slit assembly (excitation side) (3) by the concave mirror (4). A portion of the light isolated by the concave grating (5) passes through the outlet slit, travels through the condenser lens (11) and illuminates the sample cell. (The concave grating in both the monochromators is a highly-efficient ion-blazed holographic grating.) To achieve light-source compensation, a portion of the excitation light is reflected by the beam splitter quartz plate (6) and directed to the Teflon reflector plate 1 (7). The diffusely reflected light from the reflector plate 1 (7) then passes through the aperture for light quantity balancing (21) and illuminates the Teflon reflector plate 2 (8). Reflected by the reflector plate 2 (8), the diffuse light is attenuated to a specific ratio by the optical attenuator (9) and then reaches the photomultiplier for monitoring (10).

The fluorescence occurring on the cell is directed through the lens (13) to the emission monochromator that comprises the slit assembly (14) and the concave grating (15). Then, the isolated light is introduced through the concave mirror (16) into the photomultiplier for photometry (17) and the resultant electrical signal is fed to the preamplifier.

4.3.2 Procedures for Measurement of the Excitation and Emission Spectra

A powder sample cell was used to record the photoluminescence spectra. The sample cell consists of a round sample holder, quartz disc (window), and a threaded cap. The quartz disc was fixed into the sample holder and powder sample was spread on it. Then the threaded cap was fitted to hold the powder sample. The metal frame was put on the sample cell, containing sample so that the front protrusion of the cell could fit into the metal frame aperture. When analyzing the sample, optical axis runs along the center line of powder surface (quartz window).

First, the excitation (EX) spectra were recorded by setting the emission wavelength at zero order and keeping other parameters as specified in the manual. The excitation bands (EX) were identified from these spectra and the emission (EM) spectra were scanned for identified excitation wavelengths.

It was necessary to know approximate nature of EX and EM spectra. While doing so, the direct scattered light may superimpose on the EX spectrum, so that it is necessary to select a particular band in the emission for scanning the EX. Therefore, for proper excitation wavelengths EM was set at the position as identified from the earlier emission spectrum. Again the same procedure was followed for identifying correct EX positions and EM was recorded for each EX band separately.

In the ordinary measurements, a spectrum is affected by wavelength characteristics of the analysis system (monochromatic, photo multiplier etc.). Measuring of spectrum correction was performed using Rhodamine B as a standard. Similarly, emission spectrum was corrected by using diffuser and attenuator mentioned in the instrument manual. Both the spectra were correctable in the range of 220–600 nm. The sample whose emission wavelengths were within 220–600 nm was scanned in the correct spectrum mode and the samples whose wavelengths were beyond 600 nm were scanned in ordinary mode.

Emission spectra were recorded with excitation band pass 5 nm and emission band pass 1.5 nm, while the excitation spectra were recorded with excitation band pass of 1.5 nm and emission band pass of 5 nm.

4.4 Scanning Electron Microscopy (SEM)

In the SEM (see Fig. 4.7) an electron beam is focused into a fine probe and subsequently raster scanned over a small rectangular area. As the beam interacts with the sample it creates various signals (secondary electrons, internal currents, photon emission, etc.), all of which can be appropriately detected. These signals are highly localized to the area directly under the beam. By using these signals to modulate the brightness of a cathode ray tube, which is raster scanned in synchronism with the electron beam, an image is formed on the screen. This image is highly magnified and usually has the "look" of a traditional microscopic image but with a much greater depth of field. With ancillary detectors, the instrument is capable of elemental analysis.

Fig. 4.7 Photo of the Scanning Electron Microscopy (SEM)

4.4.1 Specifications of Scanning Electron Microscope

Name	**JEOL-JSM 6380A**
Main use	High magnification imaging and composition (elemental) mapping
Destructive	No, some electron beam damage
Magnification range	10–300,000×; the typical operating range
Beam energy range	500 eV–30 keV
Sample requirements	Minimal, occasionally coated with a conducting film; must be vacuum compatible
Sample size	Less than 0.1 mm, up to 10 cm or more
Lateral resolution	1–50 nm in secondary electron mode
Depth sampled	Varies from a few nm to a few pm, depending upon the accelerating voltage and the mode of analysis
Bonding information	No
Depth profiling	Only indirect capabilities

4.4.2 Physical Basis of Operation

For the purpose of a detailed materials characterization, two modes of EM exist i.e., (1) Transmission Electron Microscope (TEM) and (2) Scanning Electron Microscope (SEM). Because of its reasonable cost and the wide range of information that it provides in a timely manner, the SEM is the preferred starting tool for materials studies.

The SEM provides the investigator with a highly magnified image of the surface of a material that is very similar to what one would expect if one could actually “see” the surface visually. This tends to simplify image interpretations considerably, but reliance on intuitive reactions to SEM images can, on occasion, lead to erroneous results. The resolution of the SEM can approach a few nm and it can operate at magnifications that are easily adjusted from about 10–300,000x. Not only topographical information is produced in the SEM, but information concerning the composition near surface regions of the material is provided as well. There are also a number of important instruments closely related to the SEM, notably the electron microprobe (EMP) and the scanning Auger microprobe (SAM).

The principle images produced in the SEM are of three types: secondary electron images, backscattered electron images, and elemental X-ray maps. Secondary and backscattered electrons are conventionally separated according to their energies (see Fig. 4.8).

They are produced by different mechanisms. When a high-energy primary electron interacts with an atom, it undergoes either inelastic scattering with atomic electrons or elastic scattering with the atomic nucleus. In an inelastic collision with an electron, some amount of energy is transferred to the other electron. If the energy transfer is very small, the emitted electron will probably not have enough energy to exit the surface. If the energy transferred exceeds the work function of the material, the emitted electron can exit the solid. When the energy of the emitted electron is less than about 50 eV, by convention it is referred to as a secondary electron (SE), or simply a secondary. Most of the emitted secondaries are produced within the first few nm of the surface. Secondaries produced much deeper in the material suffer additional inelastic collisions, which lower their energy and trap them in the interior of the solid (see Fig. 4.9).

4.4.3 Instrumentation

Figure 4.7 shows a photograph of a JEOL 6380A model SEM. The main features of the instrument are the electron column containing the electron source (i.e., the gun),

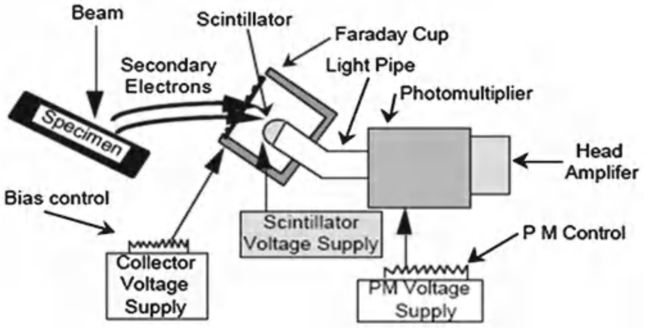

Fig. 4.8 Schematics of the secondary electron detector [10]

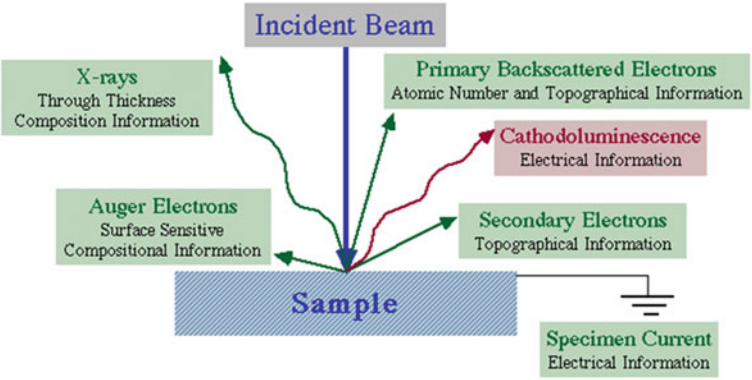

Fig. 4.9 Information obtained from various electron interactions [11]

the magnetic focusing lenses, the sample vacuum chamber and stage region (at the bottom of the column) and the electronics console containing the control panel, the electronic power supplies, and the scanning modules. A solid state EDS X-ray detector is usually attached to the column and protrudes into the area immediately above the stage. The overall function of the electron gun is to produce a source of electrons emanating from as small a "spot" as possible. The lenses act to demagnify this spot and focus it onto a sample. The gun itself produces electron emission from a small area and then demagnifies it initially before presenting it to the lens stack. The actual emission area might be a few pm in diameter and will be focused eventually into a spot as small as 1 or 2 nm on the specimen.

There are three major types of electron sources: thermionic tungsten, LaB_6, and hot and cold field emission. In the first case, a tungsten filament is heated to allow electrons to be emitted via thermionic emission. Temperatures as high as 3,000 °C are required to produce a sufficiently bright source. These filaments are easy to work with but have to be replaced frequently because of evaporation. The material LaB_6 has a lower work function than tungsten and thus can be operated at lower temperatures, and it yields higher source brightness. However, LaB_6 filaments require much better vacuum than tungsten to achieve good stability and a longer lifetime. Brighter the source, higher is the current density in the spot, which consequently permits more electrons to be focused onto the same area of a specimen. Later, field emission electron sources were produced. These tips are very sharp; the strong electric field created at the tip extracts electrons from the source even at low temperatures. Emission can be increased by thermal assistance but the energy width of the emitted electrons may increase somewhat. The sharper the energy profile, lesser the effect of chromatic aberrations of the magnetic defocusing lenses. Although they are more difficult to work with, they require very high vacuum and occasional cleaning and sharpening via thermal flashing, enhanced resolution, and low voltage applications of field emission tips are making them the source of choice in newer instruments that have the high-vacuum capability necessary to support them. The basic principle of the system is that, the electron beam impinges the surface and generates a splash of electrons with kinetic energies much lower than the primary incident electrons called secondary electrons. An image of the sample surface is constructed by measuring the secondary electron intensity as a function of the primary beam position. The SEM has many advantages over traditional microscopes. It has a large depth of field, which allows more of a specimen to be in focus at one time. The SEM also has much higher resolution, so closely spaced specimens can be magnified at much higher levels. Because the SEM uses electromagnetic lenses, the researcher has much more control in the degree of magnification. All of these advantages, as well as the actual strikingly clear images, make the scanning electron microscope one of the most useful instruments in research today. A simplified layout of a SEM is shown in Fig. 4.10.

The beam is defocused by a series of magnetic lenses as shown in Fig. 4.10. Each lens has an associated defining aperture that limits the divergence of the electron beam. The top lenses are called condenser lenses, and are often operated as if they were a single lens. By increasing the current through the condenser lens, the focal length is decreased and the divergence increases. The lens therefore passes less beam current on to the next lens in the chain. Increasing the current through the first lens reduces the size of the image produced (thus the term spot size for this control). It also spreads out the beam resulting in beam current control as well. Smaller spot sizes, often given higher dial numbers to correspond with the higher lens currents required for better resolution, are attained with less current (signal) and a smaller signal-to-noise ratio. Very high magnification images therefore are inherently noisy.

The beam next arrives at the final lens-aperture combination. The final lens does the ultimate focusing of the beam onto the surface of the sample. The sample is attached to a specimen stage that provides x and y motion, as well as tilt with respect to the beam axis and rotation about an axis normal to the specimen's surface. A final "z" motion allows adjustment of the distance between the final lens and the sample's surface. This distance is called the working distance.

The working distance and the limiting aperture size determine the convergence angle shown in the figure. Typically the convergence angle is a few mrad and it can be decreased by using a smaller final aperture or by increasing the working distance. Smaller the convergence angle, the more variation in the z-direction topography that can be tolerated still remaining in focus to some prescribed degree. This large depth of focus contributes to the ease of observation of topographical effects.

4.5 Transmission Electron Microscopy (TEM)

Transmission electron microscopy (TEM) is an imaging technique whereby a beam of electrons is transmitted through a specimen, and then an image is formed. The image is then magnified and directed to appear either on a fluorescent screen or layer of photographic film, or to be detected by a sensor such as a CCD camera. The system can study small details in the cell or different materials down to near

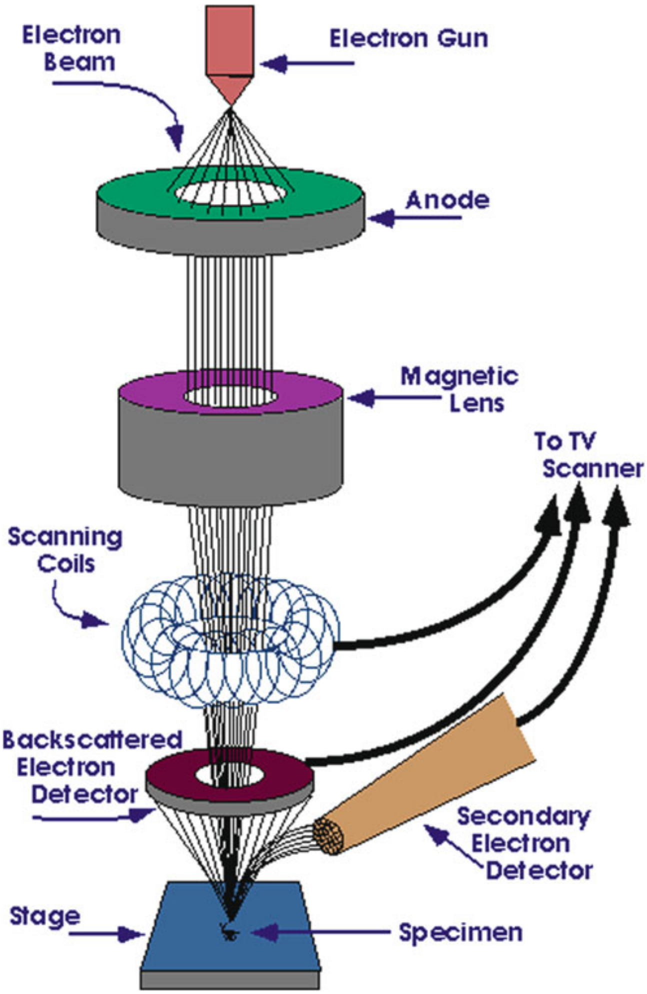

Fig. 4.10 Schematic diagram of SEM showing all the basic components [12]

atomic levels. It can investigate the size, shape, and arrangement of the particles which make up the specimen as well as their relationship to each other on the scale of atomic diameters. Materials to be analyzed with this technique need to have dimensions small enough to be electron transparent and that can be produced by the deposition of a dilute sample containing the specimen onto support grids. The suspension is normally a volatile solvent, such as ethanol, ensuring that the solvent rapidly evaporates allowing a sample that can be rapidly analyzed. The possibility for high magnifications has made the TEM a valuable tool in medical, biological, and material sciences research. In all cases, the specimens must be very thin and able to withstand the high vacuum present inside the instrument. For biological

Fig. 4.11 Photo of the Transmission Electron Microscope [14]

specimens, the maximum specimen thickness is roughly 1 μm. To withstand the instrument vacuum, biological specimens are held at liquid nitrogen temperatures [13]. In material science/metallurgy the specimens tend to be naturally resistant to vacuum and must be prepared as a thin foil, or etched so that some portion of the specimen is thin enough for the beam to penetrate. The system can also be used for the determination of the electron diffraction patterns of the crystalline structures. A crystalline material interacts with the electron beam mostly by diffraction rather than absorption. The intensity of the transmitted beam is affected by the volume and density of the material through which it passes. The intensity of the diffraction depends on the orientation of the planes of atoms in a crystal relative to the electron beam. At certain angles, the electron beam is diffracted strongly from the axis of the incoming beam, while at other angles the beam is largely transmitted.

Figure 4.11 shows a photograph of a TEM. In Transmission Electron Microscopy (TEM) a thin solid specimen (<200 nm thick) is bombarded in vacuum with a highly-focused, monoenergetic beam of electrons. The beam is of sufficient energy to propagate through the specimen. A series of electromagnetic lenses then magnifies this transmitted electron signal. Diffracted electrons are observed in the form of a diffraction pattern beneath the specimen. This information is used to determine the atomic structure of the material in the sample. Transmitted electrons form images from small regions of sample that contain contrast, due to several scattering mechanisms associated with interactions between electrons and the atomic constituents of the sample. Analysis of transmitted electron images yields information both about atomic structure and about defects present in the material [13, 14].

4.5.1 Specifications of Transmission Electron Microscope

Name	
Range of elements	TEM does not specifically identify elements measured
Destructive	Yes, during specimen preparation
Chemical bonding Information	Sometimes, indirectly from diffraction and image simulation
Quantification	Yes, atomic structures by diffraction; defect characterization by systematic image analysis
Accuracy	Lattice parameters to four significant figures using convergent beam diffraction
Detection limits	One monolayer for relatively high-Z materials
Depth resolution	None, except there are techniques that measure sample thickness
Lateral resolution	Better than 0.2 nm on some instruments
Imaging/mapping	Yes
Sample requirements	Solid conductors and coated insulators. Typically 3-mm diameter, <200-nm thick in the center
Main uses	Atomic structure and Microstructural analysis of solid materials, providing high lateral resolution

4.6 Thermal Analysis

Thermal Analysis techniques are used in virtually every area of modern science and technology. The basic information that these techniques provide, such as crystallinity, specific heat, and expansion, are relied on heavily for the research and development of new products. Thermal Analysis techniques also find increasing use in the area of quality control and assurance, where demanding requirements must be met in an increasingly competitive world. And of course, thermal analysis instruments are used in universities for applications ranging from basic undergraduate studies to the most sophisticated postgraduate research. Thermal analysis includes a group of techniques in which specific physical properties of a material are measured as function of temperature. The production of new high technology materials and the resulting requirement for a more precise characterization of these substances have increased the demand for thermal analysis techniques. Thermal analysis instrument can measure transition temperatures, weight losses, energies of transitions, dimensional changes, modulus changes, etc. This technique is useful in both quantitative and qualitative analysis. Samples may be identified and characterized by qualitative investigations of their thermal behavior.

The main thermal analysis techniques which we used for characterizations are:

(a) Differential Thermal Analysis (DTA).

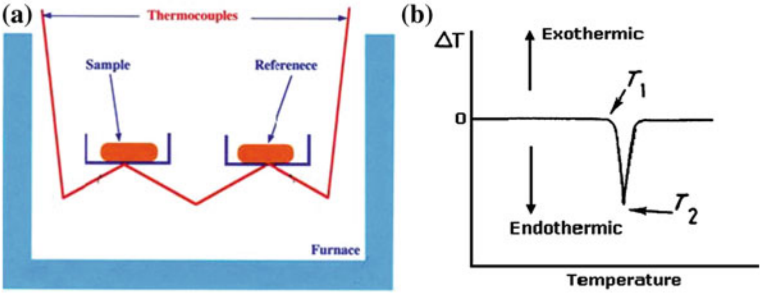

Fig. 4.12 Experimental arrangement of DTA (**a**) and a DTA trace (**b**) [16]

(b) Thermogravimetric Analysis (TGA).
(c) Differential Scanning Calorimetry (DSC).

4.6.1 Differential Thermal Analysis

DTA finds a wide application in the identification and characterization of materials. Particularly, it is considered to be a unique technique for obtaining the vital information about the specific chemical or physical change that is accompanied, either by evolution or absorption of heat in test materials during heating or cooling.

Le Chatelier used this technique for the first time in 1887 to investigate the thermal behavior of clay [15]. The arrangement used in DTA is shown in Fig. 4.12a. Sample and reference are placed side by side in a heating block which is heated or cooled at a constant rate; identical thermocouples are placed in each and are connected 'back to back'. When the sample and reference are at the same temperature, the net output of this pair to thermocouples is zero.

When a thermal event occurs in the sample, a temperature difference, ΔT, exists between sample and reference which is detected by the net voltage of the thermocouples. A third thermocouple (not shown) is used to monitor the temperature of the heating block and the results are presented as ΔT against temperature as shown in Fig. 4.12b.

A horizontal baseline, corresponding to $\Delta T = 0$, occurs and superposed on this is a sharp peak due to the thermal event in the sample. The temperature of the peak is taken either as the temperature at which deviation from the baseline begins, T_1, or as the peak temperature, T_2, The size of the ΔT peak may be amplified so that events with very small enthalpy changes may be detected [16].

In general, we can say that each substance give a DTA curve in which the number, shape, and position of the various endothermic and exothermic features serve as a means of qualitative identification of the substance. When an endothermic change occurs, the sample temperature lags behind the reference temperature because of the heat in the sample. The initial point for a phase change or chemical reaction is

Fig. 4.13 Experimental setup of TG/DTA

the point at which the curve first deviates from the baseline. When the transition is complete, thermal diffusion brings the sample back to equilibrium quickly. The peak (or minimum) temperature indicates the temperature at which the reaction is completed. Thermal analysis was done by Perkin Elmer Diamond TG/DTA as shown in Fig. 4.13.

DTA allows the detection of every physical or chemical change whether or not it is accompanied by a change in weight. The origin of the temperature difference in the sample (ΔT) lies in energy difference between the products and the reactants or between the two phases of a substance. This energy difference is manifested as enthalpic changes, such as exothermic and endothermic. In most of the cases, physical changes give rise to endothermic curves where as chemical reactions (particularly those of an oxidative nature) give rise to exothermic peak.

4.6.2 Thermogravimetric Analysis (TGA)

Thermogravimetry measures the change in mass of a substance as a function of temperature or time. TG can be used in the kinetic analysis of polymer stability but also compositional analysis of polymer stability. More precisely, the thermogravimetric analysis is a technique whereby the weight of a substance, in an environment heated or cooled at a controlled rate, is recorded as a function of time or temperature. The basic requirements are a method of heating (or cooling) and a means of weighing. Three types of thermogravimetry are [17]:

- **Isothermal or static thermogravimetry**: In this technique, the sample weight is recorded as a function of time at constant temperature.
- **Quasistatic thermogravimetry**: In this technique, the sample is heated to constant weight at each of a series of increasing temperatures.

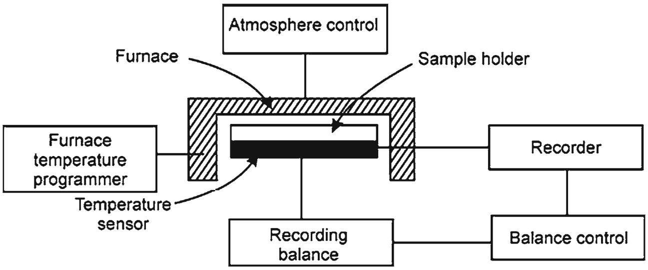

Fig. 4.14 Schematic diagram of a modern thermobalance [18]

- **Dynamic thermogravimetry**: Here, the sample is heated in environments whose temperature is changing in a predetermined manner, generally at a linear rate. Most of the studies are generally carried out with dynamic thermogravimetry. Therefore, it is generally referred to as thermogravimetry.

4.6.2.1 Instrumentation

The principle of thermogravimetry is based on the simple fact that the sample is weighed continuously as it is being heated to elevate temperature. A modern thermobalance is shown in Fig. 4.14. The various components are (1) recording balance (2) furnace (3) furnace temperature programmer or controller and (4) recorder. The specific details of each component depend on the particular application.

The usual temperature range for TG is from room temperature to 1,200 °C in either inert or reactive atmosphere.

4.6.2.2 Recording of Results

TGA/DTA measurements were done by Perkin Elmer Diamond TG/DTA as shown in Fig. 4.13. The instrument for thermogravimetry is known as thermobalance, which is a precision balance programmed for a linear rise of temperature. The results appear as a continuous record as shown in Fig. 4.15. The results from the programmed operation of a thermo balance are represented by a plot of mass versus temperature or time. This plot is referred to as the thermo gravimetric curve or TG curve. The sample is heated at constant rate and has a constant mass, M_i, until it begins to decompose at temperature T_i. Under conditions of dynamic heating, decomposition usually takes place over a range of temperatures, T_i to T_f, and a second constant-mass plateau is observed above T_f, which corresponds to the mass of the residue M_f.

The masses M_i and M_f and the difference ΔM are fundamental properties of the sample and can be used for quantitative calculations of compositional changes, etc. By contrast, T_i and T_f depend on variables, such as heating rate, the nature of the solid (e.g., its particle size), and the atmosphere above the sample [19–22].

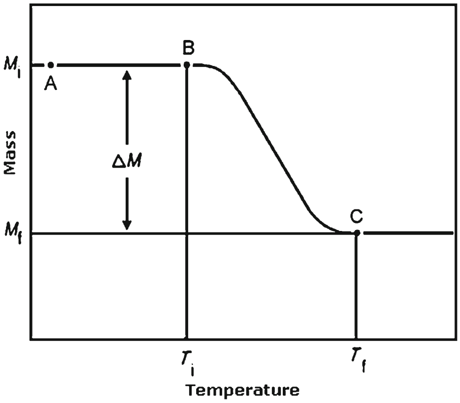

Fig. 4.15 A typical TG curve [19]

4.6.3 Differential Scanning Calorimetry (DSC)

In DSC, the equipment is designed to allow a quantitative measure of the temperature and the enthalpy of a transition or the heat of a reaction. The differential scanning calorimeters are able to measure the amount of energy absorbed or released during transitions only by observing the difference in heat flow between the sample and reference material. The recording of this balancing energy yields a direct calorimetric measurement of the energy associated with the transition [23].

Following are the two main types of differential scanning calorimeters:

- Heat flux DSC
- Power compensation DSC

The basic principle underlying the DSC technique is that, when the sample undergoes a physical transformation such as phase transitions, more (or less) heat will need to flow to it than the reference to maintain both at the same temperature. Whether more or less heat must flow to the sample depends on whether the process is exothermic or endothermic. For example, as a solid sample melts to a liquid it will require more heat flowing to the sample to increase its temperature at the same rate as the reference. This is due to the absorption of heat by the sample as it undergoes the endothermic phase transition from solid to liquid. Likewise, as the sample undergoes exothermic processes (such as crystallization) less heat is required to raise the sample temperature. An experimental arrangement of differential scanning calorimetry is shown in Fig. 4.16. DSC measurements are recorded on Mettler Toledo DSC 821e system (Fig. 4.17) at VNIT, Nagpur.

Thermal properties were studied using a Mettler Toledo DSC 821e differential scanning calorimeter (DSC) under a nitrogen atmosphere. Samples of about 10 mg were heated at a rate of 10 °C/min from 25 to 340 °C. The idea of a DSC experiment is to heat up or cool down a sample and a reference according to a set temperature

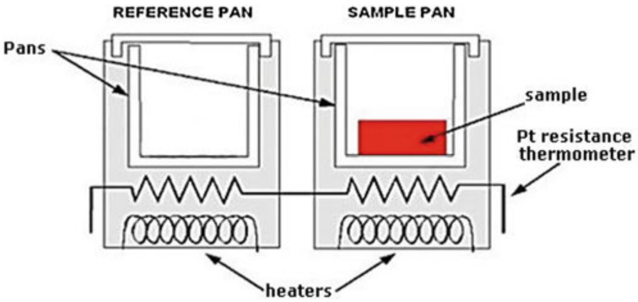

Fig. 4.16 Experimental arrangement of Differential Scanning Calorimetry

Fig. 4.17 Experimental setup of Differential Scanning Calorimetry

programme. The sample and reference are maintained at the same temperature during the whole experiment. When a thermal event occurs in the sample certain additional amount of energy has to be supplied to or withdrawn from the sample to maintain zero temperature difference between the sample and the reference. Therefore, the reference should not undergo any physical or chemical changes at the temperature range of the experiment. The sample and reference are placed in identical environments—metal pans on individual bases, each of which contains a platinum resistance thermometer (or a thermocouple) and a heater (Fig. 4.16). Changes in the sample that are associated with absorption or evolution of heat cause variations in the differential heat flow which are then recorded as peaks. The area of an individual peak is directly proportional to the enthalpy change of the sample and the direction of the peak indicates whether the thermal event is exo- or endothermic.

References

1. X-ray Panalytical Diffractometer Instruction Manual
2. H.J. Goldschmidt, High-Temperature X-ray Diffraction Techniques. (International Union of Crystalography) Bibliography 1, 1964
3. B. Post, Low-Temperature-X-ray Diffraction. (InternationalUnionof Crystalography) Bibliography 2, 1964
4. B.D. Cullity, *Elements of X-ray Diffraction*, 1st edn. (Addison Wesley, Reading, 1956), p. 182

5. B.D. Cullity, *Elements of X-ray Diffraction*, 2nd edn. (Addison-Wesley, Reading, 1978), p. 161
6. R. Jenkins, R.L. Snyder, *Introduction to Powder Diffractometry* (Wiley-Interscience, New York, 1996), p. 403
7. R. Jenkins, *X-ray Techniques: Overview in Encyclopedia of Analytical Chemistry*, ed. by R.A. Meyers (Wiley, Chichester, 2000), p. 5
8. Hitachi F-4000 Fluorometer Instruction Manual (2001)
9. Applied Engineering Division, Shimadzu Corporation, Principles, Application, Application, and Equipment Structure of Fluorescence Analysis, Shimadzu Fluorescence Analysis Course, Shimadzu Corporation
10. R.E. Lee, *Scanning Electron Microscopy and X-ray Microanalysis*, Prentice-Hall (QH212S3L44) for undergraduate students (1993), pp. 150–156
11. C.E. Lyman, D.E. Newbury, J.I. Goldstein, D.B. Williams, A.D. Romig, J.T. Armstrong, P. Echlin, C.E. Fiori, D.C. Joy, E. Lifshin, K.-R. Peters, *Scanning Electron Microscopy, X-Ray Microanalysis and Analytical Electron Microscopy: A Laboratory Workbook* (Plenum Press, New York, 1990)
12. J. Schweitzer, Radiological and Environmental Management (REM) (2008), http://www.purdue.edu/REM/rs/sem.htm
13. B. Bouchet, C. Gaillard, Principles of transmission electron microscopy (2005), pp. 1–2, http://www.scribd.com/doc/92505015/TEM-Principle
14. P.J. Goodhew, F.J. Humphreys, *Electron Microscopy and Analysis* (University of Surrey, UK Imperial College, London, 1988), pp. 106–113
15. G.R. Chatwal, S.K. Anand, *Instrumental Methods of Chemical Analysis* (Himalaya Publishing House Pvt.Ltd., Mumbai, 1979)
16. M.E. Brown, *Introduction to Thermal Analysis* (Kluwer Academic Publisher, London, 2001)
17. H.K.D.H. Bhadeshia, *Differential Thermal Analysis* (University of Cambridge, Materials Science and Metallurgy, Cambridge, 1974), pp. 106–112
18. C. Duval, *Inorganic Thermogravimetric Analysis* (Elsevier, Amsterdam, 1962), p. 112
19. P.D. Garn, *Thermoanalytical Methods of Investigations* (Academic Press, New York, 1965), p. 606
20. W.W. Wandlandt, *Thermal Analysis* (Wiley, New York, 1986), p. 17
21. A. Blazek, *Thermal Analysis* (Van Nostrand Reinhold, London, 1972), p. 61
22. H. Gunzzler, A. Williams, *Hand Book of Analytical Techniques*, vol. 2 (Wiley-VCH, Weinheim, 2001)
23. A.R. West, *Solid State Chemistry and it's Applications* (Wiley, New York, 1985)

Chapter 5
Some Orthophosphate Phosphors

5.1 Introduction

The orthophosphate group, $PO_4{}^{3-}$, is the most common phosphorus oxoanion also known as phosphoric acid. All four oxygen atoms, are usually coordinated to cations in solid orthophosphates leading to strongly bonded, extended structures. The acid orthophosphate anions, hydrogen phosphate, $HPO_4{}^{2-}$, dihydrogen phosphate, and $H_2PO_4{}^{-}$ are also found in many materials. Almost every metallic element forms an orthophosphate, and a range of oxidation states is stabilized for transition elements. The orthophosphates were the last family of phosphors to be introduced before the present material yttrium vanadate came into service. They are all activated with tin, which must be in the divalent state to give luminescence. All tin-activated phosphors are characterized by their very broad spectral energy emission. Typically, they cannot achieve such a deep red emission as it is possible from previously mentioned materials, but their quantum efficiency is remarkably high, as much as 87 % for magnesium orthophosphate. They are colorless so the light transmission is high, and because the emission is at wavelengths to which the human eye is more sensitive, lamps with remarkably high luminous efficacy can be fabricated. They do, however, leave a lot to be desired in terms of their color rendering properties, but from the early 1960s until the late 1980s many manufacturers offered two different kinds of mercury lamp—types with good color rendering, and types with high efficacy at the expense of color properties. Strontium orthophosphate, $(Sr,Mg)_3(PO_4)_2{:}Sn^{2+}$ modified with Mg to adjust the crystal lattice structure was the most commonly employed material in high-efficacy lamps. Its emission peak lies at 630 nm at room temperature, decreasing to shorter wavelengths quite dramatically at lamp operating temperatures but the light emission remains high. By 330 °C the red emission peak has shifted to 570 nm and thus it is clearly evident that color rendering of these lamps suffers. While a magnesium germanate 400 W lamp gives a red ratio of about 7.5 %, the strontium orthophosphate lamps only manage about 5 %. Similar performance was attained from calcium orthophosphate, modified with Mg and this material found preference with some of the Eastern European manufacturers. It has slightly higher

K. N. Shinde et al., *Phosphate Phosphors for Solid-State Lighting*,
Springer Series in Materials Science 174, DOI: 10.1007/978-3-642-34312-4_5,

efficiency again, but red ratio falls further to 4.4 %, really not better than the first MAF type lamps. Meanwhile, Sylvania in the USA developed materials based on calcium-zinc orthophosphates, and a particular 400 W lamp attained an efficacy of 59.5 lm/W. This was excellent by comparison with the 49 lm/W attainable from red-emitting phosphors at the time, and is still impressive compared with the 55 lm/W of present-day lamps with vanadate-based coatings. When vanadate coatings became available in the late 1960s, they entirely superseded the high-efficacy line of mercury lamps in all countries except the USA, where a demand curiously continued for the old-fashioned inefficient coatings for nearly 20 years more. The vanadate phosphors offered 10 % higher luminous efficacy and considerably enhanced color rendering properties as well while also being pure white in color, for the first time satisfying all of the requirements of a mercury lamp phosphor.

As an important family of luminescent materials, orthophosphates have been paid intense attention because of their excellent properties. The phosphors based on phosphate host matrices have become the subject of great interest for an extensive investigation due to their wide applications in lighting and displays. Solid-state lighting using light-emitting diode (LED) and phosphor material to generate white light is the current research focus in the lighting industry. Solid-state lighting technology has several advantages over conventional fluorescent lamps, such as reduced power consumption, compactness, efficient light output, and longer lifetime. Solid-state lighting will have its impact in reducing the global electricity consumption. White LEDs can save about 70 % of the energy and do not need any harmful ingredient in comparison with the conventional light sources, such as incandescence light bulbs and luminescent tubes, thus white LEDs have a great potential to replace them and are considered as next generation solid-state light devices. The research on tricolor phosphors suitable for near ultraviolet/ultraviolet excitation has attracted considerable attention because of their important applications in solid-state lighting. Orthophosphates with the general formula $ABPO_4$ (A and B are mono- and divalent cations, respectively) have shown a rising interest for their remarkable applications as luminescence hosts. For example, Eu^{2+}-doped $NaCaPO_4$ [1, 2], $KBaPO_4$ [3, 4], $KSrPO_4$ [5], $ABaPO_4$ ($A = Na, K$) [6], and $LiSrPO_4$ [7] have been recently reported to be the new luminescent materials applied in white LEDs and plasma display panel (PDP). Very recently, Shinde et al. reported [8] effect of temperature on intense green emitting $Na_2Ca(PO_4)F{:}Mn^{2+}$ phosphor. The choice of the host material, is a very crucial part of a luminescence study. In this context, selecting a suitable host that can be activated by different ions emitting in different regions of the visible spectrum is a challenge for the solid material synthesis. It is important to get different regions of visible spectrum in a matrix, whose different activation ions can be structurally substituted for cation sites. The formation of β-$NaCaPO_4$ with a β-K_2SO_4 structure (space group *Pnam*), was reported earlier (JCPDS No. 29-1193). β-$NaCaPO_4$ is stable at the temperature below 650 °C and transforms to the α-form at around 650 °C. First, α-$NaCaPO_4$ (space group *Pmn21*) was found by Olsen [9]. Later, the crystal structure of α-$NaCaPO_4$ (JCPDS No. 76-1456, $a = 20.397$ nm, $b = 5.412$ nm, $c = 9.161$ nm) with β-K_2SO_4 structure was studied by Ben Amara et al. [10]. The difference of β-$NaCaPO_4$ (*Pnam*) and α-$NaCaPO_4$ (*Pmn21*) confirms the presence of small intensity superstructure reflections because of three different orientations adopted by the three independent [PO_4] tetrahedral. In the present study, the $NaCaPO_4$ was reported as the host material because of its excellent chemical and thermal stabilization [7]. Phosphate compounds are known as multifunctional materials. In particular, orthophosphates have been extensively investigated due to their structural diversity. Phosphates are used as elements of optical devices, fluorescent lamps, plasma panel display, super ionic conductors (NASICON), and matrices for long time storage of many radioactive substances waste, etc.

Recently, it has been found that NASICON also has luminescence characteristics and there are limited reports on this effect in the literature [11–13]. NASICON (Na^+ super ionic conductor) is a name for compounds that has a three-dimensional (3D) framework structure and possesses a high Na ionic conductivity [14]. NASICON compounds are characterized by an anionic framework of PO_4 or SiO_4 tetrahedral linked by shared oxygen ions in an octahedral frame [15]. These properties make it suitable for use in electrochemical devices [16]. Beside this, while investigating the luminescent mechanism of NASICON, He et al. [11] reported the PL properties of un-doped and doped-NASICON materials. Hirayama et al. [12] and Masui et al. [17] reported Eu^{2+} emission in $A_{0.5}Zr_2(PO_4)_3$ (A = Ca, Sr, Ba) phosphors with the NASICON structure. Mouline et al. [18] reported the copper(I) and manganese(II) luminescence in the NASICON-type structure $Cu^{I}\ 0.5Mn^{II}_{0.25}Zr_2(PO_4)_3$, which crystallizes in the rhombohedral (hexagonal cell) system with the efficient energy transfer from $Cu^+ \rightarrow Mn^{2+}$ site. Chukova et al. [19] reported the possibility of incorporation of f-element impurities of rare earth elements (Dy, Sm, Nd) into NASICON matrix of the phosphates.

In this chapter, we focused on preparation of $NaCaPO_4$, $Na_3Al_2(PO_4)_3$, $K_3Al_2(PO_4)_3$, $AlPO_4$, and $Na(BaSr)PO_4$-doped with Eu^{3+}, Ce^{3+}, Dy^{3+}, Mn^{2+}, and Gd^{3+} by both conventional solid-state reaction and novel combustion synthesis which has advantages over the other systems. There are currently very few references on the use of Eu^{3+}, Ce^{3+}, Dy^{3+}, Mn^{2+}, and Gd^{3+} phosphors as illumination sources with these hosts. Therefore, it is important to study phosphors for lighting materials and for medical applications.

5.2 Photoluminescence Studies of $NaCaPO_4$:RE (RE = Dy^{3+}, Mn^{2+}, and Gd^{3+}) by Solid-State Reaction [20]

5.2.1 Experimental

The Dy, Mn, and Gd-doped $NaCaPO_4$ phosphate-based phosphors, were synthesized by solid-state reaction. The starting materials like Na_2CO_3, $CaCO_3$, and $NH_4H_2PO_4$ of analytical grade (pure) were used. These materials were weighed in the proper molar ratio, and then Dy_2O_3 was introduced as a dopant followed by mixing and grinding homogeneously in an agate mortar. The mixture was heated at 500 °C in a silica crucible for 2 h. The vapors extraneous to the desired product which was evolved during the process were allowed to be released. After grinding, the mixture was heated at 800 °C for 24 h. A white phosphor powder was obtained. Similar procedure was followed for Mn and Gd activated $NaCaPO_4$. The manganese and gadolinium were introduced as $(CH_3COO)_2Mn{\cdot}4H_2O$ and Gd_2O_3, respectively.

Several complementary methods were used to characterize the prepared phosphors. The prepared host lattice was characterized for their phase purity and crystallinity by X-ray powder diffraction (XRD) using PAN-analytical diffractometer (Cu-Ká radiation) at a scanning step of 0.01°, continue time of 20 s, in the 2θ range from 10° to 80°; the average crystallite size was calculated from the broadening of the X-ray line (311) using Scherer's equation. The photoluminescence (PL) measurement of excitation and emission was recorded on the Shimadzu RF5301PC spectrofluorophotometer. The same amount of sample (2 g) was used for each measurement. Emission and excitation spectra, were recorded using a spectral slit width of 1.5 nm. The morphology of the products, was examined by scanning electron microscopy (SEM, JEOL 6380A).

5.2.2 *Results and Discussion*

5.2.2.1 XRD and SEM of $NaCaPO_4$

Figure 5.1 shows the XRD pattern of the obtained $NaCaPO_4$ which agrees well with the report of the Joint Committee on Powder Diffraction Standards (JCPDS No. 029-1193). The XRD pattern did not indicate the presence of constituents which is a direct evidence of the formation of the desired compound. These results indicate that the final product is in a crystalline and homogeneous form. The typical morphological images are represented in Fig. 5.2. The particles possess foam-like morphology

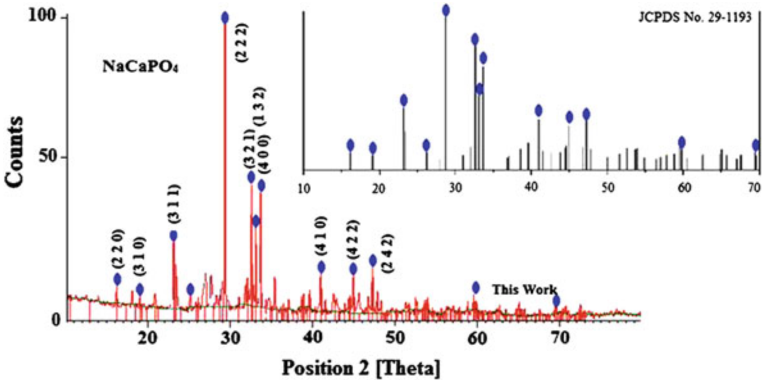

Fig. 5.1 XRD of the $NaCaPO_4$ host lattice

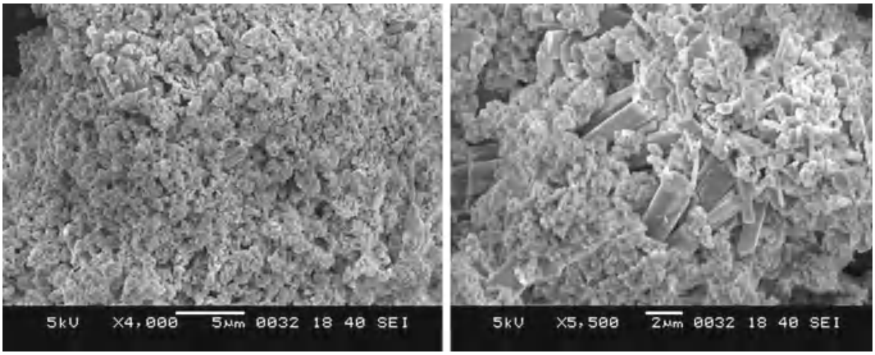

Fig. 5.2 SEM images of the $NaCaPO_4$

formed from highly agglomerated crystallites. The average crystallite size was in the submicrometer range. The formation of rod structures can be seen in the SEM images. It is clearly shown that the grains have an irregular shape with particle size of about 0.5–2 μm. The prepared sample with crystal sizes between 0.5 and 2 μm, is suitable for the solid-state lighting (coating purpose). The XRD and SEM clearly indicate that the solid-state reaction among the mixtures was successful.

5.2.2.2 Photoluminescence Study of Dy^{3+} Activated $NaCaPO_4$

The PL study of Dy^{3+} activated $NaCaPO_4$ phosphor is presented in this section. The broad band excitation peak is observed at 386 nm and is shown in Fig. 5.3. This excitation curve (386 nm) is a near UV excitation suitable for LED lighting phosphor excitation (385–395 nm). The emission spectrum is shown in Fig. 5.4. All samples showed two emission bands: one is centered at 480 nm (blue) and the other is at 573 nm (yellow). They are assigned to the Dy^{3+} electronic transitions of $^4F_{9/2} \rightarrow {}^6H_{15/2}$ and $^6H_{13/2}$ energy levels, respectively [21] as shown in the left inset of Fig. 5.4. A series of $NaCa_{1-x}PO_4{:}Dy_x^{3+}$ phosphors with various Dy^{3+} concentrations ($x = 0.1$ mol% to 1 mol%) was prepared and the effect of doped Dy^{3+}concentration on the emission intensity was investigated. Emission intensity of $NaCa_{1-x}PO_4{:}Dy_x^{3+}$ with different Dy^{3+} concentration is shown in right inset of Fig. 5.4. The position of the emission peak is not influenced by the Dy^{3+} concentration. The emission intensity increases with an increasing Dy^{3+} concentration and reaches the maximum at about 0.5 mol%. Concentration quenching occurs, when the Dy^{3+} concentration is beyond 0.5 mol%. PL results show the excitation peak at 386 nm which is away from Hg excitation and is useful for solid-state lighting in the lamp industry. PL emission peaks are observed at the blue and yellow region of the spectrum due to the Dy^{3+} ion. The excitation spectrum in the range 300–400 nm consists of the $f \rightarrow f$ transition of the Dy^{3+} ion, i.e., 386 nm ($^6H_{15/2} \rightarrow {}^6F_{9/2}$ transition). The emission spectra for the Dy^{3+} ions in $NaCaPO_4$ show emissions at 480 nm (blue) and 573 nm (yellow). It is known that

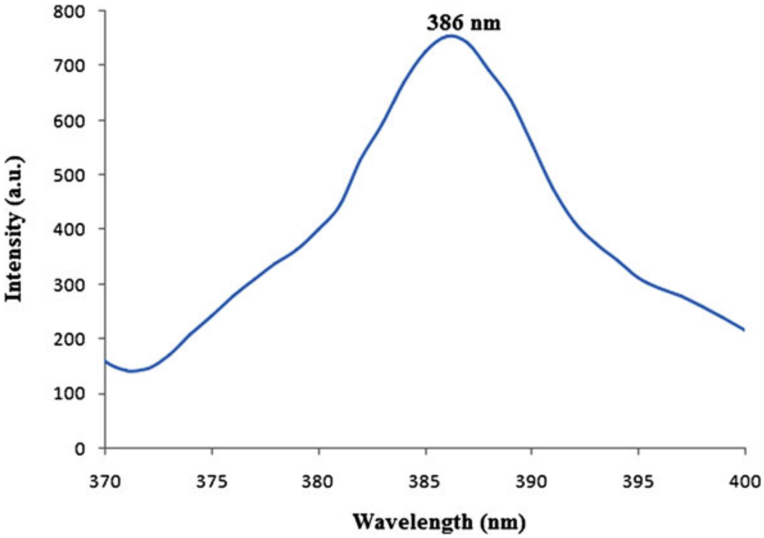

Fig. 5.3 Excitation of $NaCaPO_4:Dy^{3+}$ monitored at 573 nm

Dy^{3+} emission around 480 nm ($^4F_{9/2} \rightarrow {}^6H_{15/2}$) is of magnetic dipole origin and that around 573 nm ($^4F_{9/2} \rightarrow {}^6H_{13/2}$) is of electric dipole origin [22].

In our case, the Dy^{3+} ion may enter the host lattice to substitute Na^+ or Ca^{2+} or locate on surfaces of the crystals due to the porosity of the structure. The ionic radius of Dy^{3+} (91.2 pm) is much smaller than that of Ca^{2+} (99 pm) and Na^+ (102 pm). Therefore, most of the Dy^{3+} ions entered the lattice and only a few of them will be located at the surface of the $NaCaPO_4$ host. The occupancy of the Dy^{3+} ion into Na^+ and the Ca^{2+} sites in the $NaCaPO_4$ host would naturally cause a substantial number

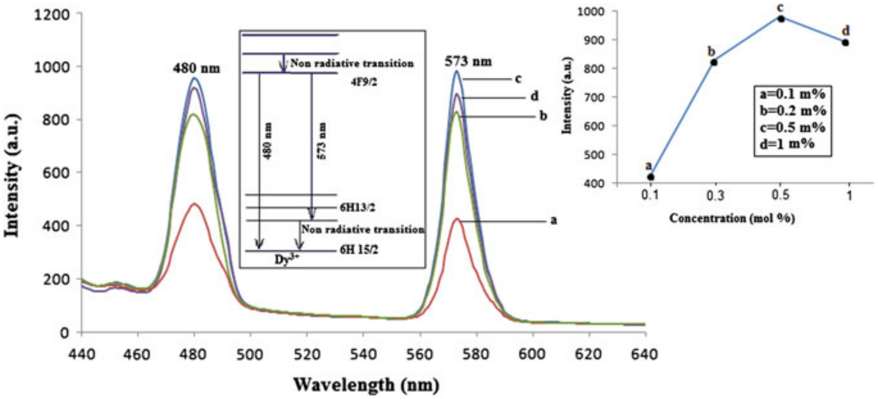

Fig. 5.4 Emission spectra of $NaCaPO_4:Dy^{3+}$ when excited at 386 nm

of vacant sites in the oxygen ion array which in turn expand the lattice to decrease the crystal density. That is, the formation of Dy^{3+} due to Na^+ or Ca^{2+} in $NaCaPO_4$ host induces more oxygen vacancies. Lopez et al. [23] reported that the oxygen vacancies might act as sensitizers for the energy transfer to the rare-earth ion due to the strong mixing of charge transfer states, resulting in highly enhanced luminescence. However, excess oxygen vacancies in the host would inevitably destroy the crystallinity, which leads to quenching of the luminescence. Of course, the primary reason for this is that more Dy^{3+} enters the lattices, which enhance the $^4F_{9/2} \rightarrow {}^6H_{15/2,\,13/2}$ transitions of the samples greatly, as shown in Fig. 5.4 (insets). From this emission spectrum, it is clearly observed that the fluorescence intensities ratio increases gradually.

5.2.2.3 Photoluminescence Study of Mn^{2+} Activated $NaCaPO_4$

The properties of Mn^{2+} are most widely studied and used in many luminescent materials. The PL excitation and emission spectra were recorded at room temperature. Figures 5.5 and 5.6 show the excitation and emission spectra of $NaCaPO_4$:Mn^{2+} powder phosphors, respectively. The emission spectrum obtained from different Mn^{2+} concentrations is as shown in Fig. 5.6. Stable green emission was observed at 520 nm when the powder was excited at 250 nm. The position of the emission peak is not influenced by the Mn^{2+} concentration. This emission can be ascribed to the $^4T_1 \rightarrow {}^6A_1$ transition of the Mn^{2+} ion shown in left inset of Fig. 5.6.

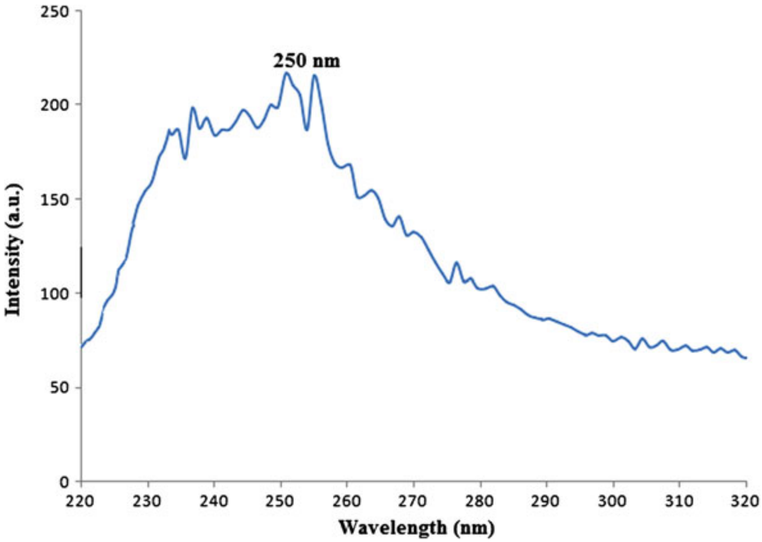

Fig. 5.5 Excitation of the $NaCaPO_4$:Mn^{2+} monitored at 520 nm

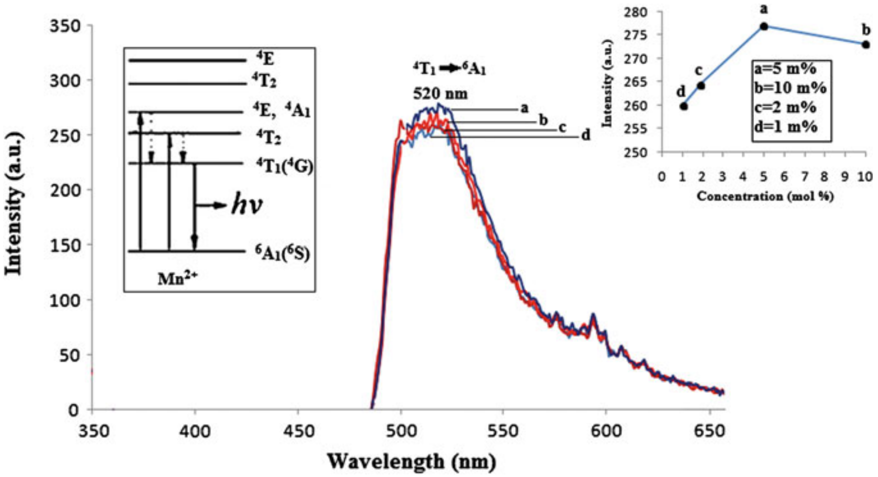

Fig. 5.6 Emission of $NaCaPO_4{:}Mn^{2+}$ when excited at 250 nm

A visible emission from Mn^{2+} ion may vary from green to orange/red [24, 25] depending on the site occupied by the ion in a host matrix. The green emission is obtained at 520 nm when Mn^{2+} occupies a site which is considerably larger than its radius. The $NaCaPO_4{:}Mn^{2+}$ (Fig. 5.6) shows a high noise signal because of the very low intensity due to the lack of efficient excitation processes. It is observed that Mn^{2+} emission is from only one site in the lattice, viz, the Ca^{2+} site, which is the most obvious site for Mn^{2+} considering valence, size, and emission wavelength. Moreover, the emission band of Mn^{2+} exhibits a shoulder peak at the side of higher wavelengths, which may be ascribed to a different Mn^{2+} center [26, 27]. Another possible explanation for the appearance of this shoulder peak in this phosphor is the formation of paired or clustered Mn^{2+} centers beside the Mn^{2+} center on the regular Ca^{2+} site in $NaCaPO_4$. It is also clearly seen (right inset of Fig. 5.6) that the intensity increases with an increase in concentration from 1 to 5 mol% of Mn^{2+} and decreases slightly when the concentration is increased above 5 mol%. The $NaCaPO_4{:}Mn^{2+}$ phosphor shows potential at shorter wavelengths.

5.2.2.4 Photoluminescence Study of Gd^{3+} Activated $NaCaPO_4$

The PL excitation and emission spectra of Gd^{3+} activated $NaCaPO_4$ phosphor are shown in Figs. 5.7 and 5.8, respectively. The Fig. 5.7 shows an excitation spectrum having multiple peaks around 260–300 nm with a maximum intensity at 274 nm. This peak is due to the $^8S_{7/2} \rightarrow {}^6I_J$ transition. Thus, for PL characterization of Gd^{3+} activated $NaCaPO_4$ phosphor we select 274 nm as excitation wavelength. This excitation peak is part of the Hg emission broad band peak as Hg gives about 85 % emission around the 254 nm broad peak and 15 % at other wavelengths. Therefore,

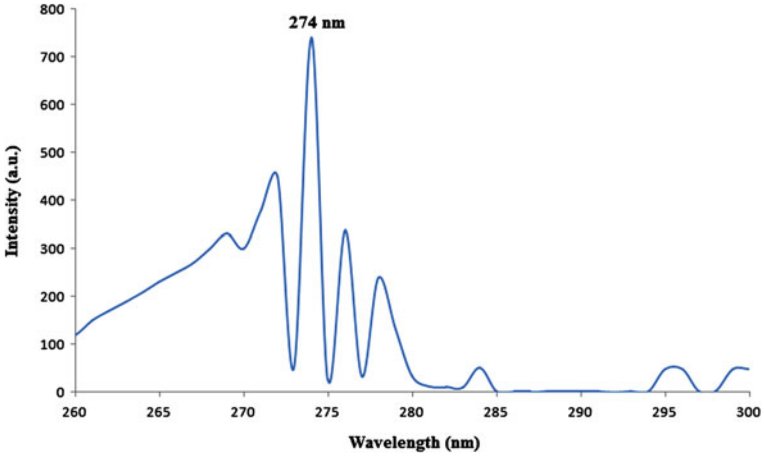

Fig. 5.7 Excitation of the $NaCaPO_4:Gd^{3+}$ monitored at 313 nm

observed excitation of prepared $NaCaPO_4:Gd^{3+}$ phosphor may be applicable in Hg excited lamps for a choice of applications.

Figure 5.8 shows the emission of $NaCaPO_4:Gd^{3+}$ phosphor when excited at a wavelength of 274 nm. The emission spectrum shows a sharp and isolated peak at 313 nm due to the $^6P_J \rightarrow {}^8S_{7/2}$ transition of the Gd^{3+} ion (see left inset in Fig. 5.8). The ionic radii of Na^+, Ca^{2+}, and Gd^{3+} ions are 102 pm, 99 pm, and 93.8 pm, respectively. Thus, the ionic radius of the Gd^{3+} ion is smaller as compared to those Na^+

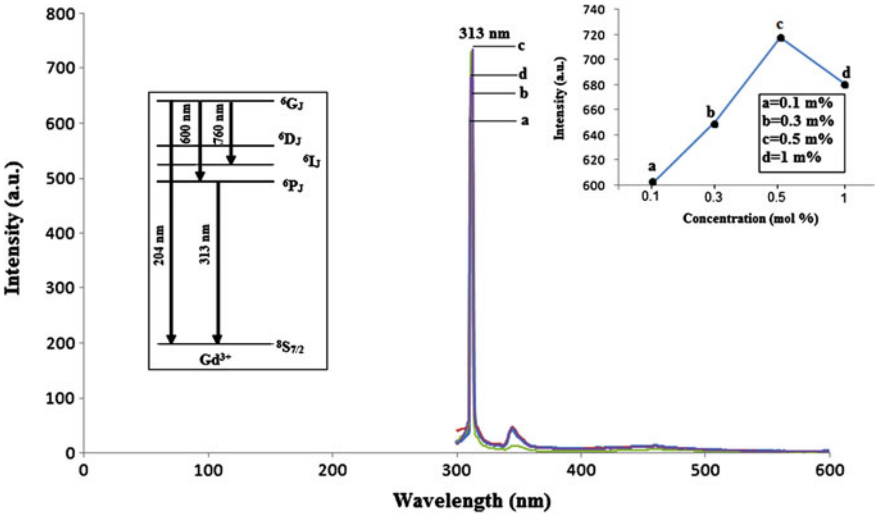

Fig. 5.8 Emission of $NaCaPO_4:Gd^{3+}$ when excited at 274 nm

and Ca^{2+} ions. Moreover, the Gd^{3+} ion is trivalent and acts as a charge compensator. Gd^{3+} ions enter the surrounding of Na^{+} (monovalent) and Ca^{2+} (divalent) ions. The ultraviolet radiation (UVR) induces a wide variety of biological responses depending on the 'action spectra' (wavelength dependence responses) and the 'absorption spectra' of chromophores in the human skin [28]. Therefore, selection of proper wavelength emitting phosphor is of prime importance. Its action spectra, should be in accordance with the biological absorption spectra of the skin (i.e., chromophores) damaged due to a particular disease. In the treatment of skin diseases, two methods are currently used: phototherapy with NB-UVB (311 nm) and photo-chemotherapy PUVA, with UVA (365 nm) and psoralens as photosensitizers. Both forms have their place in dermatology therapy [29]. In Gd^{3+} activated $NaCaPO_4$ phosphor, we observed sharp emission at 313 nm. This emission may be applicable in phototherapy for treatment of the skin, (i.e., chromophores) damaged due to a particular disease. Development of sharp emission phosphor, at 313 nm is very difficult. In this context, some researcher reported Eu^{2+} [1] and Tm^{3+} [30] emission in recent years. Usually, a low doping gives weak luminescence but excess doping perhaps causes quenching of luminescence. With the increase in concentration of Gd^{3+} ions, the peak intensity increases and maximum intensity is observed with 0.5 mol% of Gd^{3+} ion. Thus, introduction of Gd^{3+} activated $NaCaPO_4$ host can be an important development in medical science.

5.3 Conclusions

(1) In the present work, the Dy^{3+}, Mn^{2+}, or Gd^{3+}-doped $NaCaPO_4$ phosphors have been synthesized by the conventional solid-state reaction method. The formation of this compound was confirmed by the XRD technique. SEM images show foam-like morphology with average crystallite size in the submicrometer range.
(2) The emission spectrum of $NaCaPO_4$:Dy^{3+} (at 386 nm excitation) has two intense broad band centered at 480 and 573 nm, which correspond to blue and yellow regions of the visible spectrum, respectively. These two emissions could be used for the development of white LEDs.
(3) The $NaCaPO_4$:Mn^{2+}, when excited at 250 nm, shows broad band emission in the green region, i.e., at around 520 nm. Phosphor with such emission has a practical importance in lamp industry and display device applications.
(4) Gd^{3+} activated $NaCaPO_4$ phosphor, the sharp emission is observed at 313 nm. This emission may be applicable in phototherapy for treatment of the skin (i.e., chromophores) damaged due to any particular disease. The development of phosphors with sharp emission at 313 nm, as reported in this paper could be a valuable technological achievement.

5.4 Photoluminescence Studies of $NaCaPO_4$:RE (RE = Ce^{3+}, Eu^{3+}, and Dy^{3+}) and by Combustion Synthesis [31]

5.4.1 Experimental

The Ce^{3+}, Eu^{3+}, and Dy^{3+} activated $NaCaPO_4$ phosphors were prepared via combustion synthesis. The starting AR grade materials (99.99 % purity) taken were calcium nitrate ($Ca(NO_3)_2{\cdot}4H_2O$ Merck), ammonium di-hydrogen phosphate ($NH_4H_2(PO_4)$, Merck), sodium nitrate ($NaNO_3$, Merck), dysprosium oxide (Dy_2O_3, REI 99.9 %), europium oxide (Eu_2O_3, REI 99.9 %), di ammonium cerium nitrate ($(NH_4)_2Ce(NO_3)_6$, Merck), and urea (NH_2CONH_2, Merck) was used as fuel. The mixture of reagents, was mixed to obtain a homogeneous solution. Dy^{3+} ions were introduced as of $Dy(NO_3)_3$ solution, by dissolving Dy_2O_3 into diluted HNO_3 solution. For the preparation of $NaCaPO_4$:Dy^{3+} phosphor, the molar ratio of rare earth was varied in the $NaCaPO_4$:Dy^{3+} phosphor relative to the Ca^{2+} ions. For various compositions of the metal nitrates (oxidizers) the amount of urea (fuel) was calculated by maintaining total oxidizing and reducing valences of the components equal to unity, so that the heat liberated during combustion is a maximum. After stirring for about 30 min, the precursor solution was transferred to a furnace preheated to 550–650 °C and the porous products were obtained. The stoichiometric amount of redox mixture, when heated rapidly at ~600 °C got boiled, underwent dehydration followed by decomposition generating combustible gases such as oxides of N_2, H_2O, and nascent oxygen. The volatile combustible gases ignited and burnt as a flame, and thus provided conditions suitable for the formation of phosphor lattice with dopants. Large amounts of escaping gases dissipated heat and prevented the material from sintering, and thus provided conditions for the formation of crystalline phase. Rare-earth ion doped $NaCaPO_4$ phosphors were prepared by introducing Ce, Eu, and Dy ions as $(NH_4)_2Ce(NO_3)_6$, $Eu(NO_3)_3$, and $Dy(NO_3)_3$, respectively in solutions with different concentrations and the procedure was repeated as explained above.
The chemical reaction is given as follows:

$$\mathbf{NaNO_3 + Ca(NO_3)_2 \cdot 4H_2O + NH_4H_2(PO_4) + 2NH_2CONH_2}$$
$$\mathbf{\rightarrow NaCaPO_4 + 8H_2O + 2CO_2 + 4N_2}$$

Several complementary methods were used to characterize the prepared phosphor. The prepared host lattice was characterized for their phase purity and crystallinity, by XRD using a PAN-analytical diffractometer (Cu-Ká radiation) at a scanning step of 0.010, continue time 20 s, in the 2θ range from 10 to 120 °; the average crystallite size was calculated from the broadening of the X-ray line (311) using Scherer's equation. The PL measurement of excitation and emission was recorded on the Shimadzu RF5301PC Spectrofluorophotometer. The same amount of the sample 2 g was used for each measurement. Emission and excitation spectra were recorded using a spectral slit width of 1.5 nm. The morphology of the products were examined by scanning electron microscopy (SEM, JEOL 6380A).

5.4.2 Results and Discussion

5.4.2.1 Structural Behavior, XRD, and Morphology of $NaCaPO_4$

As an important family of luminescent materials, orthophosphates have been paid intense attention because of their excellent properties, e.g., the large band gap and the high absorption of PO_4^{3-} in VUV region, moderate phonon energy, the high thermal and chemical stability, and the exceptional optical damage threshold [32–34]. The Fig. 5.9 shows that the $NaCaPO_4$ has an orthorhombic crystal structure (Buchwaldite) and their lattice parameters values are $a = 0.6797$ nm, $b = 0.9165$ nm, and $c = 0.5406$ nm [35]. Figure 5.10 shows the XRD pattern of $NaCaPO_4$ and it agrees well with Joint Committee on Powder Diffraction Standards (JCPDS No. 029-1193). The XRD pattern did not indicate the presence of the constituents like, $Ca(NO_3)_2{\cdot}4H_2O$, $NaNO_3$, or $NH_4H_2PO_4$ and other likely phases,

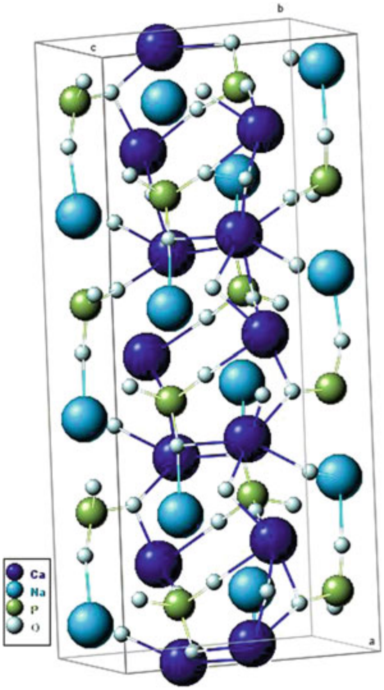

Fig. 5.9 Crystal structure of the $NaCaPO_4$ [35]

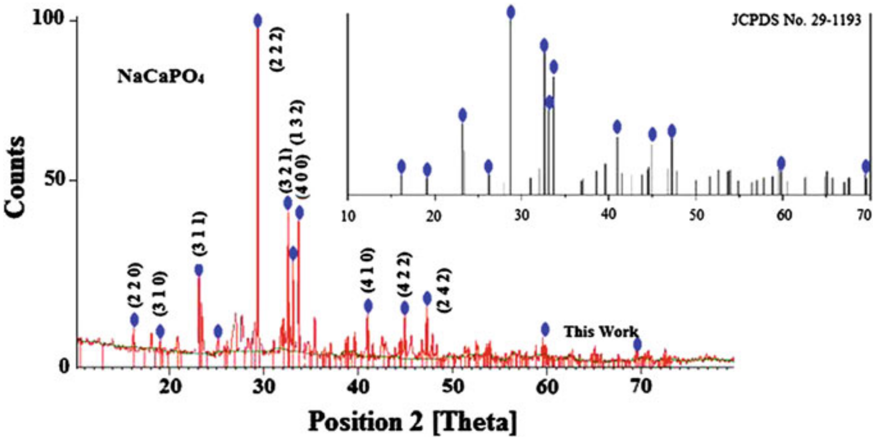

Fig. 5.10 XRD of the $NaCaPO_4$ host lattice

which is a direct evidence for the formation of the desired compound. These results indicate that the final product was formed in crystalline and homogeneous form.

Axial Ratios: $a:b:c = 0.558:1:0.7276$

Cell Dimensions: $a = 5.167$, $b = 9.259$, $c = 6.737$, $Z = 4$;

$V = 322.31$ Den(Calc) $= 3.26$

Crystal System: Orthorhombic-Pyramidal

Formula: $NaCa(PO_4)$

Fig. 5.11 SEM images of the $NaCaPO_4$

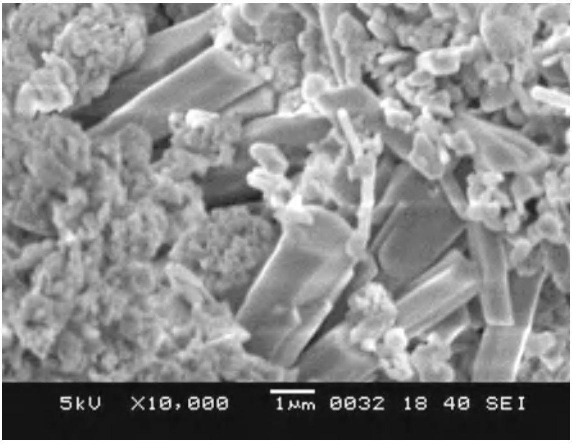

It is clearly seen from Fig. 5.11 that the grains have an irregular shape of particles with a size of about 0.5–1 μm. This shows that the combustion reactions of the mixture took place well. The typical morphological images are represented in Fig. 5.11. The particles possess foamy-like morphology formed from highly agglomerated crystallites and the particles are globular in appearance. An average crystallite size is in submicrometer range and formation of rod type structure is seen in SEM images. This indicates that this experimental processing is favorite for the crystalline growth of Buchwaldite type of crystal structure.

5.4.2.2 PL Properties of $NaCaPO_4:Ce^{3+}$

Ce^{3+} is a very good candidate as activator as well as sensitizer, for studying the behavior of 5*d* electrons. Ce^{3+} has only one outer electron and only two spin-orbital splitting 4*f* states ($^2F_{5/2,\,7/2}$). Thus, its excited state energy structure is simpler than that of the other trivalent rare-earth ions. PL excitation spectra of the $NaCaPO_4:Ce^{3+}$ phosphor are shown in Fig. 5.12. The broad band is observed at 249–251 nm with a prominent shoulder ($\lambda_{emi} = 367$ nm). Figure 5.13 shows the PL emission spectra of Ce^{3+} ions in the $NaCaPO_4$ phosphor with different concentrations under the same excitation (i.e., 251 nm) wavelengths of light. Two emission peaks are observed from 350 to 370 nm, which are assigned to the 5*d*–4*f* transition of Ce^{3+} ions. The highest intensity observed at 367 nm due to the $^2D(5d) \rightarrow {}^2F_{7/2}(4f)$ transition between two peaks. The increase in the concentration of Ce^{3+} ion, increases the corresponding intensity of all the peaks up to the higher concentration of 2 mol% of Ce^{3+} ions. This indicates a change of the surrounding of Ce^{3+} ions, at higher concentration in the $NaCaPO_4$ lattice. The intensity of the Ce^{3+} emission, at 367 nm is greater than

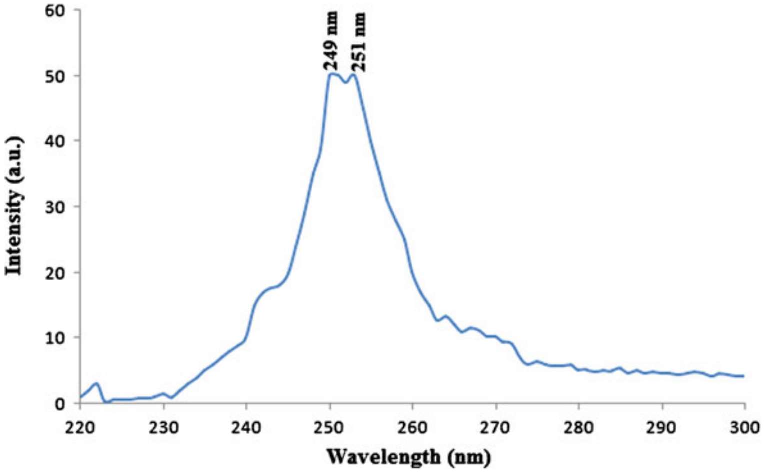

Fig. 5.12 PL excitation spectra of the $NaCaPO_4:Ce^{3+}$ when monitored at 367 nm

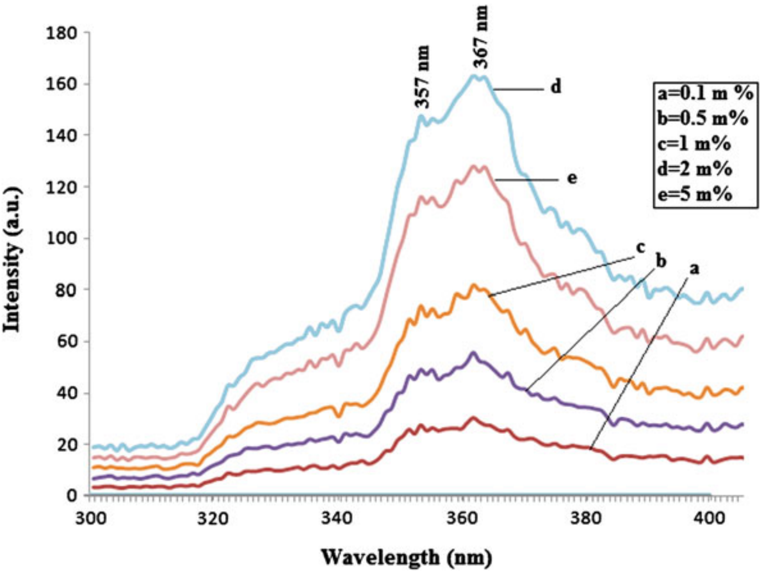

Fig. 5.13 PL emission spectrum of the NaCaPO4:Ce^{3+} when excited at 251 nm

other observed peaks. Variations observed in the PL emission intensities, may have cross relaxation between Ce^{3+} ions in the case of a highly doped concentration of Ce^{3+}. The Ce^{3+} ion can be used as sensitizer as well as an activator, depending on the splitting of the 5*d* excited levels by the crystal field symmetry.

Ce^{3+} can be used as a probe or reference of 5*d* states for other rare-earth ions in a specific host lattice based on the following considerations (Fig. 5.14). First, Ce^{3+} ions are represented by a simple one-electron system. The electron configurations of the ground and excited states of Ce^{3+} are $^4f_1 5d_0$ and $^4f_0 5d_1$, respectively. Therefore, no extra line or band is caused by the interactions of f–f or f–d electrons occurred in its excitation spectrum, and the excitation spectrum directly exhibits the information on the crystal field splitting of the 5*d* states [36]. Second, it is known that the lowest 5*d* state energy of different rare-earth ions in same host lattice site can be analyzed quantitatively [37], therefore, the lowest 5*d* energies for other RE^{3+} ions can be predicted when the lowest 5*d* energy of Ce^{3+} in same host lattice site is known. Third, a general similar 5*d* crystal field splitting is expected for different RE^{3+} ions in the same host lattice site, therefore, all split 5*d* energies for other RE^{3+} can be estimated largely in terms of the spectrum of the Ce^{3+} ion. In this presentation, the emission of the Ce^{3+} might be applicable for applications in a scintillator.

Theoretical calculation has confirmed that the lowest intramolecular $2t_2 \rightarrow 2a$, $3t_2$ transition energy of the tetrahedral $PO_4{}^{3-}$ molecule is around 177–124 nm [38]. It is evident that the intrinsic absorption of PO_4^{3-} is located around this range. The wavelength region from 200 to 350 nm is due to allowed transitions from the ground state to the crystal field splitting of 5*d* level. It is known that the 4*f* configuration of

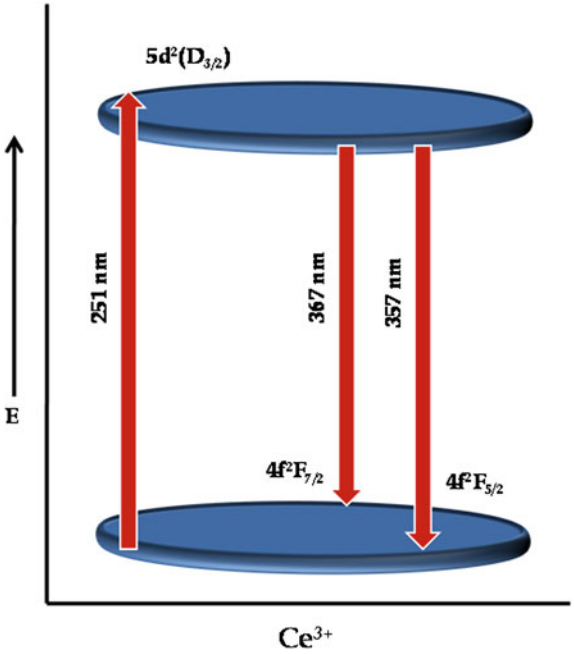

Fig. 5.14 Schematic energy level diagram of Ce^{3+} in $NaCaPO_4$

Ce^{3+} ion has one electron and irradiation of UV photon will excite this 4*f* electron into a 5*d* orbital, leaving the 4*f* shell empty (see Fig. 5.14). So the excitation spectrum of Ce^{3+} ion shows the direct splitting information of 5*d* orbital in the crystal field. It has been reported that the *f*–*d* transition of Ce^{3+} ion will exhibit subtle structure due to the influence of crystal field splitting and spin–orbit coupling [39]. According to the curve shape of Fig. 5.12, it can be seen that the *f*–*d* excitation spectrum of Ce^{3+} has been split into two different crystal field components of 249 and 251 nm respectively. Generally, the emission spectra of Ce^{3+} ions have a doublet character due to the spin–orbit splitting of ground state. Under the 251 nm excitation, the Ce^{3+} ions show efficient ultraviolet luminescence. The two $5d\ (1) \rightarrow 2F_J$ ($J = 5/2, 7/2$) subbands are well resolved at room temperature and curve is shown in Fig. 5.13. The emission band has two maxima at 357 and 367 nm.

5.4.2.3 PL Properties of $NaCaPO_4$:Eu^{3+}

Eu^{3+} ions emit a characteristic red light with several narrow lines due to the $4f \rightarrow 4f$ ($^5D_0 \rightarrow {}^7F_{i=0,1,2,3,4}$) transitions [40, 41]. The luminescence spectrum of Eu^{3+} ion is slightly influenced by the surrounding ligands of the host material, because the transitions of the Eu^{3+} involve only a redistribution of electrons within the inner 4*f* sub-shell [42]. Fluorescence spectra of Eu^{3+}-doped $NaCaPO_4$ were measured at room temperature (Fig. 5.15), the following emission transitions are observed:

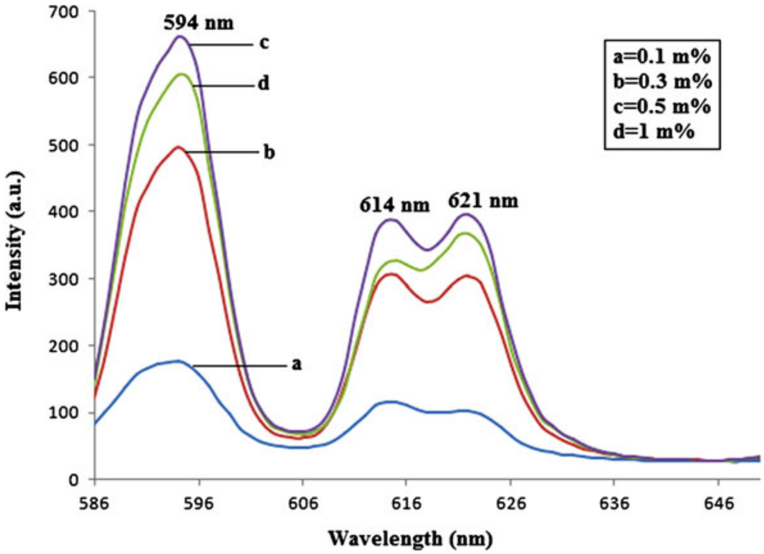

Fig. 5.15 PL emission spectrum of $NaCaPO_4:Eu^{3+}$ when excited at 393 nm

${}^5D_0 \rightarrow {}^7F_1$ at 594 nm and ${}^5D_0 \rightarrow {}^7F_2$ at (611–620 nm). Out of them, the ${}^5D_0 \rightarrow {}^7F_1$ transition is the strongest. Due to the magnetic dipole transitions ${}^5D_0 \rightarrow {}^7F_1$ and electric dipole transitions ${}^5D_0 \rightarrow {}^7F_2$, this phosphor exhibits orange color emission. According to the Judd–Ofelt theory, the magnetic dipole transition is permitted. But, the electric dipole transition is allowed exceptionally on the condition that the Eu ion occupies a site without an inversion center, and is sensitive to local symmetry. Consequently, the ${}^5D_0 \rightarrow {}^7F_1$ transition should be relatively strong when the Eu^{3+} ions occupy inversion center sites, while the ${}^5D_0 \rightarrow {}^7F_2$ transition must be relatively weak [43]. Also, according to Rambabu et al. and Yu et al., the transition ${}^5D_0 \rightarrow {}^7F_1$ displayed more intensity (1u.a) than ${}^5D_0 \rightarrow {}^7F_2$ transition (0.44 u.a) due to the localized energy transfer [43, 44]. The intensity of these emission transitions is usually used to gage the quality of the luminescent material. The highest intensity of the ${}^5D_0 \rightarrow {}^7F_1$ transition indicates that Eu^{3+} ions have centro-symmetrical environment in the *P*21/*n* structure. Due to the little difference between ionic sizes of Eu^{3+} ion (94.7 pm) and Ca^{2+} ion (99 pm), we presume that Eu^{3+} ions can occupy Ca^{2+} ion sites, which causes a characteristic crystal splitting of the energy levels. The transitions are found to be split into components depending on the host matrix composition. Due to the dependency between ${}^5D_0 \rightarrow {}^7F_1$ emissions and the crystal field, ${}^7F_1$ associated with (one) site symmetry can split into three Stark lines in the crystal field and the ${}^5D_0 \rightarrow {}^7F_2$ transition of Eu^{3+} can split into, at most, five lines in the crystal field [45].

In our case, the PL excitation spectra of the prepared Eu activated $NaCaPO_4$ phosphor are shown in Fig. 5.16. The prominent excitation band at 393 nm may be due to $f-f$ transitions of the Eu^{3+} ion. The PL excitation spectrum is broad

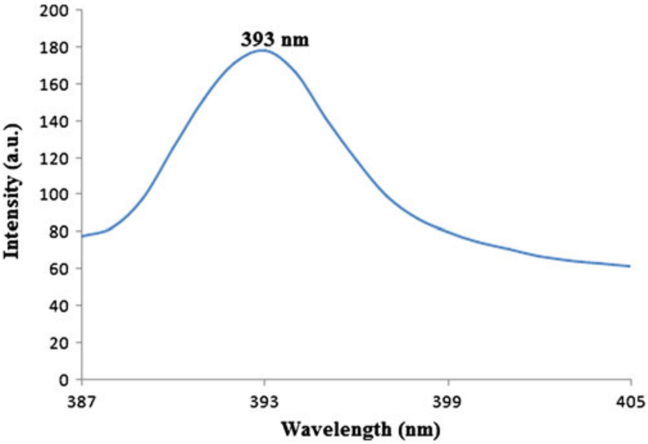

Fig. 5.16 PL Excitation spectra of NaCaPO4:Eu^{3+} when monitored at 594 nm

and maximizes at 393 nm in the LED phosphors excitation region. The PL emission spectrum ($\lambda_{exc} = 393$ nm) consists of the intense peak at 594 nm (orange) that can be ascribed to $^5D_0 \rightarrow {}^7F_1$ transition of Eu^{3+} ion and other peaks at 614 nm (red) and 621 nm (red) which can be associated with the $^5D_0 \rightarrow {}^7F_2$ and $^5D_0 \rightarrow {}^7F_3$ transition, respectively of the Eu^{3+} ion, respectively shown in Fig. 5.15. The 594, 614, and 621 nm emission of the Eu^{3+} ion in the host of the $NaCaPO_4$ material was very applicable as an orange/red phosphor for solid-state lighting. The excitation wavelength of this phosphor is 393 nm, which is far away from Hg excitation as well as this excitation is the main characteristic of solid-state lighting (in the range 365–395 nm near UV region) in the lamp industry. The broadness of the excitation spectrum means that the phosphors can be well excited by near UV light in the range 365–395 nm, matching well with the emission bands of the near UV LED chips [46]. The excitation spectra show that these phosphors can be well excited by near UV light which is exactly required by UV chip pumped multi-phosphor converted white LEDs. The Commission International de l′Éclairage (CIE) chromaticity coordination (x, y) of the NaCaPO4:Eu^{3+} phosphor, calculated from the emission spectrum is (0.5976, 0.4017), which locates in the red region in the CIE map. These results indicate that NaCaPO4:Eu^{3+} is a promising red phosphor candidate for LEDs.

Therefore, this phosphor is one candidate of orange/red phosphor for LED lighting. The PL intensity increased with concentration from 0.1 to 1 mol% and it decreased at more than 0.5 mol% probably due to concentration quenching effect. For the Eu^{3+} ion, the relative intensity of the 594 nm to the 621 nm peaks strongly depends on the local site symmetry around the Eu^{3+} ions.

The energy level diagram (Fig. 5.17) shows the states involved in the luminescence process and the transition probabilities for Eu^{3+} ions. According to this model, the system is first excited from the ground state ($^5D_3$ configuration) to the singlet state of the $^5D_{3,2,1,0}$ configuration and then the electrons pass to the triplet state, mainly to

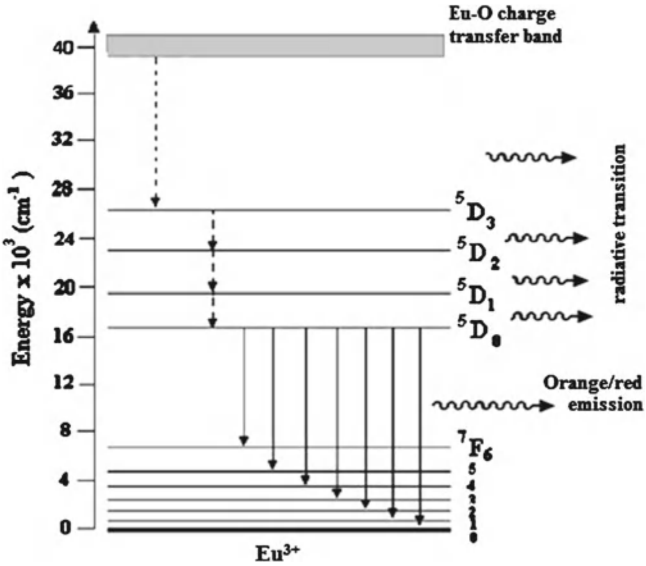

Fig. 5.17 Energy level of Eu^{3+} ion diagram showing the states involved in the luminescence process and the transition probabilities

level 4 because of symmetry reasons. The last transition ^{5}D$_0$ is so much faster than any other step of the luminescent process, that it may be considered instantaneous; it follows that the singlet state does not affect the luminescent process. Non-radiative transitions may occur between 3 energy levels of the triplet state, named ^{5}D$_3$, ^{5}D$_2$, ^{5}D$_1$, and ^{5}D$_0$ with probabilities from level 3 to level 2, from level 2 to level 1, and level 2 to level 0, i.e., ^{5}D$_0$. From level ^{5}D$_0$ to level ^{7}F$_{0,1,2,3}$ radiative transitions to the ground state (level 1) ^{5}D$_0$ →^{7}Fj states occur, respectively. The PL intensity of Eu^{3+} emission at 614 and 621 nm is less as compared to the 594 nm peaks. The increase of PL emission intensity observed may be due to the decrease of cross-relaxation between Eu^{3+} ions (in this process, excited ion transfers only part of energy to another ion) in case of higher concentration of Eu^{3+}.

5.4.2.4 PL Properties of NaCaPO$_4$:Dy^{3+}

The emission and excitation spectra of NaCaPO$_4$:Dy^{3+} phosphors are presented in this section. The intense excitation peak is observed at 349 nm and other weak peaks are also observed at 325–387 nm as shown in Fig. 5.18 and only emission intensity varies with respect to all three excitation wavelengths. In this context, excitation curve 387 nm peak is near UV excitation which is more applicable (i.e., 385–395 nm) for LED phosphor. Accordingly, out of all three peaks we select the 387 nm peak for excitation in the experimental work. The emission spectrum

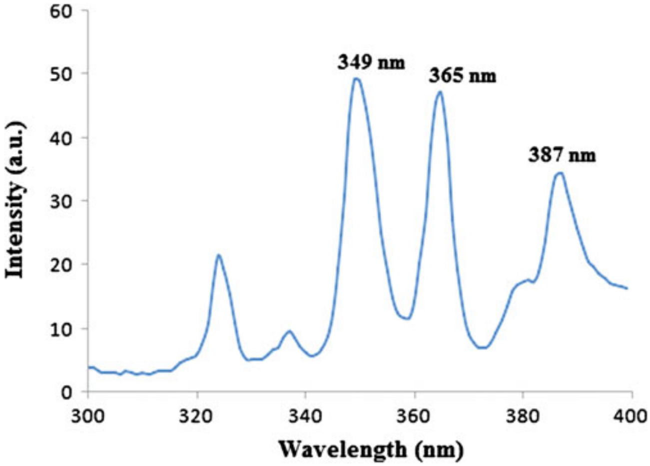

Fig. 5.18 PL excitation spectra of $NaCaPO_4$:Dy^{3+} when monitored at 482 nm

shows (Fig. 5.19) that and all the samples have two emission bands: one is centered at 482 nm (blue) and another at 576 nm (yellow). They are assigned to the Dy^{3+} electronic transitions of $^4F_{9/2} \rightarrow {}^6H_{15/2}$ and $^6H_{13/2}$ energy levels, respectively. A series of $NaCa_{1-x}PO_4$:Dy_x^{3+} phosphor with various Dy^{3+}concentrations ($x = 0.1$ mol% -1 mol%) was prepared and the effect of doped Dy^{3+}concentration on the emission intensity was investigated.

Emission intensity of $NaCa_{1-x}PO_4$:Dy_x^{3+} with different Dy^{3+} concentration is shown Fig. 5.19. The positions of the emission peak are not influenced by the Dy^{3+} concentration. The emission intensity increases with increasing of Dy^{3+} concentration and reaches the maximum at about 0.5 mol%. Concentration quenching occurs,

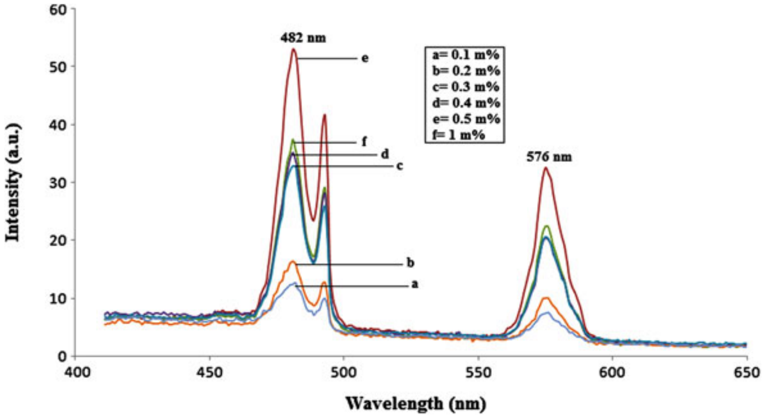

Fig. 5.19 PL emission spectrum of $NaCaPO_4$:Dy^{3+} when excited at 387 nm

when the Dy^{3+} concentration is beyond 0.5 mol%. PL results show the excitation peak at 387 nm, which is away from Hg excitation and is useful for solid-state lighting in lamp industry. PL emission peaks are observed at blue and yellow region of the spectrum due to Dy^{3+} ion. Thus, PL characterization of $NaCaPO_4$:Dy^{3+} phosphors show that it could be applicable for LED phosphor.

The excitation spectrum in the range 300–400 nm consists of the $f \rightarrow f$ transition of the Dy^{3+} ion, i.e., 387 nm ($^6H_{15/2} \rightarrow {}^6F_{9/2}$ transition). The emission spectra for the Dy^{3+} ions in $NaCaPO_4$ show emissions at 482 nm (blue) and 576 nm (yellow). These two different emission bands originated from one origin due to their excitation at same 387 nm wavelength. The transitions involved in blue and yellow bands of Dy^{3+} ion are well-known and have been identified as $^4F_{9/2} \rightarrow {}^6H_{15/2}$ and $^6H_{13/2}$ transitions, respectively [47]. The energy levels of Dy^{3+} ion and emission transitions are presented in Fig. 5.20 [48]. It is known that Dy^{3+} emission around 482 nm ($^4F_{9/2} \rightarrow {}^6H_{15/2}$) is of magnetic dipole origin and 576 nm ($^4F_{9/2} \rightarrow {}^6H_{13/2}$) is of electric dipole origin. $^4F_{9/2} \rightarrow {}^6H_{15/2}$ is predominant only when Dy^{3+} ions are located at low-symmetry sites with no inversion centers [49]. The low-symmetry location of Dy^{3+} results in the predominate emission of $^4F_{9/2} \rightarrow {}^6H_{15/2}$ transition (see Fig. 5.19). Since emission at 482 nm is predominant, it suggests that there is a very little deviation from inversion symmetry in this matrix. The optical properties of the materials are often influenced by the structure of the matrix and synthesis technique [50]. Thus, the yellow–blue ratio, known as the asymmetry ratio of Dy^{3+},

Fig. 5.20 The energy levels of Dy^{3+} ion and emission transitions

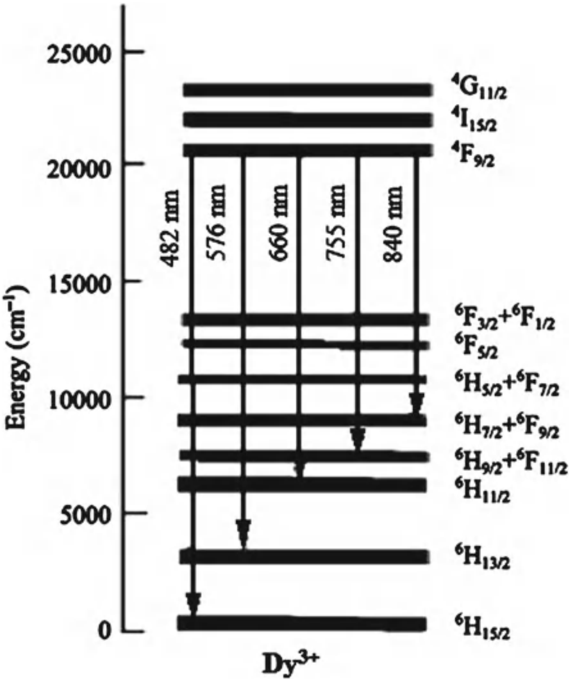

varies while locating in different host lattices. Kuang et al. [47] reported that, in the Dy^{3+}-doped $SrSiO_3$ system, with increasing calcining temperature, the yellow–blue ratio increased due to the change in the local site symmetry around the Dy^{3+} ion. In our case, Dy^{3+} ion may enter the host lattice to substitute Na^+ or Ca^{2+} or locate on surfaces of the crystal due to the porosity of the structure. The ionic radius of Dy^{3+} (91.2 pm) is much smaller than that of Ca^{2+} (99 pm) and Na^+ (102 pm). Therefore, most of the Dy^{3+} ions entered the lattice with few of them located at the surface of the $NaCaPO_4$ host. The occupation of Dy^{3+} ion into Na^+ and Ca^{2+} sites in $NaCaPO_4$ host would naturally cause a substantial number of vacant sites in the oxygen ion array and then expand the lattice to decrease crystal density. That is, the formation of Dy^{3+} due to Na^+ or Ca^{2+} in $NaCaPO_4$ host induces more oxygen vacancies. Lopez et al. [23] reported that the oxygen vacancies acted as sensitizers for the energy transfer to the rare-earth ion due to the strong mixing of charge transfer states, resulting in highly enhanced luminescence. However, excess oxygen vacancies in the host would inevitably destroy the crystallinity, which lead to quenching of the luminescence. Of course, the more important reason is that more Dy^{3+} entered the lattice, which can enhances the ${}^4F_{9/2} \rightarrow {}^6H_{15/2,13/2}$ transitions of the samples greatly, as shown by Fig. 5.19. From this emission spectrum, it is clearly observed that the fluorescence intensities ratio increases gradually. Different doping of activator ions can influence photoluminescence characteristics of a phosphor. Usually, a low doping gives weak luminescence, but excess doping can cause quenching of luminescence. With increasing concentration of Dy^{3+} ions the peak intensity increased and maximum intensity was observed for 0.5 mol% Dy^{3+} ion. The increase in the luminescence intensity with increase in concentration of Dy ion can be explained as follows: the luminescence spectrum of Dy^{3+} ion was slightly influenced by the surrounding ligands of the host material, because electronic transitions of Dy^{3+} involve only redistribution of electrons within the inner $4f$ sub-shell. Crystallinity of phosphor could be increased due to the increase in concentration of the Dy ion, since clearly the addition of Dy ion into the $NaCaPO_4$ host increased the crystallinity. An increase in the concentration of Dy ions increased the particle size as well as its complexity. Hence, there was an increase in photoluminescence intensity. This indicates that the $NaCaPO_4$ lattice is more suitable for higher concentrations of Dy^{3+} ions.

5.4.2.5 Chromatic Properties

Most lighting specifications refer to color in terms of the 1931 CIE chromatic color coordinates which recognize that the human visual system uses three primary colors: red, green, and blue [51, 52]. In general, the color of any light source can be represented on the (x, y) coordinate in this color space. The color purity was compared to the 1931 CIE Standard Source C (illuminant Cs (0.3101, 0.3162)). The chromatic coordinates (x, y) was calculated using the color calculator program radiant imaging [53]. The coordinates of the $NaCaPO_4$:Eu^{3+} phosphors of color orange ($x \approx 0.5976$, $y \approx 0.4017$) and $NaCaPO_4$:Dy^{3+} phosphor of color range

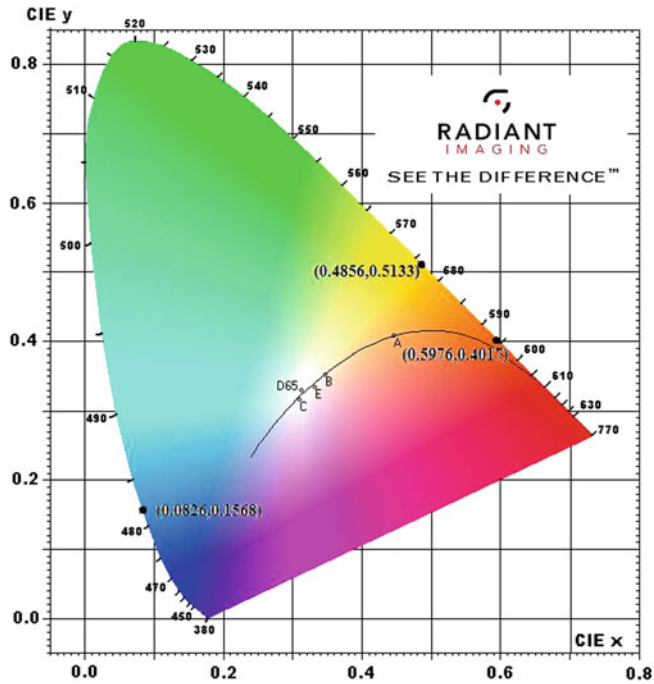

Fig. 5.21 CIE chromatic diagram showing the chromatic coordinates

blue ($x \approx 0.0826$, $y \approx 0.1568$) / yellow ($x \approx 0.4856$, $y \approx 0.5133$) are shown in Fig. 5.21 by solid circle sign (•). The location of the color coordinates of the Eu^{3+} and Dy^{3+} $NaCaPO_4$ phosphate-based phosphor on the CIE chromaticity diagram, presented in Fig. 5.21, indicates that the color properties of the phosphor powder prepared by combustion method is approaching those required for field emission displays. The dominant wavelength is the single monochromatic wavelength that appears to have the same color as the light source. The dominant wavelength can be determined by drawing a straight line from one of the CIE white illuminants (*C*s (0.3101, 0.3162)), through the (x, y) coordinates to be measured, until the line intersects the outer locus of points along the spectral edge of the 1931 CIE chromatic diagram.

All the results calculated from the emission spectra in Figs. 5.15 and 5.19 are plotted in the Commission International de l′E′clairage (CIE) 1931 chromaticity diagram, as shown in Fig. 5.21. It indicates that present phosphors are close to the edge of the CIE diagram, which indicates the high color purity of these phosphors. By connecting these two points as a triangle (included white light point (0.31, 0.32)) the intermediate compositions can generate warm white light with a particular ratio of this phosphor.

5.5 Conclusions

In this chapter, sodium calcium phosphate doped with rare-earth ions Ce^{3+}, Eu^{3+} and Dy^{3+} prepared by the combustion method and confirmed by XRD is described. The photoluminescence characterization of prepared phosphors shows the role of rare-earth ions in the host lattice. The PL spectroscopic characterizations of the prepared phosphors are done using excitation and emission spectra. Under UV excitation (251 nm) $NaCaPO_4$:Ce exhibits Ce^{3+} émission (367 nm) in UV range. This émission of Ce ions might be applicable in a scintillator. In the Eu activated $NaCaPO_4$ phosphor the emission spectrum shows a dominant peak at 594 nm (orange) while others is at 614 nm (red) when excited at 393 nm. When $NaCaPO_4$:Dy^{3+} phosphor excited at 387 nm, the emission spectrum shows intense bands at 482 nm (blue), and 576 nm (yellow). Both Eu^{3+} and Dy^{3+} activated $NaCaPO_4$ phosphors show the excitation in the range of 365–395 nm of LED excitation and emission observed in the red and blue/yellow region of the spectrum. These results show that the $NaCaPO_4$:Dy^{3+} and $NaCaPO_4$:Eu^{3+} phosphors could be applicable for LED phosphors. This chapter includes synthesis of efficient phosphate-based phosphors via combustion method, characterized by X-ray diffraction (XRD) pattern, morphological examination by SEM, and photoluminescence (PL) behavior of $NaCaPO_4$-doped with Ce^{3+}, Eu^{3+}, and Dy^{3+}. Results show that these phosphors have potential application in the field of scintillation (Ce activated) and LED (Dy and Eu activated)-based lighting.

5.6 Photoluminescence Studies of Na_3 $Al_2(PO_4)_3$:RE (RE = Ce^{3+}, Eu^{3+} and Mn^{2+}) Phosphor Combustion Synthesis [54]

5.6.1 *Experimental*

The $Na_3Al_2(PO_4)_3$:Ce^{3+}/Eu^{3+}/Mn^{2+} phosphors were prepared via the combustion method. The starting AR grade materials with 99.99 % purity used for the preparation were sodium nitrate ($NaNO_3$), aluminium nitrate ($Al(NO_3)_3{\cdot}9H_2O$), ammonium dihydrogen phosphate ($NH_4H_2(PO_4)$), europium nitrate $Eu(NO_3)_3$, cerium nitrate $Ce(NO_3)_3$, and manganese acetate ($(CH_3COO)_2Mn{\cdot}4H_2O$). Urea ($NH_2CONH_2$) and ammonium nitrate NH_4NO_3 were used as fuel and flux for the synthesis, respectively. Appropriate amounts of (in metrological proportions) these were taken stoichiometrically, homogenized thoroughly, and ground using a mortar and pestle for 30 min. The mixture was stirred for about 30 min, then heated rapidly at ~600 °C. The mixture underwent dehydration followed by decomposition generating combustible gases. The volatile and/or combustible gases such as N_2, H_2O, and nascent O_2 escaped from a firing container leaving behind voluminous foaming fine powder occupying the entire volume of the container. The basic combustion reaction for the formation of $Na_3Al_2(PO_4)_3$ can be described by the following equation:

$$\mathbf{3NaNO_3 + 2Al(NO_3)39H_2O + 3NH_4H_2(PO_4) + 20NH_2CONH_2 + 20NH_4(NO_3)} \\ \mathbf{\rightarrow Na_3Al_2(PO_4)_3 + 47N_2\uparrow + 20CO\uparrow + 85H_2O\uparrow}$$

The dopant concentrations were varied between 0.5 and 5 mol% for Ce^{3+}, 0.2 and 2 mol% for Eu^{3+}, and 5 and 15 mol% for Mn^{2+}.

5.6.2 Results and Discussion

5.6.2.1 XRD and Morphology

Figure 5.22 shows the XRD pattern from un-doped $Na_3Al_2(PO_4)_3$ powder. The patterns were matched with hexagonal (rhombohedral) symmetry of $Na_3Al_2(PO_4)_3$ referenced in JCPDS card No. 31-1265. These patterns are consistent with the ball and stick model of the rhombohedral NASICON structure of $Na_3Al_2(PO_4)_3$ proposed by Shrivastava et al. [55]. The SEM images in Fig. 5.23 show that the particles were

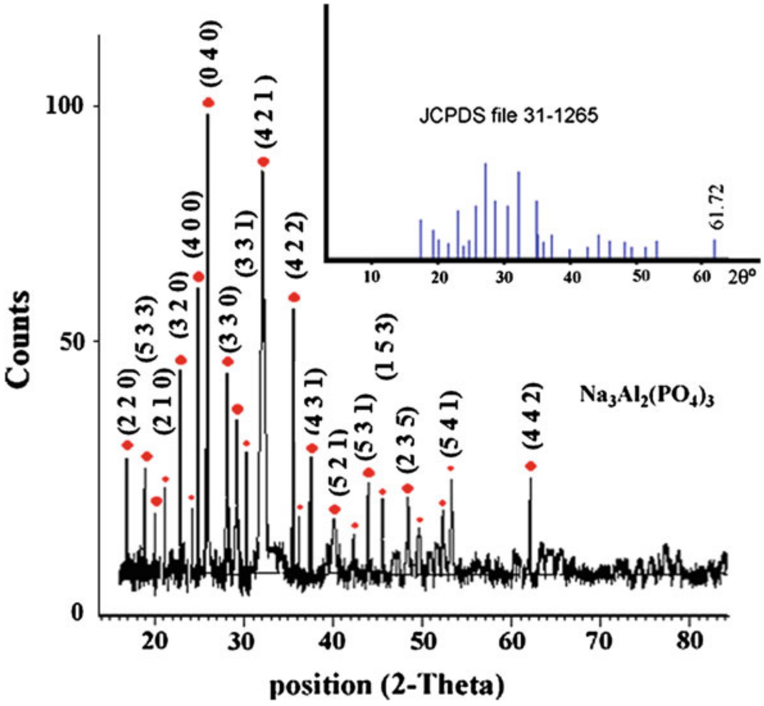

Fig. 5.22 X-ray diffraction pattern of the $Na_3Al_2(PO_4)_3$ host lattice

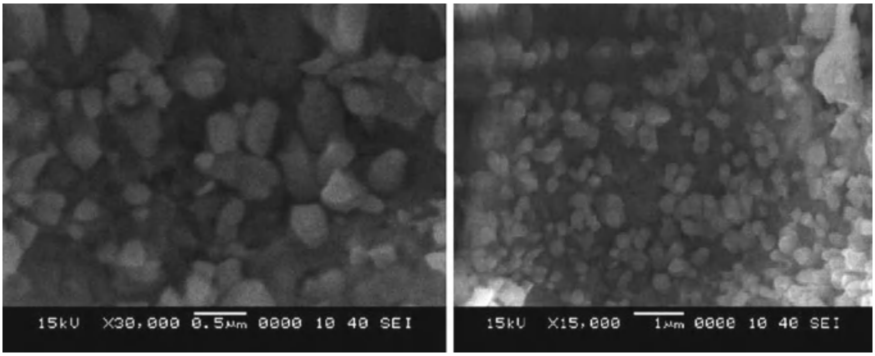

Fig. 5.23 SEM image of $Na_3Al_2(PO_4)_3$ phosphor at different magnifications

spheroidal in shape and the average particle size was estimated to be 0.1–0.4 μm in diameter.

5.6.2.2 PL Properties of $Na_3Al_2(PO_4)_3$:Ce^{3+}

PL excitation (1) and emission (2) spectra of $Na_3Al_2(PO_4)_3$:Ce^{3+} powder phosphor are shown in Fig. 5.24. The emission spectra were measured for the different Ce^{3+} concentrations as indicated. The emission spectrum (excited at 242 nm) has a maximum at 328 nm and a shoulder at 350 nm due to the crystal field splitting of the 4*f* ground state. As shown in the inset of Fig. 5.24, the emission occurs from the

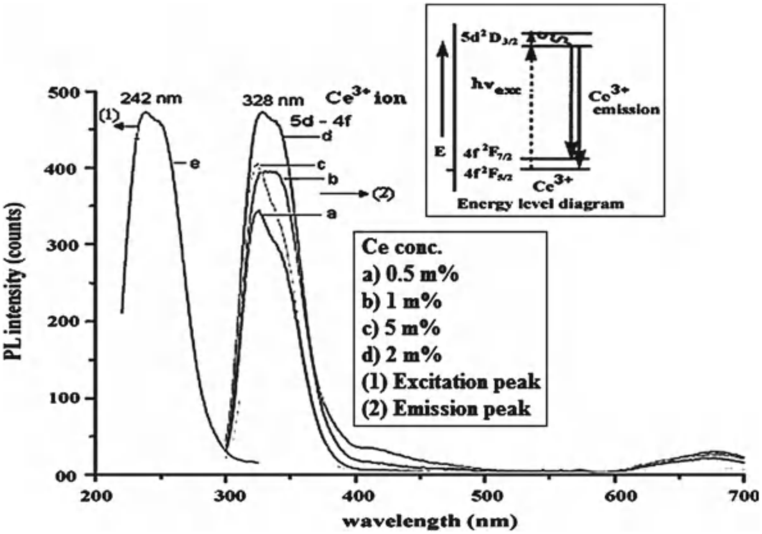

Fig. 5.24 PL emission and excitation spectra of the $Na_3Al_2(PO_4)_3$:Ce^{3+} phosphor, the emission peaks were monitored at $\lambda_{exc} = 242$ nm.

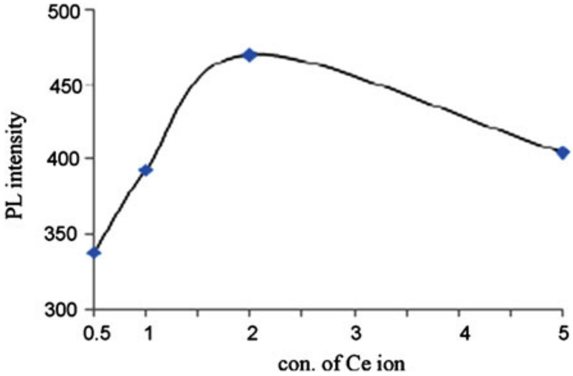

Fig. 5.25 Variation in the PL intensity as function of the Ce^{3+} ion concentration

lowest component of the 5*d* configuration to the two-crystal field split levels ($^2F_{5/2}$ and $^2F_{7/2}$) of the 4*f* ground state. The PL excitation at 242 nm in spectrum (1) is for the 328 nm UV emission. The PL emission intensity was shown to increase with concentration from 0.5 to 2 mol% of Ce^{3+} and quenching occurred at 5 mol% of Ce^{3+} as shown in Fig. 5.25. This decrease in the PL intensity is due to concentration of quenching effects. The observed Ce^{3+} emission in this phosphor can be used in scintillators according to an energy transfer process explained by Lempicki et al. [56] and Wojtowicz et al. [57, 58]. According to this process, Ce^{3+} captures primary excitation energy (hυ) and becomes Ce^{4+}. After capturing a free electron (ec) from the conduction band, Ce^{4+} will be converted to an excited Ce^{3+} ion or $(Ce^{3+})^*$. Relaxation to the ground state will be accompanied by emission of the scintillation photon hυ. This process can be summarized as follows:

$Ce^{3+} + h\upsilon \rightarrow Ce^{4+}$
$Ce^{4+} + e_c \rightarrow (Ce^{3+})^*$
$(Ce^{3+})^* \rightarrow Ce^{3+} + h\upsilon.$

5.6.2.3 PL Properties of $Na_3Al_2(PO_4)_3$:Eu^{3+}

Figures 5.26 and 5.27 represent the PL excitation and emission spectra of $Na_3Al_2(PO_4)_3$:Eu^{3+} powder phosphors, respectively. The emission spectra are from the different Eu^{3+} concentrations as indicated. The PL excitation spectrum is broad and maximizes at 243 nm. This excitation can be ascribed to the $Eu^{3+} \rightarrow O^{2-}$ charge transfer transition. This transition should be followed by nonradiative relaxation to ^5D_J ($J = 0, 1, 2, 3, \ldots$) levels and then radiative transitions from $^5D_0$ to ^7F_J levels of the ground state. The PL emission spectrum of Fig. 5.27 consists of a major line emission at 615 nm and minor emission at 593 nm which can be ascribed to the $^5D_0 \rightarrow {}^7F_2$ and $^5D_0 \rightarrow {}^7F_1$ transitions of Eu^{3+}, respectively. The inset of Fig. 5.27 is a simplified energy level diagram showing nonradiative transitions from charge transfer states followed by radiative transitions from the $^5D_0$ to the ground state. A plot of maximum PL intensity versus concentration in Fig. 5.28 shows that the

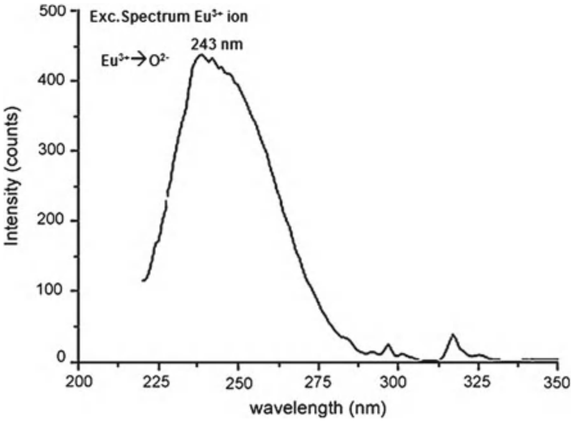

Fig. 5.26 PL excitation spectrum of the $Na_3Al_2(PO_4)_3$:Eu^{3+} phosphor, the excitation peak was monitored at $\lambda_{emi} = 615$ nm

intensity increased with Eu^{3+} concentration from 0.5 to 1 mol% and it decreased slightly when the concentration was increased to 2 mol%. The fact that the excitation wavelength ($\lambda_{exc} = 243$ nm) of the $Na_3Al_2(PO_4)_3$:Eu^{3+} is similar to the discharge wavelength of the fluorescent mercury lamp suggests that this material can be used as a lamp phosphor.

5.6.2.4 PL Properties of $Na_3Al_2(PO_4)_3$:Mn^{2+}

Figure 5.29 shows the PL excitation (1) and emission (2) spectra from $Na_3Al_2(PO_4)_3$:Mn^{2+} powder phosphors. The emission spectra were obtained from different

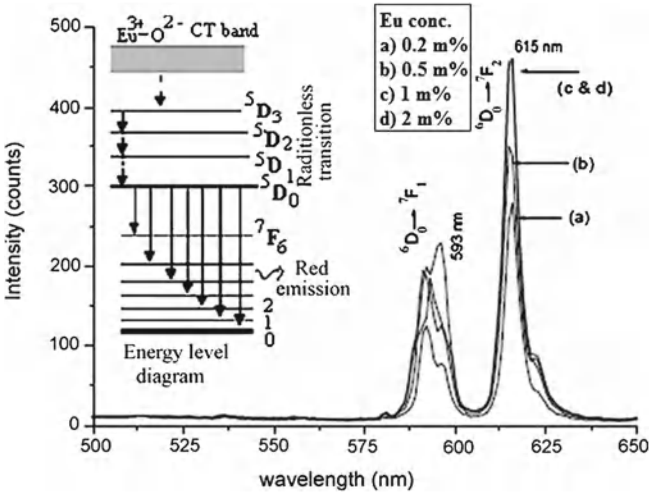

Fig. 5.27 PL emission spectra of the $Na_3Al_2(PO_4)_3$:Eu^{3+} phosphor the emission peaks were monitored at $\lambda_{exc} = 243$ nm. The PL mechanism is shown as *inset*

Fig. 5.28 Variation in the PL intensity as function of the Eu^{3+} ion concentration

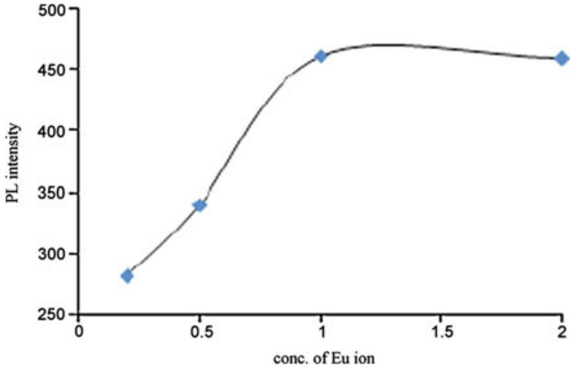

Mn^{2+} concentrations, as indicated. Stable green emission was observed at 515 nm when the powder was excited at 288 nm. This emission can be ascribed to the $^4T_1 \rightarrow {}^6A_1$ transition of the Mn^{2+} ion as shown in inset of Fig. 5.29. A visible emission from Mn^{2+} ion may vary from green to orange/red [24, 25] depending on the site occupied by the ion in a host matrix. The green emission is often obtained at 512 nm when Mn^{2+} occupies a site which is considerably larger than its radius [59]. A plot of maximum PL intensity versus concentration in Fig. 5.30 shows that the intensity increased with concentration from 5 to 10 mol% of Mn^{2+} and it decreased slightly when the concentration was increased to 15 mol%. Photoluminescence application of

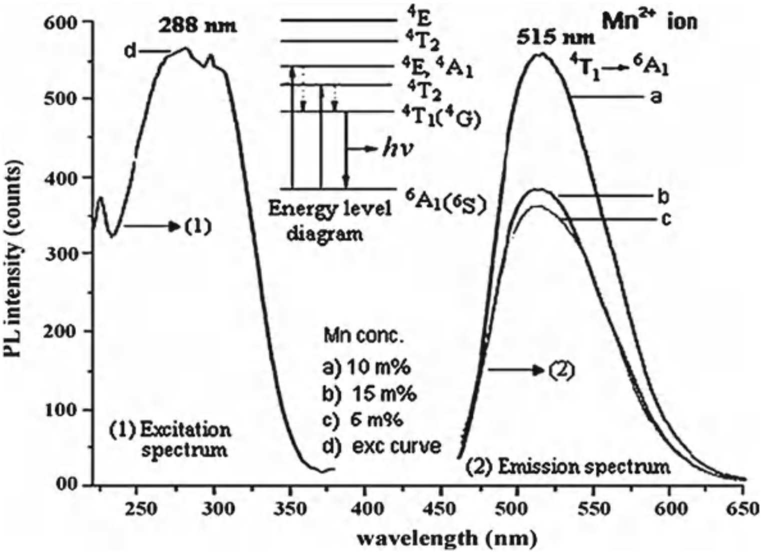

Fig. 5.29 PL emission and excitation spectra of the $Na_3Al_2(PO_4)_3:Mn^{2+}$ phosphor, the emission peaks were monitored at λ_{exc} = 288 nm. The PL mechanism is shown as *inset*

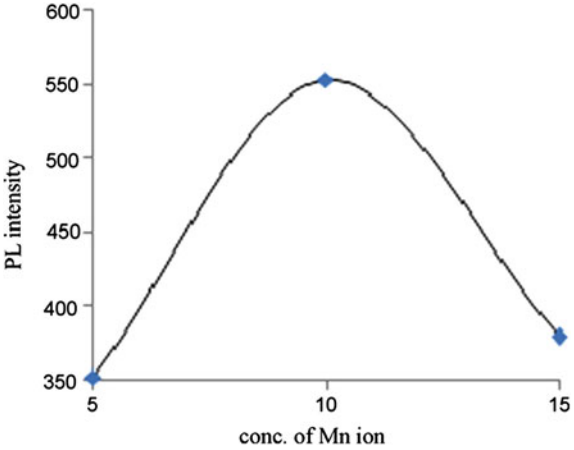

Fig. 5.30 Variation in the PL intensity as function of the Mn^{2+} ion concentration

$Na_3Al_2(PO_4)_3$:Mn^{2+} phosphate is strongly more promising at shorter wavelengths than that of the existing ZnS:Mn EL displays, which should be a candidate to realize the extremely reliable color displays for multimedia use.

5.7 Conclusions

The present data shows that $Na_3Al_2(PO_4)_3$, $Na_3Al_2(PO_4)_3$:Ce^{3+}, $Na_3Al_2(PO_4)_3$:Mn^{2+}, and $Na_3Al_2(PO_4)_3$:Eu^{3+} phosphors can be easily prepared by the combustion method. The XRD data confirmed the formation of crystalline $Na_3Al_2(PO_4)_3$ host lattice having hexagonal (rhombohedral) symmetry NASICON-type with spheroidal particles of 0.1–0.4 μm size. The PL data suggest that dominant $Na_3Al_2(PO_4)_3$:Ce^{3+} may be used in scintillators (ionizing radiation), while $Na_3Al_2(PO_4)_3$:Eu^{3+} and $Na_3Al_2(PO_4)_3$:Mn^{2+} may be used in phosphor lamps, PDP, and solid-state lighting devices.

5.8 Photoluminescence Studies of $K_3Al_2(PO_4)_3$:RE (RE = Dy^{3+}, Eu^{3+}) Phosphor by Combustion Synthesis [60]

5.8.1 *Experimental*

The Eu^{3+} activated $K_3Al_2(PO_4)_3$ phosphors were prepared via combustion synthesis. The starting AR grade materials (99.99 % purity) used were potassium nitrate (KNO_3), ammonium di-hydrogen phosphate ($NH_4H_2PO_4$), aluminum nitrate ($Al(NO_3)_2{\cdot}9H_2O$), europium oxide (Eu_2O_3), and urea (NH_2CONH_2) was used as fuel. In the present investigation, materials were prepared according to the chemical formula $K_{3-x}Al_2(PO_4)_3$:Eu_x. Eu^{3+}, ions were introduced as $Eu(NO_3)_3$ solutions by dissolving Eu_2O_3 into dilted HNO_3 solution for the preparation of $K_{3-x}Al_2$ $(PO_4)_3$:Eu_x phosphor. After mixing all reagents for about 30 min, the mixture was transferred to a furnace preheated at 550 °C and porous products were obtained. The same procedure was followed for the $K_{3-x}Al_2(PO_4)_3$:Dy_x phosphor. The prepared host lattice was characterized for its phase purity and crystallinity by XRD using PAN-analytical diffractometer (Cu-Ká radiation) at a scanning step of 0.010, continue time of 20 s, in the 2θ range from 10 to 60°. The PL measurement of excitation and emission were recorded on the Shimadzu RF5301PC spectrofluorophotometer. Emission and excitation spectra were recorded using a spectral slit width of 1.5 nm.

5.8.2 Results and Discussion

5.8.2.1 X-Ray Diffraction Study of Host Lattice

Figure 5.31 shows the XRD pattern of the host $K_3Al_2(PO_4)_3$ powder. The pattern of prepared compound was matched with the JCPDS card No. 00-028-0732. This shows

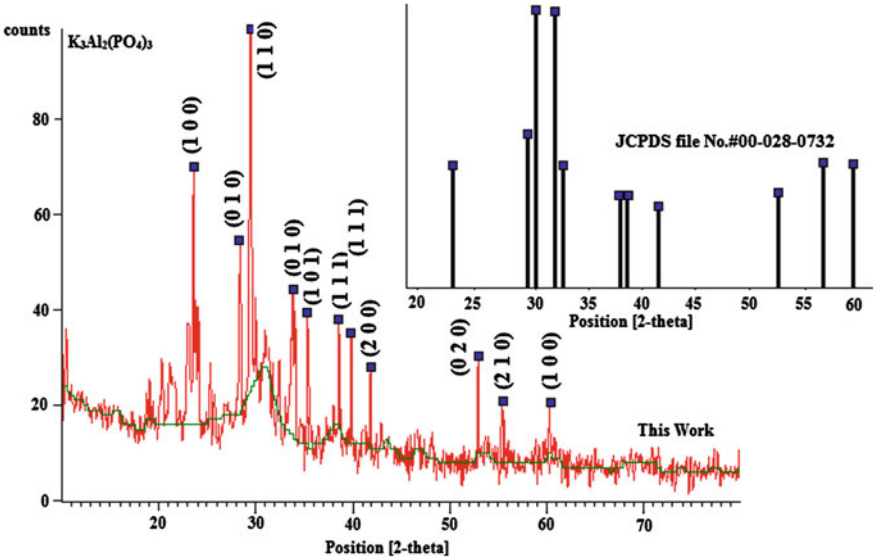

Fig. 5.31 XRD pattern of $K_3Al_2(PO_4)_3$ host lattice compared with JCPDS file No. 00-028-0732 (*inset*)

that the final product was formed in crystalline, homogeneous form, and combustion reactions of the mixtures took place well.

5.8.2.2 Photoluminescence Studies of $K_3Al_2(PO_4)_3$:Dy^{3+}

Figure 5.32 shows the excitation and emission spectrum of the $K_3Al_2(PO_4)_3$:Dy^{3+} phosphor. The excitation peaks are observed at 351 and 385 nm due to the $^6H_{15/2} \rightarrow {}^6F_{9/2}$ electronic transition of the Dy^{3+} ion. From these two excitation bands we choose 385 nm because it is suitable for solid-state lighting. It is known that Dy^{3+} emits around 484 nm ($^4F_{9/2} \rightarrow {}^6H_{15/2}$) due to magnetic dipole transition and 576 nm ($^4F_{9/2} \rightarrow {}^6H_{13/2}$) due to electric dipole moment.

The transition $^4F_{9/2} \rightarrow {}^6H_{13/2}$ is predominant only when Dy^{3+} ions are located at low-symmetry sites with no inversion centers [61]. A slight marginal shift in the peak position of Dy^{3+} ions with respect to Dy concentration is observed in all prepared phosphors. Such behavior is as expected for the emission involving $f \rightarrow f$ transitions, where ligand field changes with the host matrix. This excitation and emission of Dy^{3+} ion indicates that it is suitable for white light-emitting phosphor. As the ionic radii of Dy^{3+}(91.2 pm) is much larger than Al^{3+} (50 pm) and smaller to the K^+ (133 pm) so most of the Dy^{3+} ions are entering the lattice $K_3Al_2(PO_4)_3$ phosphor and few of them are located at the surface. The charge compensating defects in the immediate vicinity is likely to influence the local site symmetry. This is reflected in the emission spectra, wherein asymmetry factor is higher in $K_3Al_2(PO_4)_3$. As Dy^{3+} ions progressively replace the Al^{3+} ions, an increase in PL emission intensity is observed and asymmetry factor progressively reduces. The low-symmetry location of Dy^{3+} results in emission of $^4F_{9/2} \rightarrow {}^6H_{15/2}$ transition. Hence, $K_3Al_2(PO_4)_3$ phosphors show strong PL emission intensity at 484 and 576 nm in Fig. 5.32. Usually, a low doping gives weak luminescence, but excess doping perhaps causes quenching of luminescence. The maximum intensity of Dy^{3+} is observed at 0.5 mol%.

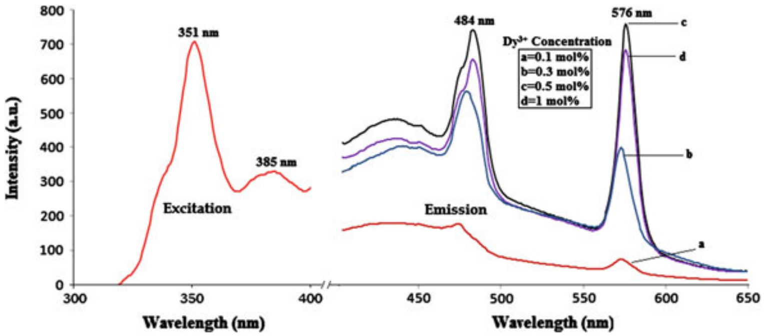

Fig. 5.32 PL emission spectra of $K_3Al_2(PO_4)_3$:Dy^{3+} under $\lambda_{exc} = 385$ nm and the excitation spectrum obtained while monitoring the emission wavelength at 576 nm

5.8.2.3 Photoluminescence Studies of $K_3Al_2(PO_4)_3$:Eu^{3+}

Figure 5.33 presents the excitation and emission spectra of the $K_3Al_2(PO_4)_3$: Eu^{3+} phosphor. Under the excitation of 393 nm (i.e., excitation of the LED lighting), the phosphor $K_3Al_2(PO_4)_3$: Eu^{3+} has the orange and red emission bands at 592 and 614 nm. The main emission line is located at 614 nm, attributed to forced electric dipole transition $^5D_0 \rightarrow {}^7F_2$ of Eu^{3+} ion, which is allowed as the Eu^{3+} does not occupy a center of symmetry site in the host lattice. Other transitions from the $^5D_0$ excited levels to ^7F_J ground states, such as $^5D_0 \rightarrow {}^7F_1$ lines in the 570–600 nm range which is advantageous for obtaining a phosphor with good CIE chromaticity coordinates. The excitation band, 393 nm, which is caused by $f-f$ transitions from ^7F_J of Eu^{3+} to excited levels, that is to say, the transition $^7F_0 \rightarrow {}^5L_6$ of Eu^{3+} attributes to the 393 nm which is stronger excitation band. In the $K_3Al_2(PO_4)_3$: Eu^{3+} phosphor, one Eu^{3+} ion is expected to replace one Al^{3+} ion which will induces the lattice distortion and affects the luminescent intensity of $K_3Al_2(PO_4)_3$:Eu^{3+}. It is a good phenomenon that our phosphors can strongly absorb near UV light (393 nm), which is well in agreement with the near UV or blue output wavelengths of GaN-based LED chips. The linear emission peaks of Eu^{3+} can be observed in the range of 550–700 nm and ascribed to the transition $^5D_0$ level to $^7F_1$ and $^7F_2$ levels of Eu^{3+}, respectively, such as $^5D_0 \rightarrow {}^7F_1$ (589, 593 nm) and $^5D_0 \rightarrow {}^7F_2$ (610, 623 nm). It is well known that the $^5D_0 \rightarrow {}^7F_1$ transition belongs to the magnetic dipole transition which scarcely changes the crystal field strength around the Eu^{3+} ions and this transition is independent of the symmetry and the site occupied by Eu^{3+} ions in the host. While the transition of $^5D_0 \rightarrow {}^7F_2$ belongs to a forced electric dipole transition and its intensity is very sensitive to the site symmetry of the Eu^{3+} ions. Thus, the ratio of $R = {}^5D_0 \rightarrow {}^7F_2/{}^5D_0 \rightarrow {}^7$F1 can measure the distortion from the inversion symmetry of the Eu^{3+} ion local environment [62–64].

In Fig. 5.33, the transition $^5D_0 \rightarrow {}^7F_2$ is much stronger than the transition $^5D_0 \rightarrow {}^7F_1$, which suggests that the Eu^{3+} is located in a distorted (or asymmetric) cation environment. The variations of PL intensity ($^5D_0 \rightarrow {}^7F_2$ transition of Eu^{3+})

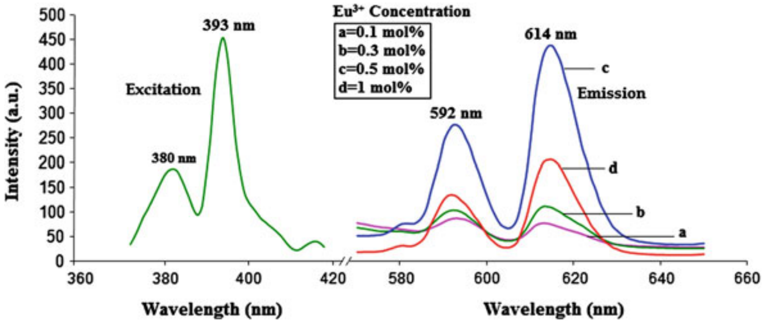

Fig. 5.33 PL emission spectra of $K_3Al_2(PO_4)_3$:Eu $^{3+}$ under λ_{exc} = 393 nm and the excitation spectrum obtained while monitoring the emission wavelength at 614 nm

with different Eu^{3+} content are shown in Fig. 5.33. The intensity of the emission transitions was found to increase with an increase in the Eu^{3+} concentration up to 0.5 mol% and then it decreases because of concentration quenching.

5.8.2.4 Photoluminescence Studies of $K_3Al_2(PO_4)_3$:Ce^{3+}

Ce^{3+} is a very good candidate as activator, as well as sensitizer, for studying the behavior of 5*d* electrons. Ce^{3+} has only one outer electron and only two spin–orbital splitting 4*f* states ($^2F_{5/2,\ 7/2}$). Thus, its excited state energy structure is simpler than that of the other trivalent rare-earth ions. Photoluminescence excitation spectra of $K_3Al_2(PO_4)_3$:Ce $^{3+}$ phosphor shown in Fig. 5.34. The broad band is observed around 307 nm with a prominent shoulder ($\lambda_{emi} = 357$ nm). Figure 5.35 shows the PL emission spectra of Ce^{3+} ions in $K_3Al_2(PO_4)_3$ phosphor with different concentrations under the same excitation (i.e., 307 nm) wavelengths of light. Three emission peaks are observed from 350 to 450 nm, which are assigned to the $5d - 4f$ transition of Ce^{3+} ions. The highest intensity observed at 357 nm due to $^2D(5d) \rightarrow {}^2F_{7/2}(4f)$ transition among three peaks. The concentration of Ce^{3+} ion increases the corresponding intensity of all peaks and at higher concentration (5 mol%) of Ce^{3+} ion. This indicates a change of the surrounding of the Ce^{3+} ions at higher concentration in the $K_3Al_2(PO_4)_3$ lattice. The intensity of Ce^{3+} emission at 357 nm is greater than other observed peaks. Variations observed in PL emission intensities, may be cross-relaxation between Ce^{3+} ions in the case of heavy concentration of Ce^{3+}. The Ce^{3+} ion can be used as sensitizer as well as an activator, depending on the splitting of 5*d* excited levels by the crystal field symmetry. Much work has been done on the Ce^{3+} to different activator ions in different host lattice.

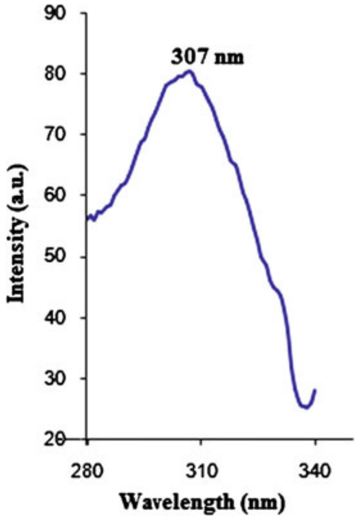

Fig. 5.34 Excitation graph of $K_3Al_2(PO_4)_3$:Ce^{3+} when monitored at 357 nm

Fig. 5.35 Emission graph of $K_3Al_2(PO_4)_3$:Ce^{3+} when excited at 307 nm

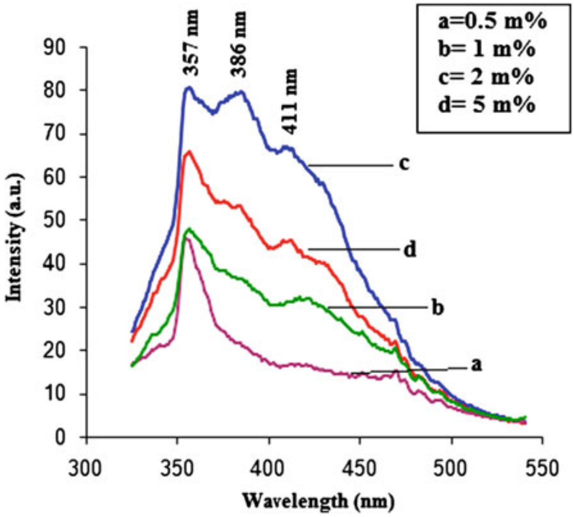

5.9 Conclusions

In the present work, Dy^{3+} and Eu^{3+} activated $K_3Al_2(PO_4)_3$ phosphors, were prepared by a combustion synthesis. Under the excitation of 385 nm, PL emission spectra of K_3Al_2 $(PO_4)_3$:Dy^{3+} phosphor emits distinctive colors specifically blue and yellow, whereas under the excitation of 393 nm (i.e., excitation of the LED lighting) the PL emission spectra of the K_3Al_2 $(PO_4)_3$: Eu^{3+} phosphor show orange/red emission bands at 592 and 614 nm respectively. Dy^{3+} and Eu^{3+} activated $K_3Al_2(PO_4)_3$ phosphors exhibiting a strong absorption between 340–400 nm suggest that present phosphor is a promising candidate for producing white LEDs. Under UV excitation (307 nm) $K_3Al_2(PO_4)_3$:Ce^{3+} exhibits Ce^{3+} émission (357 nm) in the UV range. We get highest intensity at 5 mol%. This émission of Ce ions might be applicable for a scintillator.

5.10 Photoluminescence Studies of $AlPO_4$:RE (Eu^{3+} and Dy^{3+}) by Solid-State Reaction [65]

5.10.1 Experimental

The Eu^{3+} and Dy^{3+} activated $AlPO_4$ phosphors with different doping concentration were prepared by solid-state reactions. Raw materials used in the experiment were Al_2O_3, $NH_4H_2PO_4$, Eu_2O_3, and Dy_2O_3. Both Al_2O_3 and $NH_4H_2PO_4$ have the purity quotient higher than 99.9 %. Eu_2O_3 and Dy_2O_3 have a purity of 99.99 %. The raw materials with stoichiometrical ratio were weighed and mixed in mortar sufficiently. In order to obtain the target compound with pure phase, two firing steps were necessary. The mixture was firstly heated at 500 °C for 2 h in a covered alumina crucible, then reground thoroughly after cooled down to room temperature. The second firing was conducted at 1,000 °C for 24 h.

5.10.2 Results and Discussion

Figure 5.36 represents the XRD patterns of $AlPO_4$:0.03Eu^{3+} and JCPDS data (No. 11-0500). The figure shows that the predominant reflections of both the prepared sample and JCPDS data correspond to each other well, which means the sample $AlPO_4$:0.03Eu^{3+} is phase pure. It is important to note that the XRD pattern of the phosphor sample is absent of the reflections of Eu_2O_3, which is a clear indication of an excellent RE ion incorporation into the $AlPO_4$ lattice achieved by the high temperature solid-state reactions.

Figure 5.37 represents the PL excitation spectrum of $AlPO_4$:Eu^{3+} with the detected wavelength 598 nm. A broad excitation centered at 255 nm is attributed to the charge transfer band (CTB) of Eu–O in the $AlPO_4$ host. The narrow excitation lines appeared at longer wavelengths correspond to the characteristic f → f transitions of Eu^{3+}. These lines are assigned as follows: $^7F_0 \rightarrow {}^5H_3$ (316 nm), $^7F_0 \rightarrow {}^5D_4$ (350 nm), $^7F_0 \rightarrow {}^5G_{2-6}$ (380 nm), and the main excitation line $^7F_0 \rightarrow {}^5L_6$ (393 nm). Figure 5.38 shows the PL emission spectrum of $AlPO_4$:0.03Eu^{3+} obtained under the excitation of $\lambda_{exc} = 393$ nm. The strongest doublet peak located at 590 and 598 nm contributes the orange–reddish emission, which are mainly from the $^5D_0 \rightarrow {}^7F_1$

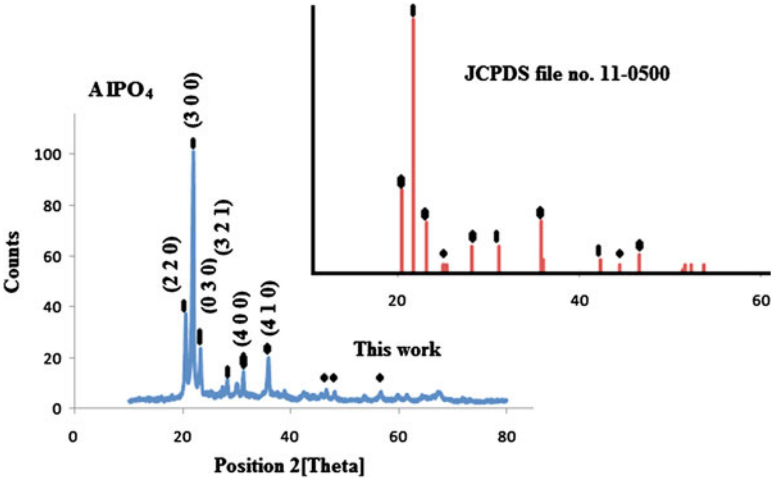

Fig. 5.36 XRD pattern of $AlPO_4$:0.03Eu^{3+} matched with the JCPDS file no. 11-0500

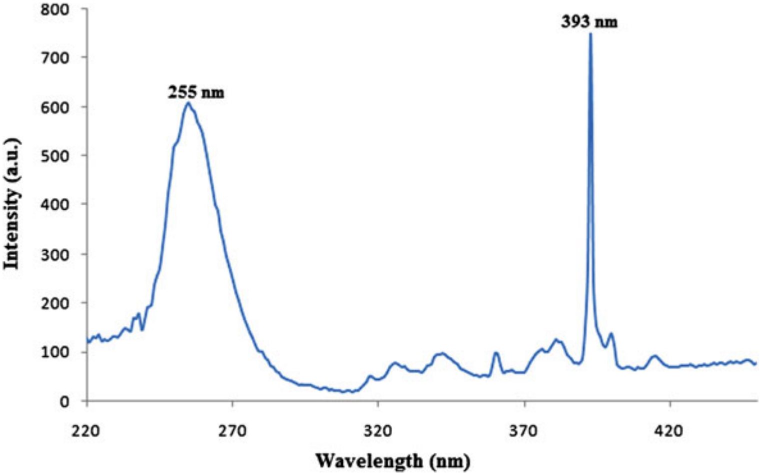

Fig. 5.37 PL excitation spectrum of $AlPO_4$:$0.03Eu^{3+}$ monitored at $\lambda_{emi} = 598\,nm$

magnetic dipole transitions of Eu^{3+} ions and the weak red emissions peaked at 622 and 625 nm are due to the hypersensitive $^5D_0 \rightarrow {}^7F_2$ electric dipole transition. Various emission intensities of $AlPO_4$:Eu^{3+} were shown in inset of Fig. 5.38 plotted against the concentration of Eu^{3+}. As we could see from this figure, the most intense peak was observed at a concentration of 0.03, and then the intensities decreased

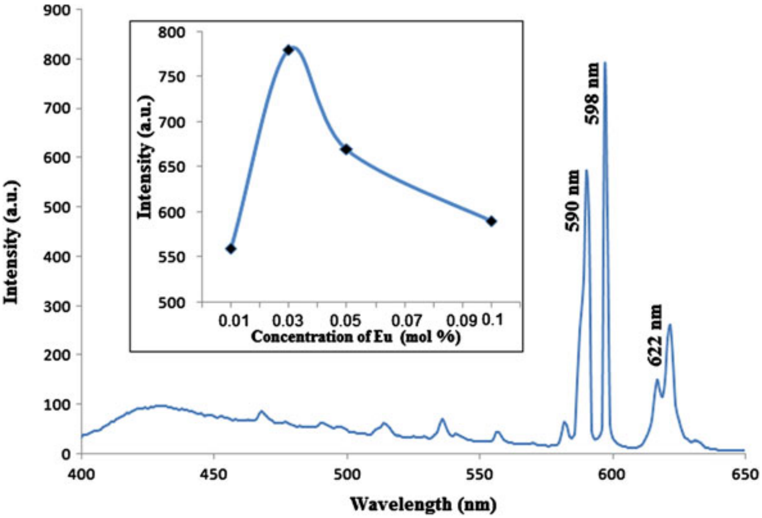

Fig. 5.38 PL emission spectra of $AlPO_4$:$0.03Eu^{3+}$ at $\lambda_{exc} = 393\,nm$ with concentration dependence of relative emission intensity (*inset*)

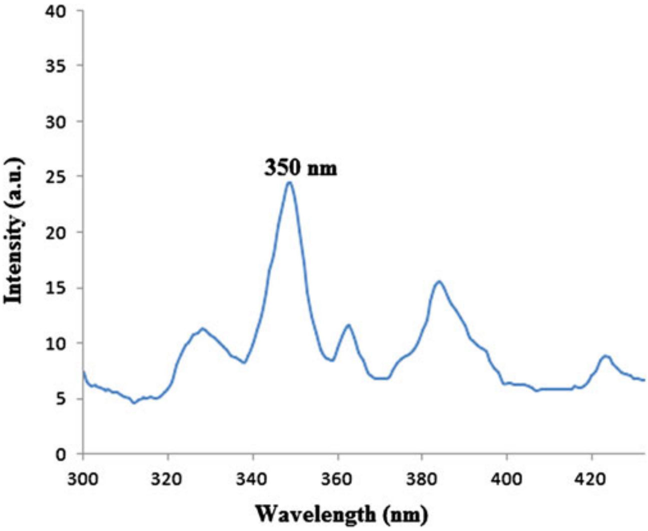

Fig. 5.39 PL excitation spectrum of $AlPO_4$:0.5Dy^{3+} monitored at $\lambda_{emi} = 477$ nm

gradually owing to the energy transfer between the neighboring Eu^{3+} ions, which was corresponding to the quench of the emission of Eu^{3+}.

The broad band excitation peak is observed at 350 nm and is shown in Fig. 5.39. The excitation spectrum monitored at the blue emission from Dy^{3+}. The excitation spectrum in the range 300–400 nm consists of the $f-f$ transition of Dy^{3+}, i.e., 350 nm ($^6H_{15/2} \rightarrow {}^6F_{9/2}$) was observed. Among the several excitation bands we choose 350 nm, because curve is a near UV excitation which is suitable for solid-state lighting. The emission spectrum is shown in Fig. 5.40. All samples have two

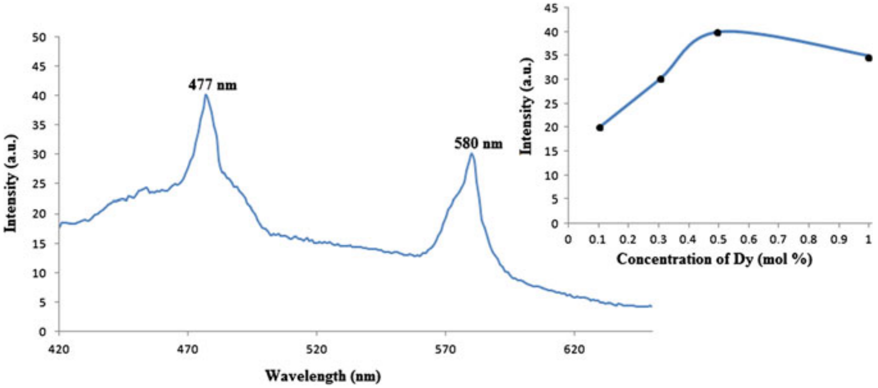

Fig. 5.40 PL emission spectra of $AlPO_4$:0.5Dy^{3+} at $\lambda_{exc} = 350$ nm with concentration dependence of relative emission intensity (*inset*)

emission bands: one is centered at 477 nm (blue) and the other is at 580 nm (yellow). They are assigned to the Dy^{3+} electronic transitions of $^4F_{9/2} \rightarrow {}^6H_{15/2}$ and $^6H_{13/2}$ energy levels as shown in left inset of Fig. 5.40. A series of $Al_{1-x}PO4{:}Dy_x^{3+}$ phosphors with various Dy^{3+} concentrations ($x = 0.1$–1 mol%) were prepared and the effect of doped Dy^{3+}concentration on the emission intensity was investigated (inset of Fig. 5.40). The position of the emission peak is not influenced by the Dy^{3+} concentration. The emission intensity increases with increase in Dy^{3+} concentration and reaches the maximum at about 0.5 mol%. Concentration quenching occurs, when the Dy^{3+} concentration is beyond 0.5 mol%. PL results show the excitation peak at 350 nm, which is away from Hg excitation and is useful for solid-state lighting in lamp industry.

5.11 Conclusions

Luminescent materials $AlPO_4{:}Eu^{3+}$ and $AlPO_4{:}Dy^{3+}$ were successfully prepared by solid-state reactions at 1,000 °C. PL emission spectrum showed strong orange–reddish emission lines due to the Eu^{3+} ions. The PL excitation spectrum is composed of CTB of Eu–O and excitation lines of Eu^{3+} ions. The strongest excitation lines appeared at 393 nm, which indicated this material would be an excellent red component for w-LED applications. The near UV excited (350 nm) luminescent properties of all prepared phosphors are investigated. PL emission spectra show two emissions (477 and 580 nm) in Dy^{3+}-doped $AlPO_4$ phosphate phosphors. Later, when the concentration of doped Dy^{3+} is 0.5 mol% in $AlPO_4$ phosphors have the strongest PL emission intensity observed due to concentration quenching.

5.12 Photoluminescence Studies of $Na(Ba_{0.45}Sr_{0.55})PO_4$:RE ($Dy^{3+}$ and Eu^{2+}) by Combustion Method [66]

5.12.1 Experimental

For the preparation of Dy activated $NaBa_{0.45}Sr_{0.55}PO_4$ phosphors, the starting AR grade materials with 99.99 % purity used were sodium nitrate ($NaNO_3$), strontium nitrate ($Sr(NO_3)_2$), Barium nitrate ($Ba(NO_3)_2$) di-ammonium hydrogen phosphate ($(NH_4)_2HPO_4$), dysprosium oxide (Dy_2O_3), and nitric acid (con.HNO_3) as raw materials, and urea (CH_4N_2O) used as a fuel. The mixture of reagents was united together to obtain a homogeneous solution. For these compositions of the metal nitrates (oxidizers) and urea (fuel) were calculated using the total oxidizing and reducing valencies of the components, which serve as the numerical coefficients, so that the equivalence ratio is unity and the heat liberated during combustion is at a maximum. After stirring for about 30 min, precursor solution was transferred to a furnace preheated to 600 °C, the porous products were obtained. The prepared phosphors were used for further characterization.

Chemical Reaction is as follows:

$$\mathbf{2NaNO_3 + 2Ba(NO_3)_2 + 2Sr(NO_3)_2 + 2(NH_4)_2HPO_4 + 7NH_2CONH_2}$$
$$\mathbf{\rightarrow 2NaBa_{0.45}Sr_{0.55}PO_4 + 7CO_2 + 23H_2O + 14N_2}$$

5.12.2 Results and Discussion

5.12.2.1 Structural Behavior

As an important family of luminescent materials, orthophosphates have been paid intense attention because of their excellent properties, e.g., the large band gap and the high absorption of PO_4^{3-} in UV region, moderate phonon energy, the high thermal and chemical stability, and the exceptional optical damage threshold [32–34].

Axial Ratios: a:c = 1:1.2661

Cell Dimensions: $a = 5.558$, $c = 7.037$, $Z = 2$; $V = 188.26$ Den(Calc) = 4.02

Crystal System: Trigonal-Hexagonal Scalenohedral

Formula: $NaSr_{0.55}Ba_{0.45}(PO_4)$

In 1980, sodium strontium barium phosphate as a new mineral named as Olgite, has been approved to save up in some nature rocks, such as nepheline, syenite pegmatite. Its empirical formula is $NaSr_{0.55}Ba_{0.45}(PO_4)$, which has a hexagonal structure and a space group of *P3* with lattice constants of $a = 5.565$, $c = 7.050$ [67, 68] (Fig. 5.41). However, there are very few reports investigated on the synthesis and luminescence based on this rare-earth doped sodium barium strontium triple phosphate by Huang et al. [69].

5.12.2.2 XRD of $NaBa_{0.45}Sr_{0.55}PO_4$

XRD pattern of the sample shown in Fig. 5.42 which is compared with Olgite $NaBa_{0.45}Sr_{0.55}(PO_4)$ and well match with the standard JCPDs file no. 33-1212. The XRD pattern did not indicate the presence of the constituents such as, $Sr(NO_3)_2$, $Ba(NO_3)_2$, $NaNO_3$, or $NH_4H_2PO_4$ and other likely phases which are an indirect evidence for the formation of the desired compound. These results indicate that the final product was formed in crystalline and homogeneous form.

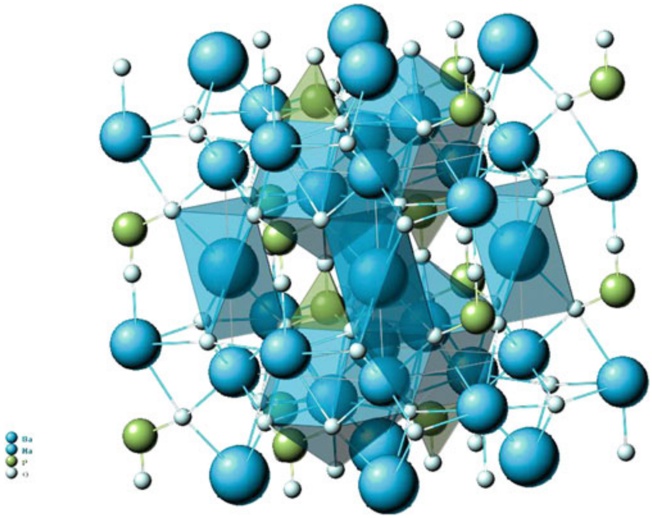

Fig. 5.41 Crystal structure of $NaBa_{0.45}Sr_{0.55}PO_4$ [67]

5.12.2.3 PL Properties of $NaBa_{0.45}Sr_{0.55}PO_4$:Dy^{3+}

Measurements of the excitation spectra were made by monitoring the peak wavelength of the Dy^{3+} emission of the blue and yellow emission bands, respectively.

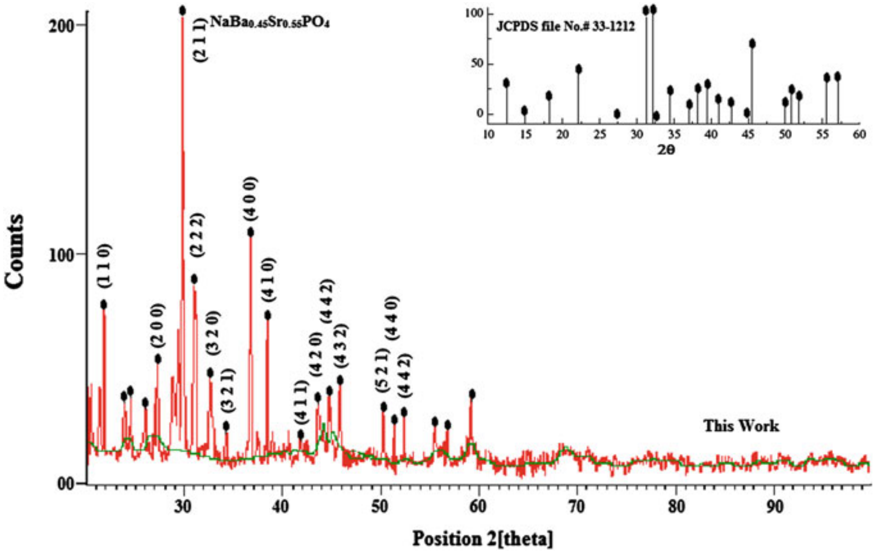

Fig. 5.42 X-ray diffraction pattern of $NaBa_{0.45}Sr_{0.55}PO_4$ host

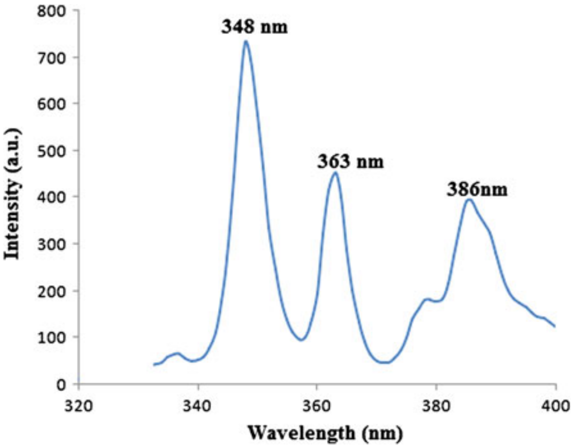

Fig. 5.43 Excitation graph of $NaBa_{0.45}Sr_{0.55}PO_4:Dy^{3+}$ when monitored at 576 nm

Figure 5.43 shows the excitation spectrum of the $NaBa_{0.45}Sr_{0.55}PO_4:Dy^{3+}$ phosphor. The excitation spectrum monitored at the yellow emission from Dy^{3+} indicates several bands. The excitation spectrum in the range 330–400 nm consists of the $f–f$ transition of Dy^{3+}, i.e., 348 nm ($^6H_{15/2} \rightarrow {}^6F_{9/2}$) was observed. The emission spectra of Dy^{3+} ions in $NaBa_{0.45}Sr_{0.55}PO_4$ show emission at 482 nm (blue) and 576 nm (yellow). These two different emission bands have one origin due to the same excitation wavelength. The transitions involved in the blue and yellow bands of Dy^{3+} were well known and identified due to the $^4F_{9/2} \rightarrow {}^6H_{15/2}$ and $^6H_{13/2}$ transitions, respectively. It is known that the Dy^{3+} emission around 482 nm ($^4F_{9/2} \rightarrow {}^6H_{15/2}$) is of magnetic dipole origin and 576 nm ($^4F_{9/2} \rightarrow {}^6H_{13/2}$) is of electric dipole origin. $^4F_{9/2} \rightarrow {}^6H_{15/2}$ is predominant only when Dy^{3+} ions are located at low-symmetry sites with no inversion center (Fig. 5.44). The increase in the luminescence intensity with an increase in concentration of the Dy ion can be clarified as follows: the luminescence spectrum of Dy^{3+} ion was slightly influenced by the surrounding ligands of the host material, because electronic transitions of Dy^{3+} involve only redistribution of electrons within the inner $4f$ sub-shell. Crystallinity of phosphor could be increased due to the increase in concentration of the Dy ion, since it is clear that the addition of Dy ion into the $NaBa_{0.45}Sr_{0.55}PO_4$ host increased the crystallinity. An increase in the concentration of Dy ions increased the particle size as well as its complexity. Hence, there was an increase in photoluminescence intensity. Usually, low doping gives weak luminescence but excess doping perhaps causes quenching of luminescence. The maximum intensity of Dy^{3+} is observed at 0.5 mol%. The 300–400 nm is Hg-free excitation (Hg excitation is 85 %, 254 nm wavelength of light, and 15 % other wavelengths), which is characteristic of solid-state lighting phosphors.

Figure 5.45 shows a schematic energy level diagram indicating the states involved in the luminescence process and the transition probabilities for Dy^{3+} ions in $NaBa_{0.45}Sr_{0.55}PO_4:Dy^{3+}$. It is known that Dy^{3+} emission around 482 nm ($^4F_{9/2} \rightarrow {}^6H_{15/2}$) is of magnetic dipole origin and 576 nm ($^4F_{9/2} \rightarrow {}^6H_{13/2}$) is of

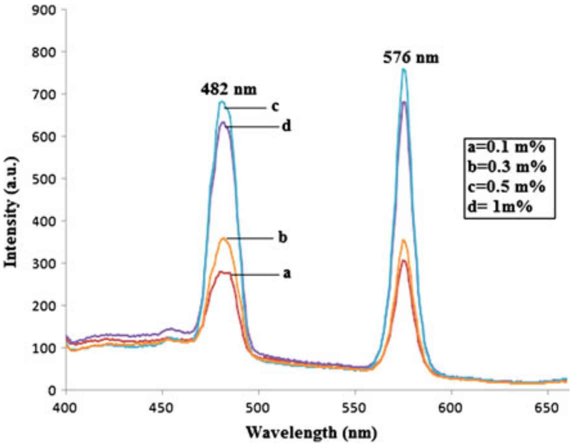

Fig. 5.44 PL emission spectra of $NaBa_{0.45}Sr_{0.55}PO_4:Dy^{3+}$ phosphor ($\lambda_{exc} = 348\,nm$)

electric dipole origin. According to this model, the system is first excited from the ground state and finally Dy^{3+} comes to the ground state via a series of nonradiative and radiative transitions.

5.12.2.4 PL Properties of $NaBa_{0.45}Sr_{0.55}PO_4:Eu^{2+}$

The PL excitation and emission spectra of $NaBa_{0.45}Sr_{0.55}PO_4:Eu^{2+}$ are depicting in Figs. 5.46 and 5.47, respectively. It can be seen from Fig. 5.46 that the PL excitation spectrum shows a broad absorption band from 330 to 370 nm, which can be

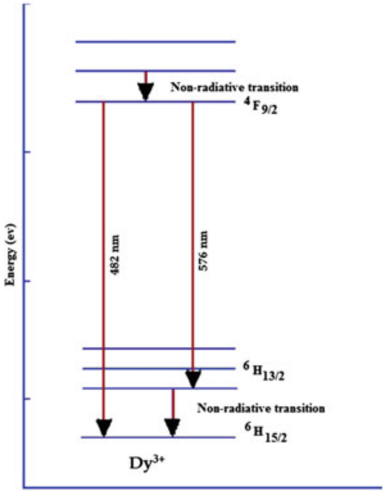

Fig. 5.45 Schematic energy level diagram of Dy^{3+}

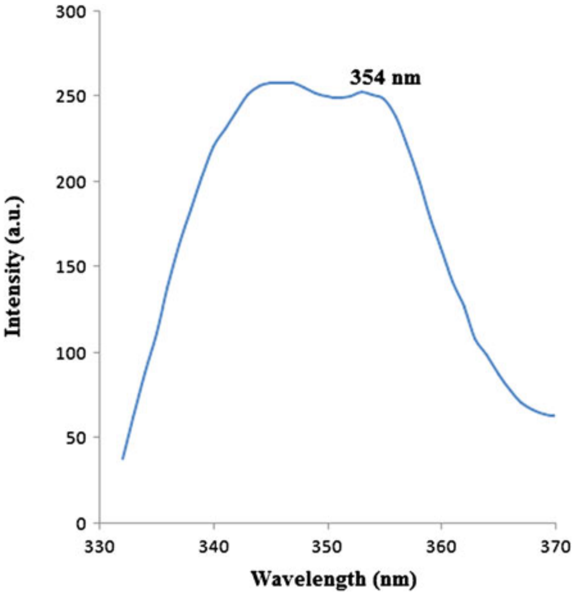

Fig. 5.46 Excitation graph of $NaBa_{0.45}Sr_{0.55}PO_4:Eu^{2+}$ when monitored 470 nm

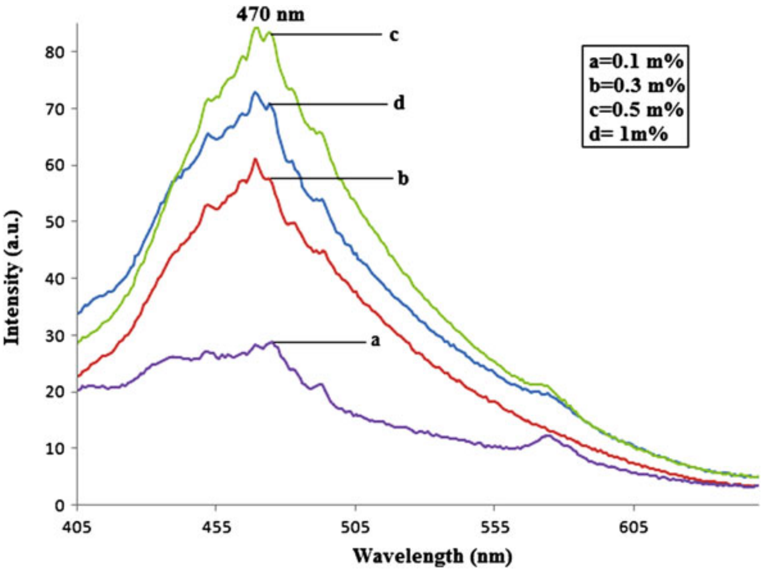

Fig. 5.47 PL emission spectra of $NaBa_{0.45}Sr_{0.55}PO_4:Eu^{2+}$ phosphor ($\lambda_{exc} = 354$ nm)

assigned to the f–d transition of Eu^{2+} which indicates that this phosphor can be well-excited at the wavelength range of deep UV to near UV. The PL emission spectra (Fig. 5.47) exhibit a broad blue emission band peaking at 470 nm and there is a shoulder emission in the lower energy side when excited at 354 nm wavelength. The broadband emission is characteristic of the allowed d–f transition of Eu^{2+} ions [70]. The excitation band in the range of 250–440 nm is originated from the $4f^7 \rightarrow 4f^6 5d^1$ transition of the doped Eu^{2+} ions [5]. The emission spectrum is very broad, which almost extends through the whole visible light region from 400 to 700 nm. Obviously, the emission spectrum consists of two main emission bands peaking at 470 and 475 nm, respectively. It can be presumed that the two emission bands result from the $4f^6 5d^1 \rightarrow 4f^7$ transitions of Eu^{2+} ions occupying Sr^{2+} and Ba^{2+} sites in host lattice, respectively. The effect of Eu^{2+} doping concentration on the emission intensity of $NaBa_{0.45}Sr_{0.55}PO_4$:Eu_x^{2+} with variation of the activator concentration ($x = 0.1$–1 mol%) was also investigated. The emission intensity dependence of the phosphors excited by 354 nm wavelength is presented in Fig. 5.47. A maximum intensity is achieved at a content of 0.5 mol% of Eu^{2+}, and thereafter is diminished with increasing Eu^{2+} concentration. This implies that the quenching concentration of Eu^{2+}, which is defined as the concentration at which the emission intensity begins to decrease in the $NaBa_{0.45}Sr_{0.55}PO_4$ host, is around 0.5 mol%. For this reason, the concentration of Eu^{2+} ion was fixed at 0.5 mol%. In view of application, each proper NUV-pumped WLED phosphor must meet the following necessary conditions. First, the phosphor must efficiently absorbs NUV light emitted from the InGaN chip. Second, the phosphor exhibits higher luminescent intensity under NUV light excitation. Third, the phosphor should have high color stability (Fig. 5.49) [71]. Since $NaBa_{0.45}Sr_{0.55}PO_4$:Eu^{2+} meets all the conditions, it is considered to be a potential candidate as a single-host full-color phosphor for fabrication of WLEDs.

To be closely associated, PL spectra with the host structure above, Fig. 5.48 demonstrates the energy level diagram of $NaBa_{0.45}Sr_{0.55}PO_4$:Eu^{2+} which is excited at 354 nm. In $NaBa_{0.45}Sr_{0.55}PO_4$ host, the Eu^{2+} absorbs energy and transits from $^8S_{7/2}$ ground state to $4f^6 5d$ excitation state and the energy is transferred to the $^8S_{7/2}$ ground state, inducing the blue emission band of Eu^{2+}.

5.12.2.5 Chromatic Properties

Most lighting specifications refer to color in terms of the 1931 CIE chromatic color coordinates which recognizes that the human visual system uses three primary colors: red, green, and blue [72, 73]. In general, the color of any light source can be represented on the (x, y) coordinate in this color space. Three properties, the chromatic coordinates, dominant wavelength, and color purity for $NaBa_{0.45}Sr_{0.55}PO_4$:Dy(0.5 mol%) phosphor are determined from the spectrum in Fig. 5.44. The color purity was compared to the 1931 CIE Standard Source C (illuminant Cs (0.3101, 0.3162)). The chromatic coordinates (x, y), was calculated using the color calculator program radiant imaging [53]. The coordinates of the blue $NaBa_{0.45}Sr_{0.55}PO_4$:Dy(0.5 mol%) ($x \approx 0.1266$, $y \approx 0.0534$) and yellow

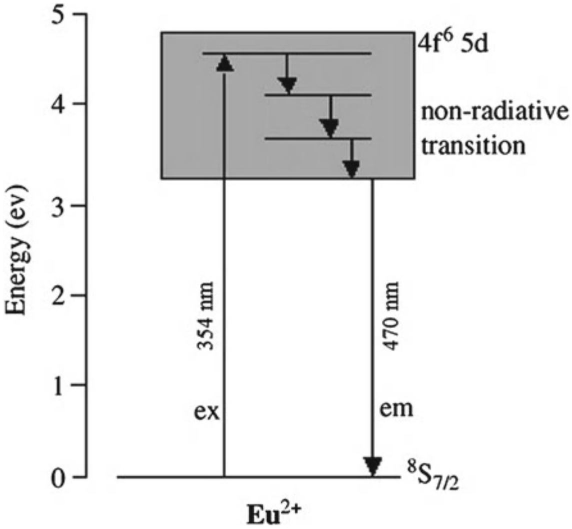

Fig. 5.48 Schematic energy level diagram of Eu^{2+}

($x \approx 0.5058$, $y \approx 0.4932$) phosphor are shows in Fig. 5.49 by white circle. The location of the color coordinates of the triple phosphate powder on the CIE chromaticity diagram presented in Fig. 5.49 indicates that the color properties of the phosphor powder prepared by combustion method are approaching those required for field emission displays. The dominant wavelength is defined as the single monochromatic wavelength that appears to have the same color as the light source. The dominant wavelength can be determined by drawing a straight line from one of the CIE white illuminants (Cs (0.3101, 0.3162)), through the (x, y) coordinates to be measured, until the line intersects the outer locus of points along the spectral edge of the 1931 CIE chromatic diagram.

All the results calculated from the spectra in Fig. 5.44 are plotted in the Commission International de $l'E'$clairage (CIE) 1931 chromaticity diagram, as shown in Fig. 5.49. It indicates that Dy^{3+} doped $NaBa_{0.45}Sr_{0.55}PO_4$ are close to the edge of CIE diagram, which indicates the high color purity of this phosphor. By connecting these two points in the form of a triangle (included white light point (0.31, 0.32)), the intermediate compositions can generate white light with a particular ratio of this phosphor.

5.13 Conclusions

The $NaBa_{0.45}Sr_{0.55}PO_4$:Dy^{3+} was prepared by facile combustion synthesis and confirmed by XRD. The PL emission of Dy^{3+} ion at the 348 nm excitation gave emission at 482 nm (blue) and 576 nm (yellow). $NaBa_{0.45}Sr_{0.55}PO_4$:Eu^{2+} exhibits blue color around 470 nm when excited at 354 nm. The 300–400 nm is Hg-free excitation (Hg

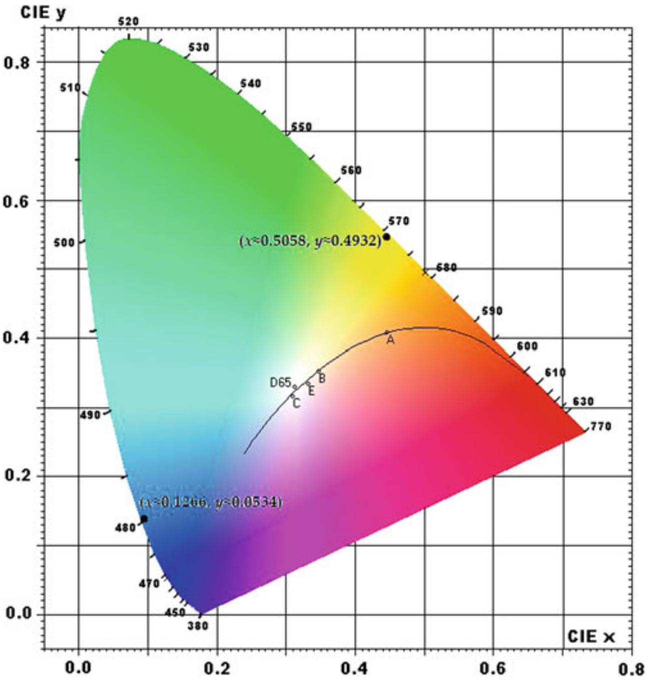

Fig. 5.49 CIE chromatic diagram showing the chromatic coordinates for $NaBa_{0.45}Sr_{0.55}PO_4:Dy^{3+}$

excitation is 85 % 254 nm wavelength of light and 15 % other wavelengths), which is characteristic of solid-state lighting phosphors. Therefore, the entire PL characteristic and chromaticity diagram indicates that Dy^{3+} and Eu^{2+}-doped $NaBa_{0.45}Sr_{0.55}PO_4$ phosphors could be good candidate for solid-state lighting devices as well as for near UV white LED purpose.

References

1. Z. Yang, G. Yang, S. Wang, J. Tian, X. Li, Q. Guo, G. Fu, Mater. Lett. **62**, 1884 (2008)
2. C. Qin, Y. Huang, L. Shi, G. Chen, X. Qiao, H.J. Seo, J. Phys. D: Appl. Phys. **42**, 185105 (2009)
3. W.B. Im, H.S. Yoo, S. Vaidyanathan, K.H. Kwon, H.J. Park, Y-Il Kim, D.Y. Jeon, Mater. Chem. Phys. **115**, 161 (2009)
4. C.C. Lin, Y.S. Tang, S.F. Hu, R.S. Liu, J. Lumin. **129**, 1682 (2009)
5. Y.S. Tang, S.F. Hu, C.C. Lin, N.C. Bagkar, R.S. Liu, Appl. Phys. Lett. **90**, 151108 (2007)
6. T. Wanjun, C. Donghua, J. Am. Ceram. Soc. **92**, 1059 (2009)
7. Z.C. Wu, J.X. Shi, J. Wang, M.L. Gong, Q. Su, J. Solid-State Chem. **179**, 2356 (2006)
8. K.N. Shinde, I.M. Nagpure, A.B. Fulke, S.J. Dhoble, Luminescence **26**, 363 (2011)
9. E. Olsen, J. Am. Mineral. **62**, 362 (1977)
10. M. Ben Amara, M. Vlasse, G. Leflem, J. Acta Cryst. **C39**, 1483 (1983)

11. Y. He, B. Quan, Y. Wang, C. Cheng, B. Wang, Mater. Lett. **61**, 4519 (2007)
12. M. Hirayama, N. Sonoyama, A. Yamada, R. Kanno, J. Solid State Chem. **182**, 730 (2009)
13. S.W. Kim, T. Masui, H. Matsushita, N. Imanaka, Chem. Lett. **38**, 1010 (2009)
14. P. Pasierb, Mater. Sci. **24**, 279 (2006)
15. N. Imanaka, A. Ogura, M. Kamikawa, Electrochem. Commun. **3**, 451 (2001)
16. J.P. Boilot, P. Salanie, G. Desplanches, D.L. Potier, Mater. Res. Bull. **14**, 1469 (1979)
17. T. Masui, K. Koyabu, S. Tamura, N. Imanaka, J. Alloys Compd. **418**, 73 (2006)
18. A. Mouline, M. Alami, R. Brochu, R. Olazcuaga, C. Parent, G. Le Flem, J. Solid State Chem. **152**, 453 (2000)
19. O.V. Chukova, R.S. Boyko, S.G. Nedilko, Funct. Mater. **11**, 147 (2004)
20. K.N. Shinde, S.J. Dhoble, Animesh Kumar. Physica B **406**, 94 (2011)
21. J. Kuang, Y. Liu, J. Zhang, J. Solid State Chem. **179**, 266 (2006)
22. M. Yu, J. Lin, Z. Wang, J. Fu, S. Wang, H.J. Zhang, Y.C. Han, Chem. Mater. **14**, 2224 (2002)
23. O.A. Lopez, J. Mckittrick, L.E. Shea, J. Lumin. **71**, 1 (1997)
24. D.T. Palumbo, J.J. Brown Jr., J. Electrochem. Soc. **117**, 1184 (1970)
25. D.T. Palumbo, J.J. Brown Jr., J. Electrochem. Soc. **118**, 1159 (1971)
26. W.J. Xie, J.Y. Tang, L.Y. Hao, X. Xu, Opt. Mater. **32**, 274 (2009)
27. S. Ye, J.H. Zhang, X. Zhang, S.Z. Lu, X.G. Ren, X.J. Wang, J. Appl. Phys. **101**, 033513 (2007)
28. F.R. de Gruijl, Radiat. Protect. Dosim. **91**, 57 (2000)
29. J.A. Parrish, K.F. Jaenicke, J. Investig. Dermatol. **76**, 359 (1981)
30. Y.Z. Li, Y.H. Wang, Z.F. Wang, Z.Y. Zhang, J. Lumin. **130**, 1225 (2010)
31. K.N. Shinde, S.J. Dhoble, A. Kumar, J. Rare Earths **29**(6), 527 (2011)
32. J.J. Lammers, H.C.G. Verhaar, G. Blasse, Chem. Phys. **16**, 63 (1986)
33. S.H.M. Poort, W. Janssen, G. Blasse, J. Alloys Compd. **260**, 93 (1997)
34. E.N. Silva, A.P. Ayala, I. Guedes, C.W.A. Paschoal, R.L. Moreira, C.K. Loong, L.A. Boatner, Opt. Mater. **29**, 224 (2006)
35. M. Ben Amara, M. Vlasse, G. Le Flem, P. Hagenmuller, Acta Crystallogr. Sect. C **39**, 1483 (1983)
36. L. van Pieterson, M.F. Reid, R.T. Wegh, S. Soverna, A. Meijerink, Phys. Rev. B **65**, 045113 (2002)
37. P. Dorenbos, Phys. Rev. B **62**, 15640 (2000)
38. S. Saito, K. Wada, R. Onaka, J. Phys. Soc. Jpn. **37**, 711 (1974)
39. T. Szczurek, M. Schlesinger, in *Rare Earths Spectroscopy*, ed. by B. Jezowska-Trzebiatowska, J. Legendziewicz, W. Strek (World Scientific, Singapore, 1985)
40. G. Blasse, J. Solid State Chem. **62**, 207 (1986)
41. L.I. Guanghuan, L. Tao, S. Yanhua, G. Guimei, X.U. Jijing, A.N. Baichao, G. Shucai, H. Guangyan, J. Rare Earths **28**, 22 (2010)
42. Z. Lou, J. Hao, Thin Solid Films **450**, 334 (2004)
43. U. Rambabu, S. Buddhudu, Opt. Mater. **17**, 401 (2001)
44. L. Yu, H. Song, S. Lu, Z. Liu, L. Yang, X. Kong, J. Phys. Chem. **108**, 16697 (2004)
45. J. Dexpert-Ghys, R. Mauricot, M.D. Faucher, J. Lumin. **69**, 203 (1996)
46. Y. Qiao, X. Zhang, X. Ye, Y. Chen, H. Guo, J. Rare Earths **27**, 323 (2009)
47. J. Kuang, Y. Liu, J. Zhang, J. Solid State Chem. **179**, 266 (2006)
48. E. Cavalli, M. Bettinelli, A. Belletti, A. Speghini, J. Alloys Compd. **341**, 107 (2002)
49. M. Yu, J. Lin, Z. Zhang, J. Fu, S. Wang, H.J. Zhang, Y.C. Ham, Chem. Mater. **14**, 2224 (2002)
50. D. Jia, W.M. Yen, J. Lumin. **101**, 115 (2003)
51. G.B. Stringfellow, M.G. Craford (ed.), vol. 48, ed. by R.K. Willardson, E.R. Weber (Academic Press, San Diego, 1997)
52. S. Shionoya, W.M. Yen, *Phosphor Handbook* (Phosphor Research Society, CRC Press, Boca Raton, 1998), p. 459
53. Color Calculator version 2, A software from Radiant Imaging, Inc., 2007
54. I.M. Nagpure, K.N. Shinde, V. Kumar, O.M. Ntwaeaborwa, S.J. Dhoble, H.C. Swart, J. Alloys Compds. **492**, 384 (2010)
55. O.P. Shrivastava, R. Chourasia, N. Kumar, Ann. Nucl. Energy **35**, 1147 (2008)

56. A. Lempicki, E. Berman, A.J. Wojtowicz, M. Balcerzyk, L.A. Boatner, IEEE T. Nucl. Sci. **40**, 384 (1993)
57. A.J. Wojtowicz, A. Lempicki, D. Wisniewaski, L.A. Boatner, *Materrials Research Society Symposium* (San Francisco, CA, 1994), p. 348
58. A.J. Wojtowicz, *Conference Record EURODIM 94* (Lyon, France, 1994)
59. T. Koskentato, M. Leskel, L. Niinisto, Mater. Ref. Bull. **20**, 265 (1985)
60. K.N. Shinde, S.J. Dhoble, J. Fluoresc. **21**, 2053 (2011)
61. M. Yu, J. Lin, Z. Wang, J. Fu, S. Wang, H.J. Zhang, Y.C. Han, Chem. Mater. **14**(5), 2224 (2002)
62. R.S. Yadav, R.K. Dutta, M. Kumar, A.C. Pandey, J. Lumin. **129**, 1078 (2009)
63. M.M. Haque, H.L. Lee, D.K. Kim, J. Alloy Compd. **481**, 792 (2009)
64. I. Omkaram, B.V. Rao, S. Buddhudu, J. Alloy Compd. **474**, 565 (2009)
65. K.N. Shinde, S.J. Dhoble, Adv. Mater. Res. **306–307**, 171 (2011)
66. K.N. Shinde, S.J. Dhoble, Optik **123** (21), 1975 (2012). doi:10.1016/j.ijleo.2011.09.033
67. E. Sokolova, F.C. Hawthorne, A.P. Khomyakov, Can. Mineral. **43**(5), 1521 (2005)
68. E.V. Sokolova, Y.K. Yegorov-Tismenko, N.A. Yamnova, M.A. Simonov, Sov. Phys. Crystallogr. **29**, 1079 (1984)
69. Y. Huang, W. Kai, K. Jang, H.S. Lee, X. Wang, Y. Zhang, D. Qin, C. Jiang, Mat. Lett. **62**, 1913 (2008)
70. G. Blasse, B.C. Grabmaier, *Luminescent Materials*, Chap. 3 (Springer, Berlin, 1994)
71. Z.-C. Wu, J. Liu, W.-G. Hou, J. Xu, M.-L. Gong, J. Alloys Compd. **498**, 139 (2010)
72. G.B. Stringfellow, M.G. Craford (eds.), in *High Brightness Light Emitting Diodes*, vol. 48, ed. by R.K. Willardson, E.R. Weber (Academic Press, San Diego, 1997)
73. S. Shionoya, W.M. Yen, *Phosphor Handbook (Phosphor Research Society)* (CRC Press, Boca Raton, 1998), p. 459

Chapter 6
Some Halophosphates Phosphors

6.1 Introduction

The halophosphate phosphor is defined as a phosphor with the apatite mineral structure. Almost all commonly found tubes on the global lighting market employ an internal coating of calcium halophosphate materials (generally known simply as 'Halophosphate' tubes). This revolutionary material was invented in 1942 by a group led by A. H. McKeag of Osram-GEC in London, and succeeded in almost doubling lamp efficiency. This breakthrough was responsible for propelling the fluorescent business into the vast market. However, by modern standards, halophosphate materials are relatively inefficient and deliver inferior lighting quality compared to newer technologies of fluorescent phosphors. Although fluorescent tubes have low initial purchase cost, this was rapidly offset by the increased electrical power consumption required to generate a given amount of light. Owing to their lesser energy efficiency, halophosphate tubes are being phased out and will shortly be replaced by other more efficient fluorescent phosphor materials. These phosphors are blends of two different materials which radiate broadly in the blue and orange parts of the spectrum, respectively. By changing the ratio of the two components a full range of warm to cool white hues can be achieved.

Halophosphate phosphors generally have the formula such as, $Ca_5(PO_4)_3$(F,Cl). The halophosphate materials may contain various activator ions which impart the phosphor property. For example, a europium (Eu)-activated halophosphate phosphor absorbs ultraviolet (UV) emission (i.e., exciting radiation) from the mercury plasma in a fluorescent lamp and emits blue–green visible light. The phosphor efficacy and lumen maintenance of the halophosphate phosphor was improved by adding cadmium to the phosphor. The addition of a few percent of cadmium to the halophosphate phosphor induced a strong absorption of the 185 nm damaging component of the mercury plasma, which reduced the intensity of this component of the plasma. Consequently, the density of the color centers created in the phosphor was reduced by adding cadmium to the phosphor. The decrease in the density of color centers in the phosphor increased the efficacy and lumen maintenance of the

K. N. Shinde et al., *Phosphate Phosphors for Solid-State Lighting*,
Springer Series in Materials Science 174, DOI: 10.1007/978-3-642-34312-4_6,

phosphor. However, the use of cadmium was later eliminated in phosphors manufactured in the United States and Japan for public health reasons. Therefore, it was desired to obtain a halophosphate phosphor with an improved efficacy and lumen maintenance, preferably without adding cadmium to the phosphor. Europium-activated strontium chlorophosphate, i.e., $Sr_{10}(PO_4)_6Cl_2{:}Eu^{2+}$ is probably the first useful narrow band blue emitting phosphor. The emission is a rather narrow band at 450 nm and it can be used in the triband lamp. Blue emitting phosphors that are commonly used in tricolor fluorescent lamps are Eu^{2+}-activated $(Sr,Ba,Ca)_5(PO_4)_3Cl$, with an apatite (halophosphate) structure. The phosphors display strong ultraviolet absorption with a narrow band emission peaking at 450 nm. The blue phosphors represent only a minor weight fraction of the triphosphor blend (about 10 % for color temperature of 4,100 K). However, blends designed for higher color temperatures, say 6,500 K, require higher amounts of the blue emitting component. Very recently, the energy transfer between Eu^{2+} and Mn^{2+} was found in the phosphor $Ca_5(PO_4)_3Cl{:}Eu^{2+}, Mn^{2+}$, and the doped phosphor can be efficiently excited by near-UV light, indicating that the phosphor is a potential candidate for an UV LED used phosphor [1].

There is a method provided for making a halophosphate phosphor on the basis of present invention. i.e., (a) one powder comprising at least one element selected from calcium, magnesium, barium, strontium, and zinc; phosphorus, and at least one halide element selected from fluorine, chlorine, and bromine; oxygen; antimony; manganese, and at least one trivalent rare earth element and (b) heating at least one powder to form a solid phosphor body. Inventors later discovered that the phosphor efficacy and lumen maintenance may be improved by doping the phosphor with suitable ions other than cadmium which preferentially trap the charge carriers generated by the damaging component of the exciting radiation, instead of by adding cadmium to the phosphor in order to reduce the intensity of the damaging 185 nm exciting radiation. The dopant ions preferably have a higher charge carrier (i.e., electron and/or hole) capture cross section than the lattice defects, and thus act as alternative charge carrier trapping centers to the lattice defects. These dopant ions alternative charge carrier trapping centers improve the phosphor efficacy and lumen maintenance by preventing a large number of charge carriers from reaching the lattice defects and forming color centers or other defects which negatively impact on the phosphor efficacy and lumen maintenance. Without a trapped charge carrier, the lattice defect does not act as a color center, because it is unable to absorb the visible light generated by the phosphor and is unable to absorb the 254 nm exciting radiation from the mercury plasma. Thus, the dopant ions decrease the number of color centers or other defects that negatively impact the phosphor efficacy and lumen maintenance.

The sole intended function of the dopant ions is to trap charge carriers in the host lattice preferentially to the defects. However, the dopant ions may perform other intended functions in the phosphor, if desired. The host material, such as the halophosphate phosphor, may contain one or more of such rare-earth ions. The concentration of rare-earth ions is preferably above the unavoidable or background concentration normally present in the phosphor and may vary between 1 and 500 parts per million (ppm). The trivalent rare-earth ions in the phosphor lattice constitute electron attracting centers, because the rare-earth ions assume a stable divalent valence state by capturing or trapping an electron: $R^{3+} + e^{-} = R^{2+}$, where R^{3+} and R^{2+} are the rare-earth ions in trivalent and divalent valence states, respectively, and e^{-} is the free electron in the conduction band. Thus, the ability to form a stable divalent valence state contributes to the electron capture cross section of the rare-earth ions. Incorporation of the dopant ions in the trivalent state preferentially traps the electrons created by the 185 nm exciting radiation compared to vacancies on the halide ion lattice site in the halophosphate lattice, because the rare-earth ions have a higher electron capture cross section than the halide vacancies. The electron capture by the dopant ions diminishes the concentration of the color centers in the lattice of the halophosphate phosphor. Hence, a higher luminous output may be obtained in the doped halophosphate phosphors due to reduced probability of color center formation. The defects responsible for the color centers have been described as halide vacancies. However, other defects may also be responsible for the color centers.

Some lattice defects in ionic crystals are responsible for a decrease in efficacy and lumen maintenance trap either holes or both electrons and holes. In the halophosphate materials, hole trapping centers have been observed and are thought to arise from the trapping of holes by “hole trapping defects.” For example, such defects may comprise a vacancy on an oxygen lattice site (i.e., an oxygen vacancy) in combination with an oxygen ion on a halide lattice site adjacent to the oxygen vacancy (i.e., a nearest neighbor oxygen vacancy–oxygen on a halide site pair). Hole trapping defects also comprise +1 metal ion, such as Na^{1+} ions, on the Ca^{2+} lattice sites. Such hole trapping defects may also negatively influence the luminous output of the halophosphate phosphor in the same way as the electron trapping halide vacancies.

Second, the preferred hole trapping dopant ions comprise trivalent rare-earth ions also exhibit a stable tetravalent valence state in the host material. Non-limiting examples of such rare-earth ions are cerium (Ce^{3+}), terbium (Tb^{3+}), and praseodymium (Pr^{3+}). The host material, such as the halophosphate phosphor, may contain one or more of such rare-earth ions. The trivalent rare-earth ions in the phosphor lattice constitute hole attracting centers, because the rare-earth ions assume a stable tetravalent valence state by capturing or trapping a hole: $R^{3+} + h^{+} = R^{4+}$, where R^{3+} and R^{4+} are the rare-earth ions in the trivalent and tetravalent valence states, respectively, and h^{+} is the hole in the valence band. Thus, the ability to form a stable tetravalent valence state contributes to the hole capture cross section of the dopant ions. Incorporation of the dopant ions in the trivalent state preferentially traps the holes created by the 185 nm exciting radiation compared to the hole trapping defect in the halophosphate lattice, because the rare-earth ions have a higher hole capture cross section than the hole trapping defects. The hole capture by the dopant ions diminishes the concentration of the defect centers in the lattice of the halophosphate phosphor. Hence, a higher luminous output may be obtained in the doped halophosphate phosphors due to reduced probability of color center formation.

Eu^{2+} and Mn^{2+} Co-doped $Ca_5(PO_4)_3Cl$ with blue and orange double-band emissions were also researched based on the optimal composition and synthesis conditions. The prominent photoluminescence (PL) emission is observed at 446 nm (excitation wavelength is 350 nm). This corresponds to the $^6P_j \rightarrow {}^8S_{7/12}$ level transition of the Eu^{2+} ion; such emission has also been observed by previous workers [2, 3]. $Sr_5(PO_4)_3Cl{:}Eu^{2+}$ was prepared in open air atmosphere at high temperature, while Noetzold et al. [4] and Sato et al. [5] prepared halophosphate in a reducing atmosphere and, therefore, the results were different. The $Sr_5(PO_4)_3Cl{:}Eu$ phosphor had well-desired characteristics like a high-temperature glow peak, linear response with gray exposure, negligible fading, and an easy method of preparation. For these reasons, it could be suitable to use phosphor in dosimetry of ionizing radiations using the TL technique. In the context of defect centers in alkaline earth halophosphates, the study by Warren [6] is mentioned. Also Dhoble et al. reported the ESR, PL and TL studies on $Sr_5(PO_4)_3Cl{:}Eu$ halophosphate phosphor [7] and combustion synthesis of Dy^{3+}, Eu^{3+} activated $Na_2X(PO_4)F$ ($X = Mg, Ca, Sr$) phosphors for lamp industry [8]. Very recently, Shinde et al. [9] reported the effects of temperature on intense green emitting $Na_2Ca(PO_4)F{:}Mn^{2+}$ phosphor. The choice of the host material is a very crucial part of the luminescence study. In this context, a host that can be activated by different ions emitting in different regions of the visible spectrum is a challenge for the solid material synthesis. It is important to get different regions of the visible spectrum in a matrix whose different activation ions can be structurally substituted for the cation sites.

The luminescent performance can be improved greatly when phosphors are doped and co-doped with suitable auxiliary activators. In this chapter, halophosphate-based systems prepared by low-cost conventional combustion synthesis, which have advantages over the other systems are presented. There are currently very few references on the use of Dy^{3+} phosphors as white LED illumination sources. Therefore, it is crucial to study in detail phosphors for white light emitting materials. At present, more and more researchers devote themselves with great interest to this work. In this chapter, (1) the synthesis of $M_5(PO_4)_3F$ ($M = Ba, Sr, Ca$) doped with Eu^{2+} and Dy^{3+} and the effect of different concentrations thereof on the intensity are presented; (2) the energy transfer mechanism of Ce^{3+} and Eu^{2+} activated $Sr_5(PO_4)_3F$ phosphor as well as their luminescent properties are investigated; (3) the effect of temperature on the intense green emitting $Na_2Ca(PO_4)F{:}Mn^{2+}$ halophosphate phosphor and the enhancement in emission intensity arising from the thermal treatment is also discussed. (4) Furthermore, rare earth-based materials developed for wide application due to the high potential characteristics of rare-earth ions, and therefore development of spectroscopic study of these materials is new the challenges in the field of inorganic materials. This work is advanced to the preparation of complex fluorides ($Na_2Sr_2Al_2PO_4F_9$) involving as many as triple components with $Eu^{3+}/Ce^{3+}/Dy^{3+}$ rare-earth ions. And last, $Sr_5(PO_4)_3Cl{:}Eu^{2+}$ (2 mol%) has been found to be an efficient phosphor.

6.2 $M_5(PO_4)_3F$ (M = Ba, Sr, Ca):Eu^{2+} and Dy^{3+} by Combustion Method [10]

$M_5(PO_4)_3F$:Dy^{3+} and Eu^{2+} (M = Ba, Sr, Ca) phosphors were prepared through combustion technique. The starting AR grade materials (99.99 % purity) taken were calcium nitrate ($Ca(NO_3)_2 \cdot 4H_2O$), strontium nitrate ($Sr(NO_3)_2 \cdot 4H2O$), barium nitrate ($Ba(NO_3)_2$), di-ammonium hydrogen phosphate ($NH_4H_2(PO_4)$), ammonium fluoride (NH_4F), dysprosium oxide (Dy_2O_3), and urea (NH_2CONH_2) were used as fuel for combustion. In the present investigation, materials were prepared according to the chemical formula $M_{5-x}(PO_4)_3F$:Dy_x. The solution of reagents was mixed together to obtain a homogeneous solution. Dy^{3+} ion was introduced in the form of $Dy(NO_3)_3$ solution by dissolving Dy_2O_3 into HNO_3 solution. The molar ratio of dysprosium rare-earth ions was changed in relation to $Ba_5(PO_4)_3F$, $Sr_5(PO_4)_3F$, and $Ca_5(PO_4)_3F$ phosphor. The compositions of the metal nitrates (oxidizers) and urea (fuel) were calculated using the total oxidizing and reducing valencies of the components, which served as the numerical coefficients so that the equivalent ratio is unity and the maximum heat is liberated during combustion. After stirring for about 15 min, precursor solution was transferred to a furnace preheated to 500–600 °C and the porous products were obtained. The stoichiometric amount of redox mixture, when heated rapidly at ~600 °C was boiled, underwent dehydration followed by decomposition generating combustible gases such as oxides of N_2, H_2O and nascent oxygen. The volatile combustible gases ignite and burn with a flame, and thus provide conditions suitable for the formation of phosphor lattice with dopants. Large amounts of escaping gases dissipate heat and prevent the material from sintering and thus provide conditions for the formation of a crystalline phase. Rare earth ion doped $Ba_5(PO_4)_3F$:Dy, $Ca_5(PO_4)_3F$:Dy, and $Sr_5(PO_4)_3F$:Dy phosphors were prepared by introducing Dy ions in the form of a $Dy(NO_3)_3$ solution with the concentration of the Dy ions varied with $x = 2.5, 2, 1.5, 1, 0.5$ mol%. For $Ba_5(PO_4)_3F$:Eu, $Ca_5(PO_4)_3F$:Eu, $Sr_5(PO_4)_3F$:Eu, the Eu ions were introduced in the form of an $Eu(NO_3)_3$ solution with the concentration of the Eu ions varied with $x = 2, 1, 0.5, 0.2, 0.1$ mol%, and the procedure is repeated as explained above.

Several complementary methods were used to characterize the properties of the prepared phosphors. The prepared powder samples were characterized for their phase purity and crystallinity by X-ray powder diffraction (XRD) using a PANalytical diffractometer (Cu Kα radiation) at a scanning step of 0.01°, at a duration of 20 s, in the 2θ range from 10° to 120°. The photoluminescent measurement of the excitation and emission was recorded with a slit width of 1.5 nm and an equal weight amount of sample (2 g) for each measurement on the Shimadzu RF5301PC spectrofluorophotometer.

6.2.1 X-Ray Diffraction Pattern of $M_5(PO_4)_3F$, ($M = Ba, Sr, Ca$) Host Lattice

The XRD patterns of $Ba_5(PO_4)_3F$ phosphor (Fig. 6.1), $Sr_5(PO_4)_3F$, phosphor (Fig. 6.2), and $Ca_5(PO_4)_3F$ (Fig. 6.3) phosphor are shown in Figs. 6.1–6.3, respectively. The XRD patterns of the prepared phosphors were well matched with the standard data files available in JCPDS file number 071-1316 for $Ba_5(PO_4)_3F$, 003-0736 for $Sr_5(PO_4)_3F$, and 015-0876 for $Ca_5(PO_4)_3F$.

The prepared $Ba_5(PO_4)_3F$, $Sr_5(PO_4)_3F$, and $Ca_5(PO_4)_3F$ fluoride phosphate, crystallizes in the hexagonal apatite crystal system with the space group P63/m [11, 12] with $Z = 2$ [13]. However, the F ions occupy 2a positions with the atomic coordinates (0, 0, 0.25). Therefore, the F ions are in the planes of the triangles formed by the Ba^{2+}, Sr^{2+}, or Ca^{2+} ions on the 6h positions in the unit cell [11, 14]. In consequence, the first coordination sphere of the divalent host ions on the 6h positions consists of only seven ligands (six oxygen ions and one fluoride ion) in the prepared host lattices. The XRD patterns indicate the presence of crystalline $Ba_5(PO_4)_3F$, $Sr_5(PO_4)_3F$, and $Ca_5(PO_4)_3F$ host lattices with less than 5 % impurity phases such as the constituents nitrate and traces of ammonia, which is an indirect evidence for the formation of the desired compound. F ions should be distributed statistically on the halide lattice position. X-ray pattern do not show super lattice peaks and full width half maximum varies only in a small range. It is independent of the fluoride content purity form in the materials, which indicates the absence of cluster of F ions.

The bond length between divalent host metal ion and fluoride i.e., $M^{2+}\pm F$ in $M_5(PO_4)_3F$ ($M = Ba$, Sr, Ca) is smaller than the sum of the ionic radii between individual host metal and F ion in case of coordination number seven [15]. Polarization

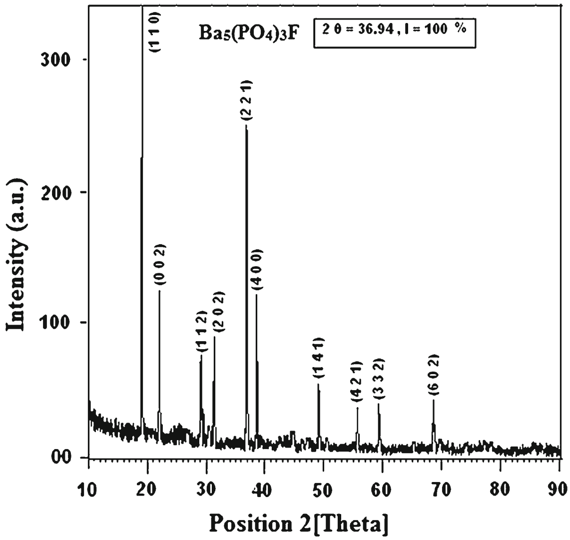

Fig. 6.1 X-ray diffraction pattern of $Ba_5(PO_4)_3F$ phosphor

Fig. 6.2 X-ray diffraction pattern of $Sr_5(PO_4)_3F$ phosphor

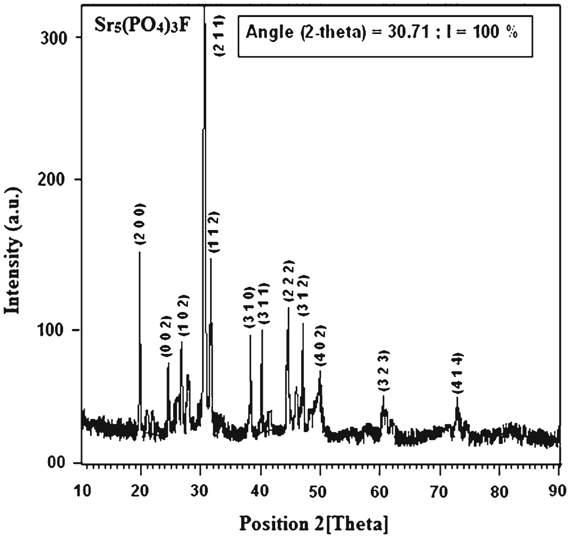

Fig. 6.3 X-ray diffraction pattern of $Ca_5(PO_4)_3F$ phosphor

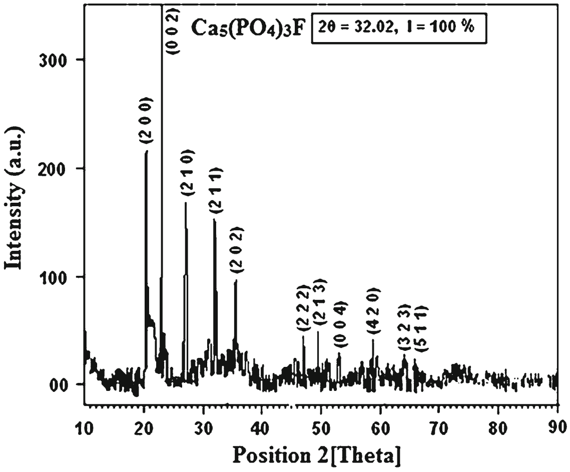

of the Ba^{2+}, Sr^{2+}, and Ca^{2+} divalent metal ions in the triangles by the small F ions could play the role in reducing effective radius in the direction toward the F ion showing more effective photoluminescent properties. The number and position of the halide ions in the first coordination sphere of M^{2+} ions depend on the fluoride content in the mixed crystals. Moreover, at constant fluoride content x different M^{2+} ions do not have the same surroundings of halide ions in their first coordination sphere in the range of $0 < x < 1$ [16]. The ionic radii of Eu ions is 94.7 pm and Dy ions is 91.2 pm for the coordination numbers 7, 8, or 9 [14]. They are similar to those of the Ca^{2+} ions (99 pm) rather than Sr^{2+} ions (112 pm) and Ba^{2+} ions (135 pm).

Therefore, Eu^{2+} or Dy^{3+} ions should occupy statistically both cation positions in the unit cell. It cannot be decided from the structural properties whether Eu^{2+} or Dy^{3+} ions prefer one of the two positions. The stoichiometric composition of the redox mixture for the combustion synthesis can be calculated according to the concept of propellant chemistry, i.e., the ratio of the oxidizing valency of metal nitrates to the reducing valency of fuel is one [17]. The theoretical quantity of the ratio of urea to M^{2+} in this study is calculated to be 2.4, combustion process was observed but non-porous fine powder was obtained under this condition. The reason for this is that urea can be easily decomposed or directly reacted with O_2 at high temperatures, thus urea must be added slightly in excess amounts, in order to achieve the optimum luminescence intensities of the samples.

6.2.2 Dy^{3+} *Photoluminescence in* $M_5(PO_4)_3F$*, (M = Ba, Sr, Ca) Phosphor*

Dy^{3+} ions in $M_5(PO_4)_3F$ phosphor gives blue, yellow, and red emission bands, respectively. PL excitation and emission spectrum of the Dy activated $Ba_5(PO_4)_3F$ phosphor is shown in Fig. 6.4, Dy activated $Sr_5(PO_4)_3F$ phosphor in Fig. 6.5, and Dy activated $Ca_5(PO_4)_3F$ phosphor in Fig. 6.6. The excitation spectrum monitored at blue emission from Dy^{3+} ion indicates several bands. Dy^{3+} with $4f^9$ configuration has complicated f-block energy levels, therefore various possible transitions between these levels are highly selective, and show sharp line spectra [18]. The excitation spectrum in the range of 250–400 nm due to $f \rightarrow f$ transition of Dy^{3+} ions having the highest intensity peak at 348 nm, which is assigned due to the $^6h_{15/2} \rightarrow {}^6m_{21/2}$ transition. The emission spectra for Dy^{3+} ions in $Ca_5(PO_4)_3F$ and $Ba_5(PO_4)_3F$ phosphor gives emission peaks at 482 nm (blue), 574 nm (yellow), and a small peak at 670 nm

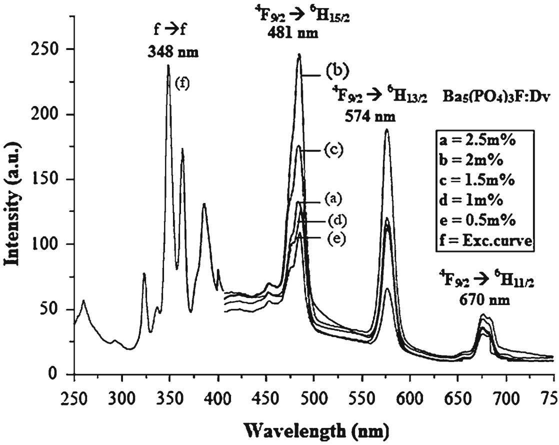

Fig. 6.4 PL excitation and emission spectra of $Ba_5(PO_4)_3F:Dy^{3+}$phosphor, with $\lambda_{exc} = 348$ nm monitored at $\lambda_{emi} = 481$ nm

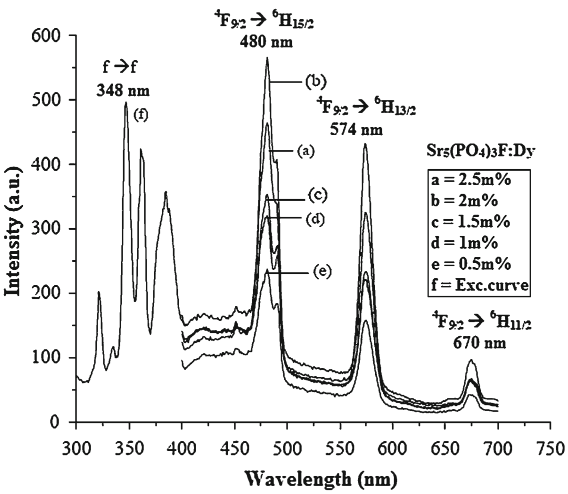

Fig. 6.5 PL excitation and emission spectra of $Sr_5(PO_4)_3F$: Dy^{3+} phosphor, when $\lambda_{exc} = 348$ nm was monitored at $\lambda_{emi} = 480$ nm

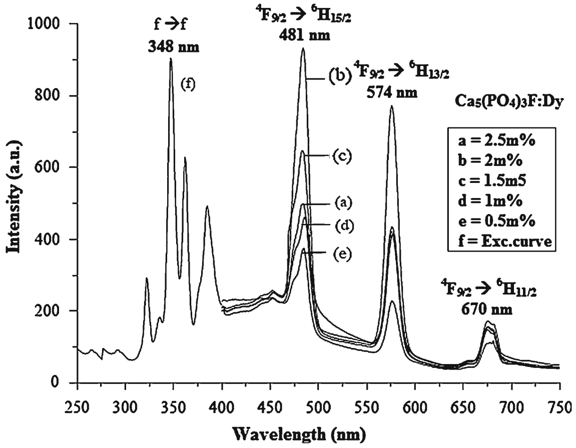

Fig. 6.6 PL excitation and emission spectra of $Ca_5(PO_4)_3F$: Dy^{3+} phosphor, when $\lambda_{exc} = 348$ nm was monitored at $\lambda_{emi} = 481$ nm

(red). Wherein, $Sr_5(PO_4)_3F$ phosphor gives emissions peak at 480, 574, and 670 nm, respectively. Three different emission bands are originated from the same excitation wavelength. The transitions involved in blue, yellow, and red bands of Dy^{3+} ions are well known. These bands have been identified as $^4F_{9/2} \rightarrow {}^6H_{15/2}$, $^6H_{13/2}$, $^6H_{11/2}$ transitions [19]. It is known that Dy^{3+} emission around 482 nm ($^4F_{9/2} \rightarrow {}^6H_{15/2}$) is due to the magnetic dipole moment and 574 nm ($^4F_{9/2} \rightarrow {}^6H_{13/2}$) due to the electric dipole moment. The transition $^4F_{9/2} \rightarrow {}^6H_{15/2}$ is predominant only when Dy^{3+} ions are located at low-symmetry sites with no inversion centers [20]. Since emission at 482 nm is predominant in $Ca_5(PO_4)_3F$, it suggests that there is little deviation from inversion symmetry in this matrix. However, in $Sr_5(PO_4)_3F$ the predominant emission is around 480 nm with a strong shoulder at 485 nm suggesting that ligands field slightly deviates from its inversion symmetry.

A marginal shift in the peak position of Dy^{3+} ions is observed in $Sr_5(PO_4)_3F$ phosphor compared to $Ca_5(PO_4)_3F$ and $Ba_5(PO_4)_3F$ phosphors. Such behavior is as expected for the emission involving $f-f$ transitions where ligand field changes with the host matrix. The excitation spectrum of the Dy^{3+} luminescence consisting of large number of sharp lines with the highest intensity at 348 nm gives blue/yellow/red ratio, known as the asymmetry ratio of Dy^{3+} ion. It varies while locating different host lattices, it is also reported in the Dy^{3+} doped $SrSiO_3$[19] system. The change in the host metal atom, changes the yellow/blue ratio due to the change of the local site symmetry around Dy^{3+} ions, gives BYR emissions. This UV excitation color co-ordinates are such that it is suitable as a white light-emitting phosphor.

In our case, the Dy^{3+} ion may enter into the host lattice to substitute Ca^{2+} or locate on the surfaces of the crystals due to the porosity of the spinal structure. As the ionic radii of Dy^{3+} is much larger than Ba^{2+} and Sr^{2+} near to Ca^{2+} or phosphate P^{5+}. The second possibility is more feasible. Most of the Dy^{3+} ions are located at the surface of $Ca_5(PO_4)_3F$ as compared to $Ba_5(PO_4)_3F$ and $Sr_5(PO_4)_3F$ phosphors and only a few of them entering into the lattice. Its substitution at Ca^{2+} site in $Ca_5(PO_4)_3F$ will lead to less distortion and induced more oxygen vacancies in the host in comparison to its substitution in $Ba_5(PO_4)_3F$ and $Sr_5(PO_4)_3F$ phosphors. The charge compensating defects in the immediate vicinity is likely to influence the local site symmetry of $Ca_5(PO_4)_3F$ host. Dy^{3+} ions should occupy statistically both cation positions ($M^{2+}\pm F$) in the unit cell. It would naturally gives rise to a substantial number of vacant sites in the oxygen ion array and then expand the lattice to decrease the crystal density. Lopez et al. reported that the oxygen vacancies might act as sensitizer for the energy transfer to the rare-earth ions due to the strong mixing of charge transfer states resulting in the highly enhanced luminescence [21]. But excess oxygen vacancies in the host would destroy the crystallinity inevitably, which lead to quenching of the luminescence [22]. This is reflected in the emission spectra, wherein the asymmetry factor is higher in the $Ca_5(PO_4)_3F$ sample compared to the $Ba_5(PO_4)_3F$ and $Sr_5(PO_4)_3F$ sample. As Dy^{3+} ions progressively replace the Ca^{2+} ions, which can enhance the PL emission intensity and the asymmetry factor progressively reduced. The low-symmetry location of Dy^{3+} results in predominant emission of $^4F_{9/2} \rightarrow {}^6H_{15/2}$ transition in the $Ca_5(PO_4)_3F$ host. Of course, $Ca_5(PO_4)_3F$ phosphors show strong PL emission intensity as compared to the $Sr_5(PO_4)_3F$ and the $Ba_5(PO_4)_3F$ phosphor (Fig. 6.7).

The emission wavelength does not vary with the Dy^{3+} concentration, but the luminescence intensity changes a lot. Different doping of activator ions can influence photoluminescence characteristics of a phosphor. Usually, a low doping gives weak luminescence but excess doping perhaps causes quenching of luminescence. With increasing concentration of Dy^{3+} ions the peak intensity increases and the maximum intensity is observed for 2 mol% of Dy^{3+} ion. The increase in the luminescence intensity with increase in concentration of Dy ions can be explained as follows: The luminescence spectrum of Dy^{3+} ion was slightly influenced by surrounding ligands of the host material, because electronic transitions of Dy^{3+} involve only redistribution of electrons within the inner $4f$ sub-shell. Crystallinity of phosphor could be increased due to increase in concentration of Dy ions. Since it is clear that

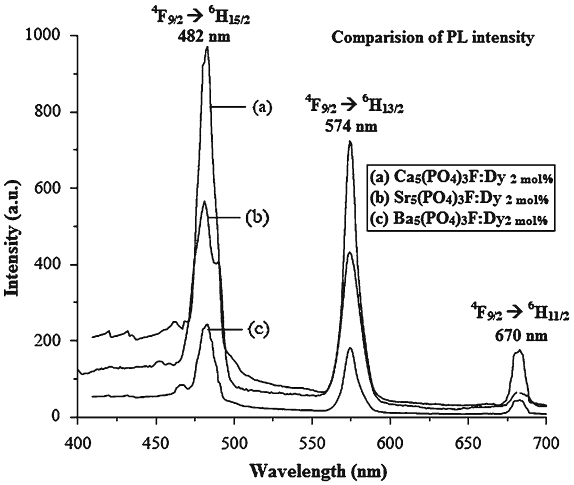

Fig. 6.7 Comparison of PL emission spectrum between Dy^{3+}ion in $Ca_5(PO_4)_3F$, $Sr_5(PO_4)_3F$, and $Ba_5(PO_4)_3F$ phosphor, monitored when $\lambda_{exc} = 348\,nm$

the addition of Dy ions into the $M_5(PO_4)_3F$ host increased the crystallinity. Increase in the concentration of Dy ions increases the particle size and its complex. Also, the increase in Dy^{3+} concentration will cause cross-relaxation between the transitions $^4F_{9/2}$–$^6F_{13/2}$ and $^6H_{15/2}$–$^6F_{11/2}$, the quenching of Dy^{3+} luminescence often occurs at low concentration [23]. Hence, there is an increase in photoluminescence intensity. This indicates that the $M_5(PO_4)_3F$ lattice is more suitable for higher concentrations of Dy^{3+} ions.

6.2.3 *Eu^{2+} Photoluminescence in $M_5(PO_4)_3F$, (M = Ba, Sr, Ca) Phosphor*

The peak wavelength of the Eu^{2+} emission has a blue broadband emission, which enables measurement of excitation spectrum. The PL excitation and emission spectrum of the Eu activated $Ba_5(PO_4)_3F$ phosphor (see Fig. 6.8), $Sr_5(PO_4)_3F$:Eu (Fig. 6.9) and $Ca_5(PO_4)_3F$:Eu phosphor (Fig. 6.10) are shown in Figs. 6.8, 6.9, and 6.10, respectively. Photoluminescence excitation spectrum appeared as sharp broadband excitation of the Eu ion. Broadband excitation is due to the Eu^{2+}–O^{2-} (CT band) charge transfer from europium to oxygen atoms. The emission peak is observed in the blue region of the visible spectrum with a maximum PL intensity at 440 nm. The excitation spectrum was recorded for the above composition ($\lambda_{emi} = 440\,nm$, Eu^{2+} emission). Ba^{2+} metal atom shows small variations in the PL emission peak compared to Sr^{2+} and Ca^{2+} ion. As seen from the figure, the emission spectrum of the prepared materials has a prominent peak at around 440 nm that can be well assigned to Eu^{2+} emission arising from transitions of the 5*d* configuration to the 4*f* level of the Eu^{2+} ion. Eu emission results from two types of transition, most common

Fig. 6.8 PL excitation and emission spectra of Ba $_5(PO_4)_3F:Eu^{2+}$phosphor, when $\lambda_{emi} = 438$ nm was monitored at $\lambda_{exc} = 350$ nm

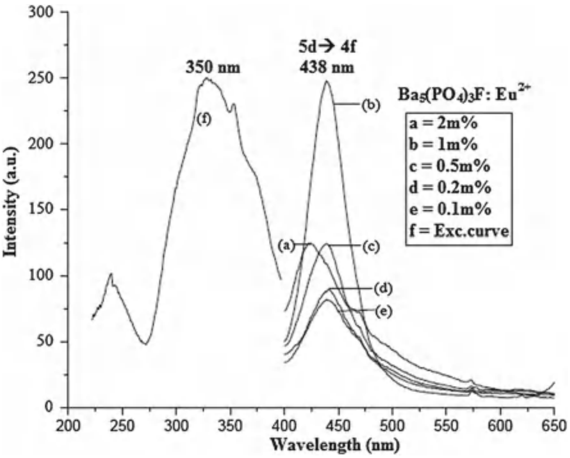

Fig. 6.9 PL excitation and emission spectra of Sr $_5(PO_4)_3F$: Eu^{2+} phosphor, when $\lambda_{emi} = 440$ nm was monitored at $\lambda_{exc} = 352$ nm

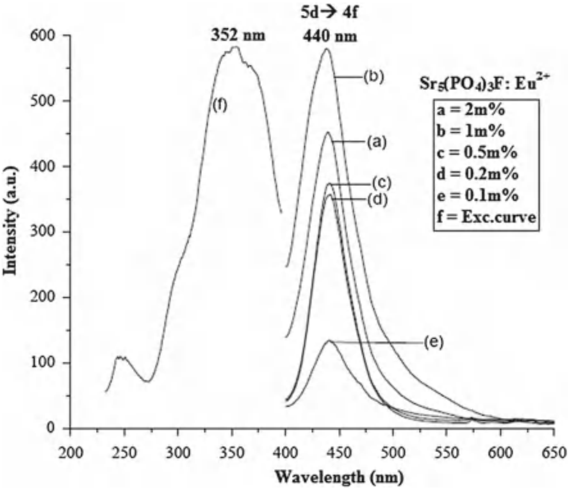

is $5d \rightarrow 4f$ transition. As the position of the band corresponding to $5d$ configuration is strongly influenced by the host, the emission can be anywhere from 365 nm (e.g.: in $BaSO_4$) to 650 nm (e.g.: in CaS). Blasse [24] has listed the Eu^{2+} doped compounds, which show that the emission color of Eu^{2+} may vary in a broad range, from ultraviolet to red. Since the $5d \rightarrow 4f$ transition is an allowed electrostatic dipole transition, the absorption and emission of Eu^{2+} is very efficient in many hosts, which makes the Eu^{2+} doped phosphors practically important. The Eu^{2+} ions have complex energy levels, which, in turn, is modified by the host matrices. The first excited $5d$ configuration lies close to the excited $4f$ levels and substituted Eu^{2+} ion is assumed to incorporate in the intermediate layer. In case of the divalent metal fluoride-based phosphate, the intermediate layer is only filled by the alkaline-earth metal atom and

Fig. 6.10 PL excitation and emission spectra of $Ca_5(PO_4)_3F$:Eu^{2+} phosphor, when $\lambda_{emi} = 440$ nm was monitored at $\lambda_{exc} = 352$ nm

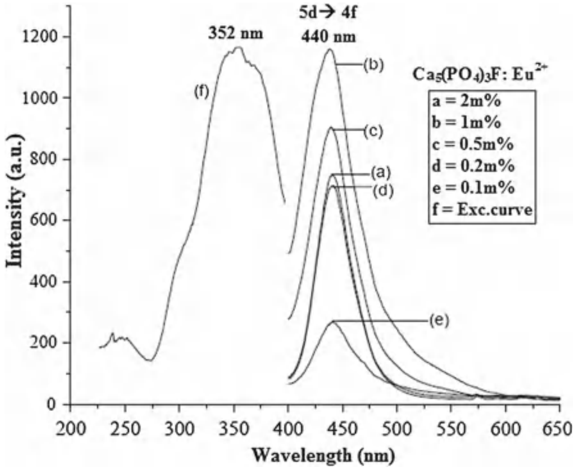

oxygen ion. This difference in coordination of Eu^{2+} results in a systematic shift of luminescence spectra as reported by Stevels et al. [25]. The unusual shape is likely associated with the presence of Eu^{2+} on Ca sites in the host and the Ca metal atom occupies a hexagonal co-ordination site. It is known that the maximum emission of Eu^{2+} ion depends on the cohesive energy exerted by the host matrix. Furthermore, due to the large spatial extension of the 5d wave function, the optical spectra due to the $5d \rightarrow 4f$ transitions usually depend on the surroundings of the Eu^{2+} ions. Thus, the choice of host is a critical parameter for determining the optical properties of the Eu^{2+} ions.

We can easily see that the ionic radii of Eu ions (94.7 pm) are similar to those of the Ca^{2+} ions (99 pm) rather than Sr^{2+} ion (112 pm) and Ba^{2+} ions (135 pm). Therefore, Eu^{2+} ions should easily substitute the calcium metal host atom to occupy statistically the cation positions in the unit cell. Hence most of Eu^{2+} occupies the sites of Ca^{2+}, it creates lower symmetry of the local environment around the Eu^{2+} ion. The ionic radius of the O^{2-} ion is 140 pm. The average value of the radius of other ions was set from the distance between ions that were measured for many oxides and the difference from the radius of the O^{2-} ion. The ionic radius of the negative ion becomes large and that of the positive ion becomes small compared to former neutral atoms. This results in a more uniform spatial distribution of the negative ions. Therefore, it is concluded that the emission originates from the Eu^{2+} ion incorporated in the spinal blocks. The Ca^{2+} ions view that their ionic radii are more easily accommodated in the Eu^{2+} ions from their spinal blocks. Consider replacement of Ba^{2+} or Sr^{2+} by Eu^{2+} ion, may cause a little decrease in PL intensity in $Sr_5(PO_4)_3F$ and $Ba_5(PO_4)_3F$ cell parameters.

Low concentration (0.2–0.5 mol%) of Eu^{2+} ion causes weak emission compared to higher concentration of the Eu^{2+} ions. It is well established that, in the case of hexa-coordination, the charge transfer band of Eu^{2+} lies in the high-energy region and it does not depend on the host lattice. Therefore, it is highly probable that in

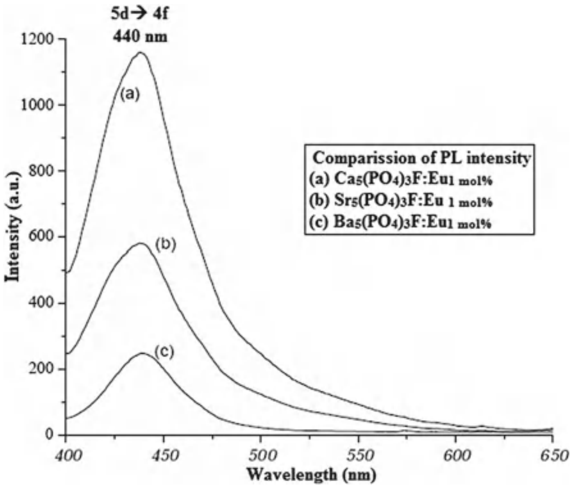

Fig. 6.11 Comparison of PL emission spectrum between Eu^{2+}ion in $Ca_5(PO_4)_3F$,$Sr_5(PO_4)_3$ F, and $Ba_5(PO_4)_3F$ phosphor, when monitored at $\lambda_{exc} = 352\,nm$

fluoride-phosphate the CT band of Eu^{2+} lies in the high energy region. Since the molar absorption coefficient of Ca^{2+} ions is very high in comparison with the Sr^{2+} and Ba^{2+} metal atoms, Eu^{2+} ions show prominent PL emission in case of Ca doped host lattices as shown in Fig. 6.11.

Similarly in case of Eu^{2+} ions the peak intensity increases and the maximum intensity is observed for 1 mol% of Eu^{2+} ion. The luminescence spectrum of Eu^{2+} ion is influenced by the surrounding ligands of the host material, because electronic transitions of Eu^{2+} involve only redistribution of electrons within the inner 4*f* subshell. Crystallinity of phosphor could be increased due to increase in concentration of the Eu ions. Since it is clear that the addition of Eu ions into $M_5(PO_4)_3F$ host increases the crystallinity, an increase in concentration of Eu ions increases the particle size as well as its complex. Hence, there is an increase in photoluminescence intensity. This indicates that the $M_5(PO_4)_3F$ lattice is more suitable for higher concentrations of Eu^{3+} ions. The emission itensity increases with the concentration from 0.1 to 1 mol%, quenching is obseverd after 2 mol% concentration of europium ion.

Although cold light emitted by a fluorescent lamp spreads around us and aids our life comfort, a shadow of extinction has been cast over the present fluorescent lamps. Generation of hazardous electrical and electric equipment waste has put restriction on the use of certain hazardous substances like mercury in electrical and electric equipment manufacture. Mercury excited (i.e., excitation wavelength 254 nm) fluorescent lamps are, therefore, likely to be prohibited in the near future, as a lighting source. Consequently, demand for new materials for modern illuminating engineering has increased recently. Hence, the importance of materials with low energy consumption and Hg-free lamps for lighting is increasing. A difference between the present mercury-based fluorescent lamp and mercury-free fluorescent lamp lies in the radiation wavelength of the gas discharge. The mercury-free fluorescent lamp requires excitation wavelength other than 254 nm. The 300–400 nm is

Hg-free excitation (Hg excitation is 85 % at a 254 nm wavelength of light and 15 % at other wavelengths), which is characteristic of solid-state lighting phosphors. Therefore, the entire PL characteristic indicates that Eu^{3+} doped $M_5(PO_4)_3F$ as well as $M_5(PO_4)_3F$ phosphors may be a good candidate for solid-state lighting devices as well as for white LED manufacture in future.

6.2.4 Conclusions

It is concluded that, Dy and Eu activated $M_5(PO_4)_3F$, (M = Ba, Sr, Ca) phosphors were synthesized by the combustion method. The PL emission spectrum of Dy^{3+} ions at 348 nm excitation gives an emission at 482 nm (blue), 574 nm (Yellow), and 670 nm (red). The low-symmetry location of Dy^{3+} results in predominance emission of the $^4F_{9/2} \rightarrow {}^6H_{15/2}$ transition. The PL revealed the presence of Dy^{3+} ions at asymmetric sites. Hence, the $Ca_5(PO_4)_3F$ phosphors show strong PL emission as compared to $Sr_5(PO_4)_3F$ and $Ba_5(PO_4)_3F$ phosphor. The BYR emission is important in the context of Dy^{3+} nonequivalent substitution in solid-state lighting phosphors (mercury-free excited lamp phosphor) and white light LED. PL emission spectra of Eu^{2+} ions give a broadband emission spectrum with a maximum intensity at 440 nm due to the $5d \rightarrow 4f$ transition of Eu^{2+} ions under 350 nm excitation and BYR emission in Dy^{3+} ion at 348 nm excitation, which may be useful for solid-state lighting and LED applications.

6.3 Energy Transfer between Ce^{3+} and Eu^{2+} in Doped $Sr_5(PO_4)_3F$ Phosphor [26]

6.3.1 Experimental

The Eu^{2+} and Ce^{3+} activated $Sr_5(PO_4)_3F$ phosphors have been prepared by combustion synthesis. The starting AR grade materials (99.99 % purity) were strontium nitrate ($Sr(NO_3)_2$), ammonium di-hydrogen phosphate ($NH_4H_2PO_4$), ammonium fluoride (NH_4F), europium oxide (Eu_2O_3), ammonium cerium nitrate ($(NH_4)_2Ce(NO_3)_6$), and urea (NH_2CONH_2) was used as fuel. In the present investigation, materials were prepared according to the chemical formula $Sr_{5-x}(PO_4)_3F{:}Eu_x$. The mixture of reagents was mixed together to obtain a homogeneous solution. Eu^{2+} ions were introduced in the form of $Eu(NO_3)_3$ solution by dissolving Eu_2O_3 into a diluted solution. HNO_3 solution and Ce^{3+} ions from $(NH_4)_2Ce(NO_3)_6$. The molar ratio of rare-earth ions was varied in the $Sr_5(PO_4)_3F$ phosphor in relation to the Sr ions. Fuel urea was taken in excess than the stoichiometric ratio for the complete combustion. After stirring for about 30 min, the precursor solution was transferred to a furnace preheated at 550–650 °C where after the porous products were obtained.

The combustion reaction is roughly described as follows:

$$\mathbf{15Sr(NO_3)_2 + 9NH_4H_2PO_4 + 19NH_2CONH_2(excess) + 3NH_4F}$$
$$\mathbf{\rightarrow 3Sr_5(PO_4)_3}\mathrm{F} + \mathbf{40N_2 + 19CO_2 + 71H_2O}$$

6.3.2 Structural, Compositional, and Morphostructural Characterizations

Figure 6.12 shows the XRD pattern of the $Sr_5(PO_4)_3F$ host lattice. The XRD pattern almost matches the standard JCPDS file No. 017-0609 for the $Sr_5(PO_4)_3F$ lattice. The prepared $Sr_5(PO_4)_3F$ phosphate, crystallized in a hexagonal crystal system, Fig. 6.13 in the space group P63/m. With $Z = 2$ [27] there are $6PO_4$ groups with their central P ions at the hexagonal corners on the reflection planes, and the F ions centered on the hexagonal faces. The XRD pattern indicates the presence of crystalline $Sr_5(PO_4)_3F$ host lattice with only a small amount of impurity phase of the P_2O_7 group, which is the indirect evidence of the formation of the desired compound. The small amount of P_2O_7 impurity phases are observed due to the rapid increase in flame temperature during the combustion synthesis. The presence of the P_2O_7 impurity in the PO_4 group having no influence on the luminescence properties is also supported by Kenji Toda et al. [28].

Energy dispersive spectrometry (EDS) analysis was employed to determine the composition of the $Sr_5(PO_4)_3F$ phosphors. Major chemical elements, namely Sr, P, O, and F were detected from the EDS data (Fig. 6.14). Atomic percentages are consistent with expected results except for O. From weight and atomic percentage ratio oxygen concentration, it was slightly higher than the expected value. This excess of oxygen in the crystal may be due to the environmental trace and combustible gases evolved during the reaction.

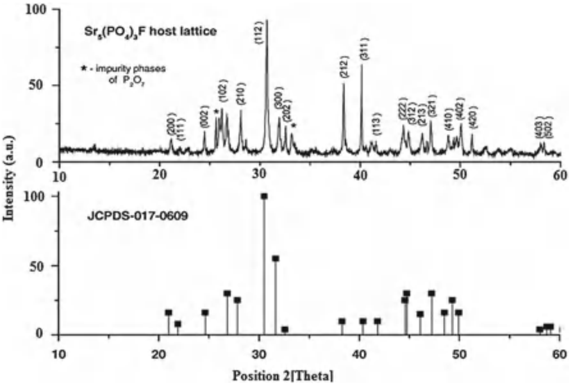

Fig. 6.12 X-ray diffraction pattern of the $Sr_5(PO_4)_3F$ host lattice

Fig. 6.13 Hexagonal crystal system of the $Sr_5(PO_4)_3F$ phosphate

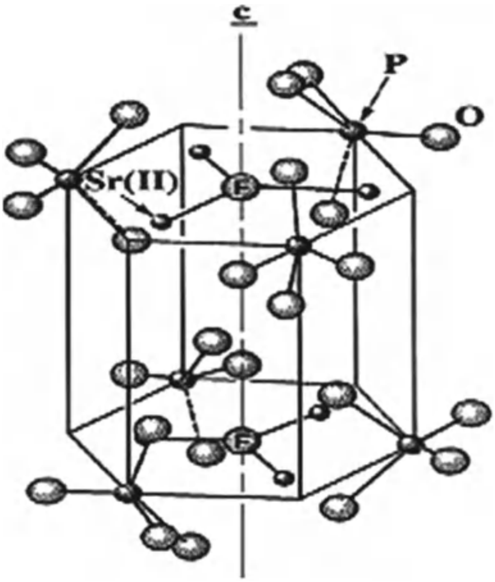

Fig. 6.14 EDS spectrum of the $Sr_5(PO_4)_3F$ as function of energy

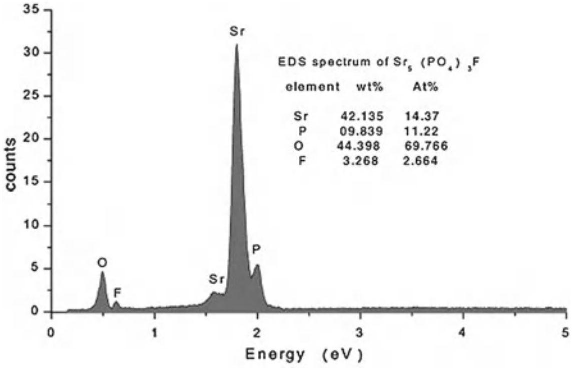

EDS spectrum of $Sr_5(PO_4)_3F$

element	wt%	At%
Sr	42.135	14.37
P	09.839	11.22
O	44.398	69.766
F	3.268	2.664

SEM micrographs of the prepared sample suggest formation of the spherical coagulated particles as shown in Fig. 6.15. It is clearly seen that the grains have irregular particle shapes with sizes between 0.5–2 μm.

6.3.3 Photoluminescence Characterization of the $Sr_5(PO_4)_3F{:}Eu^{2+}$

The dopants did not induce a significant change in the crystalline structure. Considering the effect of ionic size of cations, we proposed that Ce^{3+} and Eu^{2+} are expected

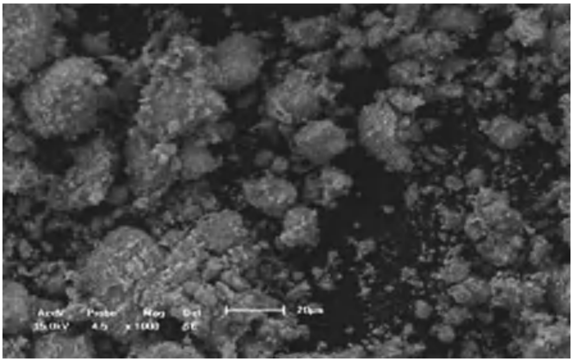

Fig. 6.15 SEM image of the $Sr_5(PO_4)_3F$ as host lattice

to preferably occupy the Sr^{2+} sites because of the ionic radii of Ce^{3+} (1.01 Å) and Eu^{2+} (1.09 Å). Figure 6.16 shows the excitation and emission spectrum of Eu^{2+} in the $Sr_5(PO_4)_3F$ host. The excitation spectrum shows two peaks located around 324 and 354 nm, which can be attributed to $4f-5d$ transitions of Eu^{2+} ions. It suggests that the $Sr_5(PO_4)_3F{:}Eu^{2+}$ phosphors can be effectively excited by UV LEDs (350–400 nm) excitation. The phosphor invariably emits blue luminescence with a peak wavelength at 440 nm under UV excitation. The luminescence of Eu^{2+} corresponds to a $5d-4f$ transition, which is an allowed electrostatic dipole transition. There are no observed differences for the emission band shape and position under differing excitation wavelengths (i.e., at $\lambda_{exc} = 324$ and 354 nm). The luminescent intensity and the emission spectrum are symmetric, which implies that Eu^{2+} ions just occupy one kind of site in the $Sr_5(PO_4)_3F$ lattice, which gives rise to a single emission center.

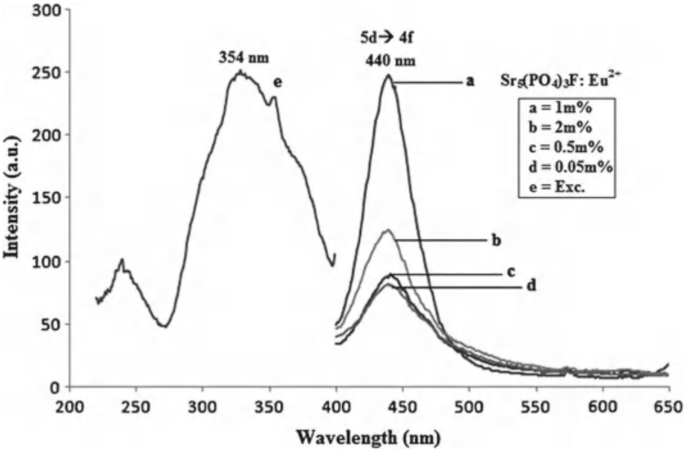

Fig. 6.16 PL excitation and emission spectra of $Sr_5(PO_4)_3F{:}Eu^{2+}$ where $\lambda_{emi} = 440$ nm monitored at 354 nm excitation

In Fig. 6.16, emission spectrum possesses a prominent peak at around 440 nm, which can be well assigned to Eu^{2+} emission. The observed 440 nm emission peaks arise from transitions of the $4f^6 5d$ configuration to the $8S_{7/2}$ level of the $4f^7$ configuration. The PL intensity increases with an increase in the concentration from 0.05 to 2 mol%. Concentration quenching effect is observed for more than 1 mol% of Eu ions.

6.3.4 Photoluminescence Characterization of the $Sr_5(PO_4)_3F:Ce^{3+}$

The trivalent Ce^{3+}-ions have an electronic structure containing one $4f$-electron, and as an activator, they generally result in phosphors having broadband UV emission. The emission and excitation spectra of Ce^{3+} activated $Sr_5(PO_4)_3F$ are shown in Fig. 6.17. Monitored at 355 nm emission, the excitation spectrum consists of a broad peak located between 240 and 270 nm. Under excitation at 254 nm at room temperature, Fig. 6.17 shows the Ce^{3+} emission consisting of a doublet broadband with a maximum at 355 nm, a shoulder around 330 nm with additional smaller broadband also observed at around 400–480 nm. The observed additional band implies that Ce^{3+} ions just occupy two different kinds of sites in the $Sr_5(PO_4)_3F$ lattice, which give rise to a single emission center. At room temperature, the first two emission peaks are sharper and resolved into two bands at 330 and 355 nm, respectively. These peaks are attributed to transitions from the Ce^{3+}-$5d$ lowest energy level to the $^2F_{7/2}$ and $^2F_{5/2}$ manifolds split by the spin-orbit interaction. The splitting energy value between $^2F_{7/2}$ and $^2F_{5/2}$ levels' Stokes shift is 2,500 cm^{-1}, at room temperature, a typical value for this luminescent ion [29]. In this host lattice, 400–480 nm additional emission broad bands observed due to $5d$ excitation bands of these Ce_2^{3+} centers. It is possible to resolve the $5d$ excitation bands of these Ce_2^{3+} centers with the same excitation wavelength (i.e., 254 nm). Probable charge compensation mechanisms, which occur

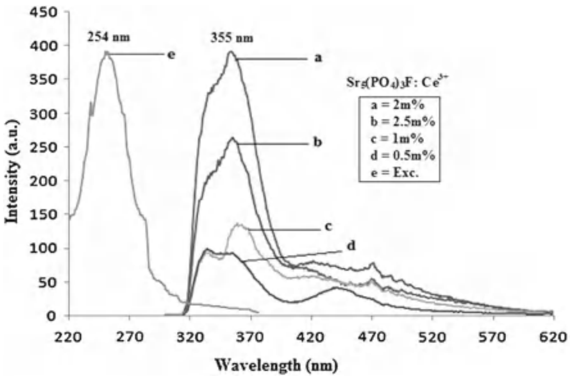

Fig. 6.17 PL excitation and emission spectra of the $Sr_5(PO_4)_3F:Ce^{3+}$ where, λ_{emi} = 355 nm monitor at 254 nm excitation

when a trivalent ion is introduced on a divalent site, can be performed by the creation of one vacancy at a strontium site per two Ce^{3+} ions or by oxygen on a fluoride site [30]. Usually Ce^{3+} centers with nearby charge compensators produce the emission at longer wavelength than isolated Ce^{3+} center [28]. The fluorescence intensity increases with an increase in Ce^{3+} concentration up to 2 mol%, beyond which the fluorescence intensity tends to quench. It is also noticed that the peak positions of the emission bands have not changed.

6.3.5 Photoluminescence Characterization of the $Sr_5(PO_4)_3F:Eu^{2+}, Ce^{3+}$

The excitation spectra of Ce^{3+} and Eu^{2+} co-activated $Sr_5(PO_4)_3F$ monitored at 440 nm (Eu^{2+} emission) are shown in Fig. 6.18, of which the excitation peak is obtained at around 354 nm. Under excitation at 354 nm, the emission spectrum consists of a strong broad band centered at about 440 nm. It can be presumed that Eu^{2+} and Ce^{3+} ions occupy different types of sites in the $Sr_5(PO_4)_3F$ host lattice, forming corresponding emission centers. Another possible reason for the broadband can be explained by the crystal field splitting effect. The emission intensity is strongly enhanced by increasing the Ce^{3+} concentration with a maximum at about 1 mol%. The PL intensity of $Sr_5(PO_4)_3F:Ce_{1\,mol\%}Eu_{1\,mol\%}$ under 354 nm excitation is nearly five times greater than that of the $Sr_5(PO_4)_3F:Eu^{2+}$ phosphor. This can be attributed to the typical energy transfer between two transition metals or rare-earth ions that is Eu^{2+} and Ce^{3+} ions. Hence, in the emitting process, Ce^{3+} ions probably act as a sensitizer, while the Eu^{2+} ions act as an activator such that the effective emitting

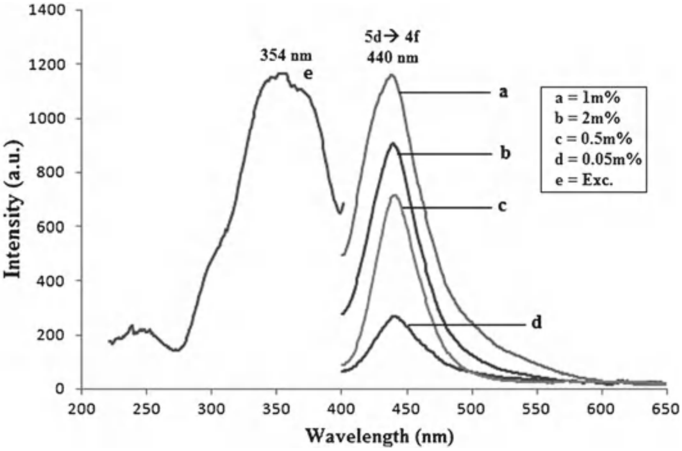

Fig. 6.18 PL excitation and emission spectra of $Sr_5(PO_4)_3F:Eu_{(x\,mol\,\%)}$,Ce where $\lambda_{emi} = 440$ nm monitored at 354 nm excitation

energy transfer from Ce^{3+} ions to Eu^{2+} ions causes enhancement in the emitting intensity.

6.3.6 Energy Transfer Mechanism Between Ce^{3+} and Eu $^{2+}$ Ion

Energy transfers are observed between two rare-earth ions and have been reported in several Ce^{3+} and Eu^{2+} co-doped phosphors, such as $Sr_3B_2O_6$:Ce^{3+},Eu^{2+} [30], $CaAl_2S_4$:Eu^{2+},Ce^{3+}, [31], and Li_2SrSiO_4:Eu^{2+},Ce^{3+} [32]. In the Inset of Fig. 6.19, the proposed energy transfer mechanism, which may be useful for presentation of results, is presented. If the energy transfer by movement of charge carriers is neglected, there can be two different mechanisms for energy transfer between sensitizer and activator: (1) radiative transfer through emission of sensitizer and reabsorption by activator and (2) non-radiative transfer associated with resonance between absorber and emitter. The efficiency of radiative transfer depends on how efficiently the fluorescence of the activator is excited by the emission of the sensitizer. It requires a significant overlap of the emission region of the sensitizer and the absorption region of the activator, and an appreciable intensity of the absorption region of the activator [33]. The energy transfer from Ce^{3+} ion to Eu^{2+} ion in $Sr_5(PO_4)_3F$:Eu,Ce can be ascribed due to the spectral overlap between the $5d-4f$ emission band of Ce^{3+} and the $4f-4f$ excitation lines of Eu^{2+}, shown in Fig. 6.19. This condition is satisfied with the energy transfer mechanism reported by Blasse et al.

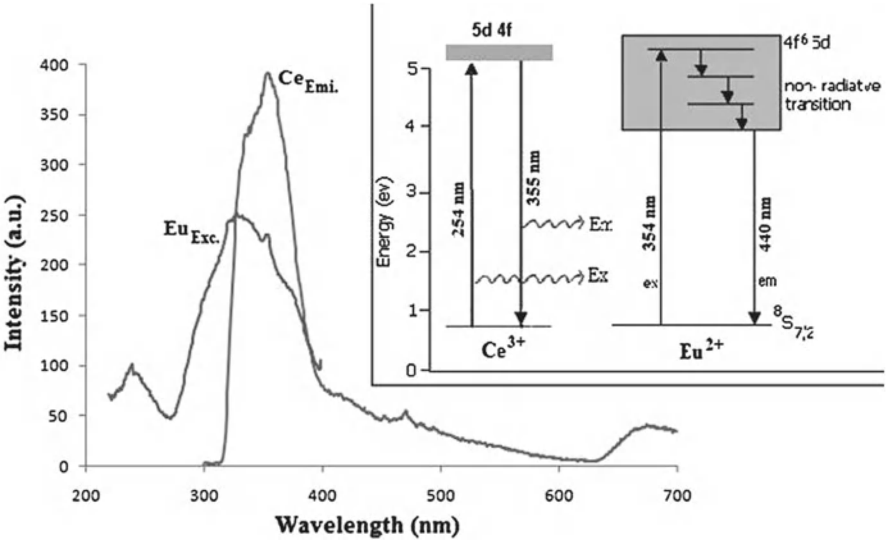

Fig. 6.19 Emission spectrum of Ce^{3+} (max) overlapped with the excitation spectrum of Eu^{2+} (max)-doped $Sr_5(PO_4)_3F$ with schematic energy transfer diagram for $Ce^{3+} \rightarrow Eu^{2+}$

[33]; as non-radiative energy transfer associated with resonance between absorber and emitter band. It appears that the emission band of the Ce^{3+} ion is in resonance with the absorber band of the Eu^{2+} ion. The Ce^{3+} ion emission goes to the non-radiative sites and transfers most of its energy to Eu^{2+} emission sites. It may be followed that the emission band of Ce^{3+} overlaps very well with the excitation band of the Eu^{2+} ion. In this case, the Ce ion acts as a sensitizer, and the Eu ion acts as activator. There is a significant overlap observed in the emission region of the sensitizer (Ce^{3+} ion) with an appreciable intensity of the absorption region of the activator (Eu^{2+} ion). Hence, the Ce^{3+} emission band simply acts as the excitation band of the $Sr_5(PO_4)_3F$:Eu,Ce phosphor. Therefore in phosphate, efficient energy transfer from Ce^{3+} to Eu^{2+} ions need to be fulfilled. It is obvious that the efficient $Ce^{3+} \rightarrow Eu^{2+}$ ion energy transfer leads to much higher emission intensity of the Eu^{2+} ion in (Ce^{3+}+Eu^{2+}) doped phosphate phosphor rather than only in Eu^{2+} doped phosphate materials. It is found that the small percentage of co-doping with Ce^{3+} ion can greatly modify the UV excitation spectra. It is therefore expected that Eu^{2+} acts as the activator ion that gives an intense blue emission with the aid of Ce^{3+} as sensitizer. From the results, it can be seen that by co-doping with a few mol percent of Ce^{3+}, the absorption at the long wavelength side is greatly increased. With such a small concentration of doping, the crystal field should not be changed notably. The emission intensity of the 440 nm emission of Eu^{2+} (Fig. 6.16) is progressively enhanced until the concentration of Ce^{3+} is up to 1 mol%. Thereafter, it starts decreasing with the increasing concentration of Ce^{3+} ion. In low concentration, a few Ce^{3+} ions can feed the absorbed energy to the nearest Eu^{2+} ions. The maximum PL intensity is observed in $Sr_5(PO_4)_3F:Eu_{1\,mol\%,}Ce_{1\,mol\%}$ phosphor as compared to other concentrations. As a result, the emission intensity of the $Sr_5(PO_4)_3F:Eu^{2+}_{1\,mol\%}$, $Ce^{3+}_{1\,mol\%}$ phosphor is significantly enhanced; nearly five times compared with the $Sr_5(PO_4)_3F:Eu^{2+}_{1\,mol\%}$ (Fig. 6.17) phosphor. The nearest Ce^{3+} and Eu^{2+} ions serve as an isolated donor–acceptor pair. With the increase in concentration of Ce^{3+} the concentration of the isolated donor–acceptor pairs progressively increases, resulting in the enhancement of the 440 nm emitting intensity of the Eu^{2+} ion. Or it can be concluded that 400–480 nm additional emission broad band due to 5*d* excitation bands of these Ce^{3+}_2 centers transfer its part of emission energy to Eu^{2+} ion. The Ce^{3+}_2 ion acts as an emission center in $Sr_5(PO_4)_3F:Eu^{2+},Ce^{3+}$ phosphor.

6.3.7 Conclusions

In conclusion, we have synthesized a series of Ce^{3+} and Eu^{2+} co-doped $Sr_5(PO_4)_3F$ phosphors, and their morphological and luminescent properties were also investigated. The spectroscopic data indicated that the energy transfer from Ce^{3+} to Eu^{2+} took place in the $Sr_5(PO_4)_3F$ host. By co-doping with Ce^{3+} ion, the UV excitation efficiency is greatly enhanced throughout the spectral range from 300 to 400 nm. It appears that the emission band of the Ce^{3+} ion is in resonance with the absorber band of the Eu^{2+} ion. The Ce^{3+} ion emission goes to the non-radiative sites and transfers most of its energy to Eu^{2+} emission sites. The enhanced PL emission intensity originates from the strong $4f^0 5d^1 \rightarrow 4f^1 5d^0$ transitions of Ce^{3+} and the energy transfer from $Ce^{3+} \rightarrow Eu^{2+}$ ion. Ce^{3+} ions play a role as a sensitizer, while Eu^{2+} ions act as activator.

6.4 Photoluminescence Properties and Effect of Temperature on Intense Green Emitting $Na_2Ca(PO_4)F{:}Mn^{2+}$ Phosphor [9]

6.4.1 Experimental

Powder samples are prepared by using simple heating treatment in a reducing charcoal environment. The starting materials used in the synthesis of the material are high-purity $CaCO_3$ (99.9 %), Na_2HPO_4 (99.99 %) $(CH_3COO)_2Mn_x$.4H2O (99.99 %), and NaF (99.99 %). The dopant concentrations of Mn ion are varied from 0.2 to 2 mol% in $Na_2Ca(PO_4)F$:Mn. The starting materials were taken stoichiometrically in appropriate amounts in metrological proportions. The homogenized mixture was ground thoroughly in a mortar and pestle for 2 h. Then the mixture was kept in a crucible covered with lead and tied with silica cotton to avoid direct environmental contamination. This covered crucible was kept in a larger stainless steel box filled with charcoal powder. The role of the charcoal environment is to avoid the possibility of oxidation of Mn^{2+} ion and also to avoid reaction of the compound with environmental oxygen [34, 35]. The sealed ceramic crucible was kept in the preheated furnace at 600, 800, and 1,000 °C for 5–7 h. The prepared sample was washed with double-distilled water for several times to remove any unreacted impurities. The sample was then dried at 80 °C to obtain a white crystalline powder. The synthesis reaction is given as follows:

$$\begin{aligned}&\mathbf{1/2Na_{(2-x)}HPO_4 + CaCO_3 + NaF + CH_3COO_3Mn_x4H_2O}\\&\mathbf{\rightarrow Na_{(2-x)}CaPO_4F{:}Mn_x + 14H_2O + 12CO_2 + 24N_2}\end{aligned}$$

6.4.2 Structural, Compositional, and Morphostructural Characterizations

The XRD pattern of the $Na_2Ca(PO_4)F$ host lattice at 600, 800, and 1,000 °C is shown in Fig. 6.20. The XRD pattern at 600 and 800 °C contains some impurity phases, indicated by asterisks. The presence of some impurity phases shows that some unreacted carbonates and some P_2O_7 phases remain in the compound. The pure phase of the X-ray diffraction pattern of $Na_2Ca(PO_4)F$ was obtained at 1,000 °C,

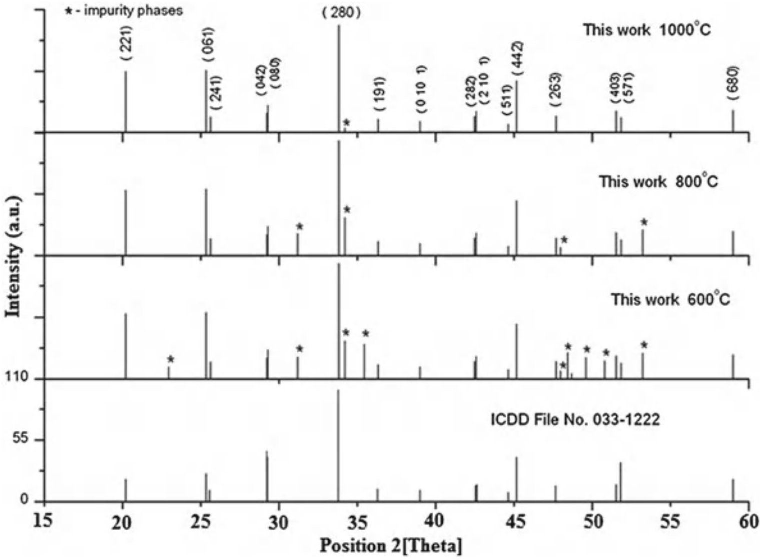

Fig. 6.20 XRD of $Na_2Ca(PO_4)F$ synthesized at 600, 800, and 1,000 °C and ICDD file

which is indirect evidence for the formation of the desired compound (Fig. 6.20). A negligible amount of unavoidable P_2O_7 phases still remained in the compound at 1,000 °C. The reducing environment, provided using charcoal, did not affect the crystal structure of the host phosphate [36]. The presence of a small amount of P_2O_7 impurity in the powder had no influence on the luminescence properties, as reported by Toda et al. [37]. The role of the charcoal environment in the synthesis process was to avoid the possibility of the oxidation of Mn^{2+} ion and contamination of sample with environmental oxygen [34, 35]. The increase in the synthesis temperature gave complete formation of the product with a orthorhombic crystal structure. The data obtained from the X-ray diffraction pattern matched well with standard ICDD file no. 033-1222.

The available crystal structure of nacaphite $Na_2Ca(PO_4)F$ from web minerals data sites [38] is shown in Fig. 6.21. It contains one Ca and two Na ion positions. The Ca site is coordinated by one F^- and four O^{2-} anions with Ca^{2+} distances in the range of 2.32–2.57 Å. The Ca^{2+} cation has five closest anions (one F^- and four O^{2-}) with a Ca^{2+} bond length of 2.29–2.37 Å. The axial indices are $a{:}b{:}c$ 0.436:1:0.2905, and cell dimensions $a = 10.65$, $b = 24.425$, $c = 7.097$, $Z = 16$; $a = 89.99°$, $b = 89.998°$, $g = 90.04°$, $V = 1846.12\,Å^3$, $\mathrm{Den(calc)} = 2.80\,\mathrm{gcm}^{-3}$. All Na^+ cations are octahedrally coordinated by four O^{2-} and one F^- anions each. The Ca^{2+} and Na^{2+} cation arrangements were parallel to the (100) plane and separated by F^- anions and $(PO_4)^{3-}$ tetrahedra.

The typical morphological images are represented by SEM images in Fig. 6.22. Initially, at 600 °C the growth of the particles was floppy but include the possible

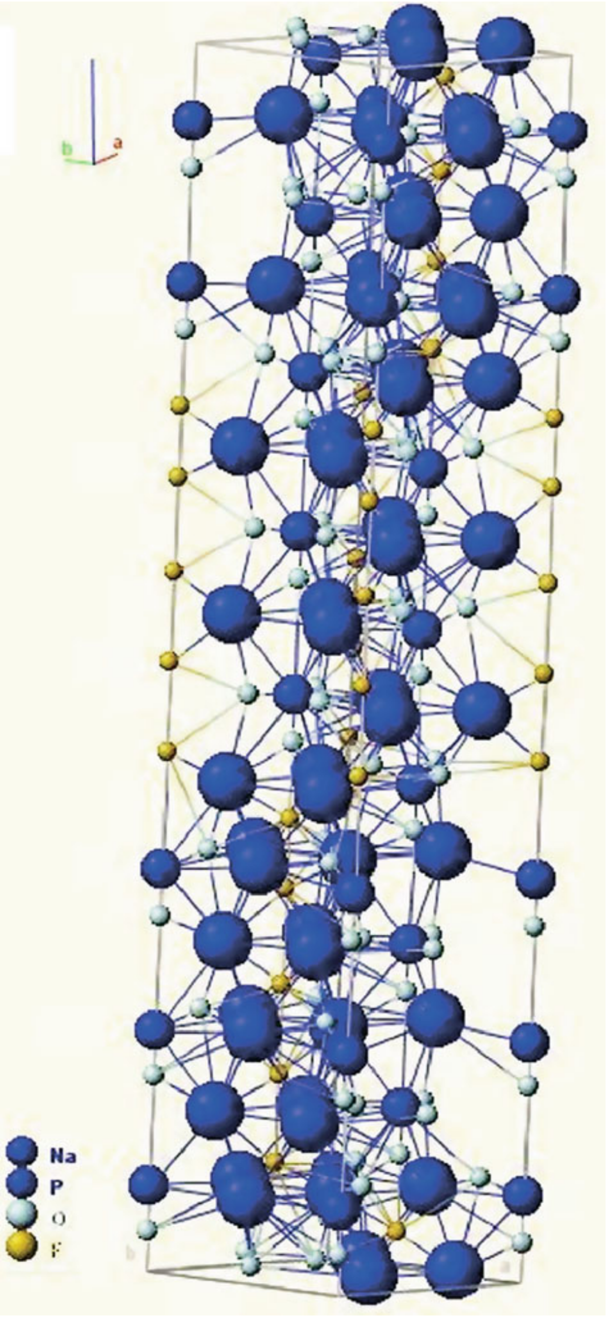

Fig. 6.21 Crystal structure of nacaphite $Na_2Ca(PO_4)F$ [38]

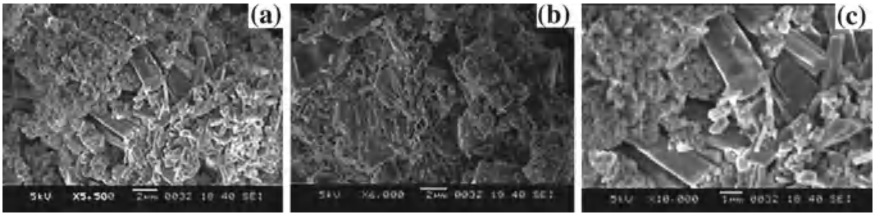

Fig. 6.22 SEM images of $Na_2Ca(PO_4)F$ at (**a**) 600 °C, (**b**) 800 °C, and (**c**) 1,000 °C synthesis temperatures

growth of rods. At the higher temperatures of 800 and 1,000°C, mixed rod shaped morphology was obtained with diameter from 0.2 to 2 mm and length 1–5 mm.

6.4.3 PL Properties of $Na_2Ca(PO_4)F:Mn^{2+}$ Phosphor

Figure 6.23 exhibits the excitation spectrum with a peak at around 259 nm (monitored at 522 nm emission) for the samples prepared at 600, 800, and 1,000°C. The overall intensity profile follows the same order as observed in the emission spectra. The phosphor prepared at 1,000 °C doped with 0.5 mol% of Mn ion gave the highest intensity with a small shift in peak position toward higher wavelengths.

Figure 6.24 shows the emission spectra of the samples at around 259 nm excitation for the different synthesis temperatures. It shows that the thermal treatment

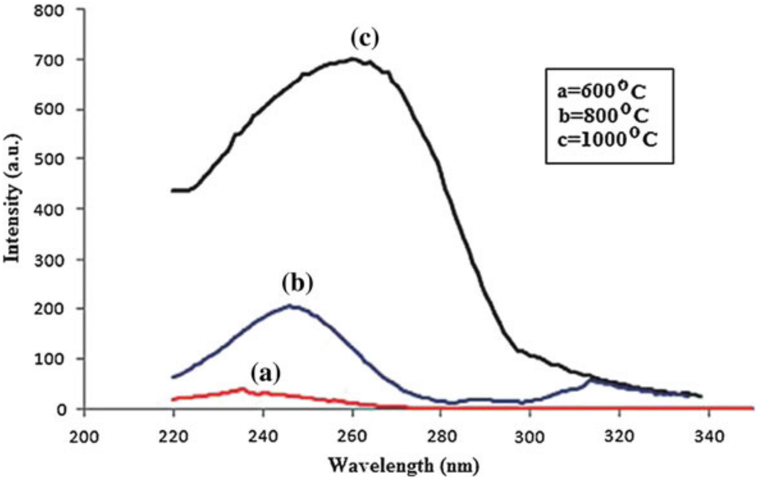

Fig. 6.23 Excitation spectrum of $Na_2Ca(PO_4)F:Mn^{2+}{}_{0.5\,\mathrm{mol\%}}$ at (**a**) 600 °C, (**b**) 800 °C, and (**c**) 1,000 °C synthesis temperatures

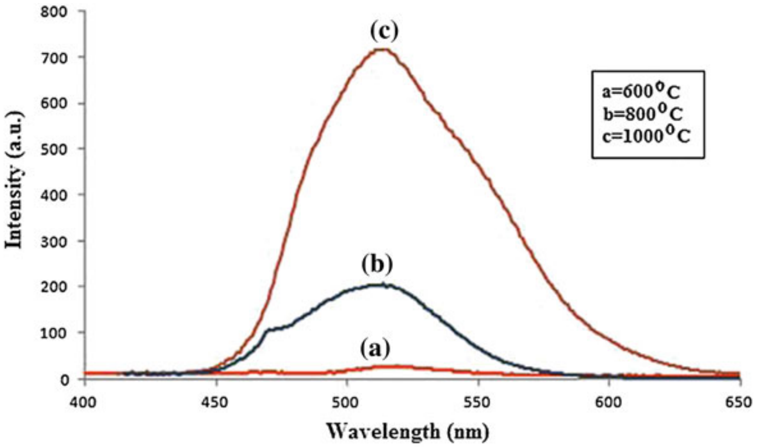

Fig. 6.24 Emission spectrum of $Na_2Ca(PO_4)F{:}Mn^{2+}{}_{0.5\,mol\%}$ at (**a**) 600 °C, (**b**) 800 °C, and (**c**) 1,000 °C synthesis temperatures

promotes the maximum PL intensity in the prepared $Na_2Ca(PO_4)F{:}Mn$ phosphor. The samples doped with 0.5 mol% Mn were more efficient phosphors than those with other concentrations of Mn ions (Fig. 6.25). In the present experiment strong Mn^{2+} emission was observed at the 522 nm wavelengths due to the $^4T_1 \rightarrow {}^6A_1$ transition of the Mn^{2+} ions. The shoulder was observed at 540 nm due to Mn ± Mn phonon pair emission. The PL emission intensity with variation of Mn^{2+} concentration is shown in Fig. 6.26.

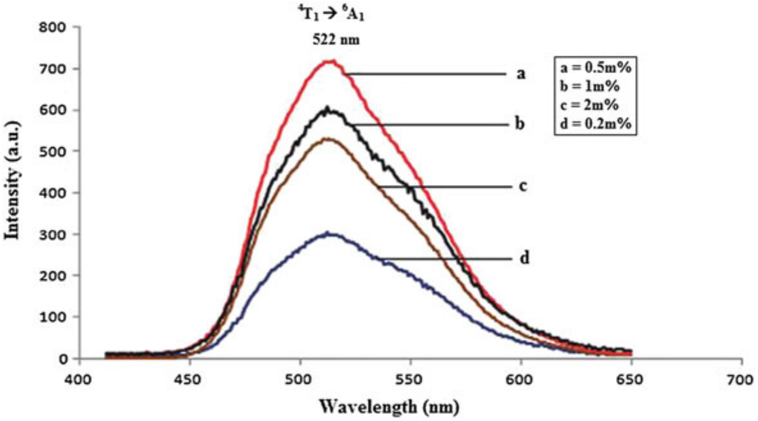

Fig. 6.25 PL emission spectrum of $Na_2Ca(PO_4)F{:}Mn^{2+}$ phosphor at a synthesis temperature of 1,000 °C

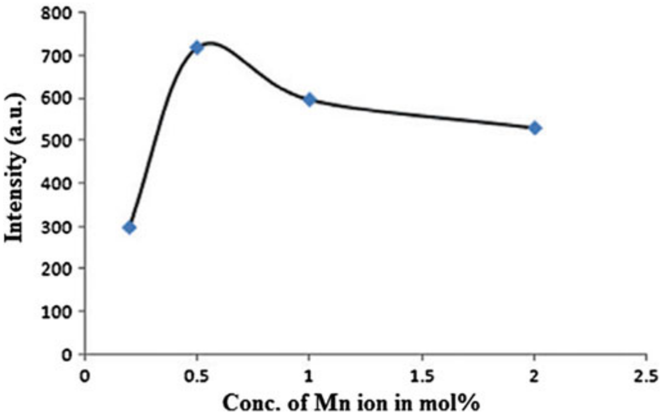

Fig. 6.26 Concentration quenching in $Na_2Ca(PO_4)F{:}Mn^{2+}$ at different Mn concentrations at 1,000 °C

Generally, Mn^{2+}-activated phosphors are divided into two classes: those with green emission and those with orange to red emission [39, 40]. Another possibility to obtain a green Mn^{2+} emission is to choose a lattice in which Mn^{2+} is on a site which is considerably larger than the Mn^{2+} radius. This requirement is met in compounds like $SrB_6O_{10}{:}Mn^{2+}$, in which the Mn^{2+} emission is at 520 nm [41]. In the present case, Mn^{2+} emission was also observed at 522 nm in the green region of the spectrum at 259 nm excitation. This green emission is due to tetrahedral coordinated or paired formation of PO_4^{2-} with host ions surrounding Mn^{2+} in the $Na_2Ca(PO_4)F$ lattice. In particular, it should be noted that, for all Mn concentrations, the emission intensity of the phosphor prepared at 1,000 °C was higher than those at 600 and 800 °C. This may be ascribed to the effect of the higher temperature. All PL emission at 522 nm emissions was measured under UV excitation. As pointed out in the literature, the higher the Mn content, the shorter will be the PL intensity. Such behavior is closely related only to the concentration quenching [42, 43]. However, it was also found that there exists two different activation centers in Na_2CaPO_4F: Na^+ and Ca^{2+}. The faster color center is predominant at higher Mn concentration, which is believed to be Mn ± Mn pairs. This suggested that the exchange interaction between Mn ions indeed results in allowed optical transitions on Mn ion pairs and hence gives rise to shortening of the PL intensity at relatively high Mn concentrations. The main objective of this investigation was to find out the origin of enhancement in emission intensity arising from the thermal treatment in the charcoal environment. The thermal treatment is considered to reduce some higher valent manganese (Mn) ions to a 2+ state, in which state Mn ions emit the green light of interest. It is thus very important to know the exact oxidation state of the Mn ions, in addition to the structural change of the $Na_2Ca(PO_4)F{:}Mn$ lattice. This may be induced at higher temperatures and eventually gives rise to the change in PL characteristics. X-ray diffraction spectra at various synthesis temperatures were measured and reported. Structural changes

Fig. 6.27 Schematic spectral energy level diagram of Mn^{2+} ion

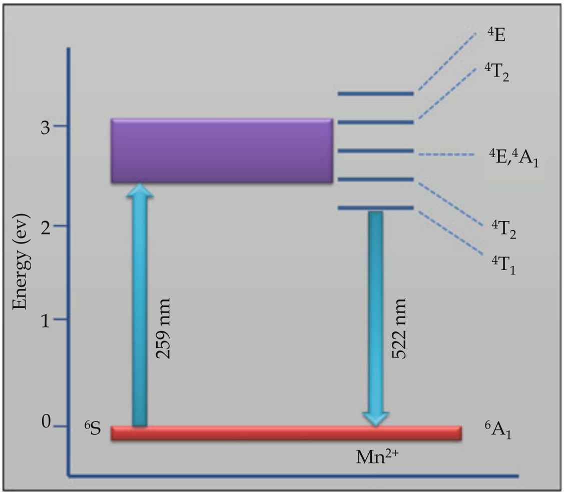

were caused by the heat treatment, such as the contraction of Mn ± O distance and the relief from distortion. These could provide direct evidence to account for the change in emission intensity. There is, however, no doubt that the structural changes observed around the Mn ions should be related to the change in PL behavior. One of the possible interpretations could be the defect impurity-related hypothesis, i.e., the heat treatment could reduce defect impurities and even eliminate some volatile impurities. Defect impurities are known to act as quenching sites in the host crystal. It is known that the existence of defect impurities acting as quenching sites causes the PL property to deteriorate.

The thermal removal of this kind of quenching site after the heat treatment could be the reason for the enhanced emission intensity. It is thus presumed that the heat treatment could restrain the non-radiative process by the elimination of impurities, so that the emission intensity could be promoted at a 1,000 °C synthesis temperature. Since the luminescence wavelength due to Mn^{2+} is sensitive to the magnitude of the crystal field, several emission bands are observed when different types of Mn^{2+} sites exist in a host crystal (Fig. 6.27). Lamp phosphors must absorb the mercury ultraviolet (UV) line at 254 nm. In most of the cases, Mn^{2+} does not have strong absorption bands in this region. In the present experiment, strong Mn^{2+} emission was observed at 522 nm due to the transition $^4T_1 \rightarrow {}^6A_1$ of Mn^{2+} ion in $Na_2Ca(PO_4)F{:}Mn^{2+}$phosphate-based phosphor when excited at 259 nm (UV-excited). The obtained results show that the present phosphor has the potential for application in green emitting phosphors for the lamp industry.

6.4.4 Conclusions

It is concluded that most Mn ions are in a 2+ valency state in the $Na_2Ca(PO_4)F$:Mn lattice. Moreover, structural disorder associated with the oxygen arrangement around the Mn ion becomes low at 1,000 °C. From the XRD pattern, it is concluded that the increase in the synthesis temperature gives the complete formation of the product with an orthorhombic crystal structure. There is no drastic change in Mn^{2+} oxidation state in a reducing environment. The reducing environment controls the oxidation state of the Mn ion. Besides the Mn valency change, some other effects should be considered to explain the enhanced PL property caused by the heat treatment. Either the removal of some impurity ions or splitting of the Mn $\pm$ Mn pair could be possible as regards the increase in PL emission intensity caused by heat treatment. The PL results show that present phosphor has potential for application in UV-excited green emitting phosphors for the lamp industry.

6.5 Ce^{3+}, Eu^{3+} and Dy^{3+} Activtated $Na_2Sr_2Al_2PO_4F_9$ Phosphors by Wet Chemical Method [44]

6.5.1 Experimental

For preparing the nanocrystalline complex fluorides' halophosphate phosphors, the wet chemical method is used; that is, constituent chlorides with stoichiometric ratios are dissolved in double-distilled deionized water in a glass beaker (Borosil) and are evaporated until the mixture becomes anhydrous. Use of chlorides as starting materials helps in preventing the hydrolysis. The $Na_2Sr_2Al_2PO_4F_9$ phosphors were prepared by a wet chemical method. NaCl, $SrCl_2.6H_2O$, $Al(NO_3)_3.9H_2O$, $NH_4H_2PO_4$, and NH_4F analar grades were taken in a stoichiometric ratio and dissolved separately in double-distilled deionized water, resulting in a solution of $Na_2Sr_2Al_2PO_4F_9$. In the present investigation, materials were prepared according to the chemical formula $Na_2Sr_{2-x}Al_2PO_4F_9:Eu_x$. Diluted HNO_3 soluble in $Eu_2O_3/(NH_4)_2Ce(NO_3)_6$ was then added to the solution to obtain $Na_2Sr_2Al_2PO_4F_9$: Eu^{3+}/Ce^{3+}. The mixture of reagents was mixed together to obtain a homogeneous solution. The molar ratio of europium RE ion was changed in relation to the $Na_2Sr_2Al_2PO_4F_9$ phosphor. The compositions of the reagents were calculated using the total oxidizing and reducing valencies of the components, which served as the numerical coefficients so that the equivalent ratio is unity. It is confirmed that no undissolved constituents were left behind and all the chemicals have completely dissolved in water. The compounds $Na_2Sr_2Al_2PO_4F_9:Eu^{3+}$ in their powder form were obtained by evaporating at 120 °C for 8 h. The dried samples were then slowly cooled to room temperature. The resultant nanocrystalline powder was crushed to fine particles in a crucible. The powder was used for further studies. This method shows the advantage in using a simple experimental procedure and chemicals that are easily available, non-toxic, and easily handled at ambient conditions of humidity and pressure.

6.5.2 Structural and Compositional Characterizations

As a member of orthophosphates, $Na_2Sr_2Al_2PO_4F_9$ boggildite (monoclinic) crystal structure with JCPDS file no. 01-084-0497 was first described by Hawthorne [45]. The Fig. 6.28 shows that the $Na_2Sr_2Al_2PO_4F_9$ has a monoclinic crystal structure (Buchwaldite). XRD pattern for $Na_2Sr_2Al_2PO_4F_9$ phosphor is shown in Fig. 6.29. The peak positions in Fig. 6.29 match well with those of the standard pattern (JCPDS 01-084-0497) for $Na_2Sr_2Al_2PO_4F_9$, which confirms that the synthesized sample is single phase. The XRD pattern did not show presence of the constituents like, NaCl, $SrCl_2.6H_2O$, Al $(NO_3)_3.9H_2O$, $NH_4H_2PO_4$ or NH_4F, and other likely phases which

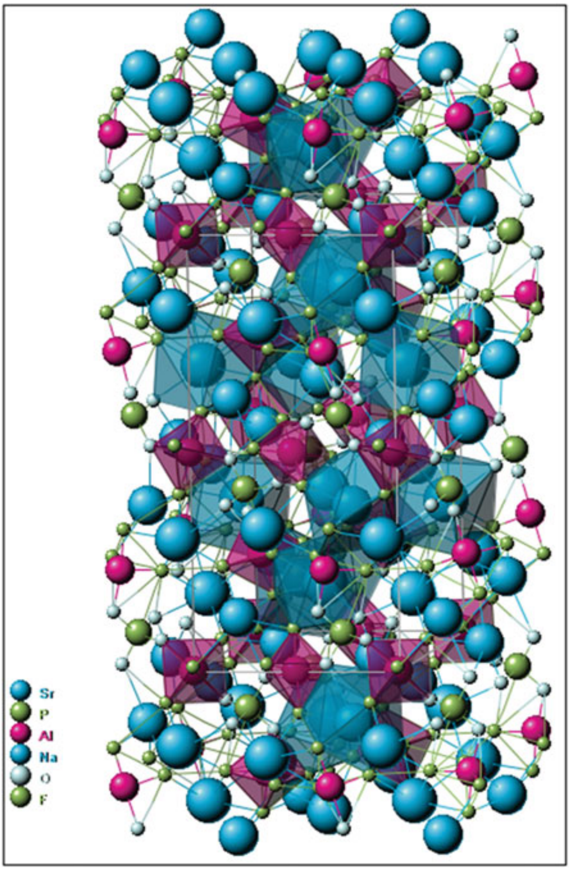

Fig. 6.28 Boggildite crystal structure of $Na_2Sr_2Al_2PO_4F_9$ [45]

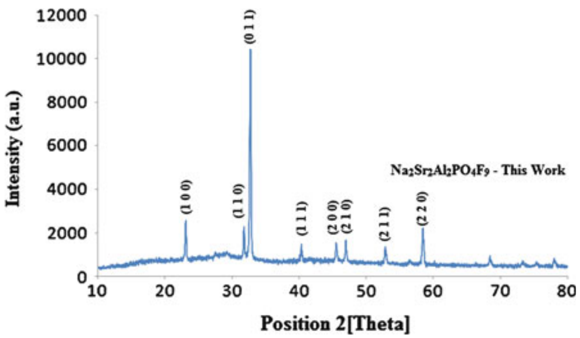

Fig. 6.29 XRD of $Na_2Sr_2Al_2PO_4F_9$ host lattice

is an indirect evidence for the formation of the desired compound. These results show that the final product was formed in nanocrystalline and homogeneous form. No differences in the XRD patterns were observed when phosphors were doped with different amounts of Ce^{3+} and Eu^{3+}. The average structural unit distance was estimated from the full width at half maximum of the diffraction peak by the Scherrer equation [46]:

$$D = k\lambda/\beta\cos\theta \tag{6.1}$$

where D is the mean crystallite diameter, k (0.89) is the Scherrer constant, λ is the X-ray wavelength (1.5406 Å), and β is the full width half maximum (FWHM) of $Na_2Sr_2Al_2PO_4F_9$ diffraction peak (0.0041 Å). The average crystallite size calculated using the most intense reflection at $2\theta = 32.74°$ is 35.37 nm.

6.5.3 PL Properties of $Na_2Sr_2Al_2PO_4F_9{:}Ce^{3+}$ Phosphor

Ce^{3+} is a very good candidate as activator as well as sensitizer, for studying the behavior of 5d electrons. Ce^{3+} has only one outer electron and only two spin-orbital splitting 4f states ($^2F_{5/2,\ 7/2}$). Thus, its excited state energy structure is simpler than that of the other trivalent rare-earth ions. Photoluminescence excitation spectra of $Na_2Sr_2Al_2PO_4F_9{:}Ce^{3+}$ phosphor are shown in Fig. 6.30. The broadband peaking is observed at 252 nm with a prominent shoulder at 270 nm ($\lambda_{emi} = 317$ nm). Figure 6.31 shows the PL emission spectra of Ce^{3+} ions in $Na_2Sr_2Al_2PO_4F_9$ phosphor with different concentrations under the same excitation (i.e., 252 nm), wavelengths of light. Two emission peaks are observed from 317 to 355 nm, which are assigned to the 5d–4f transition of the Ce^{3+} ions. The highest intensity observed at 317 nm due to the $^2D(5d) \rightarrow {}^2F_{7/2}(4f)$ transition between the two peaks. The concentration of Ce^{3+} ion increases the corresponding intensity of all peaks and at higher concentration (1 mol%) of Ce^{3+} ion. This indicates a change of the surrounding of the Ce^{3+} ions at higher concentration in the $Na_2Sr_2Al_2PO_4F_9$ lattice. The intensity

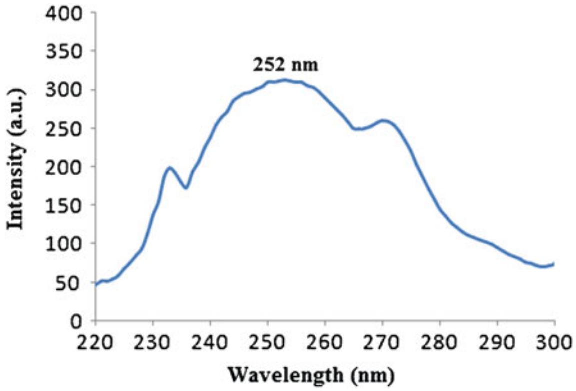

Fig. 6.30 Excitation spectrum of $Na_2Sr_2Al_2PO_4F_9$: Ce^{3+} when monitored at 317 nm

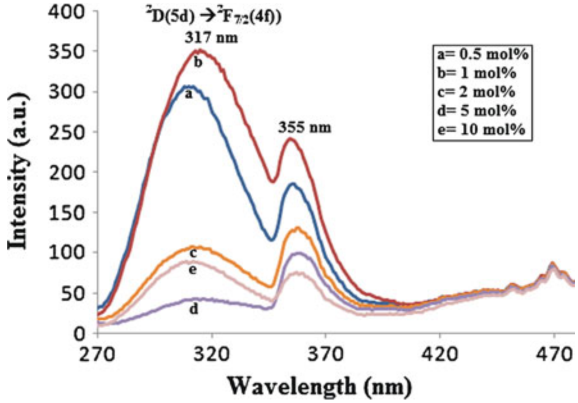

Fig. 6.31 Emission spectra of $Na_2Sr_2Al_2PO_4F_9$:Ce^{3+} when excited at 252 nm

of Ce^{3+} emission at 317 nm is greater than other observed peaks. Variations observed in PL emission intensities, may be cross relaxation between Ce^{3+} ions in the case of heavy concentration of Ce^{3+}. The Ce^{3+} ion can be used as sensitizer as well as an activator, depending on the splitting of 5*d* excited levels by the crystal field symmetry. Much work has been done on the Ce^{3+} to different activator ions in different host lattice.

6.5.4 PL Properties of Na_2Sr_2 Al_2 PO_4F_9:Eu^{3+}

Fluorescence spectra of Eu^{3+}-doped $Na_2Sr_2Al_2PO_4F_9$ were measured at room temperature (Figs. 6.32 and 6.33), the following emission transitions are observed: $^5D_0 \rightarrow {}^7F_1$ at 593 nm and $^5D_0 \rightarrow {}^7F_2$ at (619 nm). Between them, the $^5D_0 \rightarrow {}^7F_1$ transition is the strongest. Due to the magnetic dipole transitions $^5D_0 \rightarrow {}^7F_1$ and electric dipole transitions $^5D_0 \rightarrow {}^7F_1$, this phosphor exhibits orange color emission.

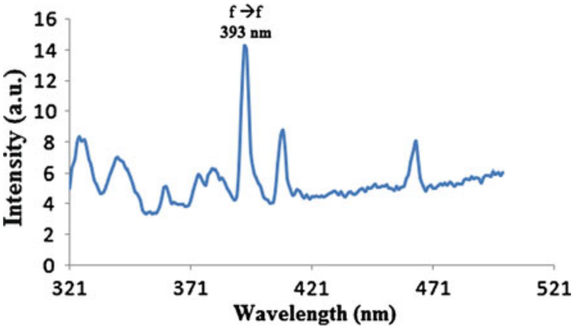

Fig. 6.32 Excitation spectrum of $Na_2Sr_2Al_2PO_4F_9$:Eu^{3+} when monitored at 593 nm

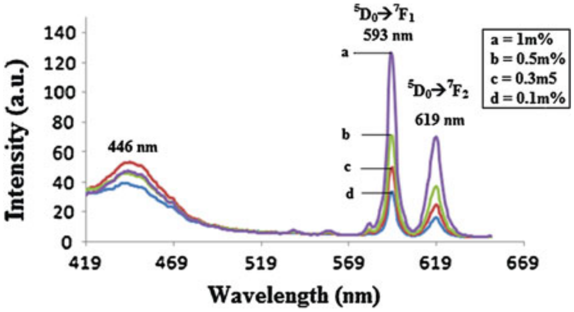

Fig. 6.33 Emission spectra of $Na_2Sr_2Al_2PO_4F_9$:Eu^{3+} when excited at 393 nm

According to the Judd-Ofelt theory, the magnetic dipole transition is permitted. But the electric dipole transition is allowed exceptionally on the condition that the europium ion occupies a site without an inversion center and is sensitive to local symmetry. Consequently, the $^5D_0 \rightarrow {}^7F_1$ transition should be relatively strong when the Eu^{3+} ions occupy inversion center sites, while the $^5D_0 \rightarrow {}^7F_2$ transition must be relatively weak [47]. Also, according to Rambabu et al. and Yu et al., the transition $^5D_0 \rightarrow {}^7F_1$ displayed more intensity than $^5D_0 \rightarrow {}^7F_2$ transition (0.44 u.a) due to the localized energy transfer [47, 48]. The intensity of these emission transitions are usually used to gauge the quality of the luminescent material. The highest intensity of $^5D_0 \rightarrow {}^7F_1$ transition indicates that Eu^{3+} ions have centro-symmetrical environment in the $P21/n$ structure. Due to the little difference between ionic sizes of Eu^{3+} ion (94.7 pm) and Sr^{2+} ion (112 pm), we presume that Eu^{3+} ions can occupy Sr^{2+} ion sites, which causes a characteristic crystal splitting of the energy levels. The transitions are found to split into components depending on the host matrix composition. Due to the dependency between $^5D_0 \rightarrow {}^7F_1$ emissions and the crystal field, $^7F_1$ associated with one site symmetry can split into three Stark lines in the crystal field and the $^5D_0 \rightarrow {}^7F_2$ transition of Eu^{3+} can split into, at most, five lines in the crystal field [49]. In this case, the photoluminescence excitation spectra of the prepared Eu-activated $Na_2Sr_2Al_2PO_4F_9$ phosphor are shown in Fig. 6.32. The prominent excitation band at 393 nm may be due to the $f-f$ transitions of the Eu^{3+} ion. The PL excitation spectrum is broad and maximizes at 393 nm in the LED phos-

Fig. 6.34 PL excitation spectra of $Na_2Sr_2Al_2PO_4F_9:Dy^{3+}$ phosphor when monitored at $\lambda_{emi} = 481\,nm$

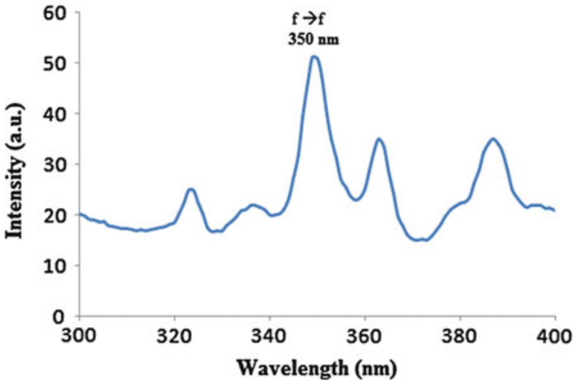

phors excitation region. The PL emission spectrum ($\lambda_{exc} = 393\,nm$) consists of the intense peak at 593 nm (orange) that can be ascribed to $^5D_0 \rightarrow {}^7F_1$ transitions of the Eu^{3+} ion and other peaks at 619 nm which can be associated with the $^5D_0 \rightarrow {}^7F_2$ transition of the Eu^{3+} ion is shown in Fig. 6.33. The 593, 619 nm emission of Eu^{3+} ion in the $Na_2Sr_2Al_2PO_4F_9$ host material was very applicable as an orange/red phosphor for the solid-state lighting. The excitation of this phosphor at 393 nm is far away from Hg excitation as well as this excitation is the main characteristic of solid-state lighting (in the range near UV region) in the lamp industry.

6.5.5 *PL Properties of $Na_2Sr_2Al_2PO_4F_9:Dy^{3+}$*

The excitation and emission spectra of the $Na_2Sr_2Al_2PO_4F_9:Dy^{3+}$ are shown in Figs. 6.34 and 6.35. The excitation spectrum is broadband centered at 350 nm. The emission spectra for the Dy^{3+}-doped samples are composed of the broad emission band and the characteristic emission lines of Dy^{3+} with $4f_9$ configuration. The blue emission peaking at 481 nm and yellow emission peaking at 575 nm were observed and can be assigned to the $^4F_{9/2} \rightarrow {}^6H_{15/2}$ and $^4F_{9/2} \rightarrow {}^6H_{13/2}$ transitions of Dy^{3+}, respectively. Thus the combination of colors gives BY (blue–yellow)

Fig. 6.35 PL emission spectra of $Na_2Sr_2Al_2PO_4F_9:Dy^{3+}$ phosphor when excited at $\lambda_{exc} = 350\,nm$

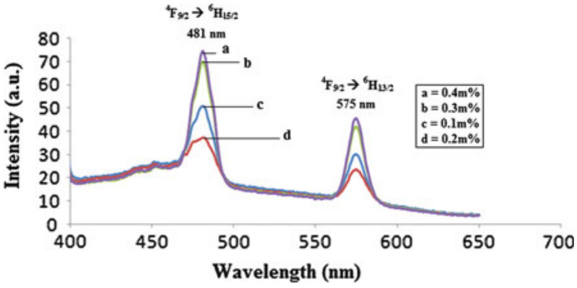

emissions which can produce white light by Hg-free excitation (Hg excitation is 85 % 254 nm wavelength of light and 15 % other wavelengths). In addition, from the figure, it also can be seen that all samples have similar excitation spectra, and the peaks that range from 300 to 400 nm are due to $4f-4f$ transitions of the Dy^{3+} ions. Recently, more research done on the development of new solid-state lighting phosphors, while, out of them maximum phosphors show the only single color visible emission. In this chapter, it first time reports the BY emission phosphor from newly developed host using the Dy ions as an activator. Hence, our results claimed the phosphor for near UV LED application by an easy preparation technique.

6.5.6 Conclusions

$Na_2Sr_2Al_2PO_4F_9:Eu^{3+}$ and $Na_2Sr_2Al_2PO_4F_9:Ce^{3+}$ high potential halophosphate-based nanophosphors have been synthesized by the wet chemical method. The XRD pattern of the prepared phosphor is well match with the standard pattern (JCPDS 01-084-0497) for $Na_2Sr_2Al_2PO_4F_9$, which confirms that the synthesized sample is single phase. The average structural unit distance was estimated from the full width at half maximum of the diffraction peak by the Scherrer equation and the average crystallite size calculated using the most intense reflection at $2\theta = 32.74°$ was 35 nm. The photoluminescence spectrum shows the main peak in the range 270–350 nm with a shoulder in the range from 350–370 nm, which may be ascribed to transitions from $5d-4f$ levels of Ce^{3+} ion in the mixed host lattice ($Na_2Sr_2Al_2PO_4F_9$). Orange/red emission observed in $Na_2Sr_2Al_2PO_4F_9$: Eu^{3+} nanophosphor due to transitions from the $^5D_0$ excited states to the ^7F_J $(J = 0 - 4)$ ground states of the Eu^{3+} ions under the 393 nm excitation and it is more favorable of solid-state lighting. The effect of rare-earth ions in the above system and its effect on the luminescence behavior of the materials was not focused by the researchers before and hence this material is considered as the main attempt in the present investigation. $Na_2Sr_2Al_2PO_4F_9:Ce^{3+}$ phosphor shows the near UV emission for development of energy transfer-based co-activated advanced phosphors for the lamp industry. Under excitation around 350 nm, the $Na_2Sr_2Al_2PO_4F_9:Dy^{3+}$ phosphor showed the blue/yellow emission from Dy^{3+}. The highest emission intensity was observed at 0.4 mol% of Dy^{3+}. This fundamental work might be important in developing new luminescent devices applicable for tricolor lamps, near UV light emitting diodes, and other fields.

6.6 $Sr_5(PO_4)_3Cl:Eu^{2+}$ Phosphor by Solid-State Diffusion [50]

$Sr_5(PO_4)_3Cl:Eu^{2+}$ phosphor was prepared by solid-state diffusion of strontium chloride, europium nitrate, and ammonium dihydrogen phosphate in stoichiometric proportions at 1,050 K in a porcelain crucible. Strontium chloride and ammonium dihydrogen phosphate doped with europium nitrate were mixed in stoichiometric

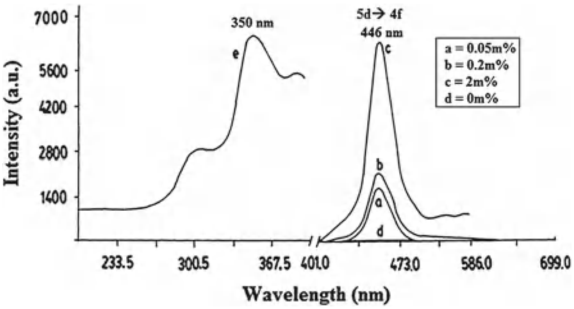

Fig. 6.36 The PL spectra of $Sr_5(PO_4)_3Cl:Eu^{2+}$ phosphor. The emission spectra (excitation wavelength was 350 nm) are shown in curves **a** 0.05 mol%, **b** 0.2 mol%, **c** 2 mol% and **d** 0 mol%. The excitation spectra of $Sr_5(PO_4)_3Cl:Eu^{2+}$ (2 mol%) (emission wavelength was 446 nm) are shown in curve (**e**)

proportions and crushed for 1 h. The crushed powder was heated at 650 K for 4 h in an air atmosphere, the resulting compound again crushed for 1 h to powder then heated to 1,050 K for 24 h in an air atmosphere. The resulting powder was again crushed and fired at 1,200 K for 1 h and quenched to room temperature. This sample was used in the next experiment. The quoted compositions of the samples are based on the starting proportions. The formation of $Sr_5(PO_4)_3Cl:Eu^{2+}$ phosphor was confirmed by taking XRD diffractograms which was compared with the standard data (JCPDs file no, 16-666). Figure 6.36 (curves a, b, c and d) shows PL emission spectra of various concentrations of Eu in $Sr_5(PO_4)_3Cl$. The prominent emission is observed at 446 nm (excitation wavelength is 350 nm). These correspond to the $^6P_j \rightarrow {}^8S_{7/2}$ transition levels of Eu^{2+}. In the pure $Sr_5(PO_4)_3Cl$ sample, the 446 nm PL peak is not seen. The PL emission peak positions do not vary with Eu concentration variation in $Sr_5(PO_4)_3Cl$, but some changes are observed in peak intensity and the maximum intensity is observed for 2 mol% of Eu.

Figure 6.36, curve e shows the corresponding excitation spectra. The excitation is in the form of a broadband around 350 nm corresponding to the Eu^{2+} (emission wavelength is 446 nm). In $Sr_5(PO_4)_3Cl:Eu^{2+}$ PL emission and excitation spectra depend on the position of the Eu^{2+} ions in the host $Sr_5(PO_4)_3Cl$ structure. The position of Eu^{2+} ions depends on the method of preparation of the sample. In the present work, $Sr_5(PO_4)_3Cl:Eu^{2+}$ is prepared in open air atmosphere at high temperature and the results presented are consistent with the Eu entering the host in a divalent form. The PL spectra consist of strong Eu^{2+} emission that is observed at 446 nm.

6.6.1 Conclusions

$Sr_5(PO_4)_3Cl:Eu^{2+}$ has been found to be an efficient phosphor. Under the 350 nm excitation the present phosphor shows excellent emission at 446 nm in the blue region. A series of $Sr_{5-x}(PO_4)_3Cl:Eu_x^{2+}$ ($x = 0, 0.2, 0.05$ and 2 mol%) phosphor is successfully prepared by solid-state diffusion method. The optimum intensity is observed at 2 mol%.

References

1. Y. Jie, C. Guo, Z. Ren, J. Bai, Opt. Laser Technol. **43**, 762 (2011)
2. M. Hirano, S. Shionoya, J. Phys. Soc. Jpn. **28**, 926 (1970)
3. D.K. Sardar, W.A. Sibley, R. Alcala, J. Lumin. **27**, 2738 (1982)
4. D. Noetzold, G. Herzog, I. Henke, Anorg. Allg. Chem. **613**, 127 (1992)
5. M. Sato, T. Tanaka, M. Ohota, J. Electrochem. Soc. **141**, 1851 (1994)
6. R.W. Warren, Phys. Rev. B **6**, 4679 (1972)
7. S.J. Dhoble, S.V. Moharil, T.K. Gundu Rao, J. Lumin. **126**, 383 (2007)
8. S.J. Dhoble, V.B. Pawade, K.N. Shinde, Eur. Phys. J. Appl. Phys. **52**, 11104 (2010)
9. K.N. Shinde, I.M. Nagpure, A.B. Fulke, S.J. Dhoble, Luminescence **26**, 363 (2011)
10. I.M. Nagpure, K.N. Shinde, S.J. Dhoble, A. Kumar, J. Alloys Compd. **481**, 632 (2009)
11. M. Kottaisamy, R. Jagannathan, P. Jeyagopal, R.P. Rao, R.L. Narayanan, J. Phys. D: Appl. Phys. **27**, 2210 (1994)
12. International Centre of Diffraction Data/Powder Diffraction File 2, 17–609, 071–1316 and 015–0876
13. A.N. Akhavan-Niaki, Ann. Chim. (France) **6**, 51 (1961)
14. K. Sudarsanan, R.A. Young, Acta Cryst. B **30**, 1381 (1974)
15. R.D. Shannon, Acta Cryst. A **32**, 751 (1976)
16. D. NoÈtzold, H. Wulff, Phys. Stat. Sol. (b) **207**, 271 (1998)
17. S.R. Jam, K.C. Adiga, V.R.P. Vemeker, Combust. Flame **40**, 71 (1981)
18. H. Choi, Ch.H. Kim, Ch.H. Pyun, S.J. Kim, J. Lumin. **82**, 25 (1999)
19. J. Kuang, Y. Liu, J. Zhang, J. Solid State Chem. **179**, 266 (2006)
20. M. Yu, J. Lin, Z. Wang, J. Fu, S. Wang, H.J. Zhang, Y.C. Han, Chem. Mater. **14**, 2224 (2002)
21. L. Sun, C. Qian, C. Liao, X. Wang, C. Yan, Solid State Commun. **119**, 393 (2001)
22. D. Jia, W.M. Yen, J. Lumin. **101**, 115 (2003)
23. Q. Su, J. Lin, B. Li, J. Alloys Compd. **225**, 120 (1995)
24. G. Blasse, Lumin. Inorg. Solids **475**, 215 (1978)
25. A. Stevels, L.N. Schrama-de Pauw, Electrochem. Soc. **123**, 691 (1976)
26. K.N. Shinde, I.M. Nagpure, S.J. Dhoble, Synth. React. Inorg. Metal-Org. Nano-Metal Chem. **41**, 107 (2011)
27. Y. Dong, G. Zhou, X. Jun, G. Zhao, F. Su, L. Su, G. Zhang, D. Zhang, H.J. Li, Mater. Res. Bull. **41**, 1959–1963 (2006)
28. K. Toda, J. Alloys Compd. **408**, 665 (2006)
29. V.P. Dotsenko, I.V. Berezovskaya, N.P. Efryushina, A.S. Voloshinovskii, P. Dorenbos, C.W.E. van Eijk, J. Lumin. **93**, 137 (2001)
30. C.-K. Chang, T.-M. Chen, Appl. Phys. Lett. **91**, 081902 (2007)
31. R. Yu, J. Wang, J. Zhang, H. Yuan, Q.J. Su, Solid State Chem. **181**, 658 (2008)
32. X. Zhang, H. He, Z. Li, T. Yu, Z. Zou, J. Lumin. **128**, 1876 (2008)
33. G. Blasse, A.J. Bril, Electrochem. Soc. **115**, 10967 (1968)
34. K.S. Sohn, B. Cho, H.D. Park, Y.G. Choi, K.H. Kim, J. Eur. Ceram. Soc. **20**, 1043 (2000)
35. V.B. Bhatkar, S.K. Omanwar, S.V. Moharil, Phys. Stat. Sol. A **191**(1), 272 (2002)
36. M. Kottaisamy, R.M. Mohan, D. Jeyakumar, J. Mater. Chem. **7**(2), 345 (1997)
37. K. Toda, Phys. Stat. Sol. **A191**(1), 272 (2002)
38. E.V. Sokolova, Y.K. Kabalov, G. Ferraris, J. Schneider, A.P. Khomyakov, Concepts. Can. Mineral **37**, 83 (1999)
39. D.T. Palumbo, J.J. Brown Jr, J. Electrochem. Soc. **117**(9), 1184 (1970)
40. D.T. Palumbo, J.J. Brown Jr, J. Electrochem. Soc. **118**, 1159 (1971)
41. T. Koskentato, M. Leskel, L. Niinisto, Mater. Ref. Bull. **20**, 265 (1985)
42. A. Morell, N. Khiati, J. Electrochem. Soc. **140**, 2019 (1993)
43. C. Barthou, J. Benoit, P. Benalloul, A. Morell, J. Electrochem. Soc. **141**, 524 (1994)
44. S.J. Dhoble, K.N. Shinde, Adv. Mat. Lett. **2**(5), 349–353 (2011)
45. F.C. Hawthorne, Can. Miner. **20**, 263 (1982)

46. B.D. Cullity, *Elements of X-Ray Diffraction* (Addision-Wesley, London, 1978)
47. U. Rambabu, S. Buddhudu, Opt. Mater. **17**, 401 (2001)
48. L. Yu, H. Song, S. Lu, Z. Liu, L. Yang, X. Kong, J. Phys. Chem. **108**, 16697 (2004)
49. J. Dexpert-Ghys, R. Mauricot, M.D. Faucher, J. Lumin. **69**, 203 (1996)
50. S.J. Dhoble, J. Phys. D: Appl. Phys. **33**, 158 (2000)

Chapter 7
Some Novel Phosphate Phosphors

7.1 Introduction

The need for mercury-free fluorescent lamps for general lighting has become an important subject for light source manufacturers, for avoiding the use of environmentally harmful materials in the lamp. Replacement of conventional fluorescent lamp by light-emitting diodes (LEDs) has been most challenging task in the higher demands for the solid-state lighting technology in recent years. LED technology has flourished for the past few decades. High efficiency, reliability, rugged construction, low power consumption, and durability are among the key factors for the rapid development of the solid-state lighting based on high-brightness visible LEDs [1].

Phosphate has become an important luminescent material for use in LEDs because of their excellent thermal stability and charge stabilization. However, the search for new luminescent materials for plasma display panels (PDPs) and mercury free lamps has been getting increasing attention on the vacuum ultraviolet (VUV, $\lambda < 200\,\text{nm}$) spectroscopic characteristics of rare-earth ions activated phosphors since the last decade [2–6]. The $f{-}f$, $f{-}d$ and charge-transfer transitions of rare-earth ions as well as the host related absorption are the main spectroscopic bands in the VUV range [7, 8]. The $f{-}f$ transitions of rare-earth ions in the VUV region have been well understood and the Dieke diagram was extended to about $65{,}000\,\text{cm}^{-1}$ [9]. However, since various factors such as the nature of the coordinating anions, the coordination number, site symmetry and the nature of the next nearest cation neighbors have an influence on the position of the $4f{-}5d$ states, a further investigations on the $f{-}d$ transitions of the rare-earth ions in the different host lattices was necessary [10, 11]. The luminescent properties can be enhanced by adding phosphors with suitable activators. Phosphors with desired colour emission and high efficiency under mercury free excitation must be developed. Recently, some phosphates have been reported, such as $LiSrPO_4{:}Eu^{2+}$ [12], $NaBaPO_4{:}Eu^{3+}$ [13], $BaSrMg(PO_4)_2{:}Eu^{2+}$ [14], $NaCa_{0.98-x}Mg_xPO_4{:}Eu^{2+}{}_{0:02}$ [15], $Na_2CaMg(PO_4)_2{:}Ce^{3+}$ [16].

A detailed literature search reveals no available data for $X_6AlP_5O_{20}$ (where $X = Sr, Ba, Ca$ and Mg) compounds. This composition can be considered as an

K. N. Shinde et al., *Phosphate Phosphors for Solid-State Lighting*,
Springer Series in Materials Science 174, DOI: 10.1007/978-3-642-34312-4_7,

alternative approach due to advantages such as lower production cost, simpler manufacture procedure, non-hygroscopic, and environmental-friendly characteristics. The aim of the present work is to investigate the luminescence properties of Dy^{3+}, Eu^{3+} and Ce^{3+}-doped $X_6AlP_5O_{20}$ (where X = Sr, Ba, Ca and Mg) novel phosphors. The crystalline phosphor phases were synthesized by the combustion method and confirmed by XRD, SEM, and PL spectra of Dy^{3+}, Eu^{3+} and Ce^{3+}. Until now, no crystallographic studies have been reported on $M_6AlP_5O_{20}$ (where M = Ba/Sr/Mg) host matrixes and there are no reports on the PL characteristics of the novel phosphors based on rare-earth activated $M_6AlP_5O_{20}$ (where M = Ba/Sr/Mg) materials.

In 2007, Ji et al. reported on a new phosphate with a crystal structure, which has a good thermal stability during the heating process [17]. Phosphate is a promising phosphor material for lamps, CRTs, and PDPs because of its high chemical stability and inexpensive cost. In this study, the luminescence property of a new phosphate phosphor, Eu and Ce-doped $Na_2Zn_5(PO_4)_4$ has been reported.

As a member of the phosphates family, $Na_2Sr_2Al_2PO_4F_9$ boggildite (monoclinic) crystal structure was first described by Hawthorne [18] (see Chap. 6). Here the Na^+ ion was replaced by the Li^+ ion (i.e. $Li_2Sr_2Al_2Po_4F_9$). In this chapter, the effect of the concentration on the luminescence properties of blue emitting Eu and Cu-doped Na_2 $Zn(PO_4)Cl$ phosphors is given and the impact of the Eu^{3+} doping on the $NaLi_2PO_4$ and its PL properties were investigated with a feasible proposed interpretation thereof. Dy and Eu-based phosphate $Na_2X(PO_4)F$ (X = Mg, Ca, Sr) phosphors were prepared by the combustion synthesis and also reported in this chapter.

7.2 PL Studies of Dy^{3+}, Eu^{3+}, and Ce^{3+}-Doped $X_6AlP_5O_{20}$ (where X = Sr, Ba, Ca, Mg) Phosphors by Combustion Synthesis [19–21]

7.2.1 *Experimental*

The Dy^{3+}, Eu^{3+}, and Ce^{3+} activated $X_6AlP_5O_{20}$ (where X = Sr/Ba/Ca/Mg) phosphors were prepared by the combustion synthesis. The starting AR grade materials (99.99 % purity) were taken as strontium nitrate ($Sr(NO_3)_2$ Merck) or barium nitrate ($Ba(NO_3)_2$ Merck), or calcium nitrate ($Ca(NO_3)_2{\cdot}4H_2O$ Merck) or magnesium nitrate ($Mg(NO_3)_2{\cdot}6H_2O$, Merck) , ammonium di-hydrogen phosphate ($NH_4H_2(PO_4)$, Merck), aluminum nitrate ($Al(NO_3)_3{\cdot}9H_2O$ Merck), dysprosium oxide (Dy_2O_3, REI 99.9 %), Eu oxide (Eu_2O_3, REI 99.9 %), ammonium cerium nitrate ($(NH_4)_2$ $Ce(NO_3)_6$, Merck), and Urea (NH_2CONH_2, Merck) was used as fuel. In the present investigation, materials were prepared according to the chemical formula $X_{6-x}AlP_5O_{20}{:}Dy_x$ (where X = Ba/Sr/Mg/Ca). The mixture of reagents was grind together to obtain a homogeneous powder. Dy^{3+} ions were introduced as a $Dy(NO_3)_3$ solution by dissolving Dy_2O_3 into a dil. HNO_3 solution.

For the preparation of the $X_{6-x}AlP_5O_{20}{:}Dy_x$ (where X = Sr/Ba/Ca/Mg) phosphors. The molar ratio of the rare earth was varied in $X_6AlP_5O_{20}{:}Dy^{3+}$ (where X = Sr/Ba/Ca/Mg) phosphors relative to the Sr/Ba/Ca/Mg ions. For various compositions of the metal nitrates (oxidizers), the amount of urea (fuel) was calculated maintaining total oxidizing and reducing valences of the components equal to unity, so that the heat liberated during combustion is a maximum [22]. After stirring for about 30 min, the precursor solution was transferred to a furnace which was preheated to 550 °C. Porous products were obtained. Rare-earth ion doped $X_6AlP_5O_{20}$ (where X = Sr/Ba/Ca/Mg) phosphors were prepared by introducing Dy, Eu, and Ce ions as $Dy(NO_3)_3$, $Eu(NO_3)_3$ and $(NH_4)_2Ce(NO_3)_6$ solutions with different concentrations, respectively, and the processes were repeated as explained above.

The chemical reactions are as follows:

$$\begin{aligned}
&\mathbf{6Sr(NO_3)_2 + Al(NO_3)_3{\cdot}9H_2O + 5NH_4H_2PO_4 + 10NH_2CONH_{2(excess)}}\\
&\quad\mathbf{\rightarrow Sr_6AlP_5O_{20} + 36H_2O + 20N_2 + 10CO_2}\\
&\mathbf{6Ba(NO_3)_2 + Al(NO_3)_3{\cdot}9H_2O + 5NH_4H_2PO_4 + 10NH_2CONH_{2(excess)}}\\
&\quad\mathbf{\rightarrow Ba_6AlP_5O_{20} + 36H_2O + 20N_2 + 10CO_2}\\
&\mathbf{6Ca(NO_3)_2{\cdot}4H_2O + Al(NO_3)_3{\cdot}9H_2O + 5NH_4H_2PO_4 + 10NH_2CONH_{2(excess)}}\\
&\quad\mathbf{\rightarrow Ca_6AlP_5O_{20} + 50H_2O + 11N_2 + 13O_2 + CO_2}\\
&\mathbf{6Mg(NO_3)_2{\cdot}6H_2O + Al(NO_3)_3{\cdot}9H_2O + 5NH_4H_2PO_4 + 10NH_2CONH_{2(excess)}}\\
&\quad\mathbf{\rightarrow Mg_6AlP_5O_{20} + 42H_2O + 20N_2 + 10CO_2}
\end{aligned}$$

7.2.2 *Results and Discussion*

7.2.2.1 XRD Patterns of $X_6AlP_5O_{20}$ (where X = Sr/Ba/Ca/Mg) New Materials

Recently, the studies on novel phosphate phosphor was a hot issue for exploring new phosphor materials, which have also been proved to be efficient in the application of light-conversion phosphors for the white LEDs. $Sr_6BP_5O_{20}$ phosphor was first reported by Murakami et al. [23] as a boron-substituted $Sr_2P_2O_7$ with a composition of 2 SrO, 0.84 P_2O_5, and 0.16 B_2O_3. The material was described in the tetragonal crystal system with $a = 6.92$ Å and $c = 9.51$ Å. The correct chemical formula was deduced by Smets [24] to be $Sr_6B(PO_4)_5$ on the basis of the lattice vectors and comparison to $Sr_2P_2O_7$. Based on the synchrotron powder diffraction and single crystal data, a complete structure model was derived and reported [25, 26]. In this study, we replaced boron by aluminum to get $Sr_6AlP_5O_{20}$ and then Sr^{2+} by Ca^{2+}, Ba^{2+}, and Mg^{2+} ions (alkali earth metals). Figures 7.1, 7.2, 7.3 and 7.4 give the XRD patterns of $X_6AlP_5O_{20}$ (where X = Sr/Ba/Ca/Mg) phosphors, respectively. However, the obtained diffraction peaks of all compounds do not match with any data in the JCPDS base. After careful comparison with the reported compounds and considering that

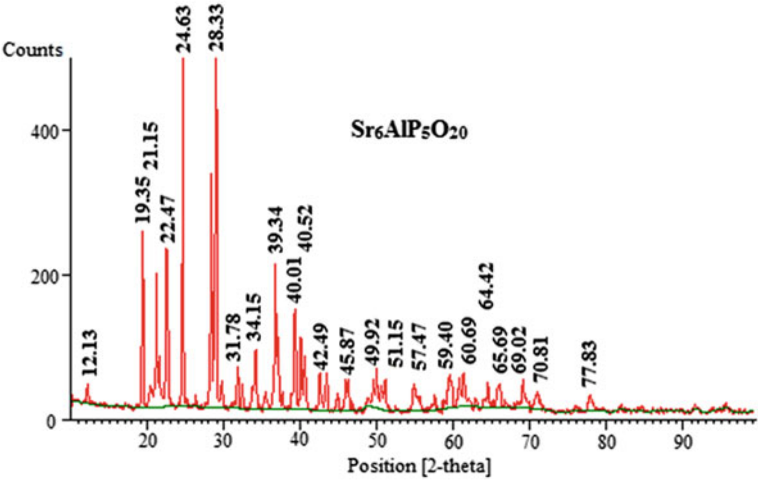

Fig. 7.1 XRD pattern of $Sr_6AlP_5O_{20}$ material

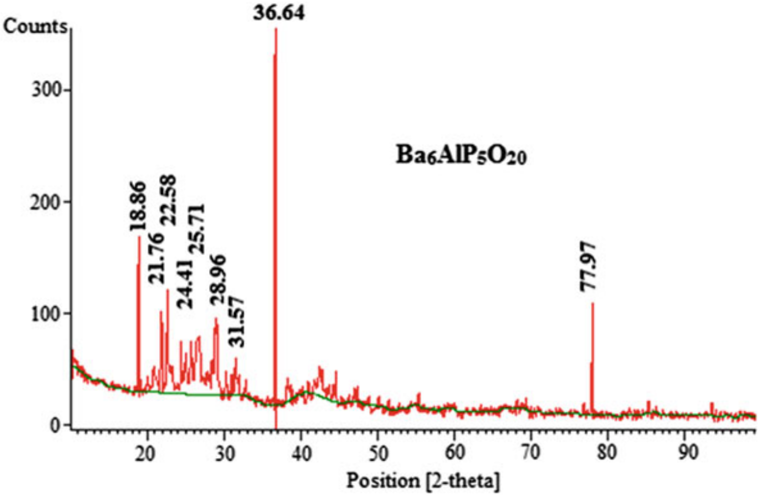

Fig. 7.2 XRD pattern of $Ba_6AlP_5O_{20}$ material

the starting materials are in proportion to weight according to the given chemical composition of $X_{6-x}AlP_5O_{20}$:Dy_x matrix, these compounds were thereby named as $X_{6-x}AlP_5O_{20}$:Dy_x (where X = Sr/Ba/Ca/Mg) phosphors in this chapter. For the obtained phase, it is carefully observed that there are no peaks of raw materials. It is found that the main phase does not agree to any JCPDS available. Different temperatures do not result in any other new phase except the unknown main phase. Consequently, we infer that the obtained unknown phase is likely to be a new phase. With respect to this point, a further study was conducted.

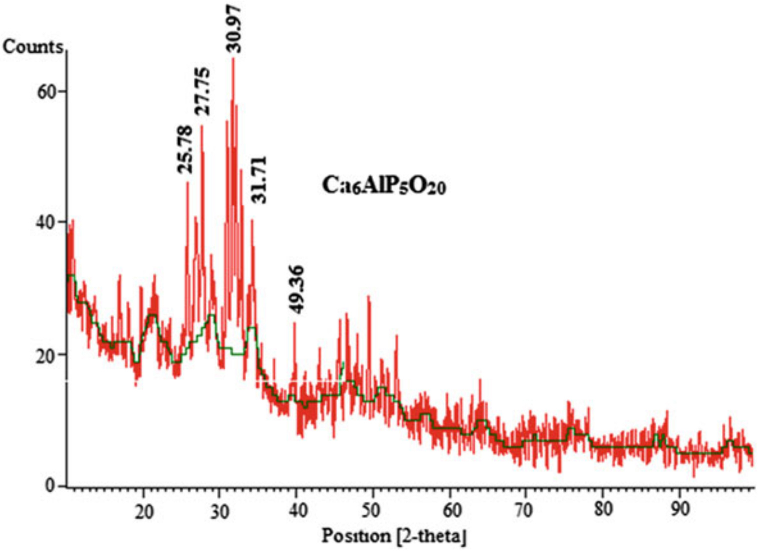

Fig. 7.3 XRD pattern of $Ca_6AlP_5O_{20}$ material

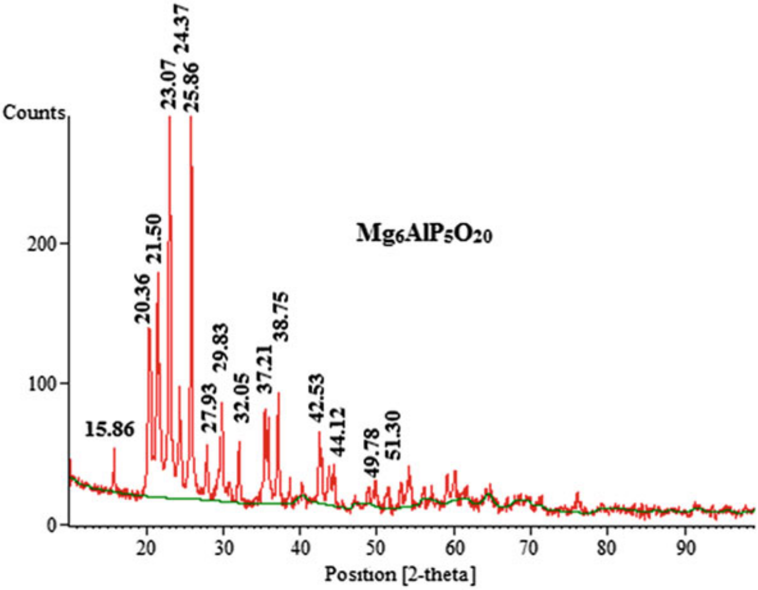

Fig. 7.4 XRD pattern of $Mg_6AlP_5O_{20}$ material

Figures 7.1, 7.2, 7.3 and 7.4 show the X-ray diffraction (XRD) pattern of $Sr_6AlP_5O_{20}$, $Ba_6AlP_5O_{20}$, $Ca_6AlP_5O_{20}$ and $Mg_6AlP_5O_{20}$ materials respectively. The XRD pattern did not indicate the presence of the constituents such as $Sr(NO_3)_2$, $Ba(NO_3)_2$, $Ca(NO_3)_2$, $Mg(NO_3)_2$, $Al(NO_3)_3$ or $NH_4H_2PO_4$ and other likely phases which are an indirect evidence for the formation of the desired compound. These results indicate that the final product was formed in crystalline and homogeneous form. The detailed structures of these materials are still under investigation.

7.2.2.2 SEM of $X_6AlP_5O_{20}$ (where X = Sr/Ba/Ca/Mg)

The typical SEM morphological images of $X_6AlP_5O_{20}$:Eu (where X = Sr/Ba/Ca/Mg) phosphors are represented in Figs. 7.5, 7.6, 7.7 and 7.8 The SEM photographs of $X_6AlP_5O_{20}$:Eu (where X = Sr/Ba/Ca/Mg) phosphors clearly show that the grains have irregular shape of particles with a size less than 3–4 μm. The particles possess foamy like morphology formed from highly agglomerated crystallites.

7.2.2.3 PL of Dy^{3+}-Activated $X_6AlP_5O_{20}$ (where X = Sr/Ba/Ca/Mg)

It is well known that the color of the trivalent dysprosium ($4f^9$ configuration) luminescence is close to white. As shown in Figs. 7.10, 7.12, 7.14 and 7.16 $X_6AlP_5O_{20}$:Dy^{3+} (where X = Sr/Ba/Ca/Mg) has mainly two emission bands, i.e., the blue bands at 476–485 nm and the yellow band at 576 nm, which are due to the transition of

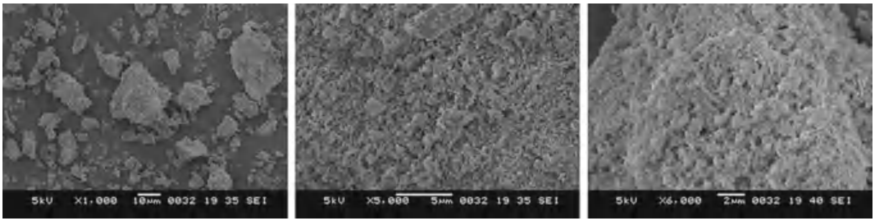

Fig. 7.5 SEM of $Sr_6AlP_5O_{20}$

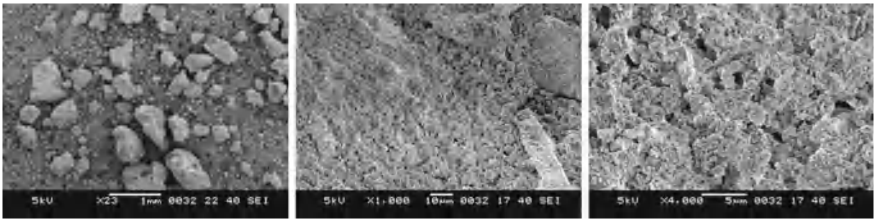

Fig. 7.6 SEM of $Ba_6AlP_5O_{20}$

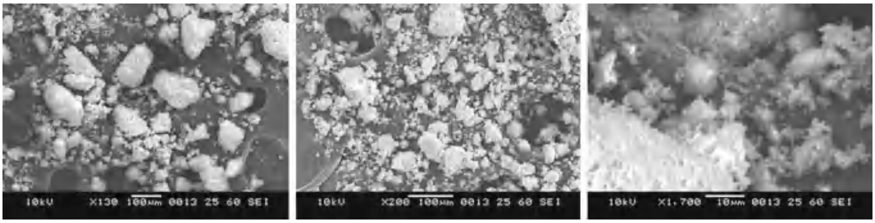

Fig. 7.7 SEM of $Ca_6AlP_5O_{20}$

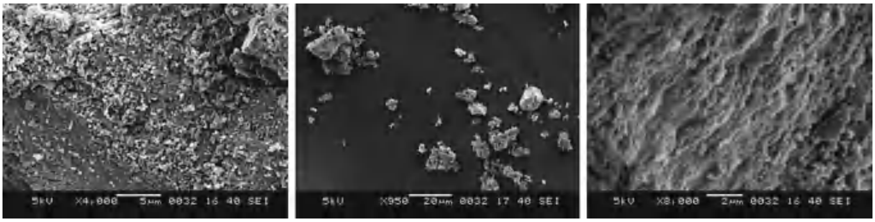

Fig. 7.8 SEM of $Mg_6AlP_5O_{20}$

$^4F_{9/2} \rightarrow {}^6H_{15/2}$ (476, 485 nm) and $^4F_{9/2} \rightarrow {}^6H_{13/2}$ (576 nm), respectively. If the ratio of yellow to blue reaches an appropriate value, Dy^{3+} can emit white light. Measurements of the excitation spectra were made by monitoring the peak wavelength of the Dy^{3+} emission of the blue and yellow emission bands, respectively. Figures 7.9, 7.11, 7.13 and 7.15 show the excitation spectrum of the $X_6AlP_5O_{20}$:Dy^{3+} (where X = Sr/Ba/Ca/Mg) phosphors. The excitation spectrum monitored at the blue emission from Dy^{3+}. The excitation spectrum in the range 300–400 nm consisting of the $f-f$ transition of Dy^{3+}, i.e. 350 nm ($^6H_{15/2} \rightarrow {}^6F_{9/2}$) was observed. Among the several excitation bands we choose 350 nm, because it is suitable for solid-state lighting. It is known that Dy^{3+} emits around 484 nm ($^4F_{9/2} \rightarrow {}^6H_{15/2}$) due to magnetic dipole moment and 576 nm ($^4F_{9/2} \rightarrow {}^6H_{13/2}$) due to electric dipole moment. In $X_6AlP_5O_{20}$:Dy^{3+} (where X = Sr/Ba/Ca/Mg), predominant emission is around 484 nm suggesting that ligand field slightly deviates from its inversion symmetry. A slight marginal shift in the peak position of Dy^{3+} ions is observed in all prepared phosphors. Such behavior is as expected for the emission involving $f \rightarrow f$ transitions where ligand field changes with the host matrix. The change in the host metal atom, yellow/blue ratio changes due to the change of local site symmetry around Dy^{3+} ion, gives blue–yellow emissions. With this excitation, color co-ordinates are such that it is suitable as a white light-emitting phosphor. In our case, the Dy^{3+} ion may enter the host lattice to substitute Sr^{2+}, Ba^{2+}, Ca^{2+}, Mg^{2+} or Al^{3+} or it may be located on surfaces of the crystals due to the porous structure. It is clear from the PL spectra that in the Dy^{3+}-doped phosphor, energy transfer from the host to the Dy^{3+} activator ions occurs. When illuminated by near UV light excitation source, excitation energy is absorbed by the host and created the self-trapped excitation (the 350 nm broad

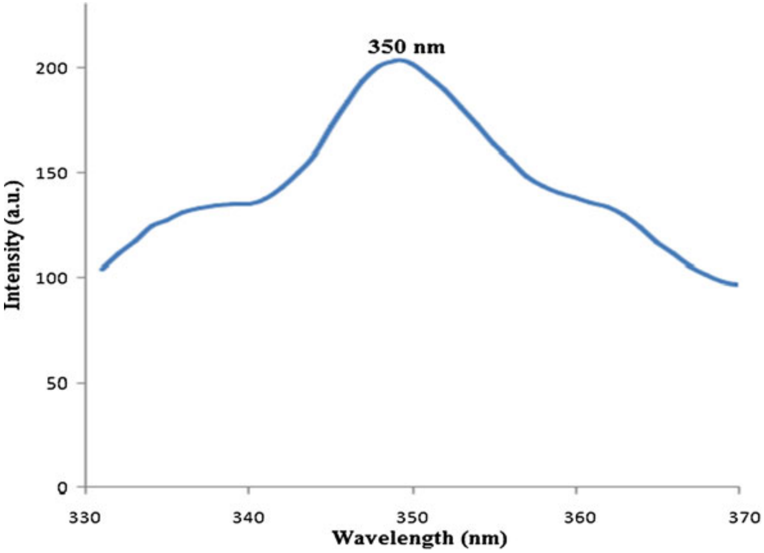

Fig. 7.9 Excitation spectrum of $Sr_6AlP_5O_{20}$:Dy^{3+} phosphor, monitored at 478 nm

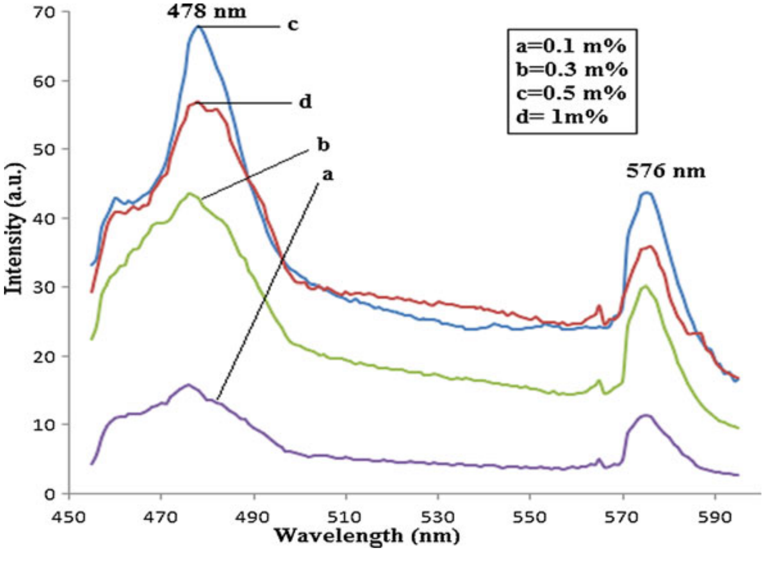

Fig. 7.10 Emission spectrum of $Sr_6AlP_5O_{20}$:Dy^{3+} phosphor, when excited at 350 nm

band) emission; meanwhile, the absorbed energy is transferred to the Dy^{3+} ion and creates the typical emissions of Dy^{3+}.

Emission spectra of Dy^{3+}-doped samples $X_6AlP_5O_{20}$:Dy^{3+} (where $X = Sr/Ba/Ca/Mg$) on excitation with light of 350 nm are shown in Figs. 7.10, 7.12, 7.14 and 7.16. The band at 350 nm is a main excitation peak matching with the emission of near

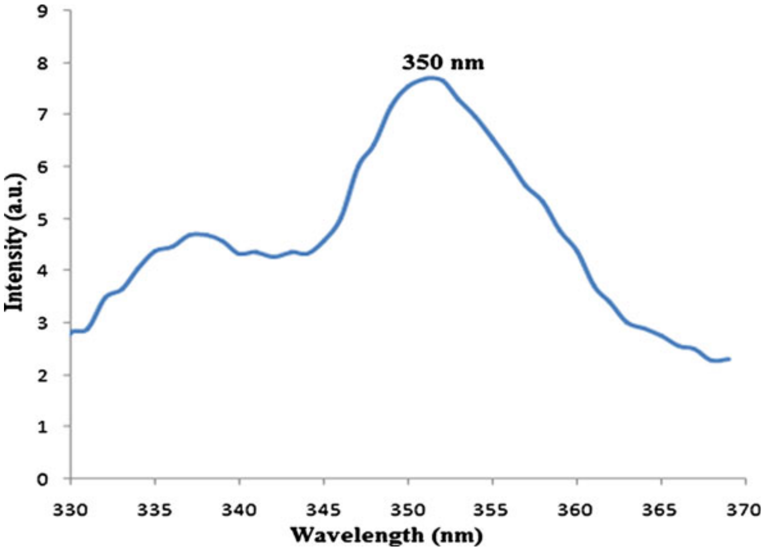

Fig. 7.11 Excitation spectrum of $Ba_6AlP_5O_{20}$:Dy^{3+} phosphor, monitored at 485 nm

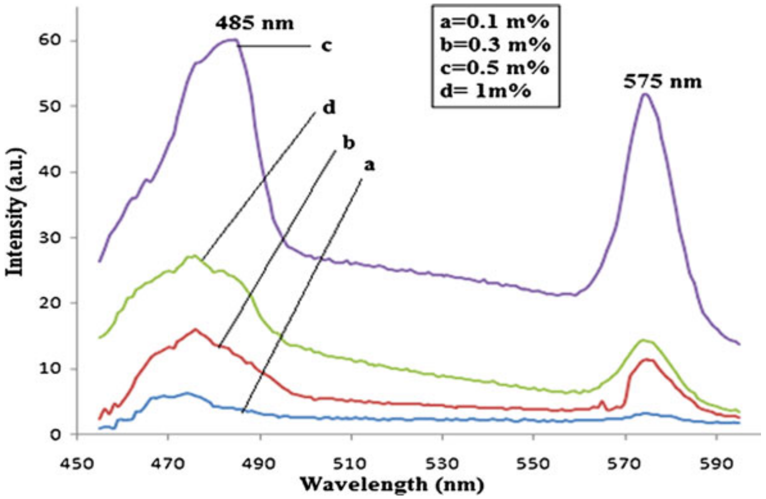

Fig. 7.12 Emission spectrum of $Ba_6AlP_5O_{20}$:Dy^{3+} phosphor, when excited at 350 nm

UV light (340–400 nm). All the four prepared phosphors have two emission bands: one is centered in the blue region and the other in the yellow region. These bands are assigned to the Dy^{3+} electronic transitions of $^4F_{9/2} \rightarrow {}^6H_{15/2}$ and $^6H_{13/2}$ energy levels, respectively. Both yellow and blue emissions showed a decrease in intensity with the change of matrix composition in the order of $Ca_6AlP_5O_{20}$, $Mg_6AlP_5O_{20}$, $Sr_6AlP_5O_{20}$ and $Ba_6AlP_5O_{20}$. The change is regular with the reduced radius, or the

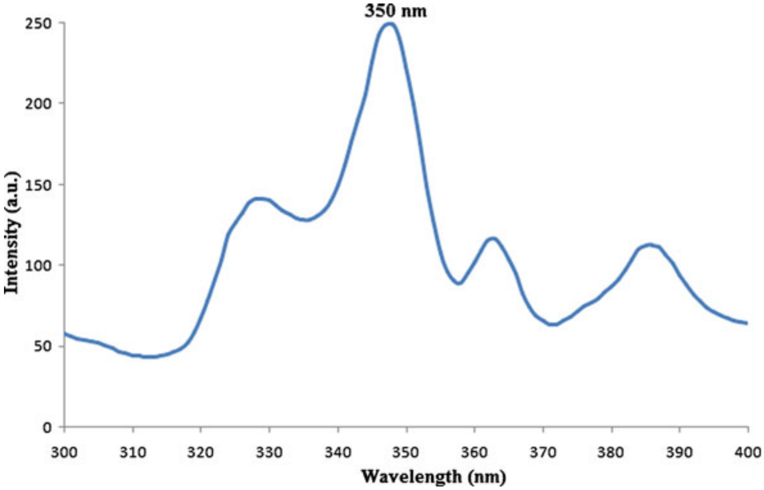

Fig. 7.13 Excitation spectrum $Ca_6AlP_5O_{20}:Dy^{3+}$ phosphor, monitored at 476 nm

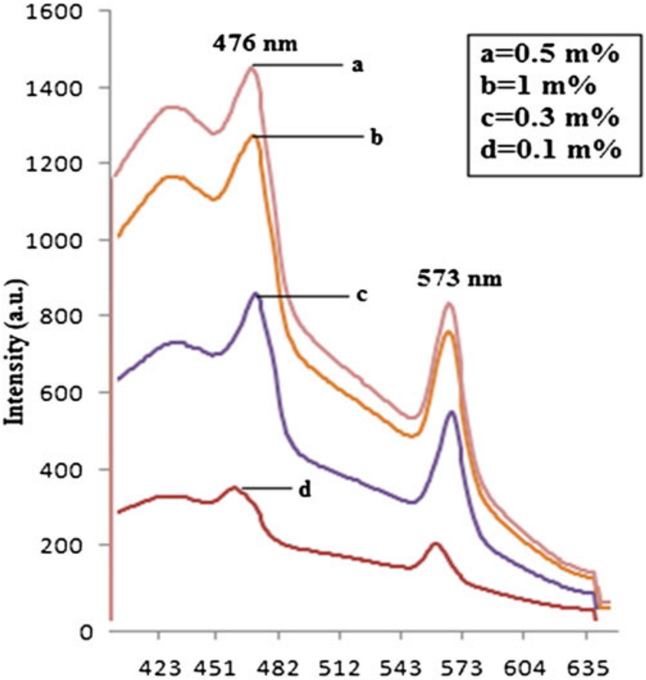

Fig. 7.14 Emission spectrum $Ca_6AlP_5O_{20}:Dy^{3+}$ phosphor, monitored at 350 nm

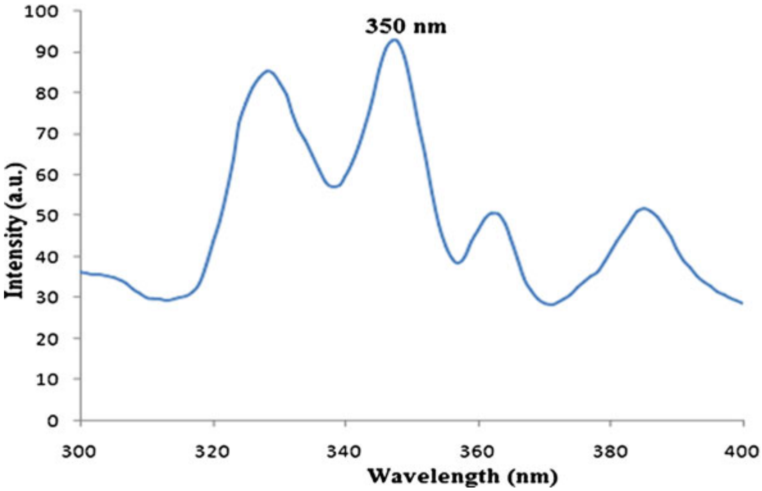

Fig. 7.15 Excitation spectrum $Mg_6AlP_5O_{20}$:Dy^{3+} phosphor, monitored at 481 nm

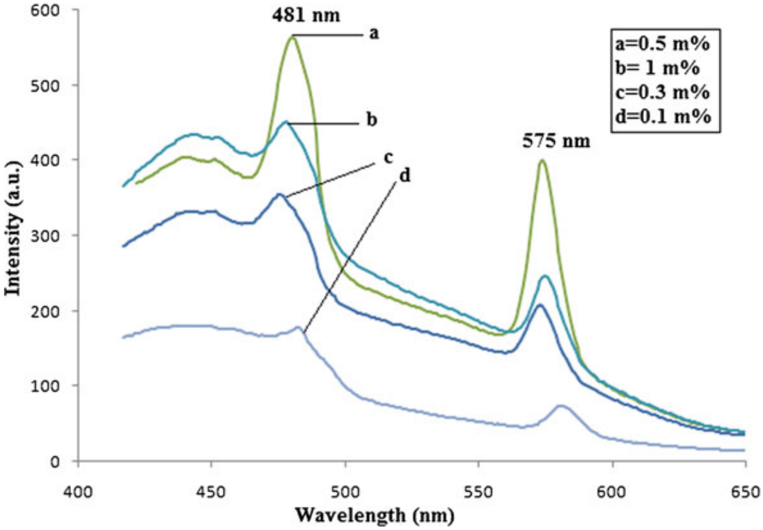

Fig. 7.16 Emission spectrum of $Mg_6AlP_5O_{20}$:Dy^{3+} phosphor, when excited at 350 nm

increased electro negativity of these alkali earth ions. The ionic radii of Dy ions is 91.2 pm which is closer to those of the Ca^{2+} ions (99 pm) rather than Sr^{2+} ions (112 pm), Ba^{2+} ions (135 pm), and Mg^{2+} (65 pm) ions. In our case, the Dy^{3+} ion may enter the host lattice to substitute Ca^{2+} or locate on surfaces of the crystals. As the ionic radii of Dy^{3+} is much larger than Ba^{2+}, $Mg^{2+}Sr^{2+}$, and near to Ca^{2+} or Al^{3+}, the second possibility is more feasible. The number of the Dy^{3+} ions located at the surface of $Ca_6AlP_5O_{20}$ shall be more as compared to those on $Ba_6AlP_5O_{20}$, $Sr_6AlP_5O_{20}$, and

$Mg_6AlP_5O_{20}$ phosphors. Its substitution at the Ca^{2+} site in $Ca_6AlP_5O_{20}$ will lead to less distortion and induce more oxygen vacancies in the host in comparison to its substitution in $Ba_6AlP_5O_{20}$, $Sr_6AlP_5O_{20}$, and $Mg_6AlP_5O_{20}$ phosphors. The charge compensating defects in the immediate vicinity is likely to influence the local site symmetry of $Ca_6AlP_5O_{20}$ host. Dy^{3+} ions should occupy statistically both cation positions (M^{2+}) in the unit cell. It would naturally cause a substantial number of vacant sites in the oxygen ion array, and then expand the lattice to decrease crystal density. Lopez et al. reported that the oxygen vacancies might acts as sensitizer for the energy transfer to the rare-earth ion due to the strong mixing of charge transfer states resulting in the highly enhanced luminescence [27]. But excess oxygen vacancies in the host would destroy the crystallinity inevitably, which might lead to quenching of the luminescence [28]. This is reflected in the emission spectra, wherein symmetry factor is higher in $Ca_6AlP_5O_{20}$ sample compared to in $Ba_6AlP_5O_{20}$, $Sr_6AlP_5O_{20}$, and $Mg_6AlP_5O_{20}$ phosphors. As Dy^{3+} ions progressively replace the Ca^{2+} ions, which can enhances PL emission intensity and progressively reduce asymmetry factor, the low-symmetry location of Dy^{3+} results in predominant emission of ${}^4F_{9/2} \rightarrow {}^6H_{15/2}$ transition in $Ca_6AlP_5O_{20}$ host. Of course, $Ca_6AlP_5O_{20}$ phosphors show strong PL emission intensity (around 25 times more) as compared to $Ba_6AlP_5O_{20}$, $Sr_6AlP_5O_{20}$, and $Mg_6AlP_5O_{20}$ phosphors (Fig. 7.17).

The energy levels of Dy^{3+} ion and emission transitions are presented in Fig. 7.18 [29]. The optical property of the material is often influenced by the structure of the matrix and synthesis technique [30]. It is known that Dy^{3+} shows intense peaks at

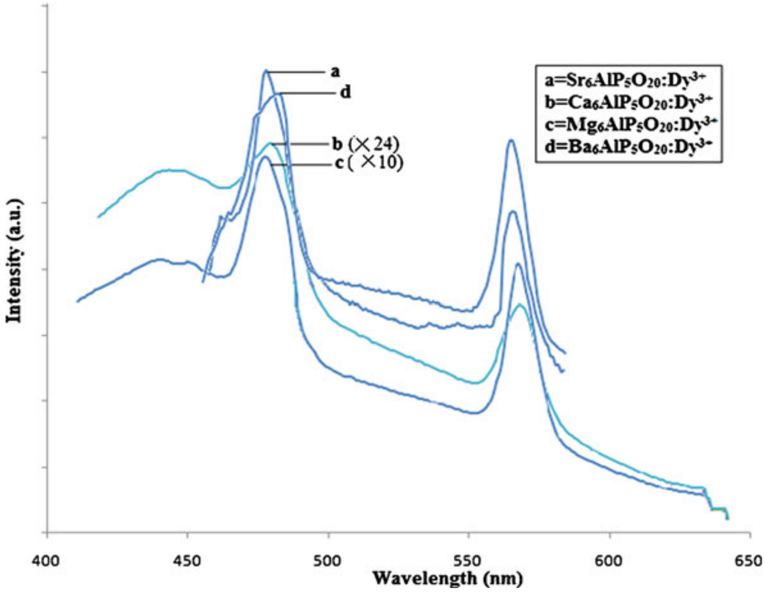

Fig. 7.17 Comparison of PL emission spectrum amongst the Dy^{3+} doped ion in $Sr_6AlP_5O_{20}$, $Ba_6AlP_5O_{20}$, $Ca_6AlP_5O_{20}$ and $Mg_6AlP_5O_{20}$ phosphors, when excited at 350 nm

Fig. 7.18 Energy levels of Dy^{3+} ion and emission transitions [29]

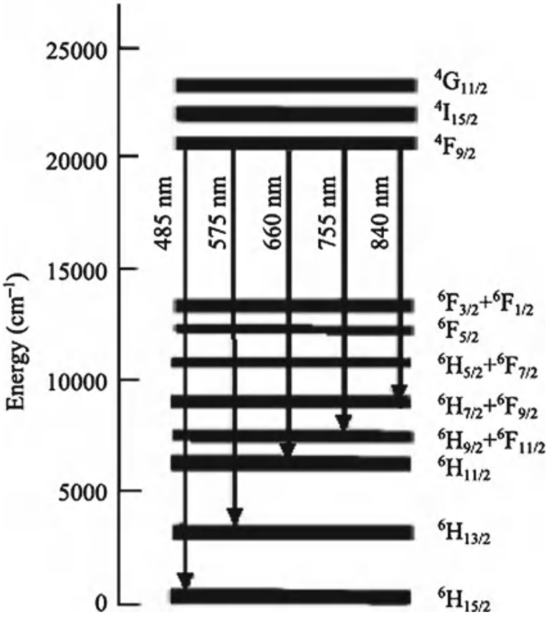

485 nm due to fluorescent transitions of $^4F_{9/2} \rightarrow {}^6H_{15/2}$, due to magnetic dipole and 575 nm due to fluorescent transitions of $^4F_{9/2} \rightarrow {}^6H_{13/2}$ due to electric dipole moment, respectively, when Dy^{3+} ions are located at low-symmetry sites with no inversion centers. Thus, the yellow to blue ratio (known as the asymmetry ratio of Dy^{3+} ion) varies with change in host lattices. Similar observations have been reported in the Dy^{3+}- doped $SrSiO_3$ system [31]. With increasing the calcining temperature, the yellow to blue ratio increases due to the change of the local site symmetry around Dy^{3+} ion.

7.2.2.4 PL of Eu^{3+}-Activated $X_6AlP_5O_{20}$ (where X = Sr/Ba /Mg)

Figure 7.19 shows the PL excitation spectrum of the $Sr_6AlP_5O_{20}$:Eu^{3+} phosphor. Two excitation bands are observed, one at 325 and other at 341 nm, which are all caused by the $f-f$ transitions. Both are observed as broad band but a maximum intensity occurred at 341 nm (stronger excitation band). Under the excitation of 341 nm, the phosphor of $Sr_6AlP_5O_{20}$:Eu^{3+} has two sharp orange/red-emission bands at 592 and 620 nm shown in Fig. 7.20. Among these two emission bands the 620 nm is main line and corresponds to the electric-dipole transition $^5D_0 \rightarrow {}^7F_2$ of the Eu^{3+}, whereas the other one corresponds to the magnetic dipole transition $^5D_0 \rightarrow {}^7F_1$ of the Eu^{3+} ion which is the less prominent. These two peaks are obtained due to the splinting of Eu^{3+} ion emission. The multiphoton relaxation derived from the vibration of phosphate groups, which can bridge the gaps between the lowest $^5D_0$ level of

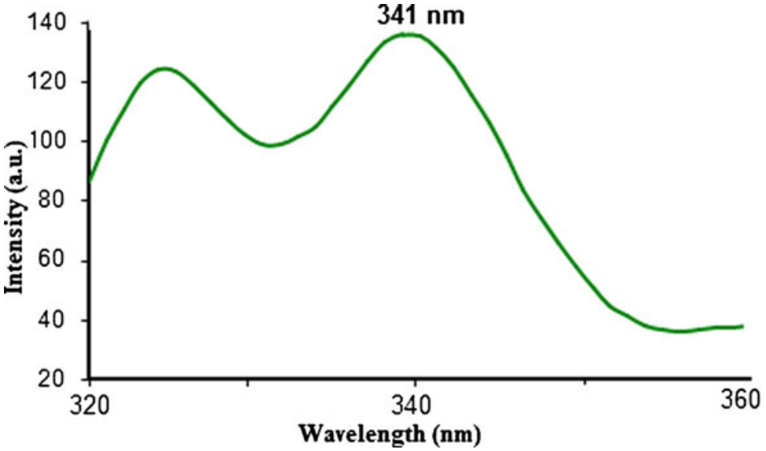

Fig. 7.19 Excitation spectrum of $Sr_6AlP_5O_{20}:Eu^{3+}$ phosphor monitored at 620nm

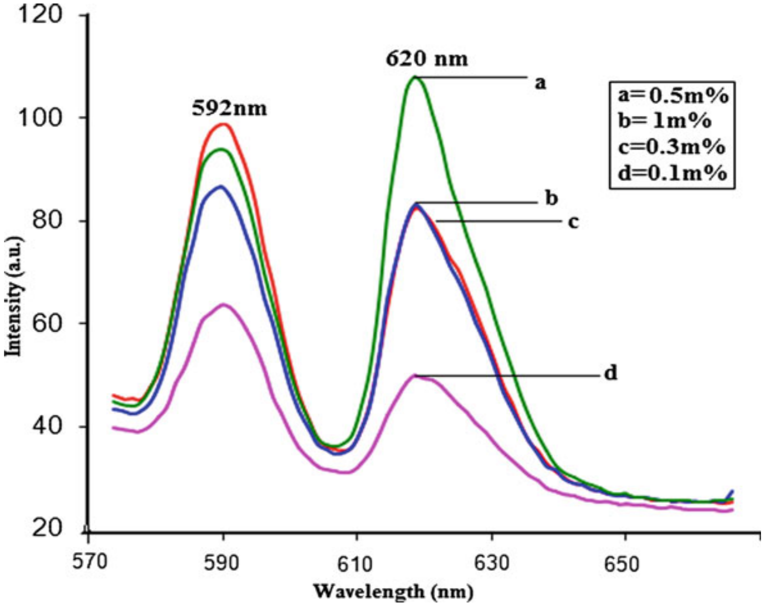

Fig. 7.20 Emission spectrum of $Sr_6AlP_5O_{20}:Eu^{3+}$ phosphor when excitation at 341 nm

Eu^{3+} and the higher energy levels ($^5D_1$, $^5D_2$) effectively, so that no emission from the higher energy levels of Eu^{3+} ion can be detected. The luminescent properties of Eu^{3+} ion in the crystalline $Sr_6AlP_5O_{20}$ phosphor are in good agreement with those obtained through other processes indicating that Eu^{3+} ions have been effectively doped into the host lattice of $Sr_6AlP_5O_{20}$. In the present case, the low contributions

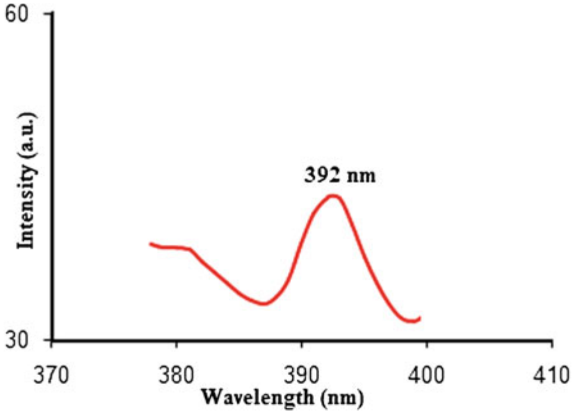

Fig. 7.21 Excitation spectrum of Ba_6 AlP_5 O_{20}:Eu^{3+} phosphor monitored at 616 nm

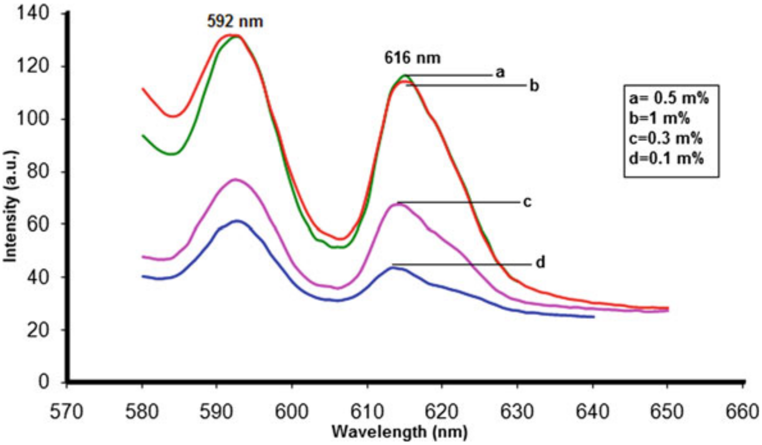

Fig. 7.22 Emission spectrum of $Ba_6AlP_5O_{20}$:Eu^{3+} phosphor when excited at 392 nm

of the orange $^5D_0 \rightarrow {}^7F_1$ emissions and the high intensity of the red $^5D_0 \rightarrow {}^7F_2$ emission result in high color purities that are adequate for lamp applications.

Figures 7.21 and 7.22 present the excitation and emission spectra of the Ba_6AlP_5 O_{20}:Eu^{3+} phosphor. Under the excitation of 392 nm, the phosphor of $Ba_6AlP_5O_{20}$: Eu^{3+} has two broad bands in the spectral range of orange and red emission at 592 and 616 nm, respectively. The main emission line is located at 592 nm, corresponding to $^5D_0 \rightarrow {}^7F_1$ transition of Eu^{3+}, which is due to the fact that the Eu^{3+} does not occupy a center of symmetry site in the host lattice. Other transitions from the $^5D_0$ excited levels to ^7F_J ground states, such as $^5D_0 \rightarrow {}^7F_2$ give rise to lines in the 580–630 nm range. The excitation at 392 nm caused by the f–f transitions from ^7F_J of Eu^{3+} to exited levels, that is to say, the transition $^7F_0 \rightarrow {}^5L_6$ of Eu^{3+} can be attributed to the 392 nm. Thus, the broad emission bands at 592 and 616 nm under the excitation

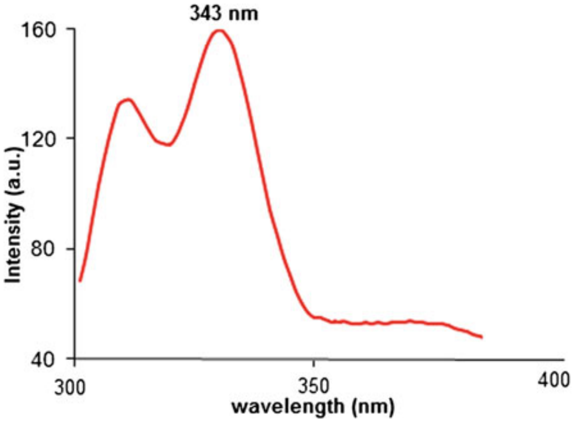

Fig. 7.23 Excitation graph of $Mg_6AlP_5O_{20}$:Eu^{3+} phosphor monitored at 615 nm

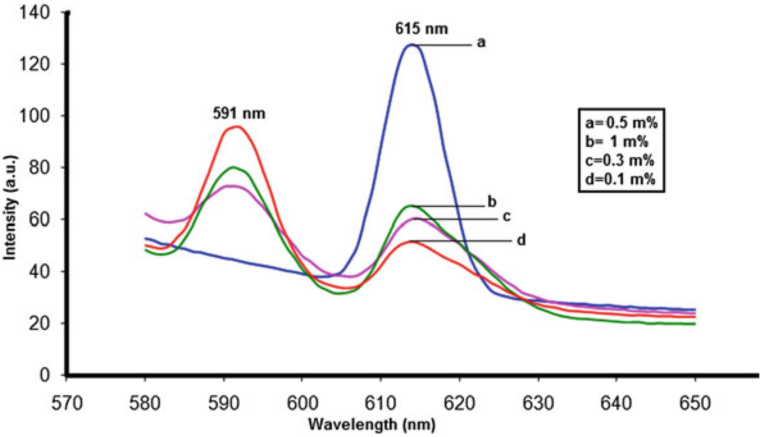

Fig. 7.24 Emission spectrum of $Mg_6AlP_5O_{20}$:Eu^{3+} phosphor when excited at 343 nm

of 392 nm show excellent orange and red emissions. The excitation spectrum shows that the 392 nm peak is the characteristic of the LED lighting due to the excitation peak observed in the range of near UV i.e., 385 nm to 395 nm and emission in the orange and red region of the spectrum shows that the $Ba_6AlP_5O_{20}$:Eu^{3+} phosphor it is perhaps the novel candidate of LED lighting.

The excitation and emission spectra of the $Mg_6AlP_5O_{20}$:Eu^{3+} phosphor at room temperature are shown in Figs. 7.23 and 7.24, respectively. The excitation spectrum exhibits two broad absorption bands peaking at 315 and 343 nm monitored at 615 nm. Two well-resolved peaks observed at 591 and 615 nm are due to $^5D_0 \rightarrow {}^7F_1$ and $^5D_0 \rightarrow {}^7F_2$ transitions, respectively. It was well-known that the $^5D_0 \rightarrow {}^7F_1$ lines originate from magnetic dipole transition, while the $^5D_0 \rightarrow {}^7F_2$ lines originate from electric dipole transition. With increasing concentration of Eu^{3+} ions intensity of both peaks increases relatively. In this case, it is found that the PL intensity increased with concentration from 0.1 to 1 mol% and it decreased at more than 1 mol% probably due to concentration quenching effect. At higher concentration, i.e., at 0.5 mol% the orange band (591 nm) was completely suppressed, which mean at this concentration the first magnetic dipole transition of Eu^{3+} ion becomes forbidden and only the second electric dipole transition was allowed. In the case of the Eu^{3+} ion, the relative intensity of the 615 nm to the 591 nm peak strongly depends on the local site symmetry around the Eu^{3+} ions.

7.2.2.5 PL of Ce^{3+}-Activated $X_6AlP_5O_{20}$ (where X = Sr/Ba/Ca)

The $5d$-level spectroscopy of Ce^{3+} is related to PL of Ce^{3+}. In the excited state, the $4f$-shell is empty and there is only one single $5d$-electron interacting with the crystalline environment. In the ground state, Ce^{3+} ion has the (Xe) $4f^1$ configuration, which results in only two $4f^1$ energy levels: the ${}^2F_{5/2}$ and ${}^2F_{7/2}$. These energy levels are approximately 2,000 cm^{-1} apart. At higher energy, the $4f^05d^1$ bands can be found. The energy of the bands is strongly dependent on the host lattice. The $4f^1$ ground state is separated about 51,000 cm^{-1} from the excited $5d^1$ configuration. In a crystalline environment, the $5d$ configuration may split by as much as 25,000 cm^{-1} into at the most five distinct $5d$ states. In addition, the average energy of five $5d$-levels may shift downwards by 22,000 cm^{-1}. The red shift of the first f–d-transition in Ce^{3+} when introduced to a crystalline host is a result of two mutually independent contributions: (1) The centroid shift, defined as the lowering of the average energy of the Ce^{3+} $5d$ configuration relative to the value for Ce^{3+} as a free ion. (2) The total crystal field splitting; defined as the energy difference between lowest and highest $5d$-level. The $4f-5d$ transitions corresponding to optical absorption and fluorescence of Ce^{3+} in crystals are parity- and spin-allowed, so that lifetimes of the fluorescence are in the range of 10–60 ns. The spatially diffused $5d$-electron orbital extends outward from the ion to overlap the neighboring ligand ions, and is more strongly influenced by their motion. In consequence, the optical properties depend strongly on the structure of host crystals. Both absorption and emission have usually a broad band character, showing splitting characteristic of ${}^2F_j$ states. As the position of $5d$ band itself depends on the host, not only the Stoke's shift but also the spectral positions of both the excitation and emission bands are host dependent. In phosphate, the emission is expected to be in the UV region. Luminescence of Ce^{3+} gets quenched above concentration of about 2 %. The quenching temperature is usually high.

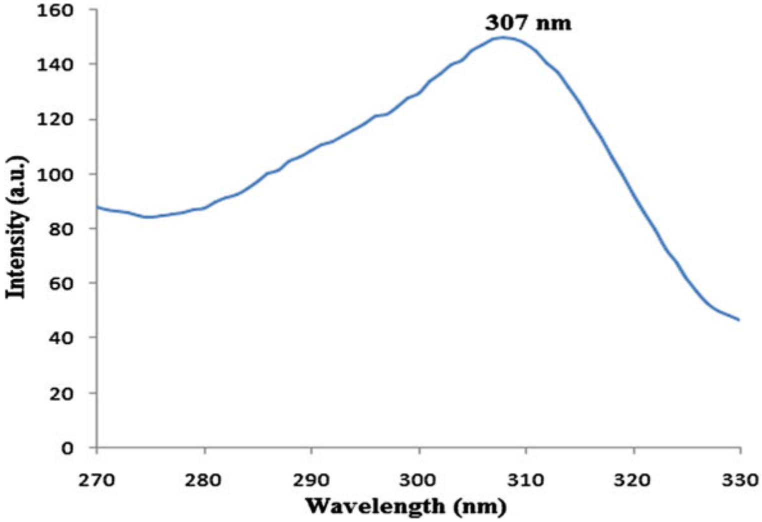

Fig. 7.25 Excitation spectra of $Ba_6AlP_5O_{20}$:Ce^{3+} monitored at 355 nm

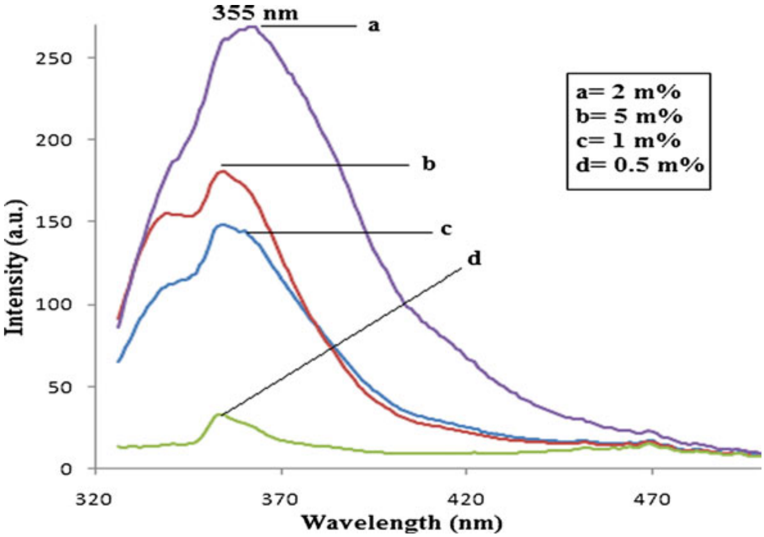

Fig. 7.26 Emission spectrum $Ba_6AlP_5O_{20}$:Ce^{3+} when excited at 307 nm

Figures 7.25, 7.26, 7.27, and 7.28 show the PL excitation and emission spectra of Ce^{3+} ions in $Ba_6AlP_5O_{20}$ and $Sr_6AlP_5O_{20}$ phosphors with different concentrations under excitation at 307 nm wavelength of light. The unresolved peaks are observed at 355 nm, which are assigned to the $5d-4f$ transition of Ce^{3+} ions. With increasing concentration of Ce^{3+} ions, the peak intensity of the 355 nm peak increases and the maximum intensity is observed for 2 mol% of Ce^{3+} ions. This indicates

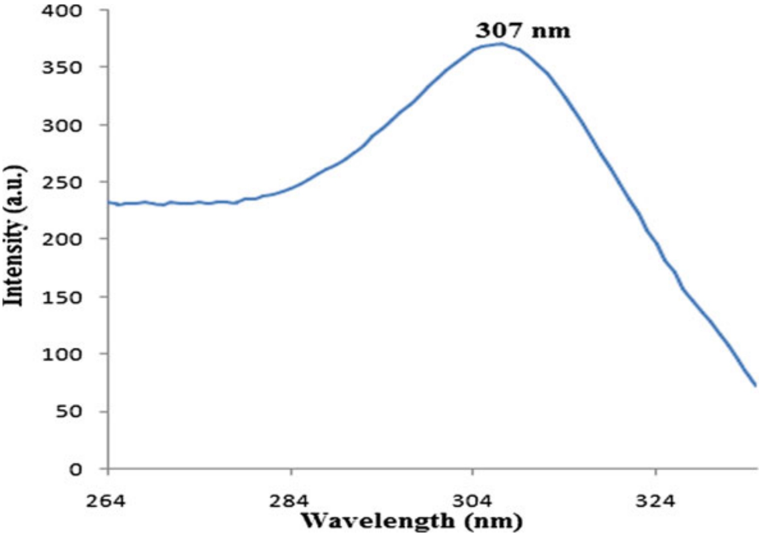

Fig. 7.27 Excitation spectra $Sr_6AlP_5O_{20}$:Ce^{3+} monitored at 355 nm

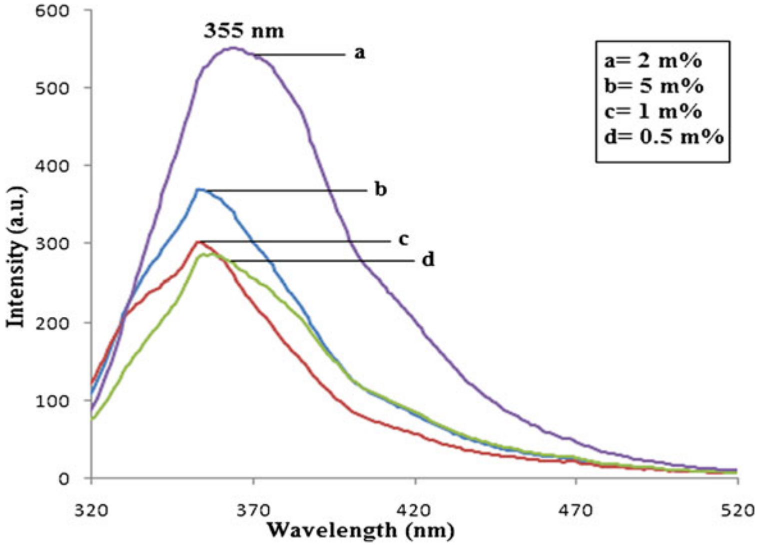

Fig. 7.28 Emission spectrum of $Sr_6AlP_5O_{20}$:Ce^{3+} when excited at 307 nm

that the $Ba_6AlP_5O_{20}$ and $Sr_6AlP_5O_{20}$ lattice is more suitable for higher concentrations of Ce^{3+} ions. The PL emission spectra of both $Sr_6AlP_5O_{20}$:Ce (2 mol%) and $Ba_6AlP_5O_{20}$:Ce (2 mol%) phosphor show the Ce^{3+} emission at 355 nm occurs due to the $5d-4f$ transmission of the Ce^{3+} ion. The variation of the PL emission intensity observed may be due to cross-relaxation between Ce^{3+} ions (in this process, excited ion transfers only a part of energy to another ion) in case of heavy concentration of Ce^{3+}. Energy transfer between pairs of rare-earth ions at dilution levels below the self-quenching limits is known to take place generally through multipolar interactions like dipole–dipole or dipole–quadrupole interactions [32–34]. The Ce^{3+} ion can be used as a sensitizer as well as an activator, depending on the splitting of the 5*d* excited levels by the crystal field symmetry. Much work has been done on the energy transfer from Ce^{3+} to different activator ions in different host lattice [35–37]. PL spectra of $Ba_6AlP_5O_{20}$:Ce^{3+} and $Sr_6AlP_5O_{20}$:Ce^{3+} phosphors were observed at 355 nm emission due to $^2D(5d) \rightarrow {}^2F_{7/2}(4f)$ transition. The $5d \rightarrow 4f$ transition of Ce^{3+} ion, hence, Ce^{3+} ion was excited in this lattice with 307 nm to check for its suitability for application in scintillating mechanism. The emission occurs from the lowest component of the 5*d* configuration to the two-crystal field split levels ($^2F_{5/2}$ and $^2F_{7/2}$) of the 4*f* ground state. As the concentration of Ce^{3+} ion increases, PL intensity also increases in $Ba_6AlP_5O_{20}$ and $Sr_6AlP_5O_{20}$ lattice up to 2 mol%. The 300–400 nm PL emission was dominated at 2 mol% of the Ce^{3+} ions. The observed Ce^{3+} emission in this phosphor can be used in scintillators according to an energy transfer process explained by Lempicki et al. [38] and Wojtowicz et al. [39, 40]. According to this process, Ce^{3+} captures primary excitation energy ($h\upsilon$) and becomes Ce^{4+}. After capturing a free electron (e_c) from the conduction band, Ce^{4+} will be converted into an excited Ce^{3+} ion or $(Ce^{3+})^*$. Relaxation to the ground state will be accompanied by emission of the scintillation photon $h\upsilon$. This process can be summarized as follows:

$$
\begin{aligned}
&Ce^{3+} + h\upsilon \rightarrow Ce^{4+} \\
&Ce^{4+} + e_c \rightarrow (Ce^{3+})^* \\
&(Ce^{3+})^* \rightarrow Ce^{3+} + h\upsilon.
\end{aligned}
$$

PL excitation spectra of Ce^{3+} activated $Ca_6AlP_5O_{20}$ phosphor show broad band at 245 nm ($\lambda_{emi} = 357$ nm). Figures 7.29 and 7.30 show the PL excitation and emission spectra of Ce^{3+} ions in $Ca_6AlP_5O_{20}$ phosphor with different concentrations under excitation at 245 nm wavelength of light. The unresolved peaks are observed at 357 nm, which are assigned to the $5d{-}4f$ transition of the Ce^{3+} ions. With increasing concentration of the Ce^{3+} ions, the peak intensity of the 357 nm peak increases and the maximum intensity is observed for the 2 mol% of Ce^{3+} ions. This indicates that the $Ca_6AlP_5O_{20}$ lattice is more suitable for higher concentrations of Ce^{3+} ions. The PL emission spectra of $Ca_6AlP_5O_{20}$:Ce (2 mol%) phosphor show the Ce^{3+} emission at 357 nm due to $5d - 4f$ transmission of Ce^{3+} ion. The variation of PL emission intensity observed may be due to cross-relaxation between Ce^{3+} ions (in this process, excited ion transfers only a part of energy to another ion) in case of large concentration of Ce^{3+}. Energy transfer between pairs of rare-earth ions at dilution levels below the self-quenching limits is known to take place generally through multipolar interactions like dipole–dipole or dipole–quadrupole interactions.

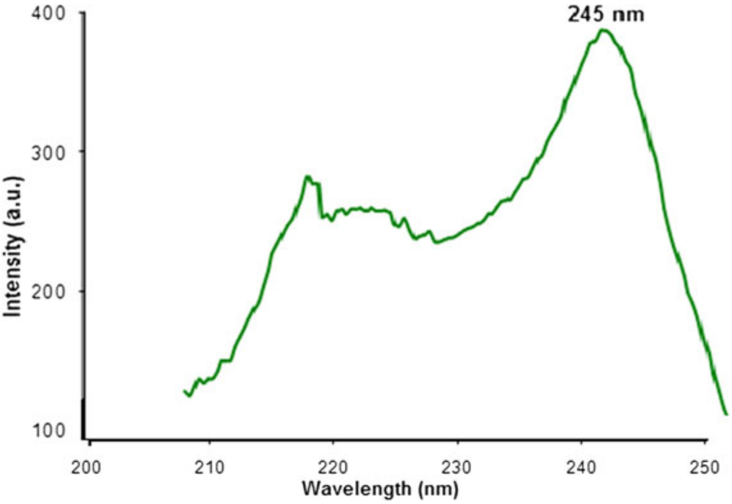

Fig. 7.29 Excitation graph of $Ca_6AlP_5O_{20}$:Ce phosphor, monitored at 357 nm

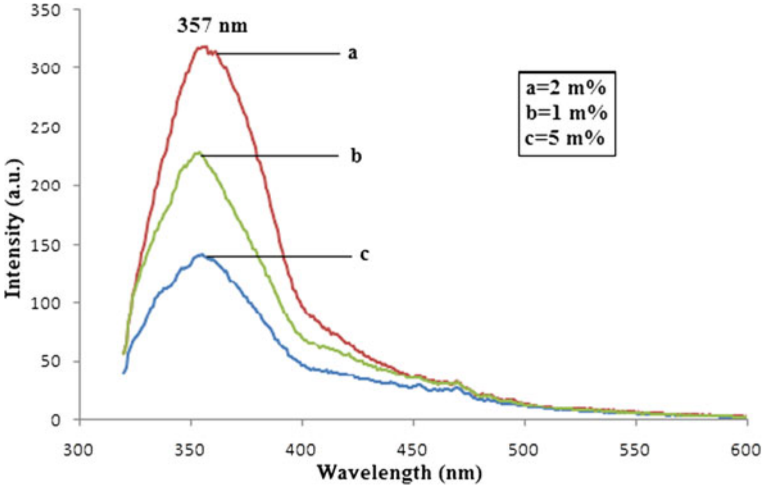

Fig. 7.30 Emission of $Ca_6AlP_5O_{20}$:Ce phosphor, when excited at 245 nm

7.3 Conclusions

- The novel trivalent Dy-doped $X_6AlP_5O_{20}$ (where X = Sr, Ba, Ca and Mg) phosphate phosphors were prepaperd by the combustion synthesis and confirmed by XRD. SEM images show that the grains have irregular shape with a size less than 3–4 μm. The near UV excited (350 nm) luminescent properties of all four prepared phosphors were investigated. PL emission spectra show two emissions (485 and 573 nm) in Dy^{3+}-doped $X_6AlP_5O_{20}$ (where X = Sr, Ba, Ca, and Mg) phosphate phosphors. In the later case, the strongest PL emission intensity was observed when the concentration of the doped Dy^{3+} was 0.5 mol%. The intensity decreased at higher concentrations due to concentration quenching. $Ca_6AlP_5O_{20}$ phosphors show strong PL emission intensity around 25 times more as compared with $Ba_6AlP_5O_{20}$, $Sr_6AlP_5O_{20}$ and $Mg_6AlP_5O_{20}$ phosphors. The results indicate that trivalent Dy^{3+}-doped $X_6AlP_5O_{20}$ (where X = Sr, Ba, Ca, and Mg) phosphate phosphors are potential phosphors for UV excited LEDs.

- The PL emission is strongly observed in the red region of the spectrum due to transition of the Eu^{3+} ions in the $M_6AlP_5O_{20}$:Eu (where M = Ba/Sr/Mg) phosphors. The prominent red intense emission is observed in $Ba_6AlP_5O_{20}:Eu_{0.5\,\mathrm{mol\%}}$ phosphor by near UV excitation i.e., 392 nm of GaN LED emission. In the prepared phosphors, the PL excitation of one of the $Ba_6AlP_5O_{20}:Eu^{3+}$ phosphor observed at 392 nm is matched with the requirement of a suitable red-emitting UV-LED phosphor excitation wavelength [exhibit strong and broad absorption around 400 nm (i.e. 385–395 nm) (LED emission wavelength)] as compared to other prepared phosphors. Therefore, $Ba_6AlP_5O_{20}:Eu^{3+}$ phosphor is a stable novel phosphor for solid-state lighting.
- The results show that for 2 mol% concentration of all $Ba_6AlP_5O_{20}$:Ce, $Sr_6AlP_5O_{20}$:Ce and $Ca_6AlP_5O_{20}$:Ce compounds; the highest PL emission intensity was observed. However, the PL emission spectra of the above phosphors for less than 2 mol% concentrations also show Ce^{3+} emission due to the $5d \rightarrow 4f$ transition of the Ce^{3+} ion.

All the results obtained from this study are reported for the first time in the present (hosts) phosphate-based phosphors. It may be useful for scintillation applications. This material can find appreciation in nuclear physics, X-ray and neutron diffraction, nondestructive evaluation, treaty verification and safeguards, environmental monitoring, and geological exploration. Moreover, full understanding of the nature of the competing processes and the dynamics of hole trapping by Ce^{3+} is still one of the challenging subjects in scintillation mechanism research.

7.4 PL Studies of Novel Eu and Ce-Doped $Na_2Zn_5(PO_4)_4$ by Solid-State Diffusion Method [41]

7.4.1 Experimental

The Eu and Ce-doped $Na_2Zn_5(PO_4)_4$ phosphate-based phosphor was synthesized by the modified solid-state reaction method. The raw materials used as starting materials were analytical grade pure materials ZnO, Na_2CO_3 and $NH_4H_2PO_4$. These materials were weighed in the proper molar ratio, and then Eu_2O_3 was introduced as the dopant source. The chemicals were mixed and ground homogeneously in an agate mortar. The mixture was heated to 500 °C in a silica crucible for 2 h to allow ammonia, water, and nitrogen oxides vapors to evaporate. The product, after grinding, was again heated at 800 °C for 24 h, to obtain the white phosphor powders. A similar procedure was followed for the Ce-doped $Na_2Zn_5(PO_4)_4$. Ce was introduced in the form of $(NH_4)_3Ce(NO_3)_6$. The chemical reaction is as follows:

$$\mathbf{10ZnO + 2Na_2CO_3 + 8NH_4H_2PO_4 \rightarrow 2Na_2Zn_5(PO_4)_4 + 12H_2O + 2CO_2 + 6NH_4 + N_2}$$

7.4.2 Results and Discussion

7.4.2.1 Structural Behavior, XRD, and Morphology of $Na_2Zn_5(PO_4)_4$

The structure of $Na_2Zn_5(PO_4)_4$ was solved and reported by Ji et al. [17] in 2007. $Na_2Zn_5(PO_4)_4$ crystallizes in the orthorhombic system with space group *Pbcn*, lattice parameters $a = 10.381(2)$ Å, $b = 8.507(1)$ Å, $c = 16.568(3)$ Å, and $Z = 4$. Both Zn and P atoms are tetrahedrally coordinated by oxygen atoms. [Zn(3)O_4] polyhedrons link the neighbor layers by sharing apex oxygen atoms with the [PO_4] polyhedron to form a 3D $[Zn_5P_4O_{16}]_n^{2n-}$ zincophosphate covalent framework with channels along the b-axis in which the sodium atoms are located (Fig. 7.31). Within a radius

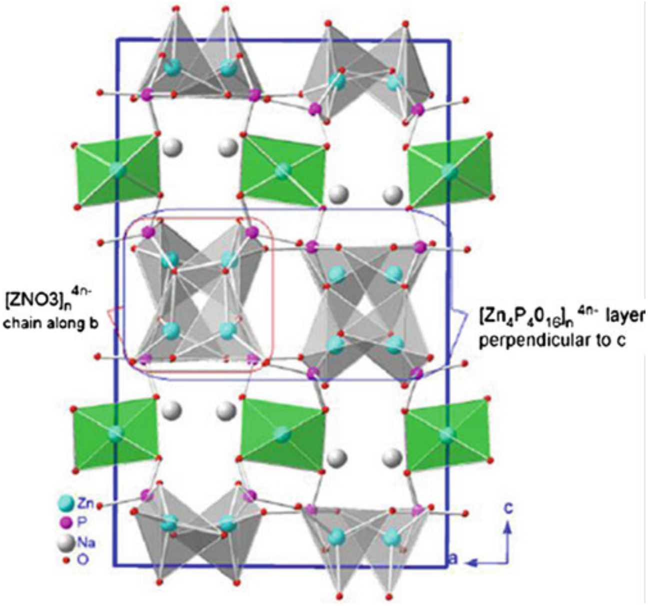

Fig. 7.31 As per the Ji et al. [17] in 2007, the crystal structure of the $Na_2Zn_5(PO_4)_4$ lattice

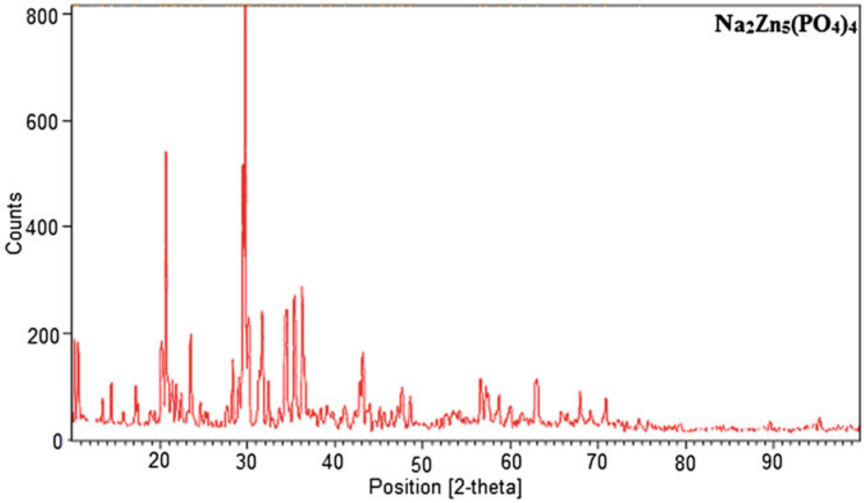

Fig. 7.32 XRD Pattern of the $Na_2Zn_5(PO_4)_4$

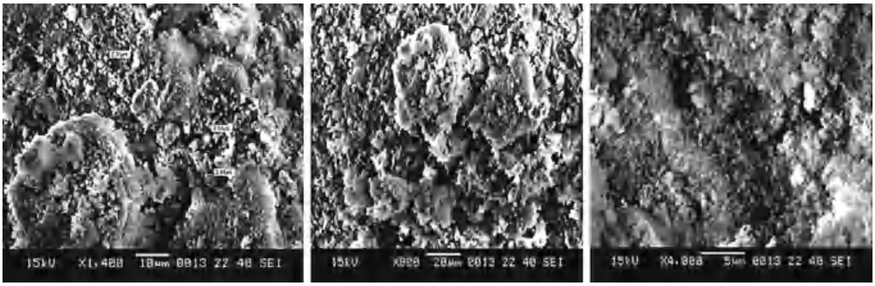

Fig. 7.33 SEM images of the $Na_2Zn_5(PO_4)_4$:Eu^{3+} phosphor

of 3 Å, Na is coordinated by 5 oxygen atoms. Four of the 5 Na–O bond lengths are in the range of 2.278(3)–2.542(3) Å while the other one is 2.938(3) Å. Figure 7.32 shows the XRD pattern of the prepared $Na_2Zn_5(PO_4)_4$ materials. The XRD pattern did not indicate the presence of any of the constituents such as, ZnO, $NaCO_3$, or $NH_4H_2PO_4$ and other likely phases which are an indirect evidence for the formation of the desired compound. These results indicate that the final product was formed in crystalline and homogeneous form. The XRD standard data of the $Na_2Zn_5(PO_4)_4$ phosphor are not available in the JCPDs files. It is clearly seen that the grains have irregular shapes. The average grain size is in the sub-micrometer range as seen in the SEM images. The size of sample prepared is 0.5–2 µm, which is suitable for the solid-state lighting (Fig. 7.33).

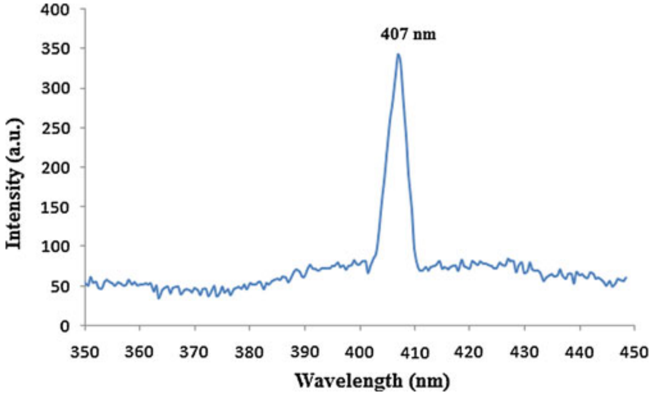

Fig. 7.34 Excitation spectra of $Na_2Zn_5(PO_4)_4$:Eu^{3+} monitored at 611 nm

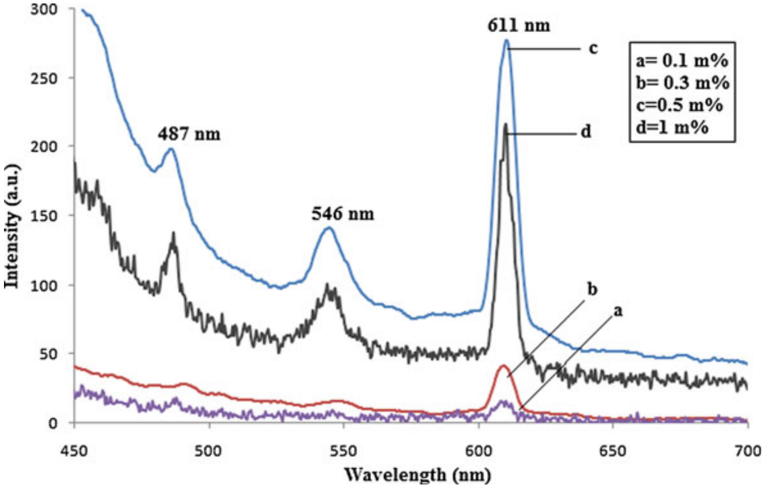

Fig. 7.35 Emission spectrum of $Na_2Zn_5(PO_4)_4$:Eu when excited at 407 nm

7.4.2.2 PL Characterization of $Na_2Zn_5(PO_4)_4$:Eu^{3+}

The PL excitation spectra of the prepared Eu activated $Na_2Zn_5(PO_4)_4$ phosphor are shown in Fig. 7.34. The prominent excitation band at 407 nm may be due to the $f-f$ transitions of the Eu^{3+} ion. The PL excitation spectrum is broad and maximizes at 407 nm. This excitation can be ascribed to the $Eu^{3+} \rightarrow O^{2-}$ charge transfer transition (Fig. 7.34). The PL emission spectrum ($\lambda_{exc} = 407$ nm) consists of the intense peak at 611 nm (red) that can be ascribed to the ${}^5D_0 \rightarrow {}^7F_2$ transition of the Eu^{3+} ion and the other two broad emission peaks are observed at 487 and 546 nm due to the Eu^{2+} ions as shown in Fig. 7.35. Eu ion shows emissions at 487, 546, and 611 nm in the blue, green, and red regions of the spectrum, respectively by 407 nm

Hg free excitation. In the present case, Eu ions simultaneously show the broad emission at 487 and 546 nm from Eu^{2+} ions and 611 nm sharp emissions of Eu^{3+} ions. This newly synthesized phosphor, synthesized by a low cost and easy technique is a novel phosphors that may be useful as a RGB phosphor for solid-state lighting application. The prominent 611 nm emission of Eu^{3+} ion in $Na_2Zn_5(PO_4)_4$ material is applicable as a red phosphor for the solid-state lighting. The PL intensity variation with the concentration from 0.1 to 1 mol% is observed and it decreased at more than 0.5 mol% probably due to concentration quenching effects. In the case of the Eu^{3+} ion, the relative intensity of the 611 nm peak strongly depends on the local site symmetry around the Eu^{3+} ions. The transition of $^5D_0 \rightarrow {}^7F_2$ belongs to a forced electric dipole transition and its intensity is very sensitive to the site symmetry of the Eu^{3+} ions. Thus, the ratio of $R = {}^5D_0 \rightarrow {}^7F_2/{}^5D_0 \rightarrow {}^7F_1$ can measure the distortion from the inversion symmetry of the Eu^{3+} ion local environment [42–44]. As shown in Fig. 7.35, the transition $^5D_0 \rightarrow {}^7F_2$ is much stronger than the transition $^5D_0 \rightarrow {}^7F_1$, which suggests that the Eu^{3+} is located in a distorted (or asymmetric) cation environment. The sites for dopants in the host are determined by their ionic radii. The radius of Eu^{3+}, Zn^{2+} and Na^+ is 95, 74 and 95 pm, respectively. Thus, the Eu^{3+} ions can readily occupy the Na^+ sites rather than the Zn^{2+} sites. Other transitions from the $^5D_0$ excited levels to ^7F_J ground states, such as $^5D_0 \rightarrow {}^7F_1$ lines in the 570–600 nm range are relatively weak, which is advantageous for obtaining a phosphor with good CIE chromaticity coordinates.

The results of Eu^{2+}/Eu^{3+} activated $Na_2Zn_5(PO_4)_4$ phosphor show that it may be applicable to LED as RGB phosphor. Hence, our results claimed it is a novel phosphor for the lamp industry. It can be synthesized by easy techniques.

7.4.2.3 PL Characterization of $Na_2Zn_5(PO_4)_4$:Ce^{3+}

Figure 7.36 shows the excitation spectrum of the Ce^{3+} activated $Na_2Zn_5(PO_4)_4$. The emission color of the $Na_2Zn_5(PO_4)_4$ that contains the 2 mol% Ce is blue (Fig. 7.37).

Fig. 7.36 Excitation spectra of the $Na_2Zn_5(PO_4)_4$:Ce^{3+} monitored at 470 nm

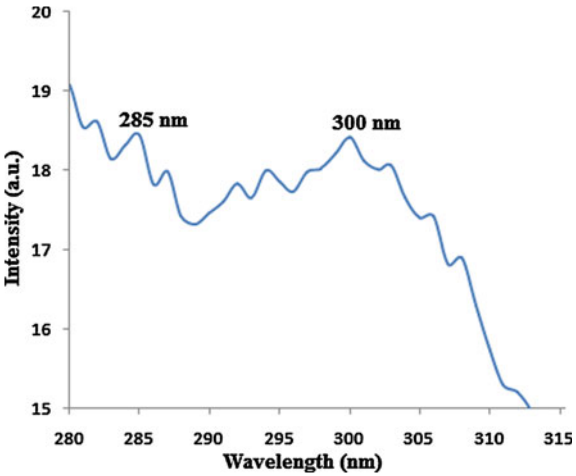

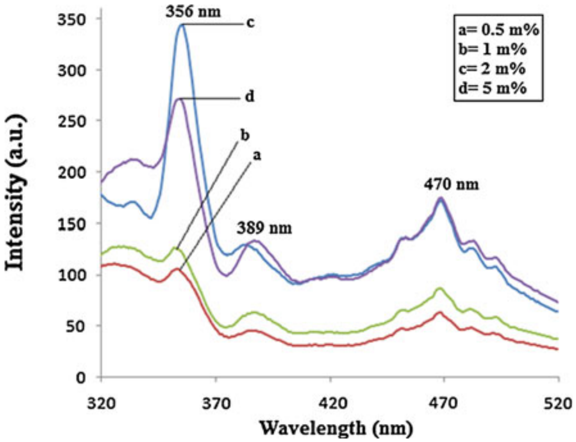

Fig. 7.37 Emission spectrum of the $Na_2Zn_5(PO_4)_4:Ce^{3+}$ when excited at 285 nm

The excitation spectrum contains several bands around 285, 294, and 300. The one at 285 nm is the most prominent. The manifold splitting of the band corresponding to the $4f^05d^1$ configuration suggests a noncubic environment for Ce^{3+}. These differences in the PL spectra may be understood in terms of effect of crystal structures on the Ce^{3+} energy levels. The spin–orbit split $^2D_{3/2}$ and $^2D_{5/2}$ states of the $5d$ configuration of free Ce^{3+} are located 49,700 and 52,100 cm^{-1} above the $4f^1$ $^2F_{5/2}$ ground state of Ce^{3+} [45]. When Ce^{3+} is introduced in a compound, the average energy of the 5d configuration is lowered and the $^2D_{3/2}$ and $^2D_{5/2}$ states are further split by the crystal field. Depending on the site symmetry, at the most five distinct $5d$ states may form. The trivalent Ce^{3+}-ions have an electronic structure containing one 4f-electron and as an activator, they generally result in phosphors that are having a broad band UV emission. In the rare-earth phosphates, the emission bands of Ce^{3+} are not like those found in other materials [46]. The broad band is observed at around 300 nm with a prominent shoulder at around 285 nm at room temperature. Figure 7.37 shows the PL emission spectra of the Ce^{3+} ions in $Na_2Zn_5(PO_4)_4$ phosphors with different concentrations under a 285 nm excitation wavelength. Peaks are observed at 356 and 470 nm which are assigned to the $5d-4f$ transition of the Ce^{3+} ions. The concentration of the Ce^{3+} ion increases the corresponding intensity of the peaks at the higher concentration (2 mol%). This indicates a change of the surrounding of the Ce^{3+} ions at higher concentration in the $Na_2Zn_5(PO_4)_4$ lattice. The observed variations of PL emission intensities may be cross-relaxation between Ce^{3+} ions in the case of higher concentration of Ce^{3+}. From the measured fluorescence spectra (Fig. 7.37) of Ce^{3+}, it is clear that the band corresponds to the transitions $5d-4f$. The emission appears more intense and broader in all the Ce^{3+} phosphors. The fluorescence intensity increases with an increase in Ce concentration up to 2 mol%, beyond which the fluorescence intensity tends to quench. It is also noticed that the peak positions of the emission bands have not changed and blue emission makes this material a candidate for the blue component of a phosphor blend for the lamp industry.

7.5 Conclusions

Eu^{3+} and Ce^{3+} activated $Na_2Zn_5(PO_4)_4$ phosphors were prepared by the well-known solid-state diffusion techniques. Ce^{3+} emission was observed at 356, 389, and 470 nm by excitation at 285 nm. The emission may be applicable for scintillators as well as a blue phosphor forthe lamp industry; i.e., only 470 nm emission of Ce^{3+} ion for Hg excited lamp. The Eu ions show emissions at 487, 546, and 611 nm in the blue, green, and red region of the spectrum, respectively from 407 nm excitation. In the present case, Eu ions simultaneously show the broad emission at 487 and 546 nm by Eu^{2+} ions and a sharp emission at 611 nm from the Eu^{3+} ions. Therefore, this newly synthesized phosphor that was made by a simple low cost technique is a novel phosphor and it can be useful as RGB phosphor for solid-state lighting applications. Recently, most research was done on the development of new solid-state lighting phosphors which shows only single color visible emission. It is, however, now reported for the first time that the newly developed host using the Eu ions as an activator can be used as an RGB emission phosphor.

7.6 New Blue-Emitting $Li_2Sr_2Al_2PO_4F_9$:Eu^{2+} Nanophosphor by Wet Chemical Synthesis [47]

7.6.1 Experimental

For preparing the nanocrystalline complex fluorides halophosphate phosphors, the one step wet chemical method was used; that is, constituent chlorides in stoichiometric ratios were dissolved in double-distilled deionized water in a glass beaker (Borosil) and were evaporated till the mixture became anhydrous. Use of chlorides as starting materials helps preventing the hydrolysis. The $Li_2Sr_2Al_2PO_4F_9$ phosphors were prepared by the wet chemical method. LiCl, $SrCl_2{\cdot}6H_2O$, $Al(NO_3)_3{\cdot}9H_2O$, $NH_4H_2PO_4$, and NH_4F analar grade were taken in a stoichiometric ratio and dissolved separately in double-distilled deionized water, resulting in a solution of $Li_2Sr_2Al_2PO_4F_9$. In the present investigation, materials were prepared according to the chemical formula $Li_2Sr_{2-x}Al_2PO_4F_9{:}Eu_x{\cdot}Eu_2O_3$ soluble in dil.HNO_3 was then added to the solution to obtain $Li_2Sr_2Al_2PO_4F_9{:}Eu^{2+}$. In this formula, the x-value indicates the concentration of the impurity in the mol%. The mixture of reagents was mixed together to obtain a homogeneous solution. The molar ratio of the Eu ion was changed in relation to the $Li_2Sr_2Al_2PO_4F_9$ phosphor. The compositions of the reagents were calculated using the total oxidizing and reducing valencies of the components, which served as the numerical coefficients, so that the equivalent ratio is unity. It was confirmed that no undissolved constituents were left behind and all the chemicals had completely dissolved in water. The compounds $Li_2Sr_2Al_2PO_4F_9$:Eu^{2+} in their powder form were obtained by evaporating the solution at 120 °C for 8 h. The dried samples were then slowly cooled to room temperature. The resultant nanocrystalline powder was crushed into fine particles in a crucible. This method has an advantage in that it uses a simple procedure and chemicals are easily available, nontoxic and easily handled at ambient conditions of humidity and pressure.

7.6.2 Results and Discussion

7.6.2.1 XRD and TEM Studies

Figure 7.38 shows the XRD pattern of the $Li_2Sr_2Al_2PO_4F_9$ material. The XRD pattern did not show the presence of the constituents, such as LiCl, $SrCl_2$, Al $(NO_3)_3$, $NH_4H_2PO_4$, or NH_4F and other likely phases which are an indirect evidence for the formation of the desired compound. These results show that the final product was nanocrystalline and homogeneous. The XRD spectra exhibit broadened diffraction peaks indicating the nanocrystalline nature. The small amount of doped RE ions has virtually no effect on phase structures. There are no characteristic peaks originating from the dopants or minor phases. This signifies that the incorporation of Eu^{2+} ion into the $Li_2Sr_2Al_2PO_4F_9$ lattice does not cause any significant change to the crystal

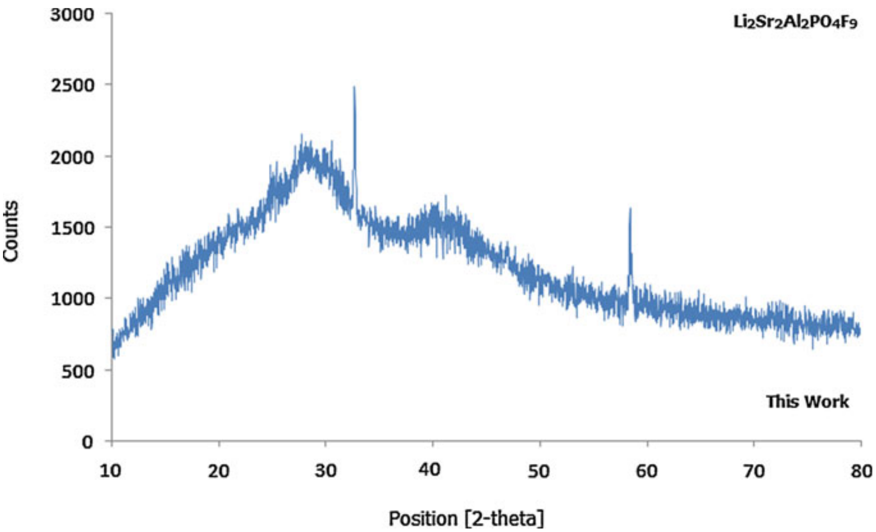

Fig. 7.38 XRD of the $Li_2Sr_2Al_2PO_4F_9$ host lattice

structure of the host matrix. All relatively sharp diffraction peaks can be perfectly indexed to the high purity and high crystallinity of the $Li_2Sr_2Al_2PO_4F_9$. Moreover, there are considerable broadenings in the XRD lines, which are due to reduction in the grain sizes. No more data related to this phosphor are available in the literature. It may also be note that the peaks of the synthesized materials exhibit a slight shift toward smaller 2θ angles in respect to the pattern of pure $Na_2Sr_2Al_2PO_4F_9$. This is an indication that the lattice parameter of these materials is larger than that in $Na_2Sr_2Al_2PO_4F_9$. The $Li_2Sr_2Al_2PO_4F_9$ compound has been prepared first time; therefore, the XRD standard data are not available in JCPDS files for comparisons. Moreover, from Fourier transform infrared (FTIR) spectra of $Li_2Sr_2Al_2PO_4F_9$:Eu^{2+} phosphor, it is observed that the active vibration modes between 400 and 1,400 cm^{-1} were ascribed to tetrahedral PO_4 anions and no pyrophosphate (P_2O_7) group, a typical band appearing at 1,265–1,267 cm^{-1} impurity could be detected. Besides, there are small fundamental H_2O vibration modes which appeared at corresponding band 1,560 cm^{-1} and but not at 3,400 cm^{-1}, because the samples were prepared via wet chemical synthesis in which water plays a vital role and heated at relatively high temperature. The FTIR spectra of $Li_2Sr_2Al_2PO_4F_9$:Eu^{2+} display only the characteristic bands of the orthophosphates. The main couple of absorption peaks is characteristics of the vibrations of phosphate groups at 563 cm^{-1} for bending vibration (v4) and at 1,050 cm^{-1} for stretching vibration (v3). As expected, this shows that there are no organic impurities in the final compositions [48]. The morphology of the $Li_2Sr_2Al_2PO_4F_9$:Eu^{2+} nanophosphor was also analyzed using TEM as shown in Fig. 7.39. It can be seen that the $Li_2Sr_2Al_2PO_4F_9$:Eu^{2+} nanophosphor has spherical and uniform morphology with a diameter of 26–50 nm. Since nanoparticles have relatively large surface areas, they tend to agglomerate to minimize the total surface energy.

7.6.2.2 PL Studies of $Li_2Sr_2Al_2PO_4F_9$:Eu^{2+} Nanophosphor

The PL excitation and emission spectra of the $Li_2Sr_2Al_2PO_4F_9$:Eu^{2+} phosphor are shown in Fig. 7.40. It can be seen from Fig. 7.40 that the PL excitation spectrum shows a broad absorption band observed at 355 nm, which can be assigned to the f–d transition of Eu^{2+}. The PL emission spectra exhibit a broad blue emission band peaking at 430 nm and there are two shoulders at the lower energy side. The broad band emission is the characteristic of the allowed d–f transition of Eu^{2+} ions. The results show that the phosphor has the highest emission intensity at 0.5 mol% of Eu^{2+}, which should be considered as the quenching concentration. $Li_2Sr_2Al_2PO_4F_9$:Eu^{2+} shows broad and intense blue emission originating from the $4f^65d^1 \rightarrow 4f^7$ electronic transition of Eu^{2+} with a peak at 430 nm and a full-width at half-maximum about 100 nm. In prepared $Li_2Sr_2Al_2PO_4F_9$:Eu^{2+} nanophosphor, the Eu^{2+} ion in the Sr^{2+} site would yield emission with higher energy than that in the Al^{3+} or Li^+ site. The reasons are as follows: (i) the Sr^{2+} is divalent and Al^{3+} is trivalent, whereas Li^+ is monovalent, so Sr^{2+} shares two electrons, Al^{3+} shares three electrons and Li^+ shares only one electron; (ii) the ionic radii of Al^{3+} (0.050 nm) and Li^+ (0.068 nm) are smaller than Sr^{2+} (0.113 nm) which result in weaker crystal-field strength. Therefore, the emission at 430 nm can be assigned to the emission of Eu^{2+} at Sr^{2+} site and the 592 and 615 nm shoulders come from the Al^{3+} site Eu^{3+} emission. In addition, the low intensity of the emissions at 592 and 615 nm may be because the Eu^{2+} preferentially takes the Sr^{2+} site. The emission intensity depends on the excitation wavelength.

The 430 nm PL emission peak intensity is observed to be maximum at the excitation wavelength of 355 nm as compared to emission intensity when excited at 345 and 380 nm. The small Eu^{3+} emissions peaks are observed at 592 and 615 nm due to some of the Eu ions which are shifted to symmetry crystal lattice during the synthesis of materials, but Eu^{3+} emissions in the red region of the spectrum are very low in intensity as compared to the blue emission; therefore, the total light output from the prepared materials can be considered in the blue region of the spectrum. The emission intensity of the blue emission increased with an increasing Eu^{2+} concentration to 0.5 mol%, and decreased with further increase in Eu^{2+} concentration. As shown in Fig. 7.40, the emission spectra showed the presence of a broad band, whose broadness indicates the existence of an interaction between the host and activator. This was attributed to the presence of excited electrons in the outer shell of the Eu^{2+} ions. The probability of energy transfer between Eu^{2+} ions increased with an increasing Eu^{2+} concentration. Nonradiative energy transfer from one Eu^{2+} ion to another usually occurs as a result of an exchange interaction, radiation re-absorption, or a multipole–multipole interaction [49]. In the case of Eu^{2+} ions, the $4f^7 \rightarrow 4f^6 5d^1$ transition is allowed, while the exchange interaction is responsible for energy transfer of the

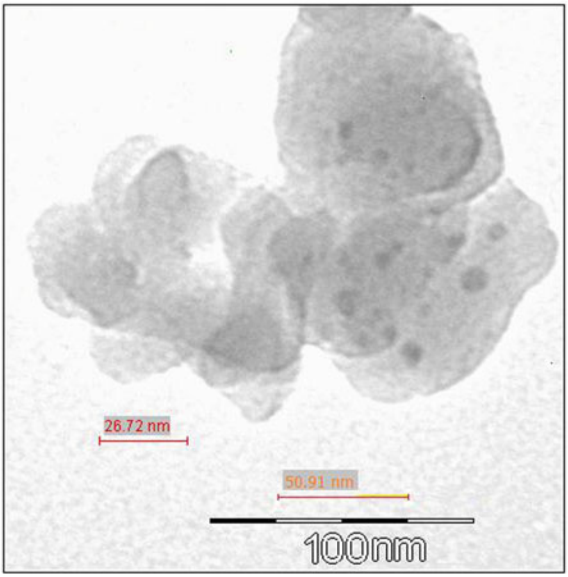

Fig. 7.39 Typical TEM of nano the $Li_2Sr_2Al_2PO_4F_9$:Eu^{2+} powders

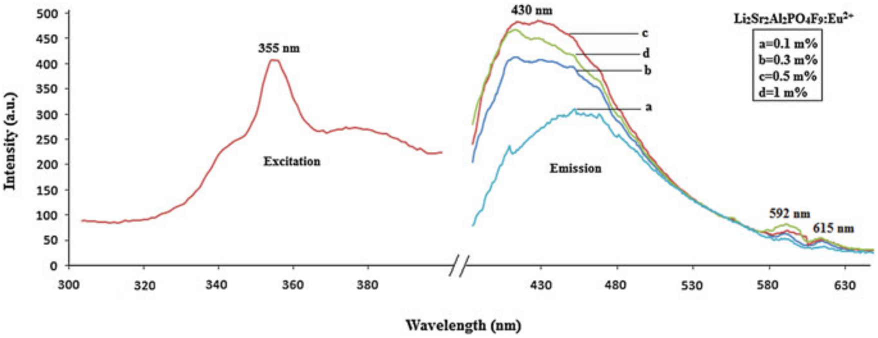

Fig. 7.40 PL emission and excitation spectra of the $Li_2Sr_2Al_2PO_4F_9$:Eu^{2+} nanophosphor monitored at the excitation wavelength of 355 nm and emission wavelength of 430 nm, respectively

forbidden transitions. As the concentration of Eu^{2+} increases, the distance between Eu^{2+} ions becomes short and the probability of energy transfer between Eu^{2+} ions increases. It is a remarkable achievement to obtain the high PL intensities in the as-precipitated powders without any thermal treatment except that needed for the drying process.

7.7 Conclusions

A Eu^{2+} activated $Li_2Sr_2Al_2PO_4F_9$ phosphor was successfully prepared by the one-step wet chemical synthesis method. XRD data of the final compound show no XRD lines of any of the starting compounds. The formation of the $Li_2Sr_2Al_2PO_4F_9$ compound was confirmed by XRD characteristics, and the FTIR data also show good agreement with the XRD results. The broad nature of the XRD patterns and the TEM observation shows an average diameter of the crystallites of the phosphor around 50 nm. The prepared phosphor exhibited intense blue emission at the 430 nm due to the Eu^{2+} ion by Hg-free excitation at 355 nm; it is a characteristic of solid-state lighting materials. All these characteristics show that the Eu^{2+} activated $Li_2Sr_2Al_2PO_4F_9$ phosphor may be one of the efficient blue component for low-energy consumption solid-state lighting and white LEDs. The results presented here show that $Li_2Sr_2Al_2PO_4F_9$ host deserves further attention and efficient phosphors may be synthesized in future by suitable combinations of activators. In this regard, the target product is a very promising phosphor. Moreover, the synthesis method is a simple low cost technique that can be readily extended to other RE phosphates.

7.8 New $Li_2Sr_2Al_2PO_4F_9$:Dy^{3+} Nanophosphor by One-Step Wet Chemical Synthesis [50]

7.8.1 Experimental

A novel $Li_2Sr_2Al_2PO_4F_9$:Dy^{3+} nanophosphor was synthesized by the one-step wet chemical synthesis technique. The preparation method is pursued as for that previously reported [51]. Ingredient chlorides with stoichiometric ratios are dissolved in double-distilled deionized water in a glass beaker (Borosil) and are allowed to evaporated till the mixture becomes anhydrous. Use of chlorides as starting materials helps preventing the hydrolysis. Materials were prepared according to the chemical formula $Li_2Sr_{2-x}Al_2PO_4F_9$:Dy_x. Diluted HNO_3 soluble in Dy_2O_3 was then added to the solution to obtain $Li_2Sr_{2-x}Al_2PO_4F_9$:Dy_x^{3+}. In this formula, the x-value indicates the concentration of the Dy impurity in the 0.1–1 mol%. It is confirmed that no undissolved constituents were left behind and all the chemicals had completely dissolved in water. The compound $Li_2Sr_2Al_2PO_4F_9$:Dy^{3+} in their powder form was obtained by allowing evaporating at 120 °C for 8 h. The dried samples were then slowly cooled to room temperature. The resultant nanocrystalline powder was crushed to fine particles in a crucible. After annealing the prepared phosphor at 600, 900, and 1,200 °C powder was used for further study.

7.8.2 Results and Discussion

7.8.2.1 XRD and TEM Studies

XRD of $Li_2Sr_2Al_2PO_4F_9$ host material is shown in Fig. 7.41. The final product was formed in nanocrystalline and homogeneous form, because the XRD pattern did not show the presence of the starting materials and other likely phases which is an indirect evidence for the formation of the desired compound. Moreover, the pattern (Fig. 7.41) pretty resemblance with previous work [51]. The obtained products are of high purity and crystallinity when prepared by the one-step wet chemical method. The XRD spectra exhibit broadened diffraction peaks indicating the nanocrystalline nature. The small amount of doped rare-earth ions has virtually no effect on the phase structures. There are no characteristic peaks originating from the dopants or minor phases. This signifies that the incorporation of Dy^{3+} ion into the $Li_2Sr_2Al_2PO_4F_9$ lattice does not cause any significant change to the crystal structure of the host matrix. All relatively sharp diffraction peaks can be perfectly indexed to the high purity and high crystallinity of $Li_2Sr_2Al_2PO_4F_9$. Besides, there are considerable broadenings in the XRD lines, which are owing to the reduction in the grain sizes. No more data related to this phosphor are available in the literature.

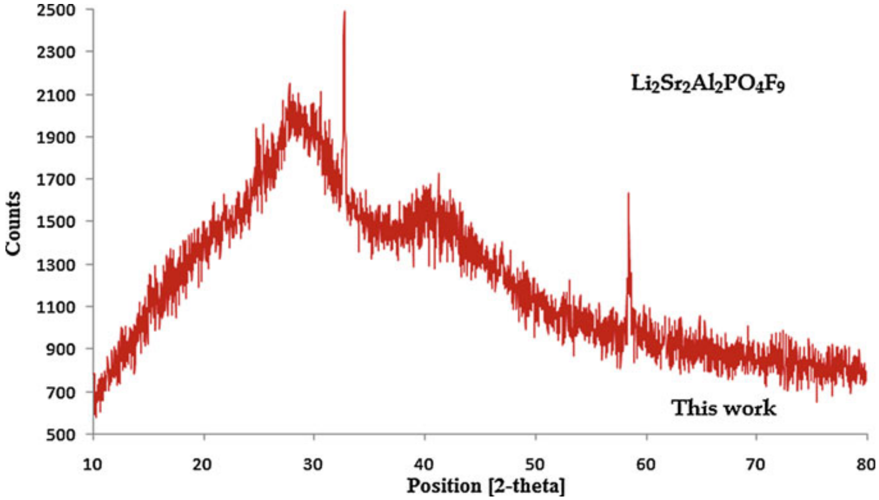

Fig. 7.41 XRD of the $Li_2Sr_2Al_2PO_4F_9$ host lattice

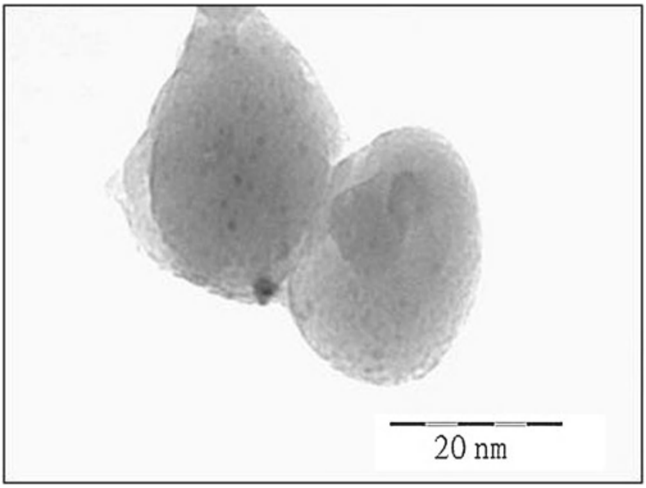

Fig. 7.42 TEM of the $Li_2Sr_2Al_2PO_4F_9{:}Dy^{3+}$ nanophosphor

The morphology of the $Li_2Sr_2Al_2PO_4F_9{:}Dy^{3+}$ nanophosphor was also analyzed using TEM as shown in Fig. 7.42. It can be seen that the $Li_2Sr_2Al_2PO_4F_9{:}Dy^{3+}$ nanophosphor has spherical and uniform morphology with a diameter of near 20 nm. Since nanoparticles have relatively large surface areas, they tend to agglomerate to minimize the total surface energy. Thus, nanoparticles of fluorides involving three components that are successfully prepared by the wet chemical method. The nanoparticles are homogeneous, which could be conveniently used for coating purpose during the manufacture of solid-state lighting.

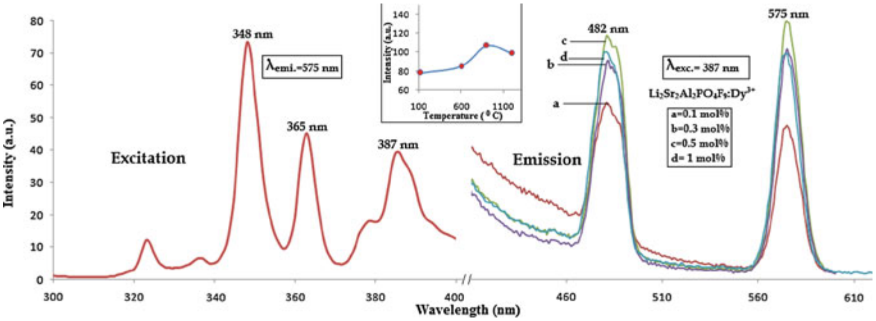

Fig. 7.43 PL emission spectra of the $Li_2Sr_2Al_2PO_4F_9:Dy^{3+}$ nanophosphor under $\lambda_{exc.} = 387$ nm and the excitation spectra by monitoring the emission wavelength at 575 nm. The effect of the temperature on the emission intensity (Peak c for $Dy^{3+}_{0.5\,mol\%}$) is shown as an inset

7.8.2.2 PL Properties of $Li_2Sr_2Al_2PO_4F_9:Dy^{3+}$ Nanophosphor

The Dy ion with a $4f^9$ configuration has complicated f-block energy levels and between these levels various transitions result in sharp line spectra [52–54]. The excitation spectra of the $Li_2Sr_2Al_2PO_4F_9:Dy^{3+}$ nanophosphors monitored at 575 nm are shown in Fig. 7.43. There are some sharp absorption peaks in the 300–400 nm wavelength region, which are due to excitation of the $f-f$ shell transitions of Dy^{3+} [54]. The several band peaks at 348, 365, and 387 nm correspond to the transitions from the ground state $^6H_{15/2}$ to the excited states $^4P_{7/2}$, $^4P_{3/2}$, and $^4F_{7/2}$ respectively, and the maximum excitation wavelength is located at 348 nm. The excitation curve at 387 nm is near the UV excitation which is more applicable (i.e. 385–395 nm) for LED phosphors. Accordingly, out of all peaks the 387 nm peak was selected for the excitation in this work.. The emission spectrum is also shown in Fig. 7.43. All the samples have two emission bands: one is centered at 482 nm (blue) and another is centered at 575 nm (yellow). They are assigned to the Dy^{3+} electronic transitions of the $^4F_{9/2} \rightarrow {}^6H_{15/2}$ and $^6H_{13/2}$ energy levels, respectively. A series of $Li_2Sr_{2-x}Al_2PO_4F_9:Dy_x$ phosphor with various Dy^{3+} concentrations ($x = 0.1 - 1$ mol %) were prepared and the effect of the doped Dy^{3+} concentration on the emission intensity was investigated.

It is known that Dy^{3+} emission around 482 nm ($^4F_{9/2} \rightarrow {}^6H_{15/2}$) is of magnetic dipole origin and 575 nm ($^4F_{9/2} \rightarrow {}^6H_{13/2}$) is of electric dipole origin. $^4F_{9/2} \rightarrow {}^6H_{15/2}$ is predominant only when Dy^{3+} ions are located at low-symmetry sites with no inversion centers [55]. The low-symmetry location of Dy^{3+} results in the predominate emission of $^4F_{9/2} \rightarrow {}^6H_{13/2}$ transition. Since emission at 575 nm is predominant, it suggests that there is a very little deviation from inversion symmetry in this matrix. The optical properties of the materials are often influenced by the structure of the matrix and synthesis technique [56]. Thus, the yellow–blue ratio, known as the asymmetry ratio of Dy^{3+}, varies while locating in different host lattices. Kuang et al. [57] reported that, in the Dy^{3+} doped $SrSiO_3$ system, with increasing calcining temperature, the yellow–blue ratio increased due to the change in the local site symmetry around the Dy^{3+} ion. In our case, it is clearly observed that the fluorescence intensities ratio increases gradually. Different doping of activator ions can influence PL characteristics of a phosphor. Usually, a low doping gives weak luminescence, but excess doping can cause quenching of luminescence. With increasing concentration of Dy^{3+} ions, the peak intensity increased and maximum intensity was observed for 0.5 mol% Dy^{3+} ion. The increase in the luminescence intensity with an increase in concentration of the Dy ion can be explained as follows: the luminescence spectrum of Dy^{3+} ion was slightly influenced by the surrounding ligands of the host material, because electronic transitions of Dy^{3+} involve only redistribution of electrons within the inner $4f$ subshell. Crystallinity of the phosphor could be increased due to the increase in concentration of the Dy ion, since clearly the addition of Dy ion into the $Li_2Sr_2Al_2PO_4F_9$ host increased the crystallinity. An increase in the concentration of Dy ions increased the particle size as well as its complexity. Hence, there was an increase in PL intensity. This indicates that the $Li_2Sr_2Al_2PO_4F_9$ lattice is more suitable for higher concentrations of Dy^{3+} ions. Figure 7.43 (inset) compares the emission intensities of $Li_2Sr_2Al_2PO_4F_9{:}Dy^{3+}_{0.5\,\mathrm{mol\%}}$ at various temperatures i.e., as-synthesized, 600, 900, and 1,200 °C. When the temperature increases, the emission intensity also increases and it reaches a maximum at 900 °C. When the temperature further increases above 900 °C, the emission intensity begins to decrease because the resonance between the activator is increased with increasing the particle size, so that the crystal surface acts as quenching centers [58]. As the calcinating temperature increases to 1,200 °C, neither appreciable changes in the intensity were observed nor were peak positions influenced by temperature.

Most lighting specifications refer to color in terms of the 1931 CIE chromatic color coordinates which recognizes that the human visual system uses three primary colors: red, green, and blue [59, 60]. In general, the color of any light source can be represented on the (x, y) coordinates in this color space. The color purity was compared to the 1931 *Commission Internationale de l' Éclairage* (CIE) Standard Source C (illuminant Cs (0.3101, 0.3162)). The chromatic coordinates (x, y) were calculated using the color calculator program radiant imaging [61]. The coordinates of the $Li_2Sr_2Al_2PO_4F_9{:}Dy^{3+}$ phosphor of color blue ($x \approx 0.0826$, $y \approx 0.1568$), yellow ($x \approx 0.4787$, $y \approx 0.5202$) phosphor are shown in Fig. 7.44 by solid circle sign (•). The location of the color coordinates of the $Li_2Sr_2Al_2PO_4F_9{:}Dy^{3+}$ phosphate phosphor powder on the CIE chromaticity diagram presented in Fig. 7.44 indicates that the color properties of the phosphor powder prepared by wet chemical method are approaching those required for field emission displays. The dominant wavelength is defined as the single monochromatic wavelength that appears to have the same color as the light source. The dominant wavelength can be determined by drawing a straight line from one of the CIE white illuminants (Cs (0.3101, 0.3162)), through the (x, y) coordinates to be measured, until the line intersects the outer locus of points along the spectral edge of the 1931 CIE chromatic diagram.

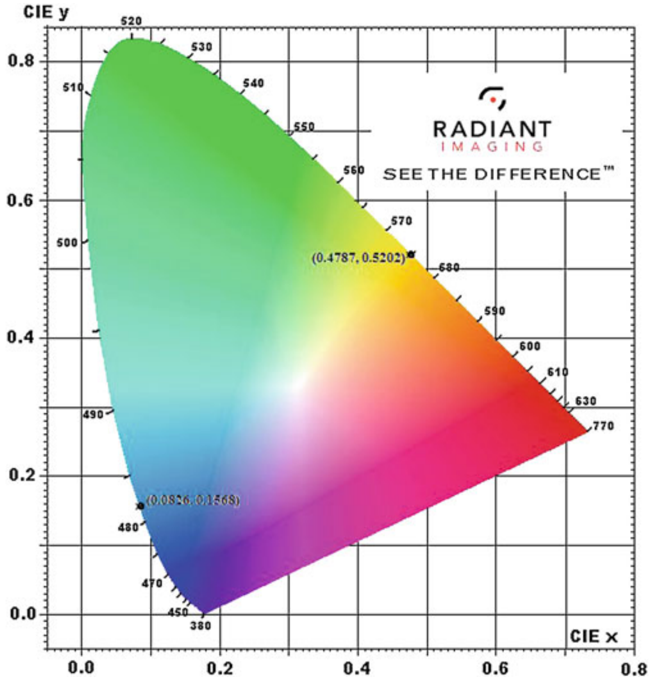

Fig. 7.44 CIE chromatic diagram showing the chromatic coordinates for $Li_2Sr_2Al_2PO_4F_9$:Dy^{3+}

All the results calculated from the spectra in Fig. 7.43 are plotted in the CIE 1931 chromaticity diagram, as shown in Fig. 7.44. It indicates that Dy^{3+} doped $Li_2Sr_2Al_2PO_4F_9$ are close to the edge of the CIE diagram, which indicates the high color purity of this phosphor. By connecting these two points in the form of a triangle (included white light point (0.31, 0.32)) the intermediate compositions can generate white light with a particular ratio of this phosphor.

7.9 Conclusions

A $Li_2Sr_2Al_2PO_4F_9$:Dy^{3+} novel nanophosphor was synthesized by one-step wet chemical method and the formation was confirmed by XRD.TEM shows spherical and uniform morphology with a diameter of near 20 nm.The emission spectrum of $Li_2Sr_2Al_2PO_4F_9$:Dy^{3+} (at 387 nm excitation) has two intense broad bands centered at 482 and 575 nm, which correspond to the blue and yellow regions of the visible spectrum, respectively. These two emissions could be used for the development of white LEDs. Development of such novel nanophosphor could be a valuable technological achievement.

7.10 Blue Emitting $Na_2Zn(PO_4)Cl$:X (X = Eu^{2+} & Cu^+) Halophosphors [62]

7.10.1 Experimental

The Eu and Cu-doped Na_2 $Zn(PO_4)$ Cl novel phosphors were prepared via facile combustion synthesis. The starting materials were nitrates of analytical grade with urea as fuel. In the present investigation, materials were prepared according to the chemical formula $Na_2Zn_{1-y}(PO_4)Cl:X_y$ (where X = $Eu_{y=0.1-1\,\text{mol\%}}$ and $Cu_{y=0.01-0.1\,\text{mol\%}}$). Eu and Cu-doped $Na_2Zn(PO_4)$ Cl novel phosphors were prepared as per recipe of previous work [19]. Some complementary methods were used to characterize the prepared phosphor.

7.10.2 Results and Discussion

Figure 7.45 gives the XRD patterns of the $Na_2Zn(PO_4)Cl$ material. The obtained diffraction peaks of all compounds do not match any data in the JCPDS base after careful comparison with the reported compounds for the obtained phase; it is carefully observed that there are no peaks of raw materials. It is found that the main phase does not agree to any JCPDS available. Consequently, it is speculated that the obtained unknown phase is likely to be a new phase.

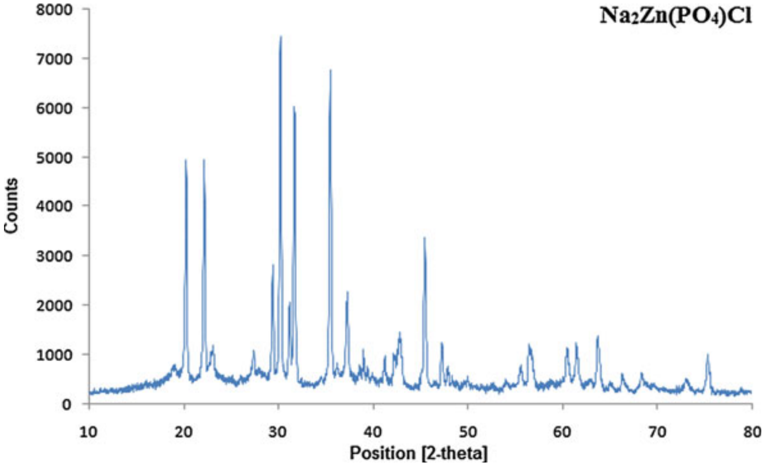

Fig. 7.45 XRD pattern of the $Na_2Zn(PO_4)Cl$ material

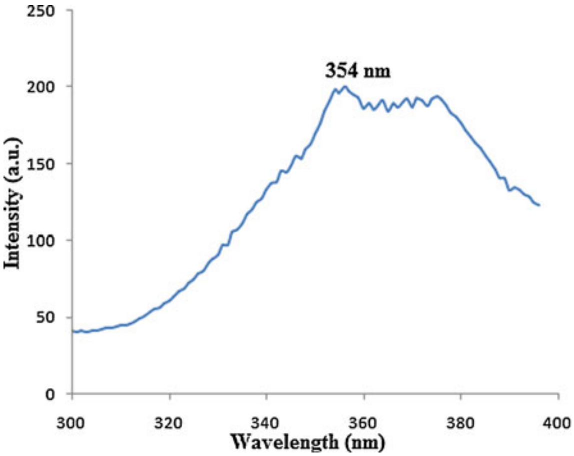

Fig. 7.46 Excitation of $Na_2Zn(PO_4)Cl:Eu^{2+}$ monitored at 450 nm

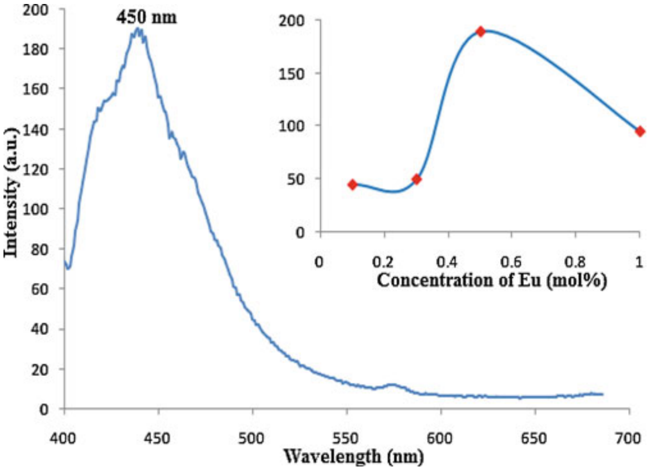

Fig. 7.47 Emission of $Na_2Zn(PO_4)Cl:Eu^{2+}$, when excited at 354 nm

7.10.3 PL Properties of $Na_2Zn(PO_4)Cl:X$ ($X = Eu^{2+}$ and Cu^+) Phosphor

PL excitation and emission spectrum of the Eu^{2+} activated $Na_2Zn(PO_4)Cl$ phosphors are shown in Figs. 7.46 and 7.47, respectively. The emission spectrum of the $Na_2Zn(PO_4)$ Cl:Eu^{2+} has a prominent peak at around 450 nm that can be well assigned to Eu^{2+} emission arising from transitions of the 5*d* configuration to the 4*f* level of the Eu^{2+} ion. Observed emission peaks arise from the PL intensity increases with an increase in the concentration from 0.1 to 1 mol% (inset Fig. 7.47). Concentration quenching effect is observed for more than 0.5 mol% of the Eu^{2+} ion. The prepared phosphors show an efficient broad band blue (450 nm) emission, which originates from the transitions of the $4f^65d$ configuration to the $8S_{7/2}$ level of the $4f_7$ configuration of the Eu^{2+} ion. The PL excitation and emission spectrum of the Cu^+ activated $Na_2Zn(PO_4)$ Cl phosphor shown in Figs. 7.48 and 7.49, respectively. In this case, the PL emission spectra of the Cu^+ ions in the $Na_2Zn(PO_4)$ Cl phosphors with different concentration were obtained under an excitation wavelength of 354 nm. The peak is observed at 470 nm which is assigned to the $3d^94s \longleftrightarrow 3d^{10}$ transitions of the Cu^+ ions. With increasing concentration of the Cu^+ ions the peak intensity increases and a maximum intensity is observed for 0.05 mol% of Cu^+ ions (inset Fig. 7.49). This indicates that the $Na_2Zn(PO_4)$ Cl lattice is more suitable for the higher concentrations of the Cu^+ ions. The 300–400 nm is Hg free excitation (Hg excitation is 85% at a 254 nm wavelength of light and 15 % to other wavelengths), which is the characteristic of solid-state lighting phosphors. Hence, PL emission in divalent Eu and Cu may be efficient PL materials for solid-state lighting phosphors as a blue component.

7.11 Conclusions

It is concluded that, Eu and Cu activated $Na_2Zn(PO_4)Cl$ novel phosphors were synthesized by facile combustion method and confirmed by XRD. The excitation spectra of the both phosphors are broad band extending from 300 to 400 nm, which are characteristics of near UV excited LEDs. Results of these phosphors show that near UV excitation and blue emission make this material a candidate for the blue component of a phosphor blend for the solid-state lighting.

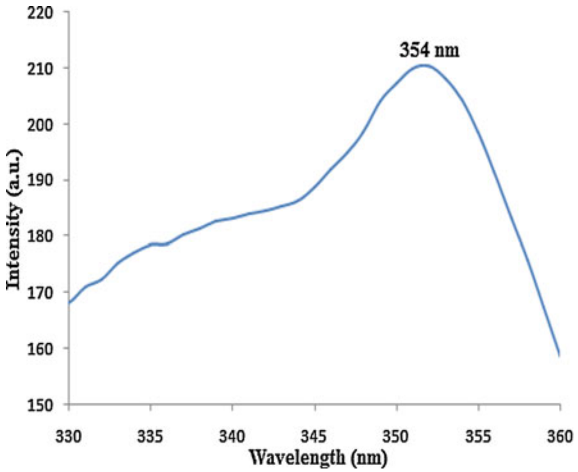

Fig. 7.48 Excitation of $Na_2Zn(PO_4)Cl:Cu^+$, monitored at 470 nm

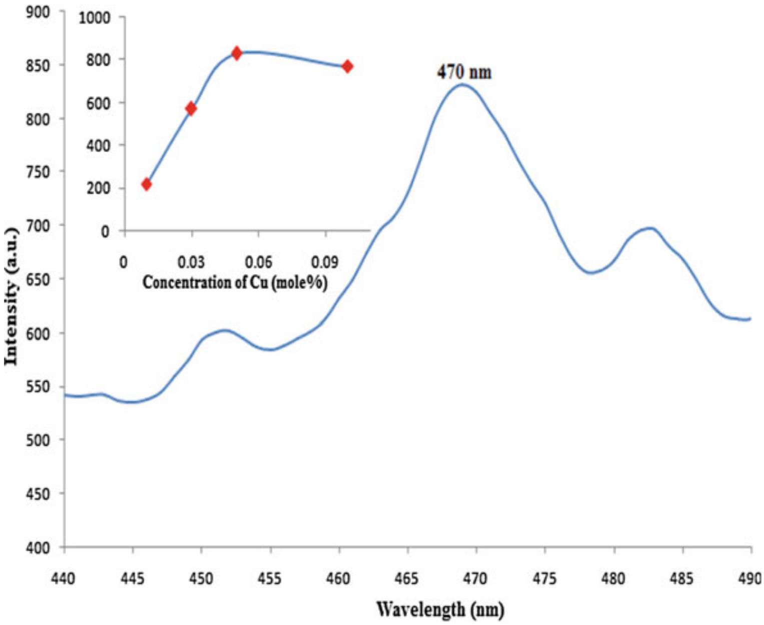

Fig. 7.49 Emission of $Na_2Zn(PO_4)Cl$:Cu^+, when excited at 354 nm

7.12 Novel Redish-Orange Emitting $NaLi_2PO_4$:Eu^{3+} Phosphors [63]

7.12.1 Experimental

The Eu-doped $NaLi_2PO_4$ phosphate phosphors were synthesized by the solid-state reaction. The starting materials, Na_2CO_3, Li_2 CO_3 and $NH_4H_2PO_4$, were of analytical grade (pure). These materials were weighed in the proper molar ratio and then Eu_2O_3 was introduced as a dopant, followed by mixing and grinding homogeneously in an agate mortar. The mixture was heated at 500 °C in a silica crucible for 2 h. The vapors extraneous to the desired product that was evolved during the process was allowed to be released. After grinding, the mixture was heated at 800 °C for 24 h, thereby obtaining the white phosphor powder.

7.12.2 Results and Discussion

Figure 7.50 shows the XRD pattern of $NaLi_2PO_4$ and it agrees well with ICDD No. 80-2110. This shows that the final product was formed in crystalline, homogeneous form, and that the solid-state reaction of the mixtures took place well.

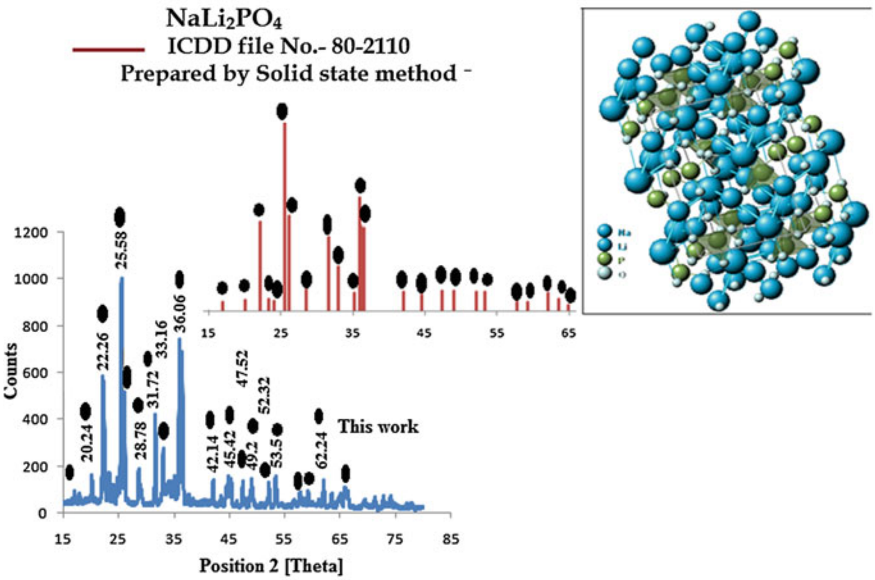

Fig. 7.50 XRD of prepared $NaLi_2PO_4$ host lattice and the crystal structure of Nalipoite (inset) [64]

$NaLi_2PO_4$ has an orthorhombic crystal structure (nalipoite) and its lattice parameter values are $a = 0.69\,\text{nm}$, $b = 1\,\text{nm}$ and $c = 0.4938\,\text{nm}$ [64]. It is important to note that the XRD pattern of the phosphor sample (Fig. 7.50) is devoid of the reflections of starting materials, which is a clear indication of an excellent homogeneous form the $NaLi_2PO_4$ lattice achieved by the high temperature solid-state reactions. It was observed that the small amount of doped Eu^{3+} ions has virtually no effect on phase structures. There are no characteristic peaks originating from the dopant or minor phases. This signifies that the incorporation of Eu^{3+} ion into the $NaLi_2PO_4$ lattice does not cause any significant change to the crystal structure of the host matrix.

7.12.3 PL Properties of $NaLi_2PO_4$:Eu^{3+} Phosphor

Figure 7.51 represents the PL excitation spectrum of $NaLi_2PO_4$:Eu^{3+} with the detected wavelength of 594 nm. A broad excitation centered at 250 nm is attributed to the charge transfer band (CTB) of Eu–O in $NaLi_2PO_4$ host. The narrow excitation lines appeared at longer wavelengths correspond to the characteristic $f \rightarrow f$ transitions of Eu^{3+}. These lines are assigned as follows: $^7F_0 \rightarrow {}^5H_3$ (300 nm), $^7F_0 \rightarrow {}^5D_4$ (350 nm), $^7F_0 \rightarrow {}^5G_{2-6}$ (380 nm) and the main excitation line $^7F_0 \rightarrow {}^5L_6$ (393 nm). Figure 7.52 shows the PL emission spectrum of $NaLi_2PO_4$:Eu^{3+} obtained under the excitation of $\lambda_{exc} = 393\,\text{nm}$. The excitation of this phosphor is 393 nm which is far

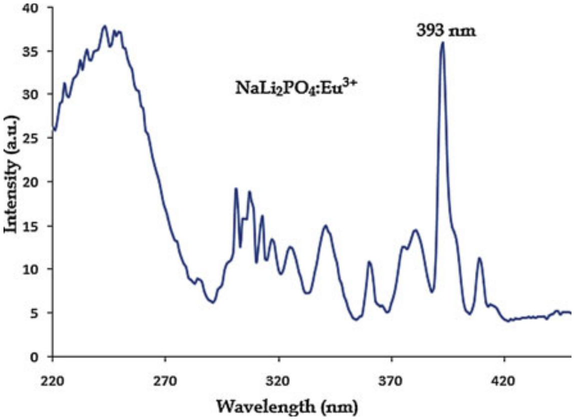

Fig. 7.51 PL excitation spectrum of NaLi$_2$PO$_4$:Eu^{3+} monitored at 594 nm

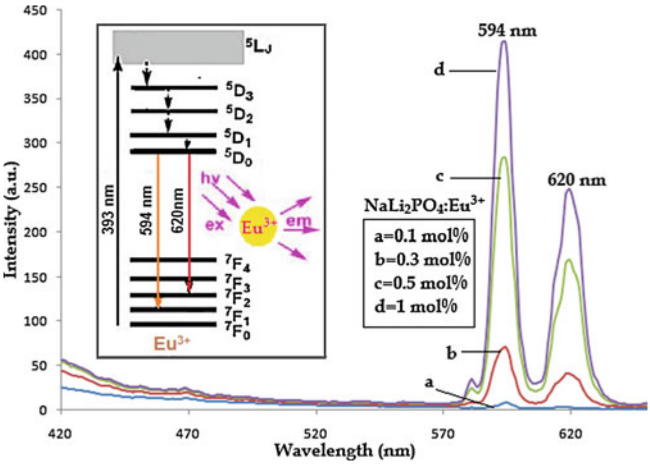

Fig. 7.52 PL emission spectrum of NaLi$_2$PO$_4$:Eu^{3+}, when excited at 393 nm (Energy level diagram in inset)

away from Hg excitation and this excitation is the main characteristic of solid-state lighting (i.e., in the range 365–395 nm near UV region) in the lamp industry. The excitation spectra show that these phosphors can be well excited by near UV-light which is exactly required by UV chip pumped multi-phosphor converted white LEDs. Therefore, this phosphor is one candidate of reddish orange phosphor for LED lighting. The strongest peak located at 594 nm contributes the orange-reddish emission, which is mainly from the $^5D_0 \rightarrow {}^7F_1$ magnetic dipole transitions of Eu^{3+}ions and the weak red emissions peaked at 620 nm is due to the hypersensitive $^5D_0 \rightarrow {}^7F_2$ electric dipole transition. Various emission intensities of NaLi$_2$PO$_4$:Eu^{3+} were shown in Fig. 7.52 against the concentration of Eu^{3+}. As we could see from this figure, the most intense peak was observed at a concentration of 1 mol%, and then the intensities decreased gradually due to the energy transfer between the neighboring Eu^{3+} ions, which was corresponding to the quench of the emission of Eu^{3+}. The results show that the phosphor has the highest emission intensity at 1 mol% of Eu^{3+}, which should be considered as the quenching concentration. The emission intensity is related to the concentration of the Eu^{3+} activator ions. With the increase of the concentration of the activator ion, the luminescent center increases and the emission intensity is enhanced. The highest luminescent intensity was obtained at Eu concentration of 1 mol% and lower or higher Eu contents results in a substantial decrease in emission intensity. The luminescence spectra depict the concentration of the activated elements, which increases as a result of the concentration quenching effect. At high concentration, the clustering of activator atoms may change a fraction of the activator into quenches, and may induce the quenching effect, this decreases the emission intensity. The quenching concentration is about 1 mol%. The oxygen vacancies might serve as a sensitizer for the energy transfer to the rare-earth ion due to the strong mixing of charge transfer states resulting in the highly enhanced luminescence [20]. But excess oxygen vacancies in the host would destroy the crystallinity inevitably, which lead to quenching of the luminescence [20]. After a careful observation without doped RE ions has virtually no effect on PL properties. There is no PL observed in the host material. This signifies that the incorporation of Eu^{3+} ion into the $NaLi_2PO_4$ lattice causes significant change to the PL property than the host matrix. The luminescent properties of the phosphors occur from the complex interaction among host structure, defects, activators, and interfaces. The charge unbalance and lattice distort could induce point defects in the structure, which would increase the nonradiative process that resulted in the reduction of luminescence intensity. For $NaLi_2PO_4{:}Eu^{3+}$ phosphors, therefore, the Eu^{3+} ions entered the host crystal lattice and preferentially substituted alkali metal ions i.e., Na^+ ions, which induced the charge unbalance and thus reduced the lattice distort, and enhanced the luminescent intensity.

The luminescence spectrum of Eu^{3+} ion is slightly influenced by the surrounding ligands of the host material, because the transitions of Eu^{3+} involve only a redistribution of electrons within the inner $4f$ subshell [65]. The transitions are found to be split into components depending on the host matrix composition. Figure 7.52 (inset) shows energy level diagram showing the states involved in the luminescence process and the transition probabilities for Eu^{3+} ions. According to that model, the system is first excited from the ground state to the singlet state of the $^5D_{3,2,1,0}$ configuration, and then the electrons pass to the triplet state, because of symmetry reasons. The last transition $^5D_0$ is so much faster than any other step of the luminescent process, which may be considered instantaneous; it follows that the singlet state does not affect the luminescent process. Nonradiative transitions may occur among $^5D_3$, $^5D_2$, $^5D_1$, and $^5D_0$ with probabilities from $^5D_3$ to $^5D_2$, from $^5D_2$ to $^5D_1$ and $^5D_2$to $^5D_0$. From level $^5D_0$ to level $^7F_{0,1,2,3}$ radiative transitions to the ground state $^5D_0 \rightarrow {}^7F_j$ states occur, respectively. The PL intensity of Eu^{3+} emission at 620 nm is less as compared to 594 nm peaks. The increase of PL emission intensity observed may be due to the decrease of cross-relaxation between Eu^{3+} ions (in this process, excited ion transfers only part of energy to another ion) in case of higher concen-

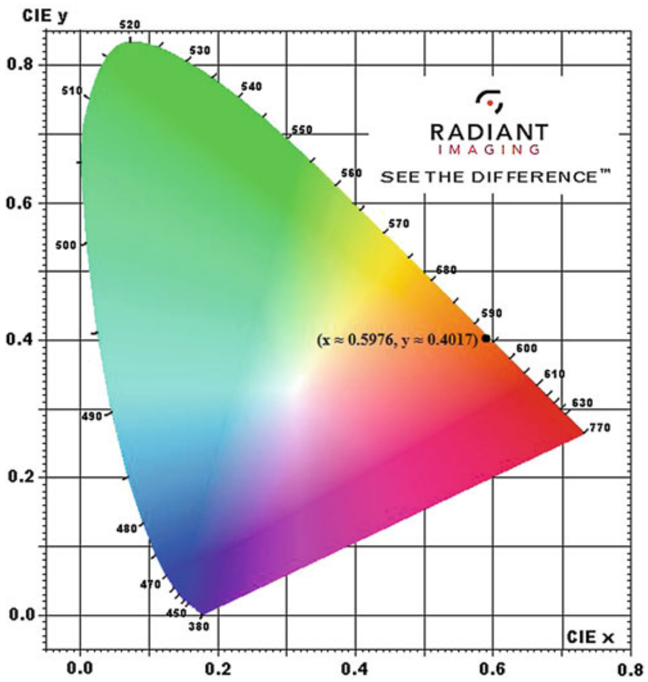

Fig. 7.53 CIE chromatic diagram showing the chromatic coordinates for $NaLi_2PO_4:Eu^{3+}$

tration of Eu^{3+}. The cross-relaxation is one-step transfer of part of the energy from excited donors to acceptors. The increased doping of Eu ions enhances the cross-relaxation, because the number of excited Eu ions increases by absorption. An excess of acceptors results in direct energy transfer from donor to acceptor. With an excess of donors, energy is transferred primarily by migration or hopping between donors until an acceptor is found. Cross-relaxation is a phonon-assisted process. Phonons can provide the additional energy to minimize the energy mismatch between coupled transitions.

$NaLi_2PO_4:Eu^{3+}$ of color red ($x \approx 0.5976$, $y \approx 0.4017$) phosphor is shown in Fig. 7.53 by solid circle (•). The color purity was compared to the 1931 CIE Standard Source C (illuminant Cs (0.3101, 0.3162)). The chromatic coordinates (x, y) were calculated using the color calculator program radiant imaging [61]. It indicates that Eu^{3+} doped $NaLi_2PO_4$ is close to the edge of CIE diagram, which indicates the high color purity of this phosphor. Hence, PL emission in trivalent Eu may be efficient PL materials for solid-state lighting phosphors as a red component and helpful to generate white light with a particular ratio of this phosphor.

7.13 Conclusions

A phosphate phosphor, $NaLi_2PO_4:Eu^{3+}$ was synthesized by a solid-state reaction method and formation of the compound was confirmed by XRD and matched well with ICDD no. 80-2110. The phosphor exhibits a strong and intense reddish orange emission under excitation of near UV (i.e. 393 nm). The critical concentration of the activator concentration (Eu^{3+}) was found to be 1 mol%. All the results indicate that this phosphor could be a good candidate as orange and red component in fabrication of phosphor-converted white LEDs.

7.14 Dy^{3+} and Eu^{3+} Activated $Na_2X(PO_4)F$ (X = Mg, Ca, Sr) Phosphors [66]

7.14.1 *Experimental*

The $Na_2X(PO_4)F:Dy^{3+}/Eu^{2+}$ $(X = \mathrm{Mg, Ca, Sr})$ phosphors were prepared via the combustion technique. The starting AR grade materials (99.99 % purity) taken were sodium nitrate ($Na(NO_3)_2{\cdot}4H_2O$), magnesium nitrate ($Mg(NO_3)_2$), calcium nitrate ($Ca(NO_3)_2$), strontium nitrate ($Sr(NO_3)_2$), di-ammonium hydrogen phosphate ($NH_4H_2(PO_4)$), ammonium fluoride (NH_4F), dysprosium oxide (Dy_2O_3), Eu oxide (Eu_2O_3), and urea (NH_2CONH_2) was used as fuel for combustion. In the present investigation, materials were prepared according to the chemical formula $Na_{2(1-x)}X(PO_4)F:Dy_x$. The mixture of reagents was mixed together to obtain a homogeneous solution. Dy^{3+} ion was introduced in the form of $Dy(NO_3)_3$ solution by dissolving Dy_2O_3 into HNO_3 solution. The molar ratio of Dy rare-earth ion was changed in relation to $Na_2Mg(PO_4)F$, $Na_2Ca(PO_4)F$ and $Na_2Sr(PO_4)F$ phosphors. The compositions of the metal nitrates (oxidizers) and urea (fuel) were calculated using the total oxidizing and reducing valencies of the components, which served as the numerical coefficients, so that the equivalent ratio is unity and the maximum heat liberated during combustion. After stirring for about 15 min, precursor solution was transferred to a furnace preheated to 500–600 °C and the porous products were obtained. Large amounts of escaping gases dissipate heat and prevent the material from sintering, and thus provide conditions for formation of crystalline phase.

The combustion reaction can be described as follows:

$$\mathbf{2Na(NO_3)_3{\cdot}4H_2O + Mg(NO_3)_2 + NH_4H_2(PO_4) + NH_4F + NH_2CONH_2 \rightarrow Na_2Mg(PO_4)F + 8N_2 + CO_2 + 13H_2O}$$

$$\mathbf{2Na(NO_3)_3{\cdot}4H_2O + Ca(NO_3)_2 + NH_4H_2(PO_4) + NH_4F + NH_2CONH_2 \rightarrow Na_2Ca(PO_4)F + 8N_2 + CO_2 + 13H_2O}$$

$$\mathbf{2Na(NO_3)_3{\cdot}4H_2O + Sr(NO_3)_2 + NH_4H_2(PO_4) + NH_4F + NH_2CONH_2 \rightarrow Na_2Sr(PO_4)F + 8N_2 + CO_2 + 13H_2O}$$

Several complementary methods were used to characterize the properties of the prepared samples.

7.14.2 Results and Discussion

7.14.2.1 X-ray Diffraction Pattern of $Na_2X(PO_4)F$ (X = Mg, Ca, Sr)

The crystalinity and purity of the samples are studied by XRD. Figure 7.54 shows the XRD pattern of $Na_2Ca(PO_4)F$ phosphors that well matched with the standard JCPDS file number 033–1222. Figures 7.55 and 7.56 show the X-ray diffraction patterns of the polycrystalline $Na_2Mg(PO_4)F$ and $Na_2Sr(PO_4)F$ materials, respectively. The $Na_2Mg(PO_4)F$ and $Na_2Sr(PO_4)F$ phosphors are prepared for first time; therefore, the XRD standard data are not available in JCPDS files. The X-ray diffraction pattern indicates presence of crystalline host lattice with less than 5 % as a foreign phase like presence of the constituents nitrate and traces of ammonia gases, which is an indirect evidence for the formation of the desired compound.

7.14.2.2 Dy^{3+} Luminescence in $Na_2X(PO_4)F$ (X = Mg, Ca, Sr)

Dy^{3+} ion in $Na_2X(PO_4)F$ phosphor gives blue, yellow and red emission bands. Figure 7.57 shows the PL excitation spectrum of Dy activated $Na_2X(PO_4)F$ phosphor. The excitation spectrum in the range of 300–440 nm due to $f \rightarrow f$ transition of Dy^{3+} ion having several intensity peaks at 348, 363 and 385 nm which is assign due to $^6H_{15/2} \rightarrow {}^6M_{21/2}$ transition. Among this excitation, we choose 385 nm because it is suitable for solid-state lighting. Figure 7.58 shows PL emission spectrum of the Dy

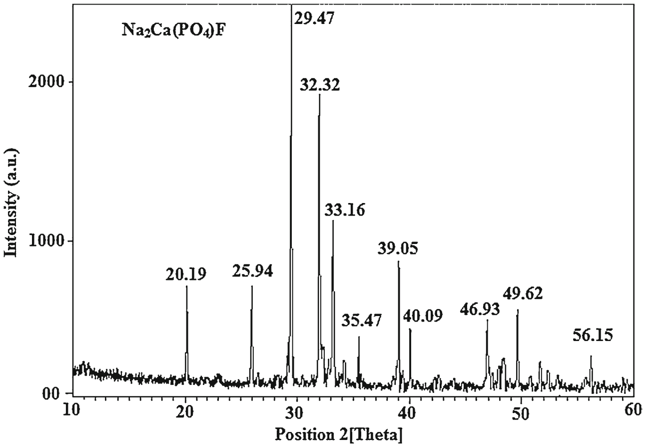

Fig. 7.54 X-ray diffraction pattern of $Na_2Ca(PO_4)F$

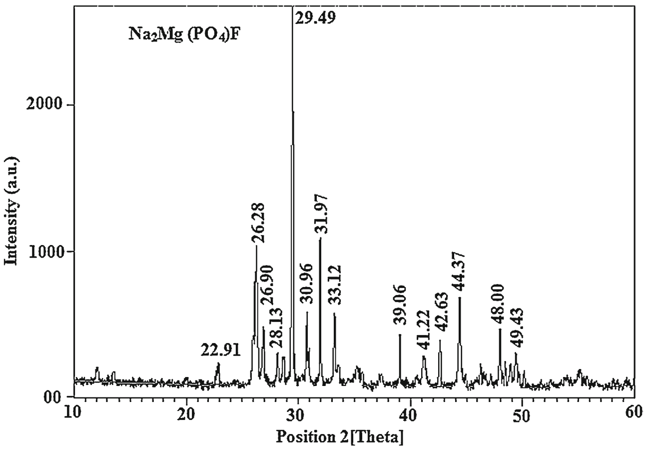

Fig. 7.55 X-ray diffraction pattern of $Na_2Mg(PO_4)F$

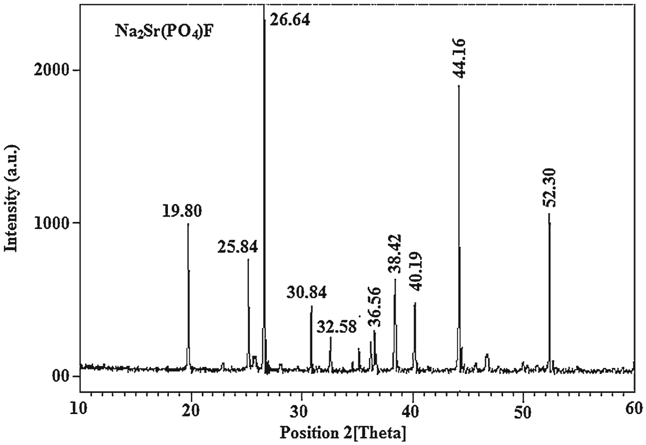

Fig. 7.56 X-ray diffraction pattern of $Na_2Sr(PO_4)F$

activated $Na_2Mg(PO_4)F$ phosphor, Fig. 7.59 shows PL emission spectrum of the Dy activated $Na_2Ca(PO_4)F$ phosphor and Fig. 7.60 shows PL emission spectrum of the Dy activated $Na_2Sr(PO_4)F$ phosphor. The excitation spectrum monitored at yellow emission of Dy^{3+} ion indicates several bands.

The emission spectra for the Dy^{3+} ions in $Na_2Mg(PO_4)F$ and $Na_2Ca(PO_4)F$ phosphor give emission peaks at 480 nm (blue), 574 nm (yellow) and a small peak at 670 nm (red). Where in, $Na_2Sr(PO_4)F$ phosphor gives prominent emissions at 482, 575, and 670 nm in blue, yellow, and red region of the spectrum, respectively. Three different emission bands are originated from the origin of same excitation wavelength. The transitions involved in blue, yellow, and red bands of Dy^{3+} ion are well-known. These bands have been identified as $^4F_{9/2} \rightarrow {}^6H_{15/2}$, $^6H_{13/2}$, $^6H_{11/2}$

Fig. 7.57 PL excitation spectrum of $Na_2Mg(PO_4)F:Dy^{3+}$ phosphor, monitored at 576 nm

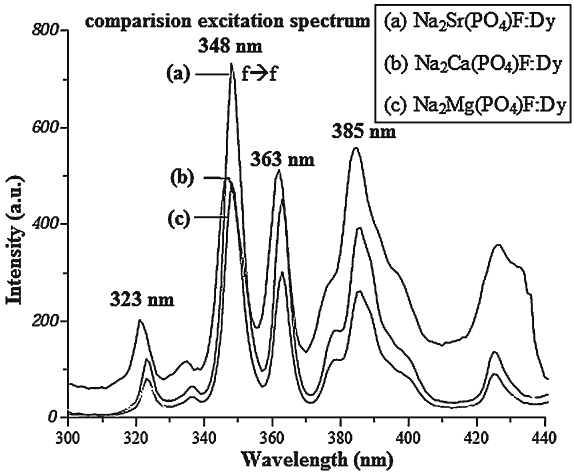

Fig. 7.58 PL emission spectrum of $Na_2Mg(PO_4)F:Dy^{3+}$ phosphor, when excited at 385 nm)

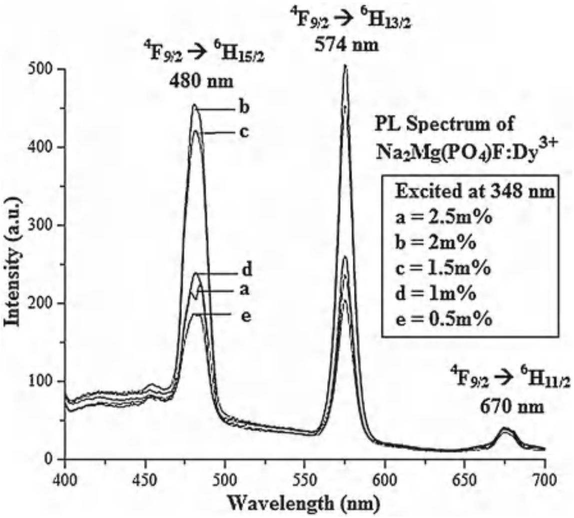

transitions [67]. It is known that Dy^{3+} emission around 480 nm ($^4F_{9/2} \rightarrow {}^6H_{15/2}$) is due to the magnetic dipole moment and 574 nm ($^4F_{9/2} \rightarrow {}^6H_{13/2}$) due to the electric dipole moment. The transition $^4F_{9/2} \rightarrow {}^6H_{13/2}$ is predominant only when Dy^{3+} ions are located at low-symmetry sites with no inversion centers [68]. The emission at 480 nm is predominant in $Na_2Ca(PO_4)F$ and the shoulder is at 485 nm. It suggests that there is little deviation from inversion symmetry in this matrix. However, in $Na_2Ca(PO_4)F$ predominant emission is around 480 nm suggesting that ligand field slightly deviates from its inversion symmetry.

A slight marginal shift in the peak position of Dy^{3+} ions is observed in all prepared phosphors. Such behavior is as expected for the emission involving $f \rightarrow f$ tran-

Fig. 7.59 PL spectrum of $Na_2Ca(PO_4)F:Dy^{3+}$ phosphor, when excited at 385 nm

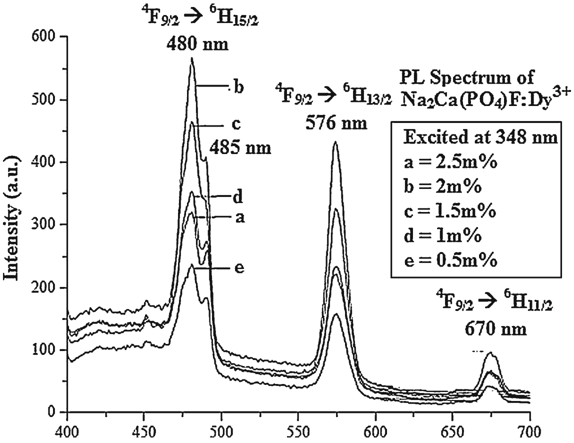

Fig. 7.60 PL spectrum of $Na_2Sr(PO_4)F:Dy^{3+}$ phosphor, when excited at 385 nm

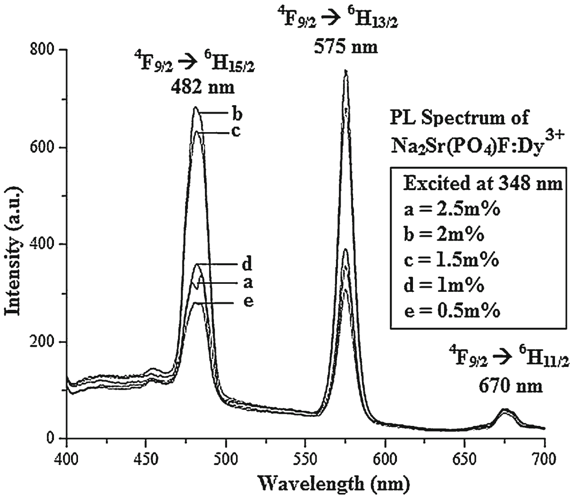

sitions where ligand field changes with the host matrix. The excitation spectrum of the Dy^{3+} luminescence consists of large number of sharp lines at 323, 348, 363, and 385 nm, with highest intensity at 348 nm gives blue/yellow/red ratio, known as the asymmetry ratio of Dy^{3+} ion. It varies while locating in different host lattices, it also reported that in the Dy^{3+} doped $SrSiO_3$ [67] system. The change in the host metal atom, yellow/blue ratio changes due to the change of local site symmetry around Dy^{3+} ion, gives BYR emissions. This UV excitation and color co-ordinates are such that it is suitable as white light-emitting phosphor.

In our case, the Dy^{3+} ion may enter into the host lattice to substitute Na^+ or Mg^{2+}/ Ca^{2+}\/Sr^{2+} or it may be located on surfaces of the crystals due to the porosity of the spinal structure. As the ionic radii of Dy^{3+} (91.2 pm) are much larger than Mg^{2+} (72 pm) and smaller to Sr^{2+} (112 pm) and Ca^{2+} (99 pm), or Na^+ (102 pm). The first possibility is more feasible. Most of the Dy^{3+} ions are entering into the lattice

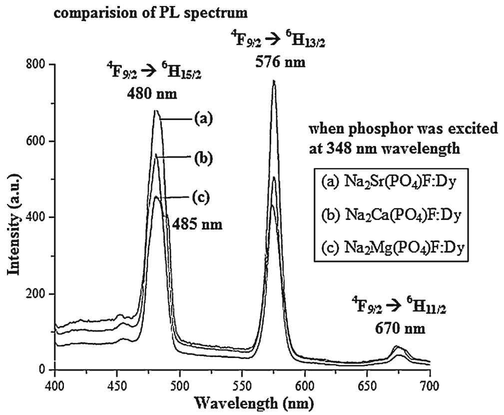

Fig. 7.61 PL comparison spectrum of $Na_2Mg(PO_4)F$:Dy, $Na_2Ca(PO_4)$ F:Dy and $Na_2Sr(PO_4)$ F:Dy phosphor

$Na_2Sr(PO_4)F$ as compared to $Na_2Ca(PO_4)F$ and $Na_2Mg(PO_4)F$ phosphors and few of them are located at the surface. Its substitution at Ca^{2+} site in $Na_2Ca(PO_4)F$ will leads to more distortion in the host in comparison to its substitution in $Na_2Sr(PO_4)F$ and $Na_2Mg(PO_4)F$ phosphors. The charge compensating defects in the immediate vicinity are likely to influence the local site symmetry. This is reflected in the emission spectra, wherein asymmetry factor is higher in $Na_2Sr(PO_4)F$ sample compared to $Na_2Ca(PO_4)F$ and $Na_2Mg(PO_4)F$ phosphors. As Dy^{3+} ions progressively replace the Sr^{2+} ions, an increase in PL emission intensity is observed and asymmetry factor progressively reduced. The low-symmetry location of Dy^{3+} results in predominant emission of $^4F_{9/2} \rightarrow {}^6H_{15/2}$ transition. Hence, $Na_2Sr(PO_4)F$ phosphors show strong PL emission intensity as compared to $Na_2Ca(PO_4)F$ and $Na_2Mg(PO_4)F$ phosphors when Dy is doped as shown in Fig. 7.61. Usually, a low doping gives weak luminescence, but excess doping perhaps causes quenching of luminescence. The maximum intensity of Dy^{3+} is observed at 2 mol% is shown in Table 7.1.

7.14.2.3 Eu^{3+} Luminescence in $Na_2X(PO_4)F$ (X = Mg, Ca, Sr)

Figure 7.62 shows the PL excitation spectrum of the Eu activated $Na_2Mg(PO_4)F$, $Na_2Ca(PO_4)F$ and $Na_2Sr(PO_4)F$ phosphors. Figure 7.63 shows PL emission spectrum of the Eu activated $Na_2Mg(PO_4)F$ phosphor, Fig. 7.64 for Eu-activated $Na_2Sr(PO_4)F$ phosphor and Fig. 7.65 for Eu-activated $Na_2Ca(PO_4)F$ phosphor.

PL excitation spectrum appeared as broad band excitation at 251 nm of Eu ion. Broad band excitation is assigned due to the Eu^{2+}-O^{2-} charge transfer from Eu to oxygen atom and absorption of energy in UV region of the spectrum. The sharp emission peak is observed at 611 nm in the red region of the visible spectrum. Figures 7.63, 7.64 and 7.65 show the PL emission spectra of Eu^{3+} ions in $Na_2X(PO_4)F$ (X = Mg, Ca, Sr) phosphors with different concentration under excitation of 251 nm wavelengths of light. That is, the externally forced energy transfers the electron of 2p oxide electronic state in the $Na_2X(PO_4)F$ lattice to the $^5D_0$ state

Table 7.1 PL emission intensity of Dy^{3+} activated phosphors

Phosphors	Emission wavelength (nm)	PL intensity (arb. unit)
$Na_2Mg(PO_4)F{:}Dy_{2.5\,m\%}$	482, 575	207.512, 237.296
$Na_2Mg(PO_4)F{:}Dy_{2\,m\%}$	480, 574	455.764, 506.124
$Na_2Mg(PO_4)F{:}Dy_{1.5\,m\%}$	481, 574	422.126, 453.584
$Na_2Mg(PO_4)F{:}Dy_{1\,m\%}$	482, 575	240.136, 260.938
$Na_2Mg(PO_4)F{:}Dy_{0.5\,m\%}$	484, 575	187.128, 205.05
$Na_2Ca(PO_4)F{:}Dy_{2.5\,m\%}$	482, 576	353.54, 221.64
$Na_2Ca(PO_4)F{:}Dy_{2\,m\%}$	480, 576	566.98, 432.56
$Na_2Ca(PO_4)F{:}Dy_{1.5\,m\%}$	482, 577	320.87, 232.87
$Na_2Ca(PO_4)F{:}Dy_{1\,m\%}$	481, 577	464.65, 325.76
$Na_2Ca(PO_4)F{:}Dy_{0.5\,m\%}$	484, 577	237.35, 157.98
$Na_2Sr(PO_4)F{:}Dy_{2.5\,m\%}$	482, 575	337.18, 355.42
$Na_2Sr(PO_4)F{:}Dy_{2\,m\%}$	482, 575	670.41, 759.71
$Na_2Sr(PO_4)F{:}Dy_{1.5\,m\%}$	483, 575	624.54, 680.65
$Na_2Sr(PO_4)F{:}Dy_{1\,m\%}$	484, 576	360.46, 391.31
$Na_2Sr(PO_4)F{:}Dy_{0.5\,m\%}$	482, 576	280.43, 307.78

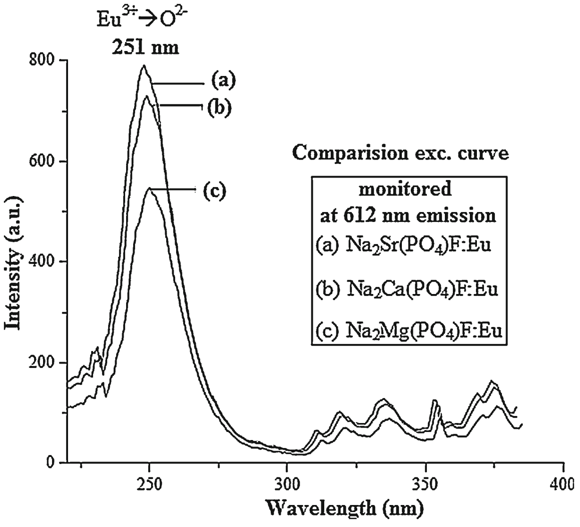

Fig. 7.62 PL excitation spectrum of Eu activated $Na_2Mg(PO_4)F$, $Na_2Sr(PO_4)F$ and $Na_2Ca(PO_4)F$ phosphors, monitored at 613 nm

in Eu^{3+} and red light is emitted by the photon generated from $^5D_0 \rightarrow {}^7F_2$ transition in the Eu^{3+} ion and secondary PL emission properties are seen at 650 nm. The peaks were observed at 593, 611, and 650 nm for $2 - 0.1$ mol% concentrations respectively, which are assigned to the $^5D_0 \rightarrow {}^7F_{0,1,2,3}$ transition of Eu^{3+} ions. The Eu^{3+} ions have complex energy levels, which in turn are modified by the host matrices. The first excited of $^5D_0 \rightarrow {}^7Fj$ configuration is due to the large spatial extension of the 5D wave function. Well-resolved peaks were observed, which are assigned to due to $^5D_0 \rightarrow {}^7F_{0,1,2,3}$ transition of Eu^{3+} ions. Asymmetry factor i.e. I ($^5D_0 \rightarrow {}^7F_2$) to I ($^5D_0 \rightarrow {}^7F_{0,1,3}$) is greater than 1 and it suggests that Eu^{3+} ions are at a site

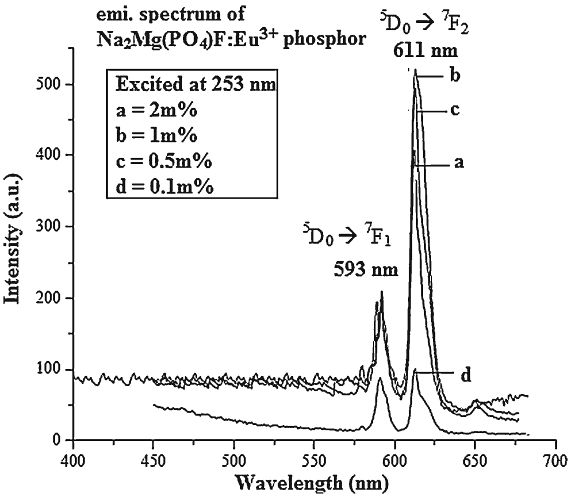

Fig. 7.63 PL emission spectrum of $Na_2Mg(PO_4)F:Eu^{3+}$ phosphor, when excited at 251 nm

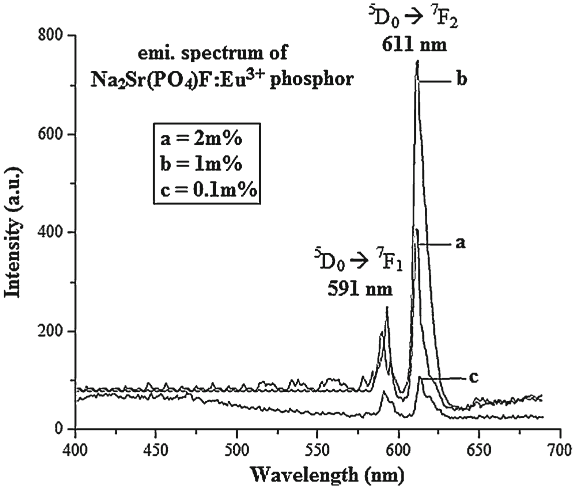

Fig. 7.64 PL emission spectrum of $Na_2Sr(PO_4)F:Eu^{3+}$ phosphor, when excited at 251 nm

lacking inversion symmetry. This emission is due to Eu^{3+} ions occupying a site with inversion symmetry which lifts the $^7F_1$ 3-fold degeneracy completely.

The forced electric-dipole transitions $^5D_0 \rightarrow {}^7F_2$ dominate and possible degeneracies are lifted: $^5D_0 \rightarrow {}^7F_0$ having no sharp line, $^5D_0 \rightarrow {}^7F_1$ having only one line at 593 nm and $^5D_0 \rightarrow {}^7F_2$ having prominent peak at 611nm and other smaller peaks were observed corresponding to Eu^{3+} transition. The 611 nm emission peak is sharp; therefore, this emission is the emission of the intrinsic Eu^{3+} ions of $Na_2Mg(PO_4)F:Eu$, $Na_2Ca(PO_4)F:Eu$ and $Na_2Sr(PO_4)F:Eu$ phosphors. With the increasing concentration of Eu^{3+} ions, the peak intensity increases and maximum intensity observed at 1 mol% for Eu^{3+} ions. This indicates that the $Na_2X(PO_4)F$ lattice is suitable for higher concentrations of Eu^{+} ions at 1 mol%. It has earlier been

Fig. 7.65 PL emission spectrum of $Na_2Ca(PO_4)F:Eu^{3+}$ phosphor, when excited at 251 nm

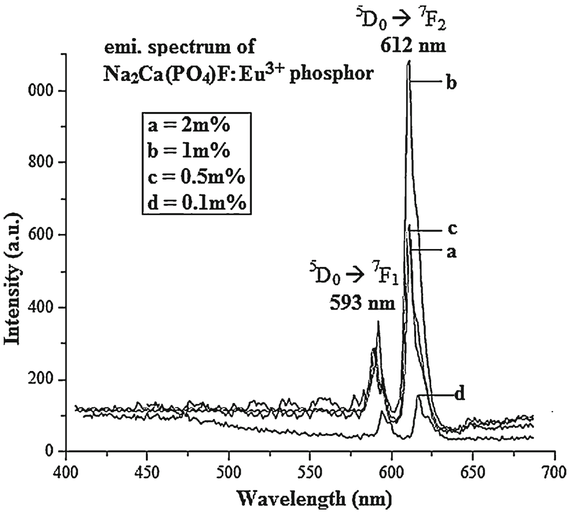

observed that depending on the method of incorporation, Eu^{3+} PL characteristics in same hosts can change. This is especially true for hosts in which the straightforward methods do not lead to the incorporation of Eu^{3+}.

Eu-doped luminescence was excited with UV light. The emission spectrum spreads over the orange and red range with the maximum at about 611 nm as it is shown in Figs. 7.63, 7.64 and 7.65. Several emission bands from crystalline Eu-doped materials have been reported in the visible range of the spectrum, all of them associated to electronic transitions $^5D_0 \rightarrow {}^7F_{0,1,2,3}$ in Eu^{3+} ions [69]. The site symmetry of the Eu^{3+} ions and the covalence degree of Eu oxygen bond determine mainly the shape of the spectrum. Emission bands peaking at the red region of the spectrum are originated by Eu^{3+} ions in tetragonal distorted sites [70].

The ionic radii of Eu ions (94.7 pm) are similar to those that of the Ca^{2+} ions (99 pm) rather than Sr^{2+} ion (112 pm) and Mg^{2+} ions (72 pm). Therefore, Eu^{3+} ions should easily substitute the calcium metal host atom to occupy statistically cation positions in the unit cell. Hence, most of Eu^{3+} occupy the sites of Ca^{2+}, it creates lower symmetry of local environment around Eu^{3+} ion. The ionic radius of O^{2-} ion is 140 pm. The average value of the radius of other ions was set from the distance between ions that were measured for many oxides and the difference from the radius of O^{2-} ion. The ionic radius of the negative ion becomes large and that of the positive ion becomes small compared to former neutral atom. This results in a more uniform spatial distribution of -ve ions. Therefore, it is concluded that the emission originates from the Eu^{3+} ion incorporated in the spinal blocks. The Ca^{2+} ions in which view of their ionic radii are more easily accommodated into the Eu^{3+} ions from their spinal blocks. Consideration about the Mg^{2+} or Sr^{2+} replacement by Eu^{3+} ion, their little decrease of PL intensity in $Na_2Sr(PO_4)F$ and $Na_2Mg(PO_4)F$ cell parameters might be expected.

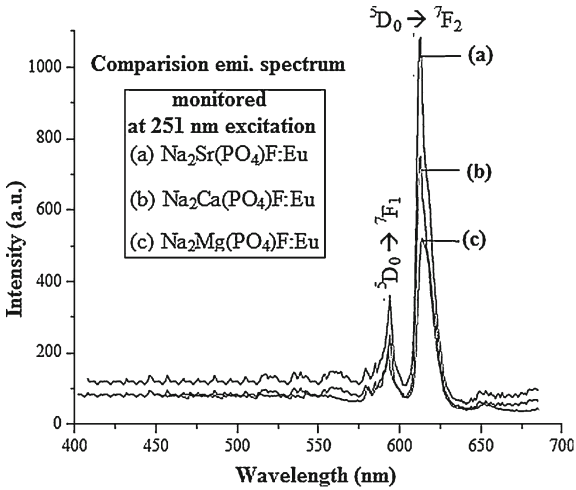

Fig. 7.66 PL comparison spectrum of, (*a*) $Na_2Ca(PO_4)F$:Eu, (*b*) $Na_2Sr(PO_4)F$:Eu and (*c*) $Na_2Mg(PO_4)$ F:Eu phosphors, when excited at 251 nm

Table 7.2 PL emission intensity of Eu^{3+} activated phosphors

Phosphors	Emission wavelength (nm)	PL intensity (arb. unit)
$Na_2Mg(PO_4)F:Eu_{2\,m\%}$	593, 610	212.87, 420.45
$Na_2Mg(PO_4)F:Eu_{1\,m\%}$	592, 611	210.90, 527.89
$Na_2Mg(PO_4)F:Eu_{0.5\,m\%}$	593, 611	209.32, 510.67
$Na_2Mg(PO_4)F:Eu_{0.1\,m\%}$	591, 610	94.67, 104.67
$Na_2Sr(PO_4)F:Eu_{2\,m\%}$	593, 610	270.65, 427.51
$Na_2Sr(PO_4)F:Eu_{1\,m\%}$	591, 611	200.09, 700.75
$Na_2Sr(PO_4)F:Eu_{0.1\,m\%}$	591, 611	80.98, 101.54
$Na_2Ca(PO_4)F:Eu_{2\,m\%}$	591, 611	309.65, 596.90
$Na_2Ca(PO_4)F:Eu_{1\,m\%}$	593, 612	379.09, 1080.65
$Na_2Ca(PO_4)F:Eu_{0.5\,m\%}$	591, 611	305.65, 620.90
$Na_2Ca(PO_4)F:Eu_{0.1\,m\%}$	595, 614	88.09, 120.00

At low concentration 0.1 mol% of Eu^{3+} ion has weak emission compared to higher concentration of Eu^{3+} ion. As is well-known, in the case of orthorhombic crystal structure, the charge transfer band of Eu^{3+} lies in the high-energy region and it is not host lattice dependent. Therefore, it is highly probable that in fluoride phosphate the CT band of Eu^{3+} lies in the high-energy region. Since the molar absorption coefficient of Ca^{2+} ions is very high as compared to Sr^{2+} and Mg^{2+} metal atoms. Since, Eu^{3+} ions show prominent PL emission in case of Ca-doped host lattices as shown in Fig. 7.66. Emission intensity increases with the concentration from 0.1 to 1 mol%. Maximum intensity is obtained at 1 mol%, quenching is obseverd after 2 mol% concentration of Eu ion shown in Table 7.2.

7.15 Conclusions

It is concluded that, Dy^{3+} and Eu^{3+} activated $Na_2X(PO_4)F$ (X = Ca, Sr, Mg) phosphors were synthesized by combustion method. The PL emission spectrum of Dy^{3+} ion at 385 nm excitation gives an emission at 480 nm (blue) and 574 nm (yellow). The PL revealed the presence of Dy^{3+} ions Sr ion at asymmetric sites, $Na_2Sr(PO_4)F$:Dy phosphors show strong PL emission as compared to $Na_2Ca(PO_4)F$:Dy and $Na_2Mg(PO_4)F$:Dyphosphors. The BY emission is important in the context of Dy^{3+} non-equivalent substitution in solid-state lighting phosphor and white light LED (385 nm excitation is the LED excitation). PL emission spectra of Eu^{3+} ion give the sharp emission spectrum with maximum intensity at 611 nm due to $^5D_0 \rightarrow {}^7F_2$ transition of Eu^{3+} ions under 251 nm UV-excitation(Hg excitation).The PL revealed the presence of Eu^{3+} ions Ca ion at asymmetric sites, $Na_2Ca(PO_4)F$:Eu phosphors show strong PL emission as compared to $Na_2Sr(PO_4)F$:Eu and$Na_2Mg(PO_4)F$:Eu phosphor. Therefore, above prepared Dy^{3+} activated phosphors are more applicable for white LED and Eu^{3+} activated phosphors are more applicable for Hg excitation lamp. Hence prepared, Dy^{3+} and Eu^{3+} activated $Na_2X(PO_4)F$ ($X = $ Ca, Sr, Mg) phosphors by combustion method are very potential application in the field of lamp industry.

References

1. F.K. Yam, Z. Hassan, Microelectron. J. **36**, 129 (2005)
2. A.M. Srivastava, D.A. Doughty, W.W. Beers, J. Electrochem. Soc. **144**, L190 (1997)
3. T. Jüstel, H. Nikol, C. Ronda, Angew. Chem. Int. Ed. **37**, 3084 (1998)
4. R.T. Wegh, H. Donker, K.D. Oskam, A. Meijerink, Science **283**, 663 (1999)
5. E. van der Kolk, P. Dorenbos, A.P. Vink, R.C. Perego, C.W.E. van Eijk, Phys. Rev. B **64**, 195129 (2001)
6. T. Jüstel, J.C. Krupa, D.U. Wiechert, J. Lumin. **93**, 179 (2001)
7. A.N. Belsky, J.C. Krupa, Displays **19**, 185 (1999)
8. H.B. Liang, Y. Tao, Q. Su, S.B. Wang, J. Solid State Chem. **167**, 435 (2002)
9. A. Meijerink, R.T. Wegh, Mater. Sci. Forum **315**, 11 (1999)
10. K.D. Oskam, K.A. Kaspers, A. Meijerink, H. Muller-Bunz, Th. Schleid, J. Lumin. **99**, 101 (2002)
11. P. Dorenbos, L. Pierron, L. Dinca, C.W.E. van Eijk, A. Kahn-Harai, J. Phys. Condens. Mater. **15**, 511 (2003)
12. Z.C. Wu., J.X. Shi, M.L. Gong, J. Wang, Q. Su, Mater Chem. Phys. **103**, 415 (2007)
13. X. Li, L. Guan, X. Li, J. Wen, Z. Yang, Powder Technol. **200**, 12 (2010)
14. Z.C. Wu, J. Liu, W.G. Hou, J. Xu, M.L. Gong, J. Alloy. Compd. **498**, 139 (2010)
15. B. Yue, J. Gu, G. Yin, Curr. Appl. Phys. **10**, 1216 (2010)
16. J. Lü, Y. Huang, Y. Tao, H.J. Seo, J. Alloy. Compd., **500**, 134 (2010)
17. L.N. Ji, H.W. Ma, J.B. Li, J.K. Lianga, B.J. Sun, Y.H. Liu, J.Y. Zhang, G.H. Rao, J. Solid State Chem. **180**, 2256 (2007)
18. F.C. Hawthorne, Can. Miner. **20**, 263 (1982)
19. K.N. Shinde, S.J. Dhoble, A. Kumar, J. Lumin. **131**, 931 (2011)
20. K.N. Shinde, S.J. Dhoble, A. Kumar, J. Lumin. **131**, 1939 (2011)
21. K.N. Shinde, S.J. Dhoble, Luminescence **27**, 69 (2012)

22. I.M. Nagpure, K.N. Shinde, S.J. Dhoble, A. Kumar, J. Alloy. Compd. **481**, 632 (2009)
23. K. Murakami, J. Narito, Y. Anzai, H. Itoh, S. Doi, K. Awazu, J. Illum. Eng. Jpn. **3**, 6 (1979)
24. B.M.J. Smets, Mater. Chem. Phys. **16**, 283 (1987)
25. N. Shin, J. Kim, D. Ahn, K.-S. Sohn, Acta Cryst. **C61**, i54 (2005)
26. Helmut Ehrenberg, S. Laubach, P.C. Schmidt, R. McSweeney, M. Knapp, K.C. Mishra, J. Solid State Chem. **179**, 968 (2006)
27. O.A. Lopez, J. Mckittrick, L.E. Shea, J. Lumin. **71**, 1 (1997)
28. D. Jia, W.M. Yen, J. Lumin. **101**, 115 (2003)
29. E. Cavalli, M. Bettinelli, A. Belletti, A. Speghini, J. Alloy. Compd. **341**, 107 (2002)
30. M. Yu, J. Lin, Z. Wang, J. Fu, S. Wang, H.J. Zhang, Y.C. Han, Chem. Mater. **14**, 2224 (2002)
31. J. Kuang, Y. Liu, J. Zhang, J. Solid State Chem. **179**, 266 (2006)
32. B.C. Joshi, U.C. Pandey, J. Phys. Chem. Solids **50**, 599 (1989)
33. A.K. Agrawal, N.C. Lohant, T.C. Pant, K.C. Pant, J. Solid State Chem. **54**, 219 (1984)
34. K.C. Sobha, K.J. Rao, J. Phys. Chem. Solids **57**(9), 1263 (1996)
35. G. Blasse, Prog. Solid State Chem. **18**, 79 (1988)
36. H.S. Kiliaan, J.K. Kothe, G. Blasse, J. Electrochem. Soc. **134**, 2359 (1987)
37. J.M. Verstegen, J.L. Sommerdijk, J.G. Erriet, J. Lumin. **6**, 425 (1973)
38. A. Lempicki, E. Berman, A.J. Wojtowicz, M. Balcerzyk, L.A. Boatner, IEEE Trans. Nucl. Sci. **40**, 384 (1993)
39. A.J. Wojtowicz, A. Lempicki, D. Wisniewaski, L.A. Boatner, Mater. Res. Soc. Symp., **348**, 123 (San Francisco, CA, 1994)
40. A.J. Wojtowicz, in Conference Record EURODIM 94, Lyon, France (1994)
41. K.N. Shinde, S.J. Dhoble, A. Kumar, Bull. Mater. Sci. **34**, 937 (2011)
42. R.S. Yadav, R.K. Dutta, M. Kumar, A.C. Pandey, J. Lumin. **129**, 1078 (2009)
43. M.M. Haque, H.L. Lee, D.K. Kim, J. Alloy. Compd. **481**, 792 (2009)
44. I. Omkaram, B. Vengala Rao, S. Buddhudu, J. Alloy. Compd. **474**, 565 (2009)
45. P. Dorenbos, J. Lumin. **91**, 155 (2000)
46. R.C. Ropp, J. Electrochem. Soc. **115**, 841 (1968)
47. K.N. Shinde, S.J. Dhoble, Micro. Nano. Lett. **5**, 340 (2010)
48. D.E.C. Corbridge, E.J. Lowe, J. Chem Soc. 493 (1954)
49. D.L. Dexter, J. Chem. Phys. **21**, 836 (1953)
50. K.N. Shinde, S.J. Dhoble, Luminescence **27**, 9 (2012)
51. K.N. Shinde, S.J. Dhoble, Micro. Nano. Lett. **5**, 340 (2010)
52. Q. Su, Z.W. Pei, J. Lin, F. Xue, J. Alloy. Compd. **225**, 103 (1995)
53. T.R.N. Kutty, Mater. Res. Bull. **25**, 485 (1990)
54. B. Yan, C. Wang, J. Alloy. Compd. **462**, 147 (2008)
55. M. Yu, J. Lin, Z. Zhang, J. Fu, S. Wang, H.J. Zhang, Y.C. Ham, Chem. Mater. **14**, 2224 (2002)
56. D. Jia, W.M. Yen, J. Lumin. **101**, 115 (2003)
57. J. Kuang, Y. Liu, J. Zhang, J. Solid State Chem. **179**, 266 (2006)
58. E. Nakazawa, in: W. M. Yen, S. Shionoya, H. Yamamoto (eds.), *Phosphor Handbook*, 2nd edn. (CRC Press, Boca Raton, 2006), p. 107 (Chapter 2)
59. G.B. Stringfellow, M.G. Craford (eds.), High Brightness Light Emitting Diodes, in *Semiconductors and Semimetals*, vol. 48, R.K. Willardson, E.R. Weber (Series Editors) (Academic Press, San Diego, 1997)
60. S. Shionoya, W.M. Yen, *Phosphor Handbook* (Phosphor Research Society, CRC Press, Boca Raton, 1998)
61. Color Calculator version 2, A software from Radiant Imaging, Inc. (2007)
62. K.N. Shinde, S.J. Dhoble, AIP Conf. Proc. **1391**, 216 (2011)
63. K.N. Shinde, S.J. Dhoble, Luminescence (2012, in press) doi:10.1002/bio.2343
64. T.S. Ercit, The crystal structure of nalipoite. Can. Mineral. **29**, 569 (1991)
65. K.N. Shinde, S.J. Dhoble, A. Kumar, J. Rare Earths **29**(6), 527 (2011)
66. S.J. Dhoble, V.B. Pawade, K.N. Shinde, Eur. Phys. J. Appl. Phys. **52**, 11104 (2010)
67. J. Kuang, Y. Liu, J. Zhang, J. Solid State Chem. **179**, 266 (2006)
68. M. Yu, J. Lin, Z. Wang, J. Fu, S. Wang, H.J. Zhang, Y.C. Han, Chem. Mater. **14**, 2224 (2002)
69. D. Jia, W.M. Yen, J. Lumin. **101**, 115 (2003)
70. S.J. Dhoble, I.M. Nagpure, J.M. Mahakode, S.V. Godbole, M.K. Bhide, Nucl. Instr. Meth. Phys. Res. B **2669**, 3437 (2008)

Chapter 8
Current Progress in Solid-State Lighting

A new era is dawning, the era of solid-state lighting in which the technical community has reason to believe that solid-state lighting will develop into a liberal technology that will benefit humanity at large. Over the past several years, phosphors have been considered as key and technologically important components as the prerequisites to the functionality and success of many lighting and display systems [1, 2]. At present, RE-based phosphors with efficiencies close to the theoretical maximum (100 %) are employed in different fluorescent tubes, X-ray imaging, and color televisions [3, 4]. Such applications depend on the luminescent properties of RE ions, e.g., sharp lines, high efficiency, and high lumen equivalent.

Lighting consumes over 20 % of all electricity produced with an associated 410 million tons of carbon emissions. Conventional lighting sources include incandescent lamps and fluorescent lamps, which are rather inefficient at converting electricity to light. Solid-state lighting sources are in the process of greatly altering the way humans generate light for general lighting applications. It is estimated that over $120 billion in energy savings could be realized by 2020 if an efficiency target of 200 lm/W can be achieved. This will also enable a significant reduction in the generation of green house gasses. Solid-state lighting (SSL), in the form of light-emitting diodes (LEDs), with a theoretical limit of $\sim$300 lm/W, has the ability to meet this target. The problem is still mainly with lighting efficiency and therefore research efforts are focused on key areas of materials and technology for solid-state lighting. It is currently expected that solid-state lighting should achieve an 80 % energy efficiency, with a corresponding luminous efficacy of close to 300 lm/W, and it will be able to run entirely off sustainable energy sources such as either solar or wind energy. Solid-state lighting sources, in addition, offer nearly an infinite field lifetime (e.g., 25–50 years). Solid-state light sources possess two highly attractive features, which put them apart from most other light sources: (i) the properties of light, such as spectral composition and temporal modulation, can be controlled to a degree that is not possible with conventional light sources such as incandescent and fluorescent lamps and (ii) they have the potential to create light with essentially unit power efficiency. The suggestions are enormous and, as a consequence, many positive developments are to be expected including a reduction in global energy consumption, reduction of

K. N. Shinde et al., *Phosphate Phosphors for Solid-State Lighting*,
Springer Series in Materials Science 174, DOI: 10.1007/978-3-642-34312-4_8,

global-warming-gas and pollutant emissions, and a multitude of new functionalities benefiting numerous applications.

Three major benefits of solid-state lighting technology, shown in Fig. 8.1, can be summarized as follows: first, the inherent capability of solid-state sources to generate light with high efficiency is resulting in giant energy savings. Second, potentially huge environmental benefits are a result of the efficiency and durability of solid-state emitters, particularly light-emitting diodes based on inorganic semiconductors. Third, solid-state emitters allow one to control the emission properties with much greater precision, thereby allowing one to custom-tailor the emission properties for specific applications.

The process assumes that the technical challenges and opportunities in SSL–LEDs are:

- Improve efficacy at all visible wavelengths to obtain 2,000 lm/W white-light sources.
- Reduce the cost of solid-state light sources so as to be competitive with traditional light sources.
- Explore the opportunities to develop new technologies and products leading to a new lighting industry enabled by the attributes of SSL–LED, such as surface mounted “smart” light sources.

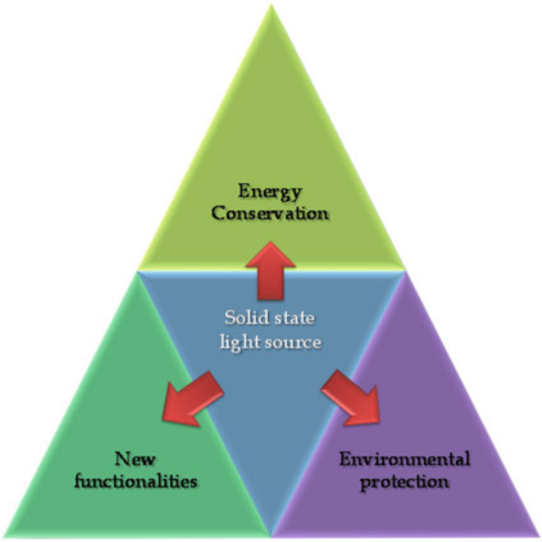

Fig. 8.1 Profit made possible by solid-state light sources

8.1 Strategies for Solid-State Lighting

Currently, there are three viable options achieving LED-based SSL white lighting.

1. Blue LED with phosphor(s),
2. UV LED with several phosphors, and
3. Three or more LEDs of different colors.

It is generally acknowledged that the ultimate performance goal will be most readily achieved by option III. This option, however, poses many challenges and will be probably the last to reach commercial applications. Various issues of lifetime, stability, photon extraction, etc, are common to all SSL white-light initiatives and will require research programs at industry, universities, and/or national laboratories to solve these problems. The following sections outline the pros and cons of each option.

8.1.1 Blue LED with Phosphor(s)

At the present time, the blue LED plus phosphor strategy has the shortest time line for commercialization. Companies such as Nichia, CREE, and others, already have demonstrated "white-light" generation by using a blue LED and a single phosphor (YAG:Ce). Part of the blue light emitted by the LED escapes and another part is converted by the phosphor to an amber color. The amber colored light is the complimentary color of the blue light emitted by the LED, thereby producing white emission.

There are two principal problems with this approach,

- The "halo effect" and
- The low level of absorption of blue light by the phosphor.

Halo Effect: The "halo effect" or bleed-through effect occurs because the light from the blue LED is directional while the amber light from the phosphor radiates over a 2π solid angle. Thus, for an observer looking from the side, the color appears multicolor—not white.

Blue Light Absorption: The second problem is the limited blue absorption by the phosphor. For rare-earth phosphors, the absorption in the blue is relatively weak, thus requiring "thick" phosphors. It is necessary either to identify new phosphors with strong absorption in the blue or to identify a sensitizer ion to facilitate energy transfer to the rare-earth ion. Current industrial research is concentrating on generating a 2π solid angle emission from the blue LED.

The blue LED approach is not limited to only one phosphor, it may be used with a two-component phosphor system (e.g. green and red) to generate high-quality white light and this also has been demonstrated experimentally. Further work is necessary to combat the “halo effect” mentioned above, as well as maintaining the highest possible conversion efficiencies. Furthermore, improving existing red and green phosphors or identifying new ones will be important in order to optimize quantum efficiency and stability with temperature. In other approaches, a semiconductor or other luminescent material becomes the wavelength converter. At a later date, other strategies might replace or surpass this technique because of the limitations of achieving a good color rendering index from using only two colors. Furthermore, when today’s phosphor conversion efficiencies are taken into account, in order to demonstrate targeted white light, the blue LED has to generate light with power conversion efficiency in excess of 60 %. This target of external quantum efficiency exceeds the highest efficiency of visible LEDs reported to date (45 % at 610 nm).

8.1.2 UV LED Plus Three or More Phosphors

This option uses output from a UV LED to pump several phosphors to simultaneously generate different colors. High color rendering indices, similar to fluorescent lamps, can be realized. Also, the fact that the UV light is not used directly (as part of the blue light used is in the previous approach) will further demand that the UV emitter efficiency be higher to account for conversion losses. Currently, efficient emitters have been demonstrated in the 400-nm regime. In fact, the highest-reported efficiency in an InGaN-based emitter is a power conversion efficiency of 21 % for a $\sim$400-nm LED. But clearly, the challenge to increase this to the 60–70 % level is a formidable one. Also, the same issues regarding absorption efficiencies by the three phosphors that were raised above for the single blue LED plus phosphor strategy also apply here. All components of the UV-pumped phosphor system must have high UV absorption, high quantum efficiency, and also, good photo- and temperature stability. New phosphors must be identified in the red, green, and especially in the blue wavelength regimes which satisfy these requirements.

8.1.3 Three or More LEDs of Different Colors

In the long term, this option may be the preferred method for producing high-quality white light for general illumination. First, the more colors one has to mix, the more control one has in producing white light with a high color rendering index. Second, photons from each LED contribute directly to the white-light intensity, i.e., no photon conversion efficiencies have to be considered. Third, by changing the relative intensity of the different color LEDs it is relatively easy to change the hue of this light source for different applications. However, the separate colors from the individual components must be mixed appropriately to achieve uniform white light. Considerable further effort is required for the multichip solution to achieve target white light. While phosphor conversion is not required, the combined multichip emitter must still operate at a power conversion efficiency of approximately 50 %. This level is a minimum requirement when taking into account color mixing losses. Also, as the three or more different color components have different voltage requirements, different degradation characteristics and different temperature dependencies, a sophisticated control system might be required. The first step, however, is to achieve 50 % conversion efficiency at red, green, yellow, and blue colors. This is a formidable task and hence it is difficult to tell when the multichip white-light sources will reach commercial implementation. Despite these challenges, multicolor sources offer the greatest brightness, the most versatile color control, and the greatest ease of integration with silicon integrated circuits to produce versatile, smart lights.

There is no physical reason why a twenty-first century lighting technology should not be vastly more efficient, thereby reducing equally vastly our energy consumption. If a 50 % efficient technology was to exist and be extensively adopted, it would reduce energy consumption in the US by about 620 billion kWh per year by the year 2025 and eliminate the need for about 70 nuclear plants, each generating a billion Watts of power. SSL is the *direct* conversion of electricity to visible white light using semiconductor materials and has the potential to be just such an energy-efficient lighting technology [5]. By avoiding the indirect processes (producing heat or plasmas) characteristic of traditional incandescent and fluorescent lighting, it can work at a far higher efficiency, “taking the heat out of lighting,” it might be said. Recently, for example, semiconductor devices emitting infrared light have demonstrated an efficiency of 76 %. *There is no known fundamental physical barrier to achieving similar (or even higher) efficiencies for visible white light, perhaps approaching 100 % efficiency*. Despite this tantalizing potential, however, SSL suitable for illumination today has an efficiency that falls short of a perfect 100 % by a factor of *fifteen*. Partly because of this inefficiency, the purchase cost of SSL is too high for the average consumer by a factor ten to a hundred, and SSL suitable for illumination today has a cost of ownership *twenty* times higher than that expected for a 100 % efficient light source. The reason is that SSL is a dauntingly demanding technology. To generate light near the theoretical efficiency limit, essentially every electron injected into the material must result in a photon emitted from the device. Furthermore, the voltage required to inject and transport the electrons to the light-emitting region of the device must be not more than that corresponding to the energy of the resulting photon. It is insufficient to generate “simple” white light; the distribution of photon wavelengths must match the spectrum perceived by the human eye to render colors accurately, with no emitted photons outside the visible range. Finally, all of these constraints must be achieved in a single device with an operating lifetime of at least 1,000 h (and preferably 10–50 times longer), at an ownership cost-of-light comparable to, or lower than, that of existing lighting technology. Where promising demonstrations of higher efficiency exist, they are typically achieved in small devices (to enhance light extraction), at low brightness (to minimize losses) or with low color-rendering quality (overemphasizing yellow and green light, to which the eye is most sensitive). These restrictions lead to a high cost of ownership for high-quality light that would prevent the widespread acceptance of SSL. All devices demonstrated to date, a very large gap is apparent between what is achievable today and the 100 % (or roughly 375 lm/W) efficiency that should be possible with SSL. Today, we cannot produce white SSL that is *simultaneously* high in efficiency, low in cost, and high in color-rendering quality. In fact, we cannot get within a factor of ten in either efficiency or cost. Doing so in the foreseeable future will require breakthroughs in technology, stimulated by a fundamental understanding of the science of light-emitting materials.

The most energy-efficient lighting products use light-emitting diode (LED) technology (Fig. 8.2). These solid-state lighting (SSL) products are more expensive today than the next best energy efficient alternative. However, ongoing development is rapidly improving SSL capability and cost-effectiveness. If all lighting was shifted to SSL, it would reduce the lighting energy consumption to less than 10 % of electricity generated. With the world's supply of non renewable energy from fossil fuels depleting rapidly, the need to reduce energy consumption is a global imperative. Developing countries want to experience the same advantages that developed countries have enjoyed. However, developed countries have shown that the insatiable demand for energy-hungry products has exceeded their capacity to generate sufficient energy to support them, especially when the energy must come from clean energy sources. China has announced plans to phase out incandescent bulbs that could be completed by 2017. Initially, compact fluorescent lighting was the solution to improve efficiency and replacement of incandescent bulbs because of its lower cost. However, CFLs contain mercury and, as such, create a hazardous waste condition when they are discarded. In contrast, LEDs do not contain hazardous materials and products can be disposed of without concern.

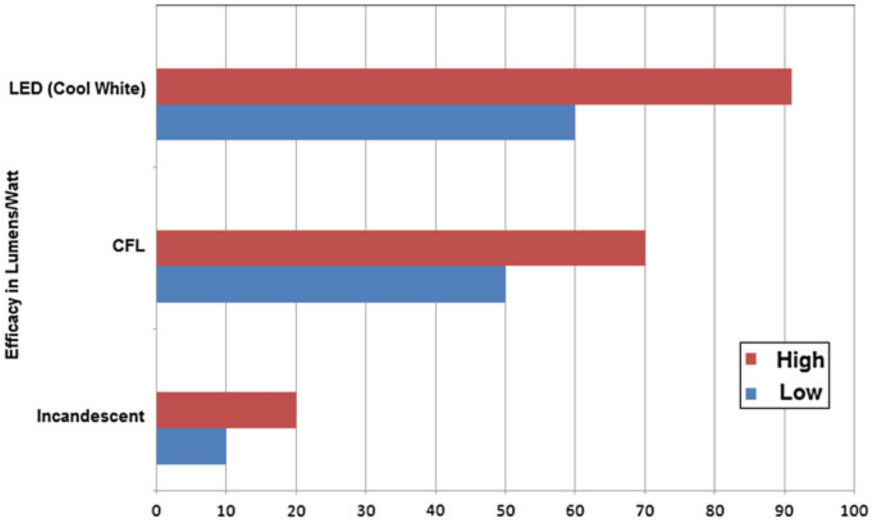

Fig. 8.2 The efficiency of traditional light sources compared to solid-state lighting (*Source* Department of energy (DoE) energy savers) http://www.ecnmag.com/articles/2011/01/introduction-solid-state-lighting

As we discussed above recently, phosphor converted-white LEDs have been highlighted due to their excellent properties, such as low power consumption, long life time, high color rendering index, and high-brightness [6]. The most common way to generate white-light emission via pc-WLEDs is to combine a III–V semiconductor-based blue LED chip and YAG:Ce^{3+} yellow phosphor. However, the given device exhibits a change of the white color gamut and color temperature with varying the input power. Recently, another approach to generate white light has been suggested which utilizes Red/Green/Blue (RGB) tri-color phosphors excited by UV light. The white LEDs employing near UV LED chips with tri-color phosphors have the advantage of less shift of color point against forward current because the white light is completely phosphor converted, which is not the case with blue LED combined with a yellow emitting YAG:Ce^{3+} phosphor [7].

Orthophosphates $ABPO_4$ (in which A and B are mono and divalent cations, respectively) have attracted much attention for their potential application as luminescent materials because of excellent thermal and hydrolytic stabilities [8]. Additionally, $ABPO_4$ compounds can crystallize with various structure types, depending on the size of both cations A and B [9]. The variety in these structures of the $ABPO_4$ family makes it possible to tailor the physical properties, e.g., Eu^{2+}-doped $LiSrPO_4$ (unsolved monoclinic structure) and $KSrPO_4$ (orthorhombic structure) show blue emission, while Eu^{2+}-doped $NaCaPO_4$ (orthorhombic structure) presents a broad green luminescence band peaked at 506 nm [10]. In $NaSrPO_4$ lattices, three different Na and Sr sites existed. Thus, we can expect the activators, e.g., Eu^{2+} and Mn^{2+} ions, to be statistically incorporated those different sites in $NaSrPO_4$ lattices, which lead to the unresolved broad emission spectra [11]. Eu^{2+} activated phosphates were known as a highly efficient blue-emitting phosphor for near UV LED excitation [12, 13]. Mn^{2+} was codoped into those blue-emitting phosphates and an intense red emission of Mn^{2+} was additionally achieved through energy transfer from Eu^{2+} to Mn^{2+} finally leads to the white emission [14, 15]. Generally, oxygen coordinated Mn^{2+} ions illuminate well-known green and red luminescence in a large number of oxide compounds [16–18]. Very recently, Choi et al. [19] reported two series of alkali–alkaline earth phosphate systems which were synthesized by conventional solid-state reaction and their photoluminescent properties were investigated. Both phosphors exhibit a broad excitation band ranging from 250 to 425 nm, which can perfectly match a near UV LED chip. In case of the Ba-including host composition, Eu^{2+} and Mn^{2+}-activated $Na(Sr,Ba)PO_4$, the energy transfer from Eu^{2+} to Mn^{2+} is more suitable and eventually a white light with chromaticity coordinates of (0.36, 0.31) is generated. The $Na(Sr_{0.5}Ba_{0.5})PO_4$:Eu^{2+} 0.01, Mn^{2+} 0.05 can be excited efficiently by light from an extended broad near UV region and the phosphor illuminates mixed blue–red emission, which is well matched with near UV LEDs. Thus, the Eu^{2+} and Mn^{2+} doped $Na(Sr,Ba)PO_4$ can be used as potential candidates for single-phased white-emitting phosphors by properly tuning the relative ratio of Eu^{2+} and Mn^{2+} in the phosphors with n-UV LED chips [19]. Zhang et al. [20] described the blue-emitting phosphor Eu^{2+}-doped $NaBaPO_4$which was synthesized by high-temperature solid-state method. The photoluminescence excitation spectrum shows a very broad band extending from 200 to 420 nm. Under near UV excitation, $NaBaPO_4$:Eu^{2+} shows strong blue light. It was suggested that the Eu^{2+} ions have two luminescence centers, the emission band 435 nm (Eu I) is ascribed to the 12-fold coordinated Ba(I) and the 470 nm to Eu(II) ions on the 10-fold coordinated Ba(II) sites in $NaBaPO_4$ host lattices. This structural site occupation was discussed on the base of the crystal structure and the luminescence spectra. The temperature dependence of luminescence shows the $NaBaPO_4$:Eu^{2+} have an excellent thermal stability on the temperature quenching with T0.5 of 550 K. However, $NaBaPO_4$:Eu^{2+}phosphor has a low QE value of 38.5 %, which may be limited the further application as LED phosphors. With increase of temperature, the emission bands show the anomalous blue-shift with increasing bandwidth. This blue-shift was described in terms of back transfer from the excited states of low-energy emission band to the excited states of high-energy emission band by assistance of thermally active phonons [20]. New Eu^{2+} and Mn^{2+} co-activated $Sr_5(PO_4)_3Cl$ phosphors were synthesized under a reduced atmosphere and reported by Guo et al. [21]. Appropriate flux H_3BO_3, annealing time and suitable excessive $SrCl_2 \cdot H_2O$ is beneficial to emission intensity. Also, the energy transfer from Eu^{2+} to Mn^{2+} took place in the $Sr_5(PO_4)_3Cl$ host, and the efficiencies of $Eu^{2+} \rightarrow Mn^{2+}$ were calculated by the changes of relative intensity of blue and orange emission from Eu^{2+} and Mn^{2+}, respectively. The relative intensity of blue and orange could be tuned by adjusting their contents. The excitation spectra of phosphors $Sr_5(PO_4)_3Cl$:Eu^{2+}, Mn^{2+} matched well with the n-UV GaN-based LED chip, therefore these phosphors are potential candidates with double-color emitting for n-UV LEDs [21].

Ren and Chen develop a novel orange-emitting phosphor, $Ca_{2.6}Sr_{2.4}(PO_4)_3Cl$:$Eu^{3+}$ [22] by the solid-state reaction. The experimental results and the theoretical calculation, the electric multipole–multipole interaction is identified to play the major role in the mechanism of concentration quenching of Eu^{3+} in $Ca_{2.6}Sr_{2.4}(PO_4)_3Cl$:$Eu^{3+}$ phosphor. When the concentration of doped-Eu^{3+} is 0.01, the $Ca_{2.6}Sr_{2.4}(PO_4)_3Cl$:$Eu^{3+}$ has the strongest emission intensity. The results indicate that the $Ca_{2.6}Sr_{2.4}(PO_4)_3Cl$:$Eu^{3+}$ is a potential orange phosphor for UV-LEDs [22]. The past decade has seen a rapid evolution of the GaN-based light-emitting diode (LED) technology, especially focused on developing advanced solid-state lighting sources. The broad band emitting rare-earth ions Ce^{3+} and Eu^{2+} are two important activators for luminescent materials, which have been studied extensively. This is primarily because of their unique emission properties, combining a broad emission spectrum (leading to good color rendering properties), relatively small Stokes shift (allowing excitation in the near-UV or blue part of the spectrum), and short decay times (avoiding saturation). Depending on the host material, high quantum efficiencies in combination with a good thermal quenching behavior can be obtained. Furthermore, the emission spectrum can be tuned from the near-UV to deep red, by appropriately choosing the host compounds. In this regard, Shang et al. [23] reports the Ce^{3+} and/or Eu^{2+} activated $Ca_8La_2(PO_4)_6O_2$ blue-emitting materials have been prepared via a Pechini-type sol–gel method recently. XRD, PL spectra, absolute quantum yield, as well as lifetimes were utilized to characterize samples. The emission of Ce^{3+} and Eu^{2+} ions at different lattice sites has been identified, discussed, and suggested that these blue phosphors might be promising for use in pc-white LEDs.

Alkemper et al. [24] reported the structure of $Na_2CaMg(PO_4)_2$ to be related to the arrangement of cations and phosphate tetrahedra in the glaserite structure and Lü et al. [25] further report the blue-emitting phosphors of Eu^{2+}-doped $Na_2CaMg(PO_4)_2$ prepared by high-temperature solid-state reaction. The luminescence properties were investigated by PL excitation and emission spectra. The phosphor exhibited the blue luminescence due to the $4f^65d^1 \rightarrow 4f^7$ transition of Eu^{2+} ions under the excitation of near UV light. The influence of temperature on the luminescence intensities and decay lifetimes of Eu^{2+} was investigated. An unusual increase of the decay lifetimes of the $4f^65d$ emission of Eu^{2+} ion is observed in $Na_2CaMg(PO_4)_2$ from 10 K to room temperature. The thermal stability of the luminescence of Eu^{2+}-doped $Na_2CaMg(PO_4)_2$ was also reported.

The phosphorescent materials used to convert the blue light of the LED into red light to achieve the LED's overall white-light emission contain rare-earth elements that are increasingly difficult to obtain on the world market. Hirokazu Masai and colleagues [26] from Kyoto University have now developed a new material for use in white LEDs that contains no rare-earth elements. Instead of using energetic states in rare-earth elements, manganese offers an alternative for light conversion at similar wavelengths. And instead of using a crystalline phosphor as a matrix for the manganese cations, here the light conversion works best if a glass is used. This has the additional benefit that the emission of the red light occurs across a broader range of wavelengths, which enhances the overall light emission. Furthermore, with conversion efficiencies that match those of the rare-earth dopants presently in use, rare-earth-free white LEDs might soon be a reality.

Visible-light persistent phosphors are being widely used as self-sustained night-vision materials because of their sufficiently strong and long afterglow (>10 h) and their ability to be excited by sunlight as well as room light. In contrast, persistent phosphors for near-infrared (NIR) wavelengths are lacking. Pan et al. [27] report a series of Cr^{3+}-doped zinc gallogermanate ($Zn_3Ga_2Ge_2O_{10}$:0.5%Cr^{3+}) NIR persistent phosphors that exhibit strong emission at 650–1,000 nm, extending beyond the typical 690–750 nm, and with a super-long afterglow of more than 360 h. These new NIR persistent phosphors are all-weather materials that can be rapidly, effectively and repeatedly charged by natural sunlight in almost all kinds of outdoor environment. Seconds to minutes of sunlight activation can result in more than two weeks of persistent NIR light emission. This new series of NIR persistent materials have potential applications in night-vision surveillance, solar energy utilization, and in vivo bio imaging.

Sm^{3+} activated $Gd_2(MoO_4)_3$:Sm^{3+} red-emitting phosphor was prepared by conventional solid-state method [28]. Its mean particle size is about 6–8 μm, which is suitable for manufacture of white LEDs. Under the 405 nm excitation, emission spectra composed of several narrow spectral lines in the range 500–750 nm. The main emission peak is observed at 650 nm. Among these emission peaks, each transition was observed to split in to several components. These emission lines can be assigned to $^4G_{5/2} \rightarrow {}^6H_{5/2}$ (564 nm), $^4G_{5/2} \rightarrow {}^6H_{7/2}$ (601 nm), $^4G_{5/2} \rightarrow {}^6H_{9/2}$ (650 nm), $^4G_{5/2} \rightarrow {}^6H_{11/2}$ (702 nm) transitions of Sm^{3+}. Its CIE chromaticity coordinates are calculated to be $x = 0.67$ and $y = 0.29$. This phosphor may be applicable as a promising red-emitting component in lamp industry. Eu^{3+} doped $NaLa(WO_4)_2$ phosphors was prepared at 950 °C by a modified solid-state reaction [29]. The grain size of the phosphor is about 30 nm. The PL spectra show the strongest emission at 616 nm corresponding to the electric dipole $^5D_0 \rightarrow {}^7F_2$ transition of Eu^{3+} in $NaLa(WO_4)_2{:}Eu^{3+}$ having excitation 396 nm. When the concentration of Eu^{3+} is beyond 5 mol%, quenching in emission intensity occurs. It is believed that the novel red-emission phosphor $NaLa(WO_4)_2{:}Eu^{3+}$ can be made good use of as a kind of luminescent material in lamp industry. $Na_3SO_4F{:}Eu^{3+}$ and $NaMgSO_4F{:}Eu^{3+}$ halosulphate phosphors prepared by a wet chemical method [30]. The PL emission spectrum of $Na_3SO_4F{:}Eu^{3+}$ phosphors under 393 nm excitation was observed at 593 and 614 nm, which are assigned to due to $^5D_0 \rightarrow {}^7F_1$ and $^5D_0 \rightarrow {}^7F_2$ transition of Eu^{3+} ion. PL emission spectrum of $NaMgSO_4F{:}Eu^{3+}$ shows strong Eu^{3+} emission at 594 and 613 nm wavelength. Both Eu^{3+} emissions may be useful for the mercury-free lamps and solid-state lightening devices. Green emitting $Ca_8Mg(SiO_4)_4Cl_2{:}Eu^{2+}$ phosphor was prepared by modified sol–gel method [31]. The mean size of the particles is about 3 μm, which is in favor of its application in LED. Under the excitation of 381 nm near UV, the phosphor $Ca_8Mg(SiO_4)_4Cl_2{:}Eu^{2+}$ gives an intense green broad band emission centered at 507 nm. The phosphor shows intense absorption in the range of 375–450 nm, which matches well with the available near-UV or blue-emitting lamp phosphor.

Dy^{3+} activated β/α-Sr_2SiO_4 phosphors were successfully prepared by solid-state reaction method [32]. The strongest line absorption was located at 349 nm, which was resulting from the $^6H_{15/2} \rightarrow {}^6P_{7/2}$ transition. The emission spectra of all samples exhibited typically Dy^{3+} line emission at 477 nm (blue, $^4F_{9/2} \rightarrow {}^6H_{15/2}$) and 570 nm (yellow, $^4F_{9/2} \rightarrow {}^6H_{13/2}$). From the PL characterization it is concluded as, this phosphor has a good possibility as phosphor candidates used for white LEDs pumped by a UV chip and the promising enhancement of light-emitting efficiency will promote its unbounded applications in lamp industry.

The $Li_2Ca_2Si_2O_7{:}Eu^{2+}$ phosphors were synthesized at the low temperature of 900 °C without any impurity phases by a solid-state reaction [33]. The excitation spectrum shows a broad peak centered at about 350 nm which ranges from 250 to 450 nm. $Li_2Ca_2Si_2O_7{:}Eu^{2+}$ phosphor exhibits green luminescence with a large stokes shift and an emission peak centered at 520 nm with a full width at half maximum (FWHM) of 250 nm. The novel $Li_2Ca_2Si_2O_7{:}Eu^{2+}$ green phosphor is a promising phosphor for white LEDs because of its effective excitation in the near UV range. $Gd_2MoB_2O_9$ doped with Sm^{3+} and Dy^{3+} were prepared by high temperature solid-state method [34]. The emission spectra of $Gd_2MoB_2O_9{:}Sm^{3+}$ phosphor under 300 and 403 nm UV light excitation are similar to each other in shape, and consist of four groups of sharp lines. The main emission line around 600 nm is assigned to the $^4G_{5/2} \rightarrow {}^6H_{7/2}$ transition. The emission spectrum of Dy^{3+} doped $Gd_2MoB_2O_9$ phosphor consists mainly of two groups of lines, which are situated around 480 (blue emission) and 575 nm (yellow emission). The decay curves of both the phosphors are nonexponential, and the average lifetimes observed in the millisecond range. PL characterization shows the phosphor may be applicable for solid-state lighting.

A series of Eu^{3+} activated $K_3Eu(PO_4)_2$ phosphors were synthesized by the solid-state reaction method [35]. The Eu^{3+} activated compounds $K_3Eu(PO_4)_2$ show strong reddish orange emission under 393 nm excitation. The emission spectrum is composed of groups of sharp peaks from the emission of Eu^{3+} intraconfigurational $4f$–$4f$ transitions ($^5D_0$–$^7F_{0-4}$) at 580, 591, 618, 655 and 705 nm, respectively. The CIE coordinates of $K_3Eu(PO_4)_2$ were measured as $x = 0.63$, $y = 0.36$. The CIE coordinates of $K_3Eu(PO_4)_2$ are in the deep reddish orange area. The results indicate that the phosphor $K_3Eu(PO_4)_2$ might find a possible application on NUV InGaN chip-based WLEDs. Novel Eu^{2+}doped $Ca_2AlSi_3O_2N_5$ phosphors with a general formula of $Eu_xCa_{2-x}AlSi_3O_2N_5$ were successfully prepared via a solid-state reaction method under a nitrogen atmosphere [36]. The excitation spectra which originate from the typical allowed $4f^7 \rightarrow 4f^65d$ transition of electrons in Eu^{2+}ions are seemingly broad and ranging from the UV to the visible spectrum of light. In the emission spectra of Eu^{2+}doped $Ca_2AlSi_3O_2N_5$ phosphors, a single intense broad emission band that peaked at about 500 nm was observed, which was attributed to the typical allowed $4f^7 \rightarrow 4f^65d$ transition in Eu^{2+} ions. The PL properties of the $Ca_2AlSi_3O_2N_5$:Eu^{2+} phosphors qualify them for consideration in potential use as green lamp phosphors.

Eu^{3+} activated $Gd_2(MoO_4)_3$ red-emitting phosphors were prepared by solid-state method [37]. The particles of the powder samples had the length of 5–12 μm and width of 3–7 μm with flake shape. Excitation spectrum of $Gd_2(MoO_4)_3$:Eu^{3+} phosphor having strongest excitation stands at ∼395 nm. The major emission peak of these phosphors was at 615 nm, corresponding to pure red emission due to the $^5D_0 \rightarrow {}^7F_2$ transition of Eu^{3+}. This phosphor may be an efficient red-emitting conversion phosphor for solid-state lighting. Blue-emitting phosphor $LiCaPO_4$:Eu^{2+} was synthesized by solid-state reaction [38]. The emission spectrum exhibits a symmetrical band between 450 and 500 nm with a peak at 470 nm due to the allowed $4f^65d^1 \rightarrow 4f^7$ transition of Eu^{2+} having excitation 400 nm. This phosphor could be efficiently excited by near-UV light-emitting diodes and is believed to be a promising blue-emitting lamp phosphor for white-light-emitting diodes.

$Ca_3ZnAl_4O_{10}$ doped with Eu^{2+} was prepared by a high-temperature solid-state reaction method [39]. The emission spectrum of $Ca_3ZnAl_4O_{10}$:Eu^{2+} phosphors under the 365 nm excitation shows bright blue luminescence with a peak wavelength at 450 nm with a full width at half maximum (FWHM) of 55 nm. The CIE color coordinates is pure blue ($x = 0.151$, $y = 0.075$). The calculated lifetime of 450 nm luminescence is 245.4 ns. The luminescence decay and the color coordinates were discussed in order to further investigate its potential applications for white-light-emitting diode phosphors pumped by a near-UV chip. Blue-emitting Ca_2PO_4Cl:Eu^{2+} phosphors prepared by solid-state reaction [40]. The phosphors presented a blue-emitting band peaking at 454 nm under optimal excitation at 370 nm and the Stokes shift was estimated to be 5000 cm^{-1}. The phosphor shows a broad absorption band, high quantum efficiency, and good thermal stability. The results indicate that Ca_2PO_4Cl:Eu^{2+} is a promising blue phosphor for application in lamp industry. Dy^{3+} doped Li_2SrSiO_4 was synthesized by a solid-state reaction method [41]. The emission spectra were monitored at 350 nm excitation. The observed emission spectra exhibited two strong bands centered at 478 nm (blue) and 572 nm (yellow), which corresponded to $^4F_{9/2} \rightarrow {}^6H_{15/2}$ and $^4F_{9/2} \rightarrow {}^6H_{13/2}$ transitions. The life time decay curves could be well fitted by single exponential function and the lifetime was about 0.9 ms. The results manifested that Li_2SrSiO_4:Dy^{3+} phosphor might be a promising candidate for lamp phosphor.

A novel green phosphor of Eu^{2+} doped $Ca_5(PO_4)_2SiO_4$ was prepared by a solid-state reaction [42]. Under the excitation at 289 nm, the phosphor exhibited a green emission band peaked at 530 nm with a shoulder in the long wavelengths at 561 and 621 nm. When the doping concentration of Eu^{2+} was 0.05 mol%, the $Ca_5(PO_4)_2SiO_4$:Eu^{2+} phosphor had the strongest emission intensity. PL characteristics indicated that this phosphor had a potential application in green emitting lamp phosphor.

Cho et al. [43] investigated the photoluminescence in the BaO–SiO_2 system of rare ion is depended on the structure and variation of the PL intensity responsible of the electronic band structure properties. Eu emission in BaO–SiO_2 system varied from orange to blue with varying crystal structure of the host materials depends on the crystal field splitting of the Eu^{2+} ions in the host lattice. We have the good supporting data on particle size of the materials that indicate the activator emission in the host lattice as well as now electronic structure also so the PL characteristics of any materials. For development of intense lamp phosphors, all these properties are most important for development of stable and quality phosphor for lamp industry.

Strong red-emission peak observed at 613 and 616 nm due to the Eu^{3+} ions in $Ca_9Y(PO_4)_7$:Eu^{3+} was prepared by high temperature solid-state diffusion at 1,200 °C. The excitation at 392 nm exactly matches well the near UV excited LED lighting. These characteristics of $Ca_9Y(PO_4)_7$:Eu^{3+} reported by Liu et al. [44] under the investigation of LED lighting phosphor. Dy^{3+} ions occupy the Y^{3+} sites with high symmetry in the host matrix of $NaYFPO_4$:5%Dy^{3+} was prepared by high-temperature solid-state reaction technique. PL characterization show the two absorption bands peak at 153 and 171 nm and some sharp peaks around 280–500 nm. Two intense emission peaks are located at 485 and 575 nm under VUV-vis excitation and the chromaticity coordinates are located in the cold-white-light region. Zhao et al. reported [45] the optical characteristics of $NaYFPO_4$:5%Dy^{3+} prepared phosphor is a promising material in application to mercury-free luminescence lamps and W-LED.

Luo et al. [46] show the green emission from Eu^{2+} activated Ca_2SiO_4 phosphors prepared by liquid phase precursor method using SiO_2 sol (LPP-SiO_2(sol)) and water-soluble silicon compound at different temperatures. These prepared compound show green emission three synthesis methods exhibited strong green luminescence centered at 502 nm and abroad excitation spectrum ranging from 225 to 450 nm due to $4f_7 \rightarrow 4f_65d_1$ transition of Eu^{2+} ion. Eu ion in very few hosts shows the green emission for lamp industry.

Red, green, and blue phosphors are mixed for the florescence lamp by using organic adhesive chemicals. The properties of chemical adhesive is more important for past all these three phosphors for fabricate the florescence lamp. Recently, Yun et al. [47] developed florescence screen by using ethylcellulose and nitrocellulose mixed solution as a binder with three primary RGB phosphors and observed exhibit and effective luminescence for synthesized the phosphor screen.

A potential white-light-emitting $Ca_xSr_{1-x}Al_2O_4$:Tb^{3+}:Eu^{3+} phosphor was synthesized by a combustion method using metal nitrates as precursors and urea as a fuel by Shaat et al. [48]. The XRD patterns from samples showed phases associated with monoclinic structures of $CaAl_2O_4$ and $SrAl_2O_4$. White photoluminescence with the CIE coordinates ($x = 0.343$, $y = 0.325$) was observed when the phosphor was excited at 227 nm using a monochromatized xenon lamp. The white PL was a result of the combination of blue and green line emissions from Tb^{3+} and red line emission from Eu^{3+}. The structure and PL properties of this phosphor are reported.

8.1.4 Past, Present, and Future Scenario of SSL

8.1.4.1 Early 1960s to Late 1990s: The Monochrome Era

LEDs first appeared on the lighting scene in the early 1960s, in the form of red diodes (see Fig. 8.3). Pale yellows and greens followed. As red LEDs improved, they began appearing in products as indicator lights and in some of the first pocket calculators. The appearance of blue LEDs in the 1990s led to the first white LEDs, which were made by coating blue LEDs with phosphor. Shortly thereafter, green, blue, and red LEDs were combined to produce white light. With the availability of white light, LEDs could now be designed for general lighting, but to realize the full potential of LEDs, vast efficiency improvement was needed.

8.1.4.2 2000–2010: LED General Illumination

In 2000, DOE and private industry partners pushed white LED technology forward with the intention to develop a high-efficiency LED packaged device. At the start, white LED devices were no more efficient than the incandescent bulb. By 2010, a comparable warm white LED replacement lamp with good color rendering showed a steady-state efficacy of about 62 lm/W compared to about 13 lm/W for incandes-

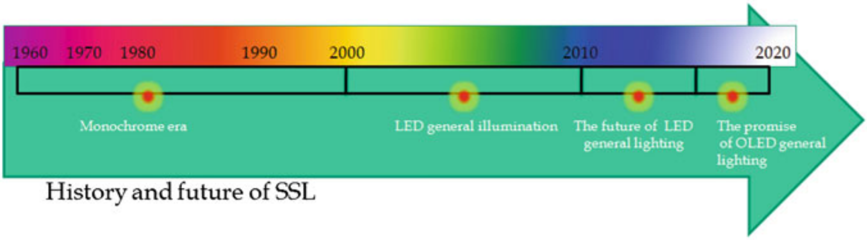

Fig. 8.3 History to future of solid-state lighting (*Source* http://www1.eere.energy.gov/buildings/ssl/sslbasics_randd.html)

cent: about three to four times more efficient, with similar quality warm light. In terms of packaged LED components, lab efficacies of 200 lm/W were demonstrated in 2010, with commercially available cool white devices producing efficacies as high as 132 lm/W.

8.1.4.3 2011–2015: The Future of LED General Lighting

Researchers believe the maximum achievable efficacy for packaged LED devices is around 250 lm/W, depending on the color temperature. Rapid progress will continue as the DOE and industry partnership pushes this technology to its efficiency limit, expected to be reached by about 2020. Properly designed LED luminaires could achieve efficacies over 200 lm/W, or up to 15 times that of incandescent lighting with improvements in luminaire components that can add to loss of light and power. LEDs, although expensive now, will continue to fall in price as new and better ways to package and manufacture them are perfected. The upward trend in the prize of rare-earth elements, which is an integral part of the LED, is, however, a point of serious concern.

8.1.4.4 2013–2018: The Promise of OLED General Lighting

While LEDs act as concentrated sources of bright light, OLEDs can be configured as larger area, more diffuse light sources. These may be more practical for general ambient lighting or, if on a flexible base material, can be shaped and integrated more tightly into architectural designs. Improvements in OLED light output continue, with reports of up to 68 lm/W for small "panel" devices that can be combined into luminaire products. While OLED efficiencies are on track to catch up with LEDs over the next several years, other challenges remain, including making larger panels of about 200 cm^2, and addressing environmental stability, lifetime, and, above all, cost and manufacturability. As soon as these challenges are overcome, OLED products will appear on the market, to compete with incumbent lighting.

8.2 Conclusions

As LED technology approaches its fiftieth anniversary it appears well positioned to penetrate the general lighting market and change the world as we know it. LED-based light sources promise to provide reduced energy consumption, longer operating lifetime (and thus reduced waste), and no generation of materials known hazardous to the environment such as lead and mercury. In addition, the low-voltage drive and fast switching speed allowed by LEDs means lighting for the future could look very different than what we know today, and may include dynamic control features for automatic mood setting or tuning of light intensity and color to improve workforce productivity or simply to elevate people's moods. These additional features, combined with the energy savings and other "green" aspects, ensure that LED-based solid-state lighting has a very bright future.

References

1. C. Feldmann, T. Justel, C.R. Ronda, P.J. Schmidt, Inorganic luminescent materials: 100 years of research and applications. Adv. Funct. Mater. **13**, 511 (2003)
2. G. Blasse, B.C. Grabmaier, *Luminescent Materials* (Springer, Berlin, 1994)
3. C.R. Ronda, Phosphors for lamps and displays: an applicational view. J. Alloy Compd. **225**, 534 (1995)
4. B. Henderson, G.F. Imbusch, *Optical Spectroscopy in Inorganic Solids* (Clarendon, Oxford, 1998)
5. Basic Research Needs for Solid-state Lightning, Report of the Basic Energy Sciences Workshop on Solid-State Lighting, 22–24 May, 2006, http://science.energy.gov/~/media/bes/pdf/reports/files/ssl_rpt.pdf
6. S. Ye, F. Xiao, Y.X. Pan, Y.Y. Ma, Q.Y. Zhang, Mat. Sci. Eng. Rep. **71**(1), 1–34 (2010)
7. S. Nakamura, G. Fasol, Proc. SPIE **26**, 3002 (1997)
8. S. Zhang, Y. Huang, Y. Nakai, T. Tsuboi, H.J. Seo, J. Am. Ceram. Soc. **94**, 2987 (2011)
9. L. Elammari, M. El Koumiri, I. Zschokke-Gränacher, B. Elouadi, Ferroelectrics **158**, 19 (1994)
10. C. Qin, Y. Huang, L. Shi, G. Chen, X. Qiao, H.J. Seo, J. Phys. D Appl. Phys. **42**, 185105 (2009)
11. S. Zhang, Y. Nakai, T. Tusboi, Y. Huang, H.J. Seo, Inorg. Chem. **50**, 2897 (2011)
12. Z.C. Wu, J.X. Shi, J. Wang, M.L. Gong, Q. Su, J. Solid State Chem. **179**, 2356 (2006)
13. Y.S. Tang, S.F. Hu, C.C. Lin, N.C. Bagkar, R.S. Liu, Appl. Phys. Lett. **90**, 151108 (2007)
14. S. Ye, Z.S. Liu, J.G. Wang, X.P. Jing, MRS Bull **43**, 1057 (2008)
15. Z.D. Hao, J.H. Zhang, X. Zhang, X.Y. Sun, Y.S. Luo, S.Z. Lu, Appl. Phys. Lett. **90**, 2611 (2007)
16. Y. Jiang, J. Chen, Z. Xie, L. Zheng, Mater. Chem. Phys. **120**, 313 (2010)
17. A. Lira, A. Mendez, L. Dagdug, H.S. Murrieta, U. Caldino, Phys. Status Solidi B **212**, 199 (1999)
18. S.J. Ramirez, E. Madrigal, F. Ramos, U.C. Garcia, J. Lumin. **71**, 169 (1997)
19. S. Choi, Y.J. Yun, H.-K. Jung, Mater. Lett. **75**, 186 (2012)
20. S. Zhang, Y. Huang, Y. Nakai, T. Tsuboi, H.J. Seo, J. Am. Ceram. Soc. **94**(9), 2987 (2011)
21. C. Guo, L. Luan, X. Ding, F. Zhang, F.G. Shi, F. Gao, L. Liang, Appl. Phys. B **95**, 779 (2009)
22. F.Q. Ren, D.H. Chen, Appl. Phys. B **98**, 159 (2010)
23. M. Shang, G. Li, D. Geng, D. Yang, X. Kang, Y. Zhang, H. Lian, J. Lin, J. Phys. Chem. C **116**, 10222 (2012)
24. J. Alkemper, H. Fuess, Z. Kristallogr. **213**, 282 (1998)
25. J. Lü, Y. Huang, L. Shi, H. J. Seo, Appl. Phys. A **99**, 859 (2010)
26. H. Masai, T. Fujiwara, S. Matsumoto, Y. Takahashi, K. Iwasaki, Y. Tokuda, T. Yoko, Opt. Lett. **36**, 2868 (2011)
27. Z. Pan, Lu.Yi.-Ying, F. Liu, Nat. Mater. **11**, 58 (2012)
28. X. He, J. Zhou, N. Lian, J. Sun, M. Guan, J. Lumin. **130**, 743 (2010)
29. Y. Guo, M. Sun, W. Guo, F. Ren, D. Chen, Opt. Laser Technol. **42**, 1328 (2010)
30. S.C. Gedam, S.J. Dhoble, R.B. Pode, J. Lumin. **132**, 2693 (2012)
31. C. Guo, M. Li, Y. Xu, T. Li, Z. Ren, J. Bai, Appl. Surf. Sci. **257**, 8836 (2011)
32. L. Zhang, Z. Lu, H. Yang, P. Han, N. Xu, Q. Zhang, J. Alloys Comp. **512**, 5 (2012)
33. J.S. Kim, H.J. Song, H.S. Roh, D.K. Yim, J.H. Noh, K.S. Hong, Mater. Lett. **79**, 112 (2012)
34. F.G. Meng, X.M. Zhang, H.J. Seo, Opt. Laser Technol. **44**, 185 (2012)
35. G. Ju, Y. Hu, L. Chen, X. Wang, Z. Mu, H. Wu, F. Kang, Opt. Laser Technol. **44**, 39 (2012)

36. C. Cai, W. Xie, L. Hao, X. Xu, S. Agathopoulos, Mater. Sci. Eng. B **177**, 635 (2012)
37. H. Xianghong, G. Mingyun, L. Zhongchun, S. Tongming, L. Ning, Z. Quanfa, J. Rare Earths **28**, 878 (2010)
38. C. Wan, J. Meng, F. Zhang, X. Deng, C. Yang, Solid State Commun. **150**, 1493 (2010)
39. S. Xiaoli, H. Yanlin, Y. Jie, S. Liang, Q. Xuebin, H.J. Seo, J. Rare Earths **28**, 693 (2010)
40. Y.C. Chiu, W.R. Liu, C.K. Chang, C.C. Liao, Y.T. Yeh, S.M. Jang, T.M. Chen, J. Mater. Chem **20**, 1755 (2010)
41. P. You, G. Yin, X. Chen, B. Yue, Z. Huang, X. Liao, Y. Yao, Opti. Mat. **33**, 1808 (2011)
42. H.S. Roh, S. Hur, H.J. Song, I.J. Park, D.K. Yim, D.-W. Kim, K.S. Hong, Mater. Lett. **70**, 37 (2012)
43. I.S. Cho, D.K. Yim, C.H. Kwak, J.S. An, H.S. Roh, K.S. Hong, J. Lumin. **132**, 375 (2012)
44. Q. Liu, Y. Liu, Z. Yang, X. Li, Y. Han, Spectrochimica Acta Part A **87**, 190 (2012)
45. W. Zhao, S. An, B. Fan, S. Li, Y. Dai, J. Lumin. **132**, 953 (2012)
46. Y.Y. Luo, D.S. Jo, K. Senthil, S. Tezuka, M. Kakihana, K. Toda, T. Masaki, D.H. Yoon, J. Solid State Chem. **189**, 68–74 (2012)
47. Y.-H. Yun, K.-Y. Kim, U.-K. Paik, Ceram. Int. **38**, 1599 (2012)
48. K.K. Shaat, H.C. Swart, O.M. Ntwaeaborwa, Opt. Mater. Express **2**(7), 962 (2012)

Index

K. N. Shinde et al., *Phosphate Phosphors for Solid-State Lighting*,
Springer Series in Materials Science 174, DOI: 10.1007/978-3-642-34312-4,